CHARACTERIZATION OF POLYCRYSTALLINE MICROSTRUCTURE USING ULTRASONIC NONLINEARITY PARAMETER

by

SAJU T ABRAHAM

ENGG02201304007

Indira Gandhi Centre for Atomic Research, Kalpakkam

A thesis submitted to the

Board of Studies in Engineering Sciences

In partial fulfillment of requirements for the Degree of

DOCTOR OF PHILOSOPHY

of

HOMI BHABHA NATIONAL INSTITUTE

October, 2020

Homi Bhabha National Institute

Recommendations of the Viva Voce Committee

As members of the Viva Voce Committee, we certify that we have read the dissertation prepared by Saju T Abraham entitled "Characterization of Polycrystalline Microstructure using Ultrasonic Nonlinearity Parameter" and recommend that it may be accepted as fulfilling the thesis requirement for the award of Degree of Doctor of Philosophy.

Chairman – Dr. S. Murugan	S. Murugan 16.2.2021
Guide / Convener – Dr. B. Venkatraman	16/2/2021
Co-guide – Dr. Shaju K. Albert	16/2/2021
Examiner – Dr. S. Gopalakrishnan	S. Gopalakrishnan 28/2/2021
Member 1 – Dr. V. S. Srinivasan	V.S. Srinivasan 16/2/2021
Member 2 – Dr. Anish Kumar	16/2/2021
Member 3 – Dr. Krishnan Balasubramaniam	16/02/2021

Final approval and acceptance of this thesis is contingent upon the candidate's submission of the final copies of the thesis to HBNI.

We hereby certify that we have read this thesis prepared under our direction and recommend that it may be accepted as fulfilling the thesis requirement.

Date: 16.02.2021

Place: Kalpakkam

16/2/2021	16/2/2021
Signature	**Signature**
Co-Guide	**Guide**

STATEMENT BY AUTHOR

This dissertation has been submitted in partial fulfilment of requirements for an advanced degree at Homi Bhabha National Institute (HBNI) and is deposited in the Library to be made available to borrowers under rules of the HBNI.

Brief quotations from this dissertation are allowable without special permission, provided that accurate acknowledgement of source is made. Requests for permission for extended quotation from or reproduction of this manuscript in whole or in part may be granted by the Competent Authority of HBNI when in his or her judgment the proposed use of the material is in the interests of scholarship. In all other instances, however, permission must be obtained from the author.

Saju T Abraham

DECLARATION

I, hereby declare that the investigation presented in the thesis has been carried out by me. The work is original and has not been submitted earlier as a whole or in part for a degree / diploma at this or any other Institution / University.

Saju T Abraham

List of Publications arising from the Thesis

Journal

1. A Novel Multi-Frequency Nonlinear Ultrasonic Approach for the Characterization of Annealed Polycrystalline Microstructure, Saju T Abraham, S. Shivaprasad, N. Sreevidya, C.R. Das, S.K. Albert, B. Venkatraman, Krishnan Balasubramaniam, Metallurgical and Materials Transactions A, 50A (2019), pp. 5567 – 5573 [https://doi.org/10.1007/s11661-019-05478-5]
2. Characterization of Heterogeneous Microstructure in Large Forged Products Using Nonlinear Ultrasonic Method, Saju T Abraham, S. Shivaprasad, C.R. Das, S.K. Albert, B. Venkatraman, Krishnan Balasubramaniam, Materials Science and Technology, Vol. 36, Issue 6 (2020), pp. 699 – 708 [https://doi.org/10.1080/02670836.2020.1732077]
3. Effect of Grain Size Distribution on the Acoustic Nonlinearity Parameter, Saju T Abraham, S. Shivaprasad, C.R. Das, S.K. Albert, B. Venkatraman, Krishnan Balasubramaniam, Journal of Applied Physics, 127(18), 185102 (2020) [https://doi.org/10.1063/1.5119760]

Conferences

1. "Nonlinear ultrasonic testing for the evaluation of micro damages in materials", Saju T Abraham, S Shivaprasad, N Raghu, B Anandapadmanaban, B Venkatraman and Krishnan Balasubramaniam; NDE-2014, Pune, 4-6 December 2014, CP-202
2. "Characterization of polycrystalline materials by non-linear ultrasonic methods", Saju T Abraham, S. Shivaprasad, B. Anandapadmanaban, B. Venkatraman, Krishnan Balasubramaniam, NDE-2016, Thiruvananthapuram, 14-17 December 2016, A00171
3. "Characterization of Grain Size Distribution Using Nonlinear Ultrasonic Parameter", Saju T Abraham, Shivaprasad S, Athmalingam S, Venkatraman B, Krishnan Balasubramaniam, NDE-2019, Bangalore, 5-7 December 2019, CP-124.

Saju T Abraham

DEDICATIONS

To

my

family

for their losses.

ACKNOWLEDGEMENTS

At the very outset, I convey my sincere gratitude to my guide and mentor ***Dr. B. Venkatraman***, Distinguished Scientist and Director, Safety, Quality & Resource Management Group, Indira Gandhi Centre for Atomic Research (IGCAR) for his guidance, encouragement and wholehearted support during the research work. The inspiration he provided throughout the career and the freedom given by him during this research has brought the thesis to the level it has reached.

I would like to extend my heartfelt gratitude to my co-guide ***Dr. Shaju K. Albert***, Outstanding Scientist and Director, Metallurgy & Materials Group, IGCAR for his encouragement, motivation and patience during the research work. The discussions which we had while preparing the manuscripts and the thesis have made this research into this level.

I express my immense gratitude from the bottom of my heart to ***Prof. Krishnan Balasubramaniam***, Head, Centre for Nondestructive Evaluation and Institute Professor, Indian Institute of Technology, Madras for allowing me to avail the facilities and the valuable discussions we had without which this thesis would not have completed.

I express my sincere gratitude to my doctoral committee ***Dr. B.P.C Rao*** (former Chairman, DC), Chairman ***Dr. S. Murugan*** and members ***Dr. V. S. Srinivasan*** and ***Dr. Anish Kumar*** for regularly evaluating the progress of the research work and giving many useful suggestions. Special thanks to Dr. Anish Kumar for his remarkable comments during the pre-synopsis presentation which has enhanced the clarity of the thesis further.

I acknowledge the contributions of ***Dr. C. R. Das***, MDTD, IGCAR for the motivation he has provided and the useful discussions we had while preparing the manuscripts. I also thank him for teaching me the art of specimen preparations and microscopy which was the backbone of this research. I would like to acknowledge former Head, QAD ***Shri. B. Anandapadmanaban*** for providing facilities and permission to continue research.

I acknowledge ***Dr. S. Shivaprasad***, Research Associate, University of Bristol (former research scholar at CNDE, IIT Madras) for his help in the data analysis part and providing all necessary supports on all weekends for several years during the course of the experiments at CNDE. His efforts on soft computing made the analysis of a large number of data files very comfortable and faster.

I take this opportunity to express my gratitude to ***Dr. Thomas Paul***, PMD and ***Smt. Sreevidya***, MDTD in helping me to prepare the metallographic specimens at the beginning of the research and acquiring the EBSD images. I also express my gratitude to ***Shri. A. Viswanath***, NDED for his valuable suggestions and sharing his experience in the field of nonlinear ultrasonics which has shown me the correct path to proceed. A special thanks go to him for the timely and fruitful corrections made on the final draft of the thesis. I am thankful to **Dr. G. K. Sharma** for his valuable comments on the final draft of the thesis. Also, the discussions with ***Shri. Anup Kumar***, SEHD and ***Dr. Anuraj V. L.***, RND on the physical aspects of nonlinear ultrasonics and elastic wave propagation are worth mentioning.

I would like to thank ***Shri. M. Krishnamoorthy***, Head, FS/CWD, ***Shri. Ramesh Babu***, Head, MS/CWD and ***Shri. Praveen Kumar***, Head, MIS/CWD, ***Shri. P. Karuppasamy***, MS/CWD, ***Shri. P. Arumugam***, EDSS/PIED for their timely help in making the specimens ready. I also express gratitude for my QAD colleagues for sparing me from works whenever required.

Finally, I remember my father ***Shri. O. T. Abraham*** and my mother ***Smt. Thressiamma*** for their patience, love and continuous prayers for the completion of the thesis work. I express my sincere and heartfelt thanks and appreciation to my wife ***Ms. Manju,*** for her love, commitment and the sacrifices she made to make this achievement a reality. It is also my duty to put on record the love and affection shown by my son ***Aiden*** and keeping my goals in his daily prayers. I feel sorry to my younger son ***Edwin*** that I was not available to him during the weekends till date. They understood my needs and spared me and kept me in their prayers during these years.

Above all, the grace of Almighty who granted me the wisdom, health and provided all necessary requirements to undertake and complete this research work is acknowledged.

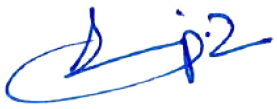

Saju T Abraham

CONTENTS

LIST OF FIGURES

LIST OF TABLES

LIST OF ABBREVIATIONS

ANP	Acoustic Nonlinearity Parameter
AISI	American Iron and Steel Institute
ASME	American Society of Mechanical Engineers
ASTM	American Society for Testing and Materials
DSO	Digital Storage Oscilloscope
EBSD	Electron Backscatter Diffraction
EDS	Energy Dispersive Spectroscopy
IPF	Inverse Pole Figure
MBE	Magnetic Barkhausen Emission
NDE	Non-destructive Evaluation
NLU	Nonlinear Ultrasonics
PAGS	Prior Austenite Grain Size
PFBR	Prototype Fast Breeder Reactor
SAFT	Synthetic Aperture Focusing Technique
SFE	Stacking Fault Energy
SNAP	System for Nonlinear Acoustic Phenomena
TOFD	Time of Flight Diffraction
XRD	X-Ray Diffraction

Chapter 8
Conclusions

8.1 Conclusions

This research work experimentally investigated the influence of the grain size distribution and the associated scattering regimes on the acoustic nonlinearity parameter. The combined effect of grain size variation and the plastic deformation on the polycrystalline materials also studied using nonlinear ultrasonics. To this end, the thesis explored the microstructural characterization on the annealed, forged and deformed microstructures of austenitic stainless steel material using the ultrasonic nonlinearity parameter. A novel multi-frequency nonlinear ultrasonic methodology is introduced in this thesis for a reliable characterization of the heterogeneous microstructures in polycrystalline materials.

The key findings this thesis has made are concluded below.

1. The acoustic nonlinearity parameter β was found reducing linearly with grain growth in the Rayleigh scattering regime and deviating from this linearity in the Rayleigh to stochastic transition zone. A reliable evaluation of grain size in polycrystalline materials using a single frequency measurement, therefore, requires the Rayleigh scattering condition to be satisfied so that the β would be independent of the scattering losses.
2. The multi-frequency approach reveals that the change in the order of β_{ω_i} or the deviation in $\Delta\beta_{\omega_{i,j}}$ with grain coarsening can be used as a precursor for undesired grain growth in polycrystalline materials. For a set of input frequencies (ω_i), these changes indicate that the mean grain size has deviated from the Rayleigh scattering regime corresponding to those frequencies. This approach can be employed as an efficient tool for rapid screening of materials with unknown process history where wide variations and distributions of grain sizes are expected. The frequencies can be chosen such that the event at which the nonlinearity parameter deviates from its linear trend may be set as the boundary where the grain size-dependent properties are extinct. Hence, this methodology can be brought out as a stand-alone technique to be deployed to characterize the microstructural variations.

3. The results further infer that the conventional single-frequency NLU measurement would not be reliable against the grain size variation or distribution as the multi-frequency approach is required to observe the changes in the linear trend of β_{ω_i} and changes in the order of β_{ω_i} and thereby the deviation in the $\Delta\beta_{\omega_{i,j}}$ with grain coarsening. The multi-frequency NLU methodology has a reasonable correlation with the microstructure, and its reliability was evaluated against the heterogeneous microstructure in large diameter forgings.
4. A study on the effect of grain size distribution on the acoustic nonlinearity parameter has revealed that the material with wide distribution exhibited reduced nonlinearity. The result infers the significance of considering the distribution width in characterizing the microstructural features from the nonlinear response of the material. Though the results discussed here are in the context of the Rayleigh scattering regime, a similar influence of the distribution on β is expected for other scattering regimes also.
5. The nonlinearity parameter is very sensitive to the variations in grain size, even in the presence of deformed microstructure. Hence, nonlinear ultrasonics is an efficient tool for characterizing the combined effect of grain size variations and plastic deformation in metallic materials.

From the present research, it is understood that the role of grain size distributions and thereby the scattering regimes need to be considered while interpreting the results based on the measured acoustic nonlinearity parameters in single-phase polycrystalline materials. This understanding is vital for reliable characterization of microstructural features and to enhance the consistency in structure-property correlations using nonlinear ultrasonics. The results obtained in this thesis infer that, the multi-frequency approach can be used as a reliable tool to

1. Measure the grain size in a polycrystalline material
2. Evaluate the grain size distribution and heterogeneity in the microstructure
3. Assess the effect of deformation in polycrystalline structural materials.

These understandings are very important in solving the inverse problems in nonlinear ultrasonics, leading to a non-destructive evaluation method of polycrystalline materials with a minimum of a priori information.

SUMMARY

Grain size and its distribution are the important parameters that influence the properties of metals and alloys. However, in large components, grain size variation occurs across the thickness or diameter, leading to corresponding material properties variations. Though in-situ metallography can be used to measure the grain size on the surface, estimation of grain size variations across the thickness is not feasible. In this context, the non-destructive evaluation (NDE) methods find widespread applications in material characterization due to their faster and reliable volumetric evaluation capabilities. Among several complementary NDE methods, ultrasonic methods are commonly employed in manufacturing and process industries owing to its applicability on any material and competence of real-time analysis. However, the traditional linear ultrasonic methods such as attenuation or velocity measurements have low sensitivity towards certain microstructural features, and their use is restricted on coarse-grained materials. In such cases, the nonlinear ultrasonic (NLU) method is an ideal choice. The response of the NLU parameters to microstructural changes is more sensitive than the conventional ultrasonic methods. Therefore, the NLU has become an active area of research with the objective of characterizing materials at various processing stages and also to understand service exposed degradation mechanisms. There is a significant amount of literature on the use of nonlinear ultrasonics for material characterization, and evaluation of grain size variation in polycrystalline structural materials is one of the areas in which unique features of NLU can be exploited.

The grain size distribution in a polycrystalline material is, most often, lognormal, and the larger the mean grain size, the wider is the distribution. The mean grain size is often used to describe the microstructure to correlate with the mechanical properties. However, the lognormal distribution of the grain size results in different acoustic scattering regimes to coexist in a polycrystalline material. Different scattering regimes can have different effects on the NLU parameters introducing uncertainty in the correlation of these parameters with the grain size variations. Therefore, characterization of such material using a single-frequency nonlinear response, assuming a mean grain size, is insufficient. In addition, it is quite possible in industries that the metallic components are supplied not always in solution annealed condition and hence deformation assisted microstructural changes may exist. Also, the heat treatment and processing conditions like annealing, normalising, ageing and hot/cold working can alter the microstructural features such as dislocation density, precipitates and secondary phases in

addition to the inherent grain size variations. Therefore, it is essential to understand how the nonlinearity parameter would be affected in the presence of not fully annealed or deformed microstructure that could be present in a component. This understanding will help to consider nonlinear ultrasonics as a potential nondestructive evaluation tool for inspection of the materials, primarily for the evaluation of the variations in grain size. Therefore, the present thesis dwells into these areas and introduces a novel multi-frequency nonlinear measurement approach.

The multi-frequency methodology presented in this thesis significantly improves the reliability of structure-property correlations in polycrystalline materials. This approach allows visualising the grain size variations and the associated scattering regimes from the nonlinear response of the material. In the Rayleigh scattering regime, the nonlinearity parameter decreases linearly with grain growth and deviates from its linearity in the Rayleigh-to-stochastic transition regime. Experimental and numerical investigations have shown that the distribution of grain size also has a considerable influence on the measured acoustic nonlinearity parameter. It is also demonstrated that, even though the NLU parameter is affected by the plastic deformation in the material, it is possible to use this parameter to study the variation of grain size in materials subjected to different levels of plastic deformation. Such investigations, which have never been explored, are important in developing nonlinear ultrasonics as a robust nondestructive evaluation technique for microstructural characterization that can be employed for field applications which include inspection, quality control, remnant life assessment and failure analysis.

Chapter 1
Introduction

1.1 Background

In metals and alloys and even in structural ceramics, grain size is an important parameter that influences the mechanical properties, thereby affecting material strength as shown by Hall[1] and Petch[2] through their famous Hall-Petch relation. Among different strengthening mechanisms available for metals and ceramics, reducing the grain size is the only mechanism that serves the twin purposes of increasing strength and ductility. However, absolute uniformity in the grain size is most unlikely in regular industrial practices. In polycrystalline materials, the grain size is seldom uniform and follow a lognormal distribution.[3] Appropriate grain size is important not only for ensuring the properties intended for the applications but also for successfully processing the material from the initial cast structure (after solidification) to the finished product. In fact, for metal forming operations, appropriate grain size and its distribution are critical to producing intermediate products that undergo further processing.

Metallography is the most widely used technique employed to measure grain sizes. Conventional microscopy techniques,[4] essentially destructive, are not always feasible during manufacturing or in finished components. The microscopy results are based on the data generated on a small set of representative test coupons. However, anomalies in the manufacturing processes can challenge the validity of the assumption that a small set of samples is representative of a batch of materials or a component in terms of microstructural properties. In reality, such a small set of samples would indicate an inaccurate statistical estimation of the properties of the actual component. On the other hand, the in-situ techniques on the components involve time-consuming surface preparation followed by replica development and microscopic analysis and therefore not been regularly practised on-site except for the life extension program. Further, the microscopy techniques are primarily confined to the surface and not suitable to study the grain size variation across the thickness. In this context, non-destructive evaluation (NDE) methods find extensive applications due to their faster and reliable volumetric evaluation capabilities. The NDE methods play a vital role in the uninterrupted and secure operation of any machinery. Ultrasonic techniques are the most

common among several complementary NDE methods due to their applicability to any material, the competence of real-time analysis and complete volumetric evaluation, which leads to a reasonable correlation between the structure and property. This technique is also well recognized for use during in-service inspection to detect the nucleation and growth of defects and to assess its acceptance and service life. Conventional ultrasonic methods used in NDE rely on the linear theory of elasticity where the field variables like stress, strain and displacement are linearly related and approximated by the first-order term of Hook's law. These ultrasonic methods measure a few specific parameters like reflectivity, velocity and attenuation. The material properties or discontinuities are characterized based on the characteristic property of such parameters. However, studies on several metallic and non-metallic materials showed that the nonlinear ultrasonic (NLU) response is the most sensitive indicator of degradations compared to the linear attenuation and velocity measurements.[5] Nonlinear ultrasonics rely on the generation of harmonics from the discontinuities in the lattice continuum. When a monochromatic elastic wave propagates through a medium, the waveform gets distorted due to the interactions with the discontinuities such as dislocations, precipitates, grain boundaries and micro-cracks. Such distortions generate harmonics of the fundamental frequency. The acoustic nonlinearity parameter is a measure of such distortions which is calculated from the amplitudes of the fundamental and harmonic components. The nonlinearity parameter can, therefore, represent the state of the material microstructure reliably. However, in nonlinear ultrasonics, the amplitude of the harmonics is orders of magnitude smaller compared to that of the fundamental component, and hence there must be a compromise on the selection of the frequencies based on attenuation and propagation distance of the medium. The NLU methods nowadays are widely used in characterizing materials at various processing stages[6–15] and also to understand the service exposed degradation mechanisms.[16–22]

1.2 Scope of the research

The scope of the present research work is to demonstrate the feasibility of the nonlinear ultrasonic technique for characterizing the grain size variations and its distribution in bulk metallic materials. In a polycrystalline material, the elastic waves undergo attenuation, which depends on the wavelength and size of the scatterer (grains), defining the so-called scattering regimes.[23] Because of the difference in their wavelength, the attenuation of the fundamental and harmonic components used in nonlinear ultrasonics is different in different scattering regimes. Therefore, the size and distribution of grain size, as well as the frequency of the

elastic waves, would influence the nonlinearity parameter as this parameter depends on the simultaneous measurements of the fundamental and harmonic amplitudes. There have been attempts for correction factors to compensate for the attenuation losses,[24–26] but these procedures require simultaneous estimation of the attenuation coefficients and the nonlinearity parameter. Such efforts are time-consuming, tedious and challenging to implement when the material is coarse-grained or thick. Also, such correction procedures are not feasible in heavy forgings or castings where all possible variations in grain sizes coexist within a single component. The nonlinearity parameter, which is conventionally measured using a single excitation frequency, would, therefore, be insufficient to characterize such a microstructure accurately. In addition, characterization of grain size variations in the components which are undergone deformation is challenging as both grain size and the deformation-induced microstructure influence the nonlinear response of the elastic waves.

Therefore, it is appropriate to investigate the effect of scattering regimes and the deformation in polycrystalline materials using ultrasonic nonlinearity parameter. A deeper understanding of the effect of different scattering regimes on the nonlinearity parameter will lead to more efficient ways of interpreting the wave-material interaction mechanisms. In characterizing highly heterogeneous structural materials and improving the correlations between structure and property, this understanding may effectively be utilized.

1.3 Objective

The primary objective of the present research is to characterize the grain size variations and the plastic deformation in polycrystalline materials using nonlinear ultrasonics, taking into account the inherent attenuation losses of the elastic waves at the fundamental and harmonic frequencies. Specifically, the objectives of the research are summarized as follows:

- Experimental investigations on the effect of scattering regimes on the measured acoustic nonlinearity parameter,
- Characterization of the microstructural heterogeneity in a component where variations in grain size coexist,
- Investigations on the effect of grain size distributions on the acoustic nonlinearity parameter, and
- Study of the combined effect of the grain size variations and the plastic deformation in polycrystalline structural materials using the acoustic nonlinearity parameter.

It is to be noted that the acoustic nonlinearity parameter used in this thesis is derived from the fundamental and second harmonic components, which is referred to as the quadratic nonlinearity parameter.

1.4 Organization of the thesis

The thesis comprises Nine chapters as outlined below:

Chapter 1 consists of the introduction to the problem and the scope and objective of the research. In **Chapter 2**, a comprehensive review of conventional, as well as non-linear ultrasonic methods used in the non-destructive evaluation of materials are presented. Formulation of the acoustic nonlinearity parameter and the factors affecting this parameter is discussed in detail. Beyond this, the chapter presents a systematic classification of microstructural characterization using the acoustic nonlinearity parameter. This chapter also describes the gap area found in the literature which has been taken up for this research. In **Chapter 3,** experimental procedures, materials and characterization methods followed in this thesis are discussed in detail. In **Chapter 4**, the effect of scattering regimes on the nonlinearity parameter is investigated on a set of annealed microstructures of SS304. A multi-frequency non-linear measurement approach is introduced for the first time in this chapter. The frequency dependence of the nonlinearity parameter is discussed in detail and correlated with the scattering related losses to the fundamental and harmonic frequency components. In **Chapter 5,** the observations derived for the annealed microstructures were extended to characterize forged materials in which all sort of grain size variations coexist in a component. The effect of grain size distribution, combined with the scattering regime, is explored for the characterization of the heterogeneous microstructure. **Chapter 6** investigates numerically and experimentally the effect of grain size distribution on the nonlinearity parameter within the context of a single scattering regime. **Chapter 7** investigates the use of non-linear ultrasonics to study the combined effect of grain size variation and plastic deformation in polycrystalline materials. **Chapter 8** presents the summary and conclusions drawn based on results and discussion. In **chapter 9**, potential areas of future work plans are discussed.

Chapter 2
Background and Literature Review

2.1 Introduction

Non-destructive evaluation (NDE) of materials is well recognized and well addressed in the design codes and standards; for example, ASME (American Society of Mechanical Engineers) Boiler and Pressure Vessel Code Section V and the associated ASTM (American Society for Testing and Materials) Standards. Among several NDE methods, the ultrasonic testing methods are the most versatile technique used for defect detection and microstructural characterization. Based on the interaction mechanism of the ultrasonic waves within a material, the ultrasonic NDE methods are broadly classified into linear and nonlinear ultrasonics. The linear ultrasonic methods are commonly used for defect detection, whereas the nonlinear methods are implemented in the microstructural characterization.

This chapter reviews the applications of linear and nonlinear ultrasonic methods in the non-destructive evaluation of microstructural features in metallic materials. Advantages of nonlinear ultrasonics over linear methods are also discussed. A comprehensive review on the nonlinear elasticity, factors affecting the acoustic nonlinearity parameter and the microstructural characterization using this parameter will be covered in this chapter. Various aspects of the polycrystalline grain boundaries and harmonic generation are also discussed. The elastic wave propagation through a polycrystalline material and the directional effects on the harmonic amplitudes are illustrated using a finite difference approach. Finally, the influence of various scattering regimes on the nonlinearity parameter is highlighted, and few gap areas were identified for investigation.

2.2 Non-destructive evaluation using linear ultrasonic methods

Ultrasonic testing is the most preferred non-destructive evaluation method for the characterization of microstructure and properties of materials. With the advancement in electronics, the reflectivity, velocity and attenuation can be measured very accurately to correlate them with various material properties with a reasonable confidence level. Conventional ultrasonic NDE of materials relies on the linear theory of elasticity where the

field variable like stress, strain and displacement are linearly related. The applications of the linear ultrasonic NDE methods are broadly classified into two; defect detection and microstructural characterization.

2.2.1 Defect detection

For several decades, ultrasonic methods have been used in the identification and characterization of defects in materials.[27–29] The technological development of ultrasonic volumetric evaluation started from the manual straight beam pulse-echo inspection to the advanced imaging formats like B-, C- or D- scans and later the application of tomography methods like synthetic aperture focusing technique (SAFT) for 3D reconstruction of the data.[30] The major drawback associated with the pulse-echo inspection, especially on coarse-grained or thick components like forgings and castings, is the weak signal-to-noise ratio (SNR). Ricci et al.[31] described a pulse-compression method to improve the SNR and demonstrated it on forged steel structures with large dimensions and high attenuation. Senni et al.[32] compared the performance of the pulse-compression technique with the conventional pulse-echo method on forged steel products and showed that the chirp-based pulse-compression technique enhances the inspection capabilities. The chirp-based approach reduces the side lobes, which is a requirement in detecting tiny defects in large structures. However, inspection of the materials having larger dimensions is challenging due to an increase in attenuation, which limits the reliability of ultrasonic testing. The synthetic aperture focusing technique (SAFT) could improve the lateral resolution by extending the aperture of a transducer and processing several successive measurements, thereby focusing the ultrasound inside the object. It also reduces the backscattering effects from the coarse grain microstructure. Fendt et al.[33] demonstrated the application of SAFT combined with the pulse-echo technique to locate and quantify small defects in steel forgings. Nevertheless, the use of single/double crystal ultrasonic transducers in the pulse-echo examination of the components cost prolonged testing and evaluation time.

The phased array ultrasonic methods, however, could replace the requirements of multiple fixed-focus transducers with a single phased array probe.[34] Dupont-Marillia et al.[35] investigated the possibility of ultrasonic phased array inspection of forged steel blocks of dimensions up to 1000 mm. Using the CIVA simulation software, they have optimized the phased array probe and the ultrasonic wave propagation sequence in a total focusing method (TFM). Based on the results, a 32-element phased array probe was fabricated and used on a forged steel block of

dimension 777 mm. Alavudeen et al.[36] used phased array technique in the investigation of fatigue cracks formed under room temperature and sub-zero temperature. Though the defect detectability of the phased array method is much higher than that of the conventional pulse-echo method, the underlying reflection properties of sound waves limits its sensitivity against defects such as crack tips. In this context, the time of flight diffraction (TOFD) technique[37,38] is found suitable to detect the extremities of the crack tips. The TOFD method is not governed by the laws of reflection and hence possess better accuracy in the detection of crack tips compared to the reflection-based methods such as pulse-echo or phased array. Abraham et al.[39] were the first to construct a 3D profile of the crack tips in a forged 17-4 PH stainless steel rod of 100 mm diameter using the TOFD technique. Due to its reduced scanning time and increased volume coverage, TOFD is a better choice to be implemented on the components at elevated temperatures.[40]

The pule-echo technique, the phased array and the TOFD are sensitive to defects whose dimensions are of the order of a wavelength. Therefore, these techniques are not used in characterizing microstructural features. In this sense, ultrasonic velocity, attenuation and backscatter analysis are the better choices, as they are influenced by the microstructure.

2.2.2 Microstructure characterization

2.2.2.1 Velocity measurements

Propagation of elastic waves in a solid is the result of infinitely small displacements of integrated crystalline lattice in the material, maintaining the law of conservation of momentum. Knowing the distance x the wave propagates in the material in time t, the velocity can be determined using the relation $dv = dx/dt$. In an elastic continuum, the velocity of an elastic wave is related to Young's modulus (E), rigidity modulus (G) and the Poisson's ratio (υ) of the medium by the following relationships:

$$c_L = \sqrt{\frac{E}{\rho}\frac{1-\upsilon}{(1+\upsilon)(1-2\upsilon)}} \tag{2.1}$$

$$c_T = \sqrt{\frac{E}{\rho}\frac{1}{2(1+\upsilon)}} = \sqrt{\frac{G}{\rho}} \tag{2.2}$$

$$c_R = \frac{0.87 + 1.12\upsilon}{1 - \upsilon}\sqrt{\frac{E}{\rho}\frac{1}{2(1+\upsilon)}} \tag{2.3}$$

where, c_L, c_T and c_R are the speed of elastic waves in the longitudinal, transverse and Rayleigh modes respectively. Equations (2.1) to (2.3) imply that the modulus of elasticity and density of the medium determines the velocity and, therefore, less sensitive to the microstructural variations, like grain size, which does not change the modulus or density considerably. For example, only a 0.5% variation in the longitudinal velocity and 1.23% variation in the shear velocity was reported in annealed AISI 316 stainless steel for an increase of 183% in the grain size.[41] It was also reported a minimal variation (< 3%) between the cold worked and recrystallization conditions in modified austenitic stainless steel.[42] Further, in a study conducted by Dupont-Marillia et al.[43] on the variations of grain size from the surface (70 μm) to the core (700 μm) in large steel-ingots, a variation of < 2% in the phase-velocity was noted, and there was no consistent trend in group-velocity variations. Similarly, little variation in longitudinal velocity but a marginal change in shear velocity (< 2%) between martensite and pearlite phases in L80 steel has also been reported.[44] Insignificant variation in longitudinal wave velocity was also noted between the surface and the core of high strength steel[45] and in P91 steel with significant changes in grain size.[46] All these results illustrate the limitations of using the change in velocity as a reliable precursor to minor variations in the microstructural features.

2.2.2.2 Attenuation measurements

Attenuation is a cumulative effect of the scattering and absorption of elastic waves in a dissipative medium. The scattering arises from the fact that the material is not strictly homogeneous, while the absorption arises from the damping effects of the dislocations and internal friction. Scattering losses, however, are orders of magnitude higher than that due to the absorption and, hence, microstructural characterization of engineering materials using ultrasonic attenuation is focused mainly on the scattering mechanisms.[23,47–49] An elastic wave propagating in a medium can be written as

$$U(x,t) = U_0 e^{j(\omega t + kx)} \tag{2. 4}$$

with ω is the angular frequency and k is the wavenumber. If the wavenumber k is a complex quantity of the form $k = \zeta + j\alpha$ with ζ and α are being real quantities, the wave propagation can be written as

$$U(x,t) = U_0 e^{j(\omega t + \zeta x)} e^{-\alpha x} \tag{2. 5}$$

with $e^{-\alpha x}$ is the exponential attenuation with α as the coefficient of attenuation. The attenuation coefficients for the longitudinal and transverse mode of elastic waves in a crystalline medium are given in the following form:[50]

$$\begin{aligned} \alpha_L &= \alpha_{LL} + \alpha_{LT} \\ \alpha_T &= \alpha_{TT} + \alpha_{TL} \end{aligned} \tag{2.6}$$

where α_{ij} quantifies the energy lost by a coherent wave of mode i by scattering into a wave of mode j, where L corresponds with longitudinal and T corresponds with transverse. In Eq. (2.6) the individual contributions of each scattering mode are observed. Experimentally, the attenuation coefficients are determined from the frequency spectrum of the first ($u_1(\omega)$) and second ($u_2(\omega)$) back-reflected echoes of frequency ω using the relation[47]

$$\alpha(\omega) = \frac{1}{2x} ln\left[\frac{V_1(\omega)}{V_2(\omega)} R_A R_B \frac{D_2(\omega)}{D_1(\omega)}\right] \tag{2.7}$$

where $V_1(\omega)$ and $V_2(\omega)$ are the spectral amplitudes of the $u_1(\omega)$ and $u_2(\omega)$, $D_1(\omega)$ and $D_2(\omega)$ are the Lommel diffraction corrections to the $u_1(\omega)$ and $u_2(\omega)$, $R = (\rho_m c_{Lm} - \rho_w c_{Lw})/(\rho_m c_{Lm} + \rho_w c_{Lw})$ defines the reflection coefficients at the top (R_A) and bottom (R_B) surfaces in which c_{Lm} and c_{Lw} are the longitudinal velocity in material and water, respectively and ρ_m and ρ_w are the density of material and water.

Ultrasonic attenuation was used to determine the volume fraction of porosity in aluminium alloy A357 where the average pore size was in the order of 100 μm, and the pore concentration varied up to 6%.[51] Palanichamy et al.[41] showed a variation in ultrasonic attenuation (using 2 MHz longitudinal waves) to be >40% with increasing grain size from 60 μm to 170 μm (183%) on the contrary to minor variations (1.23%) in the velocity. This variation in attenuation is sufficient enough to distinguish marginal variations in the grain size using ultrasonic attenuation measurements. However, one of the drawbacks associated with the attenuation

measurement is that its efficiency is affected by the metallic and non-metallic phases and texture present in the material. For example, it was shown in titanium alloy forgings that a higher loss in back reflection was not related to the grain size but the basket-weave textures and their dimensions.[52] Similarly, a comparable attenuation in P91 steel having two different grain sizes due to the presence of delta ferrite in the martensitic matrix was reported.[46] Also, similar attenuation for bainite and perlite phases was reported even though they possess different morphology. In the lamellar duplex microstructure in pearlite steel, it was shown that the lamellar spacing determines the attenuation coefficients.[53] These results, therefore, suggest that prior microstructural information is a prerequisite to derive a quantitative interpretation from the attenuation measurements. Li et al.[54] have compared the sensitivities of ultrasonic velocity and attenuation measurements over a range of grain sizes from 70 μm to 143 μm in TP304 stainless steel and found that the attenuation is much more sensitive to the grain size than the ultrasonic velocity. But this method requires tedious signal pre-processing and hence possess limited implementation in the field. Nevertheless, velocity and attenuation measurements are generally being performed in an immersion bath which limits the feasibility of these techniques on large components which are in service. To overcome this drawback, Dong et al.[49] developed a laser-based technique to perform in-situ attenuation measurements. But this technique introduced considerable error in the standard deviation in the measurements of grain size compared to that observed from the microscopic methods such as electron backscatter diffraction (EBSD) and hence not viable to distinguish minor variations in the attenuation. Laser Doppler vibrometry is another method employed for material characterization. Maio et. al.[55] have used the LDV to assess the variations in the ultrasonic velocity of guided waves in composite structures and correlated with the delamination that occurred. However, the LDV is confined to the surface characteristics and limited by the surface reflectivity of the specimen and hence rarely used in the industrial scale.

In reality, measurements of both the velocity and attenuation require that the thickness of the material or wave travelling distance to be known precisely. It is also worth noting that the power-law dependence[23] of the attenuation coefficients on the grain size (D) and wavelength (λ) confines these measurements on to the fine-grained or homogeneous materials and lower thickness range. In this context, the ultrasonic backscatter method has got its attention and has been used for material characterization.

2.2.2.3 Backscatter analysis

The ultrasonic waves scattering from the microstructural features in structural materials have a detrimental effect on ultrasonic velocity and attenuation measurements. However, the backscattering carries vital information on the material microstructure and hence is relevant for material characterization. Backscattering occurs at the grain boundaries in a polycrystalline material due to the mismatch of crystalline anisotropy.[56] Significant amount of work has been reported in ultrasonic backscattering. A realistic backscatter model was developed by Rose[57] for the detection of alpha inclusions in titanium jet engine disks. Lobkis et al.[58] have obtained an analytical solution for the dependence of the backscatter signal on the frequency and average grain size, and the result was applied on Titanium alloy duplex microstructure. It was shown that the dominant factor for the backscattering is the interaction length of the grain in the direction of wave propagation instead of the cross-section. Dupond et al.[59] have used the backscatter technique to characterize the microstructure in the forged bars of Inconel 600 alloy of diameter 135 mm. Experimental studies carried out on the specimens with different grain sizes were validated with the modelling approach and found a one-to-one correlation. Yang and Rokhlin[60] have developed a backscatter model for textured polycrystalline materials. They have modelled the realistic textures for cubic polycrystals, and the numerical results were compared with the experimental data available in the literature. In a study conducted by Zhang et al.,[61] however, it was shown that the backscattering measurements are suitable for weak scattering materials like aluminium, whereas the attenuation measurements are useful for materials with large grains such as steel and copper.

One of the major limitations of this method is its reliability in the remnant life assessment. The microscopic imperfections serving as nuclei of the material degradation are considerably smaller than the acoustic wavelength used. Therefore, the backscatter or even the attenuation and velocity measurements are not sufficiently sensitive to the early stages of degradation or microstructure evolution and hence lead to uncertainty in a reasonable estimation of the mechanical properties required to assess the remaining life of the component. Compared with the attenuation and velocity measurements, the backscatter method has no requirement of parallel smooth surfaces and precisely known thickness. However, more complicated statistical methods such as the figure of merit,[62] singly scattered response,[63] doubly scattered response[64] etc. are required to correlate the backscatter signals from a different set of microstructures at different probe positions. The above limitations encountered in linear ultrasonic methods are

overcome in nonlinear ultrasonics (NLU). In addition, the nonlinear response is more sensitive indicator of degradation compared to the linear ultrasonics.[5]

2.3 Nonlinear ultrasonics

For the last few decades, the nonlinear ultrasonics has become an active area of research in the field of material science[65,66] and bio-medical engineering.[67] The basic principle of the nonlinear ultrasonics relies on the nonlinear elasticity of the medium which responding to a finite-amplitude monochromatic elastic wave during its propagation.

2.3.1 Nonlinear elasticity

Nonlinear elasticity is the theory of elasticity under finite deformation and anharmonic interatomic forces. In a periodic crystalline lattice, elastic properties are determined by the interatomic forces acting on each atom described by, for example, the Lennard-Jones empirical relation for the interatomic potential

$$V(r) = V_0 \left[\left(\frac{r_0}{r}\right)^{12} - \left(\frac{r_0}{r}\right)^{6} \right] \tag{2.8}$$

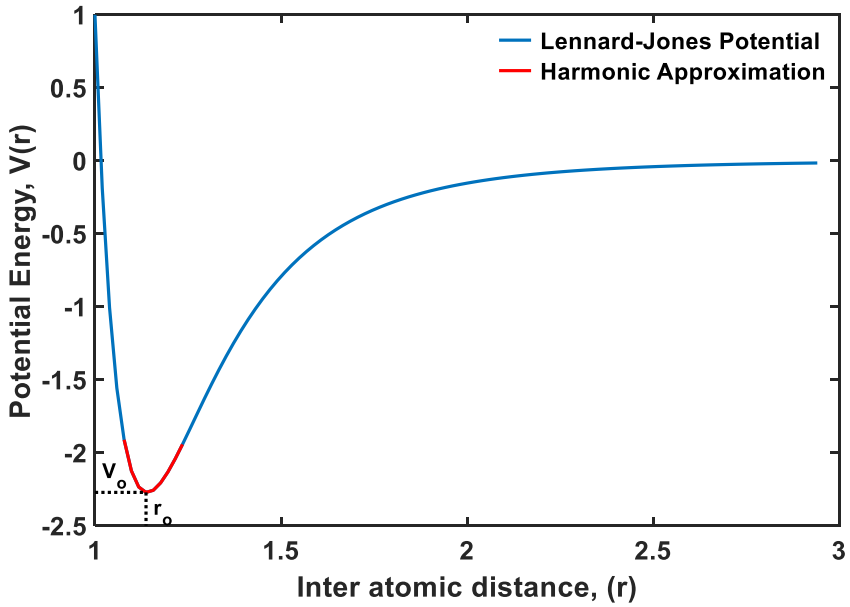

Fig. 2.1: Lennard – Jones potential curve in which the region of harmonic approximation is highlighted

where, V_0 is the depth of the potential well and r_0 is the interatomic distance at which the potential energy is zero. The interatomic forces (F) are proportional to the displacement of atoms for small displacements (r) and hence

$$F = -k(r - r_0) \tag{2.9}$$

which results in a harmonic potential

$$V(r) = \frac{1}{2}k(r - r_0)^2 \tag{2.10}$$

The above expression shows that the potential energy curve is parabolic for small displacements at which the restoring force is linear with respect to the displacement of atoms. Fig. 2.1 schematically illustrates the Lennard – Jones potential curve in which the harmonic approximation is highlighted. This assumption is valid virtually for any physically realistic system because the atoms only move within a small region around their equilibrium positions. Hence, the monochromatic nature of the elastic wave in the medium remains unchanged. However, for larger displacements, the restoring force deviates from this harmonic approximation and the higher-order terms in the Taylor expansion of the potential energy

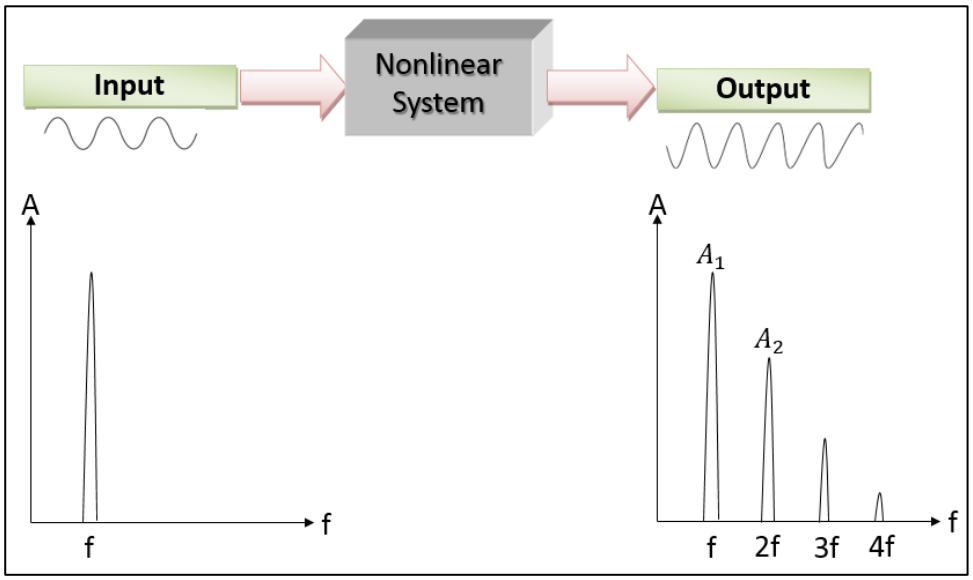

Fig. 2.2: Schematic of the harmonic generation from a nonlinear system when a monochromatic elastic wave propagates through it.

$$V(r) = V_0 + V_1(r - r_0) + \frac{1}{2!}V_2(r - r_0)^2 + \frac{1}{3!}V_3(r - r_0)^3 + \cdots \quad (2.11)$$

comes into the picture. Under this condition, the waveform gets distorted by its interactions with the higher-order lattice potential energy terms. Such interactions are nonlinear, leading to the generation of the harmonics of the fundamental frequency. Schematic representation of the harmonic generation is depicted in Fig. 2.2. Measurement of the harmonic amplitudes provides information about the nonlinear response of the medium in terms of a dimensionless quantity called the acoustic nonlinearity parameter. For a medium with quadratic nonlinearity, the one-dimensional elastic wave equation is written as[68]

$$\frac{\partial^2 u}{\partial t^2} = v^2 \left[1 - \beta \frac{\partial u}{\partial x}\right] \frac{\partial^2 u}{\partial x^2} \quad (2.12)$$

where v is the longitudinal phase velocity at the fundamental frequency, and β is the second order (quadratic) acoustic nonlinearity parameter. It should be noted that, when β becomes zero, Eq. (2.12) reduces to the linear wave equation

$$\frac{\partial^2 u}{\partial t^2} = v^2 \frac{\partial^2 u}{\partial x^2} \quad (2.13)$$

2.3.2 The acoustic nonlinearity parameter

Consider a pure sinusoidal wave of displacement amplitude

$$u = u_0 \cos(\omega t) \quad (2.14)$$

of frequency, ω is launched into a material at $x = 0$, where u is the instantaneous displacement amplitude and u_0 is the initial displacement at $t = 0$. A perturbation expansion of the displacement amplitude u can be written as[69]

$$u = u^{(1)} + u^{(2)} + \cdots \quad (2.15)$$

where, $u^{(1)}$ and $u^{(2)}$ are the displacement amplitudes of the fundamental and second-harmonic waves. The perturbation approach is adopted in order to find out the approximate solution to u by starting from the exact solution of $u^{(1)}$ which is known. The nonlinear behaviour of the

material determines subsequent terms. The contribution of $u^{(1)}$ is the solution to the linear wave equation (2.13)

$$\frac{\partial^2 u^{(1)}}{\partial t^2} = v^2 \frac{\partial^2 u^{(1)}}{\partial x^2} \tag{2.16}$$

The plane wave solution to Eq. (2.16) subjected to the boundary condition x = 0 is

$$u^{(1)} = A_1 \cos(kx - \omega t) \tag{2.17}$$

where k is the mode wave number (longitudinal bulk wave in the present thesis) and ω is the angular frequency. A first-order perturbation equation for the contribution $u^{(2)}$ is obtained by substituting Eq. (2.17) into the nonlinear term of Eq. (2.12), which yields

$$\frac{\partial^2 u^{(2)}}{\partial t^2} = v^2 \frac{\partial^2 u^{(2)}}{\partial x^2} - \frac{1}{2} v^2 \beta k^3 (A_1)^2 \, sin2(kx - \omega t) \tag{2.18}$$

It must be noted that the nonlinear term in Eq. (2.18) is a second harmonic sinusoid. A solution to Eq. (2.18) subjected to the above boundary condition is obtained by assuming a general solution of the form

$$u^{(2)} = f(x) sing2(kx - \omega t) + g(x) cos2(kx - \omega t) \tag{2.19}$$

It is assumed that the f and g are functions of x and that both the functions vanish at x = 0, since the boundary condition dictates that the second harmonic vanishes at x = 0.

Substituting Eq. (2.19) into (2.18) yields,

$$\begin{aligned} \left(4k\frac{df}{dx} + \frac{d^2 g}{dx^2}\right) cos2(kx - \omega t) - \left(4k\frac{dg}{dx} - \frac{d^2 f}{dx^2}\right) sin2(kx - \omega t) \\ = \frac{1}{2}\beta k^3 (A_1)^2 \, sin2(kx - \omega t) \end{aligned} \tag{2.20}$$

Equating the coefficients of the sinusoidal terms in Eq. (2.20) yields

$$4k\frac{df}{dx} + \frac{d^2 g}{dx^2} = 0 \tag{2.21}$$

and

$$4k\frac{dg}{dx}-\frac{d^2f}{dx^2}=-\frac{1}{2}\beta k^3(A_1)^2 \tag{2.22}$$

A consistent solution to Eq. (2.21) and (2.22) is found by assuming from (2.21) that df/dx and $d^2g/\,dx^2$ are zero. This implies that $f=f_0$ is a constant, $d^2f/\,dx^2=0$, and that $dg/dx=\ g_1$ is also a constant. Hence, Eq. (2.22) yields $dg/dx=\ g_1=-(1/8)\beta k^2(A_1)^2$ or $g=g_0-(1/8)\beta k^2(A_1)^2x$ where, g_0 is an integration constant. Since the second harmonic must vanish at $x\ =\ 0$, both f_0 and g_0 must be zero. A solution to the nonlinear wave equation (2.12) is then found from Eq. (2.16), (2.17) and (2.19) to be

$$u=A_1\,cos(kx-\omega t)-\frac{1}{8}\beta k^2(A_1)^2x\,sin2(kx-\omega t)+\cdots \tag{2.23}$$

Eq. (2.23) shows that, in addition to the fundamental wave of amplitude A_1 and angular frequency ω, a second harmonic signal of amplitude

$$A_2=\frac{1}{8}\beta k^2(A_1)^2x \tag{2.24}$$

and angular frequency 2ω is generated. The Eq. (2.24) implies that the second harmonic amplitude hinges on the nonlinearity parameter β and grows linearly with propagation distance x. Equation (2.24) also suggests that the nonlinearity parameter of the material is obtained experimentally by measuring the absolute amplitudes of the fundamental and the second harmonic components. Therefore, the second order nonlinearity parameter of a material can be written as

$$\beta=\frac{8}{k^2x}\frac{A_2}{{A_1}^2} \tag{2.25}$$

that defines the nonlinear response of the material towards a finite-amplitude acoustic wave. The Eq. (2.23) suggests that the quadratic nonlinearity parameter of a material can be calculated from the amplitudes of the fundamental and second harmonic components. Nevertheless, for an ideal material, such nonlinear response is minimal as the acoustic pressure on the atoms in a perfect periodic lattice is very small compared to the interatomic forces. However, every crystalline lattice induces an intrinsic nonlinearity (β^{lat}), referred to as the material nonlinearity, arises from the elastic constants of the medium, which is defined as[70,71],

$$\beta^{lat} = -\left(\frac{k_3}{k_2} + 3\right) \tag{2.26}$$

where, k_2 and k_3 represent the linear combinations of second-order and third-order elastic constants, respectively. The Eq. (2.26) suggests that the crystalline structure and the geometry of local atomic arrangement are the dominant factors in determining the magnitude of the nonlinearity parameter. For the principal directions in a cubic lattice, the expressions for k_2 and k_3 are given in Table 2.1.

Table 2.1: k_2 and k_3 for the principal directions in a cubic lattice

Direction	k_2	k_3
[100]	C_{11}	C_{111}
[110]	$\frac{C_{11} + C_{12} + 2C_{44}}{2}$	$\frac{C_{111} + 3C_{112} + 12C_{166}}{4}$
[111]	$\frac{C_{11} + 2C_{12} + 4C_{44}}{3}$	$\frac{C_{111} + 6C_{112} + 12C_{144} + 24C_{166} + 2C_{123} + 16C_{456}}{9}$

However, no material is perfect in nature. The atomic periodicity is distorted in the vicinity of grain boundaries, precipitates, micro cracks and dislocations due to the excess strain fields they induce into the crystalline lattice. In the vicinity of these discontinuities, the displacement potential deviates from the harmonic approximation introducing higher-order potential terms given by Eq. (2.11). In an elastic medium, distortions in the atomic arrangements due to such discontinuities induce excess nonlinearity (β^{ex}), referred as the geometric nonlinearity, in addition to the intrinsic material nonlinearity (β^{lat}). Therefore, the effective acoustic nonlinearity parameter β of a realistic crystalline material measured using Eq. (2.25) is a summation of β^{lat} and β^{ex}:

$$\beta = \beta^{\text{lat}} + \beta^{\text{ex}} \tag{2.27}$$

Experimentally, separation of the individual contribution of β^{lat} and β^{ex} is very difficult.[72,73] However, in the single-phase polycrystalline material where the change in grain size alone is studied in this thesis, the material nonlinearity may be assumed to remain the same irrespective

of the grain size. The relative variation of the nonlinearity parameter among different microstructural conditions measured and reported in this thesis, therefore, represents the change in the excess nonlinearity. The nonlinear response of the medium induced by the higher-order lattice potential terms and the discontinuities has become the basis of the non-destructive evaluation of materials using the nonlinear ultrasonic technique.

2.4 Material characterization using nonlinearity parameter

The acoustic nonlinearity parameter, β, depends on the structure, geometry and shape of the atomic arrangement in a crystalline solid. Hence the β gets affected during degradation and processing mechanisms. Monitoring the changes to β is a powerful tool to understand the state of the material. The following sections briefly review the relevant literature on the application of nonlinear ultrasonics in the context of material characterization.

2.4.1 Nonlinear response of the dislocations

Dislocations are the most common type of defects in crystalline materials at which the lattice continuity is distorted. The stress field of the dislocations in an elastic continuum creates nonlinear stress-strain behaviour in a localized volume near the dislocations and distorts the ultrasonic wave during its propagation. There exist several models to address different configurations of dislocations in metals. Hikata et al.[19] were the first to study the contributions of pinned dislocation segments to the excess acoustic nonlinearity parameter. Such pinned dislocation segments often appear in precipitate strengthened metallic materials. Bowing of the pinned dislocation under shear stress induces shear strain which gives rise to second harmonic generation. However, this model does not account for the effects of lattice resistance on the bowing of the dislocations. Cantrell et al.[74] developed a model of dislocation bowing that accounts for the lattice resistance by assuming that, in moving under the influence of applied stress, the dislocations encounter a periodic Peierls-Nabarro lattice barrier stress which changes the dynamics of dislocation bowing and leads to a periodicity in the harmonic generation amplitude. Cash and Cai[20] used dislocation dynamics (DD) simulation to demonstrate that constant dislocation line tension is insufficient to predict the contribution of dislocations to β. They have proposed a new model which accounts for the orientation-dependent line energy and provided a significant improvement over the models using constant line energy suggested by Hikata[19] and Cantrell.[74] In this model, a strong dependence of β on the orientation of

Burgers vector relative to the direction of the dislocation was shown by the DD simulations. Later, Cash and Cai[75] proposed a model which extended to an infinite dipole train and an infinite Taylor lattice. This analytical model offered an improvement over the existing models on β arising from the dislocation dipoles and multipoles. Gao and Qu[76] further developed a model for the excess acoustic nonlinearity parameter caused by extended dislocations which relate the nonlinearity parameter with the dislocation density and stacking fault energy. The separation between the two partial dislocations which forms an extended dislocation is stress-dependent implying that extended dislocations may interact with propagating waves.

The nonlinear interaction of elastic waves with dislocations has been studied extensively in the literature. The monotonic increase in β with an increase in carbon content in the quenched martensitic steel has been reported by Hurley et al.[77] and the increase in β was related to the increasing pinned dislocations affected by internal stresses, which were confirmed by XRD. Matlack et al.[14] used nonlinear ultrasound to monitor radiation damage in reactor pressure vessel steels. The increase in β from unirradiated specimen to medium dose specimen was due to an increase in dislocation density, and the decrease from the medium dose to high dose material was attributed to the formation of nanoclusters which reduce the mobility of dislocations cause reduced higher harmonic generation. The harmonics generated due to the dislocation substructures is a quantitative indication of the amount of damage that happened to a material. Hence by measuring the acoustic nonlinearity of a material, the damage associated with dislocation accumulation and the resulted microplasticity can be evaluated. The generation and accumulation of dislocations is the fundamental mechanism which governs the properties of a material during plastic deformation, fatigue and creep.

2.4.1.1 Nonlinear response arising from the plastic deformation

Plastic deformation to materials generate dislocations, and the dislocation multiplication influences the yield strength, ductility and radiation resistance.[78] To ensure continuity of strain across the grain boundaries, the boundary between the grains remains intact when a polycrystalline material gets deformed under uniaxial strain. The constraints imposed by the continuity of strain at the grain boundaries cause a considerable difference in the deformation between the nearby grains and within each grain. Such differences cause the strain in the vicinity of a grain boundary differs from that at the centre of the grain. Although the strain is continuous across the boundaries, there may be a steep strain gradient in this region. Plastic

deformation produces dislocations which result in a higher state of internal stress. For example, an annealed metal contains about 10^{13} dislocations per mm^2 while a severely plastically deformed metal can have about 10^{14} to 10^{15} mm^{-2} due to dislocation multiplication.[12] Ashby[79] suggested a dislocation model for polycrystalline deformation in which the distinction was made between the statistically stored dislocations and the geometrically necessary dislocations. The statistically stored dislocations are similar to the dislocations trapped in a single crystal, whereas the geometrically necessary dislocations are generated as a result of non-uniform strain in the grain. In this model, the polycrystal is deformed, allowing each grain to slip according to Schmid's law which generates statistically stored dislocations. The deformation process generates voids that overlap between grains, and these discrepancies are corrected by the introduction of appropriate geometrically necessary dislocations until the grains again fit together. Therefore, plastic deformation of polycrystalline materials generates dislocations, and, with an increase in strain, dislocation multiplication and pile ups occur.

Nonlinear ultrasonics has been widely used to study the effect of plastic deformation on the microstructure and material properties. The acoustic nonlinearity is a function of the micro-deformation state and the microstructure in materials.[80] The ultrasonic nonlinearity parameter (β) and microplastic deformation (ε_p) can be expressed as

$$\beta = f(\varepsilon_m, \Xi, \sigma) \tag{2.28}$$

$$\varepsilon_p = g(\varepsilon_m, \Xi, \sigma) \tag{2.29}$$

with ε_m and Ξ representing the micro-deformation state and the microstructures in materials, respectively and σ being applied stress. The local microstructures include dislocations, grain boundaries and phases and the micro-deformation state include the contributions of dislocation field and misfit field from two phases or precipitates. Therefore, from Eq. (2.28) and (2.29) it can be assumed that the acoustic nonlinearity is mainly dependent on the microplastic state

$$\beta = \psi(\varepsilon_p, \sigma) \tag{2.30}$$

In addition to the dislocation generation and pile-ups, when a metal undergoes uniaxial tension, certain crystallographic planes tend to orient themselves in a preferred manner with respect to the direction of strain. However, due to the complex interactions between the multiple slip systems in a polycrystalline aggregate, the individual grains cannot rotate freely, and hence the

lattice bending and fragmentation will occur. Nevertheless, the uniaxial tension in a polycrystalline material makes the grains elongate in the direction of tension.

Also, when austenitic stainless steel deforms, the metastable austenite can be transformed into martensite during plastic deformation.[81] Formation of the deformation-induced martensite (DIM) depends on many factors such as chemical composition, strain rate and nucleation sites. The formation of the DIM increases the strength of the material and accommodate enormous strain. Deformation induced martensite (χ) as a monotonic function of the plastic strain (ε_p)

$$\chi = 1 - \exp(-A\varepsilon_p) \tag{2.31}$$

suggests that the amount of martensite phase increases with an increase in plastic strain.[80] However, the stacking fault energy (SFE) plays a vital role in the formation of induced martensite.[82] The SFE of an alloy can be calculated using the relation[83]

$$SFE\left(\frac{mJ}{m^2}\right) = -53 + 6.2\,(\%Ni) + 0.7(\%Cr) + 3.2\,(\%Mn) + 9.3\,(\%Mo) \tag{2.32}$$

where alloys are in weight per cent. The SFE also has a dependence on the temperature; it decreases with the decrease in temperature. Formation of the DIM is much favoured in the alloys with low stacking fault energy, < 15 mJ/m^2. For the stacking fault energy more than 20 mJ/m^2, the deformation microstructure of austenite alloys will consist of the deformation twins. As the crystallographic structure of the martensite (bct) is different from that of the host austenite (fcc), the formation of the DIM distorts the elastic waves. It generates harmonics in addition to that arises from the dislocations. However, in the absence of deformation-induced phases, the plastic strain, ε_p, is a sole function of dislocation density after completely removing the external loading.[19] Hence change in the nonlinearity parameter can be approximated as

$$\beta = \beta_0 + \alpha\varepsilon_p^n \tag{2.33}$$

where α being a constant, n being an exponential index and β_0 is the nonlinearity at the reference level.

The variation in β as a function of the plastic deformation was investigated on AA7175-T735 aluminium alloy and showed two-stage dislocation dynamics.[84] The slow rate of change of the

nonlinearity parameter with strain was correlated with the increase in the dislocation density, and the higher rate was due to the formation of the cellular dislocation pattern. An analytical model was proposed by Zhang et al. to investigate the generation of harmonics during the process of multiplication and motion of dislocation in cold-rolled stainless steel.[85,86] Viswanath et al.[12] were used the acoustic nonlinearity parameter as a tool to characterize the degree of cold working in AISI type 304 stainless steel. For a cold work of 47%, the overall increase in β was found to be 170%. All these studies indicate that the nonlinear response originates from the interaction of elastic waves with the dislocations that can be used to characterize the plastic deformation.

2.4.1.2 Nonlinear response of fatigue damage

Prediction of the lifetime of cyclically loaded components and structures are crucial in the industry. The classical approach based on the fatigue life curves of the materials is a qualitative method that can predict the number of cycles required for the appearance of cracks. However, early stages of fatigue damage before crack initiation cannot be predicted by this method. This limitation is overcome using nonlinear ultrasonic measurements. During fatigue of metals, self-organized substructure arrangements of dislocations such as veins and persistent slip bands are formed. These dislocations accumulated at the grain boundaries resulting in strain localization and initiation of microcracks which finally produce substantial changes in the material nonlinearity.[87]

Nagy[5] has carried out a series of experiments on several metallic and non-metallic materials during fatigue to compare the sensitivities of different linear and nonlinear ultrasonic parameters towards fatigue damage. He has pointed out that the nonlinear ultrasonic response is prior and more sensitive indicators of degradation compared to the linear attenuation and velocity measurements. Kim et al.[88] studied the fatigue damage in nickel-base superalloy, and the effectiveness of β in characterizing the damages was demonstrated during high-cycle and low-cycle fatigue. A significant increase in β during low-cycle fatigue and a marginal variation during high-cycle fatigue was correlated with the plasticity of the specimen and quantitatively illustrated how β could be used to characterize the damage in the early stages of fatigue. Cantrell and Yost[89] demonstrated a monotonic increase of the material nonlinearity parameter with an increasing number of fatigue cycles. Nonlinear response of the ultrasonic waves was

used for the prediction of residual fatigue life of aluminium alloy specimens,[90] nickel-based superalloy[91] and in several other materials.[92–96]

2.4.1.3 Nonlinear response during creep

Creep is a permanent deformation that occurs in materials over an extended period provided the material is subjected to stress at high temperature. Creep failure is due to the excessive deformation of the material. Baby et al.[8] showed a 200% change in the nonlinearity parameter as a function of the creep fraction life in a near-α high-temperature IMI 834 titanium alloy. Their results were in good agreement with the microstructure observations. Balasubramaniam et al.[97] used a low amplitude harmonic generation method to characterize creep damage in pure copper in contrary to the traditional high amplitude methods. The low amplitude nonlinear behaviour occurs when dislocations are constrained between two quiescent lattice planes. The results were correlated with the micro-void concentrations caused by creep damage. Wang et al.[98] used a nonlinear ultrasonic technique for characterizing the creep damage in ASME T92 steel welded joints. The nonlinearity parameter has increased three folds in the heat-affected zone compared with the base metal, and this increase was due to the cavity growth as a result of creep.

The above review shows that the detection and characterization of the generation and accumulation of dislocations in materials could be used as a potential tool to evaluate the plastic deformation, fatigue damage and creep failure in their initiations states itself.

2.4.2 Second phase precipitates and the nonlinear response

Precipitation of secondary phases in the solid-solution of the metal matrix is the principal strengthening and hardening mechanisms of alloys. Generally, the precipitate has a crystalline lattice spacing that is different from that of the matrix material. The misfit parameter δ is defined as[16]

$$\delta = \frac{a_p - a_m}{a_m} \tag{2.34}$$

where, a_p and a_m are the lattice parameters of the precipitate and the matrix, respectively. For example, the lattice parameter for an fcc austenitic stainless-steel matrix is 0.359, whereas that of the $Cr_{23}C_6$ precipitate is 1.05 nm. The radial stress σ_r in the matrix at a distance r from a spherical precipitate of radius r_1 embedded in a finite body matrix is given by

$$\sigma_r = -\frac{4\mu\delta {r_1}^3}{r^3} \tag{2.35}$$

where μ is the shear modulus.

Cantrell and Yost[17,99] in their work on aluminium alloy 2024 suggest that nonlinear ultrasonic measurements are a potential technique for non-destructively assessing the optimum heat treatment time for precipitation strengthening of heat treatable alloy material. Studies on the precipitation kinetics of 18Ni maraging steel[10] showed that the nonlinearity parameter was responding differently during the nucleation of the precipitates and their subsequent growth. The results indicated that nonlinear measurements could identify different stages of the precipitation process. Mondal et al.[18] demonstrated that variations in the yield strength with quenching rate closely resemble the changes in β, and this variation has been explained by a dislocation-precipitate interaction model in week force condition. Abraham et al.[16] demonstrated that the β is very sensitive to the precipitation of chromium carbide along the grain boundaries in AISI type 304 stainless steel subjected to sensitization heat treatments. An increase in the β with the soaking time showed a one-to-one correlation with the electrochemical and microstructural observations. Matlack et al.[100] studied the effect of copper-rich precipitates in thermally aged 17-4 PH stainless steel on the acoustic nonlinearity parameter. Nonlinear ultrasonic measurements using Rayleigh waves showed a decrease in the nonlinearity parameter with increasing aging time. The results are interpreted using the precipitate-pinned dislocation model, along with hardness and microscopy observations. The strength induced by precipitation characteristics was studied using the nonlinear ultrasonic parameter in an age hardenable aluminium alloy.[18] It was shown that the nonlinearity parameter scales with coherent to incoherent precipitation phase transition. They have modified an existing model in order to account for weaker interactions between the dislocations and coherent precipitates.

2.4.3 Excess nonlinearity from cracks and interfaces

Detection of micro-cracks at the early stages of fracture is very important. Conventional ultrasonic non-destructive testing methods are sensitive to open cracks but much less sensitive to micro-cracks in their initiation stages. A crack that is perturbed by a harmonic wave responds in a nonlinear manner. When a crack is closed, it may remain undetected by the linear ultrasonic techniques,[101] but it can be excited ultrasonically to generate measurable second and higher-

order harmonic signals.[102] Nazarov and Sutin[103] have shown that the appearance of macrocracks in the material also produces large increases in β. The cracks' contribution to the acoustic nonlinearity parameter can be orders of magnitude higher than the lattice contribution, which has been verified in a compact tension specimen of Al6061 with a crack initiated by a fatigue test.[21]

Contact acoustic nonlinearity is a topic of interest to evaluate the quality of interfaces.[104] When an ultrasonic wave hit an interface, the waveform gets rectified, and the nonlinearity that arises during such interactions could be used to monitor the quality of diffusion bonds[105]. The difference in nonlinear response between strong and weak bonds manifested by the dynamic strains has been characterized by Hirsekorn.[106] Nonlinear ultrasonic evaluation was also used in the structural materials used in civil constructions. Chen[107] used the nonlinear ultrasonic method as a quantitative tool to track the evolution of microcracking in Portland cement mortar samples due to alkali-silica reaction.

The literature reviewed in this section indicates the nonlinearity parameter is a sensitive tool to characterize the microstructural changes and to detect the degradation mechanisms in their initiation stages. Nevertheless, the acoustic nonlinearity arises from the polycrystalline grain boundaries is discussed in the following sections because the main focus of this thesis relies on the harmonic generation from the grain boundaries.

2.5 Acoustic nonlinearity from polycrystalline grain boundaries

Since grains are the fundamental building block of any structural material, accurate characterization of the grain size and its distribution in any polycrystalline engineering structural material is essential. In a single-phase polycrystalline material, grain boundaries are the potential sources of harmonic generation. Propagation of elastic waves through a polycrystalline material demands continuity in the displacement and stresses at the grain boundaries. However, the nonlinear relation between the interatomic forces and displacement at the grain boundaries distorts the waveform. Hence nonlinear response of such a material is directly related to the area fraction of the total grain boundaries in a unit volume, and in turn, to the grain size. In general, a grain boundary is a planar interface at which the atomic periodicity does not retain. A widely accepted model of a grain boundary is the dislocation model and is used below to discuss the nonlinear interactions in a polycrystalline material.

2.5.1 Dislocation model of grain boundaries

The dislocation model of grain boundaries is initially suggested by Burgers[108] and Bragg.[109] In a polycrystalline material, a grain boundary can be visualized as an infinite array of edge dislocations, as schematically illustrated in Fig. 2.3. Read and Shockley[110] has provided a quantitative study of these models in which they estimated the energy of grain boundaries based on the dislocation model. They have formulated a proposition that the grain boundary energy is the sum of energies of two sets of dislocations that are originating from two neighbouring grains under an assumption of the unique geometry of the slip planes. Later, Berdichevsky[111] has shown that the above proposition is valid for arbitrary geometry of slip planes.

In a polycrystalline material, more is the angular rotation of one grain with the other, larger is the inclination of the planes that terminate as dislocations at the boundary, and closer is the spacing of the dislocations in the vertical boundary. The dislocation spacing in the boundary thus determines the angular inclination between the lattices. If the angle of rotation (θ) of the crystal structure across the boundary is assumed to be small, then

$$\theta = b/d \tag{2.36}$$

where b is the Burgers vector, and d is the dislocation spacing. It must be worth noting that the interior of the grains is free of long-range stresses. However, the atoms around a dislocation are displaced from their equilibrium positions which induce strain energy associated with the dislocation. Insertion of the half-plane of atoms into a perfect periodic lattice produces compressive stress in the half-space volume containing the extra plane of atoms and tensile stresses in the other half. The Shockley-Read equation represents the grain boundary energy is

$$\gamma_b = \frac{\mu b}{4\pi(1-\upsilon)}\theta\left(\frac{\ln\alpha}{2\pi} - \ln\theta + 1\right) \tag{2.37}$$

where, μ is the shear modulus, υ the Poisson ratio and α is a factor accounting for the dislocation core energy. Since a grain boundary consists of an array of edge dislocations, it also possesses strain energy which distorts the elastic wave and thus generates harmonics. Therefore, the harmonic generation in a polycrystalline material is directly related to the grain size. During annealing and deformation of a polycrystalline material, the size and nature of the grains change, which would cause a change in the dislocation density in the material. In

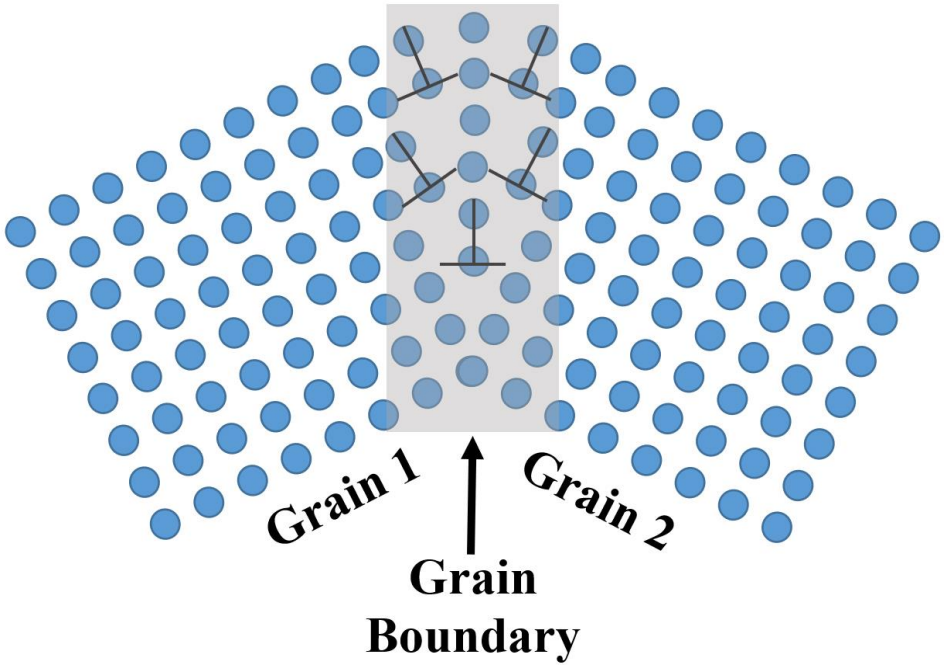

Fig. 2.3: Schematic representation of a grain boundary and an array of edge dislocations

polycrystalline materials, grain boundaries often block dislocation motion, thus creating dislocation pileups against the boundaries. Gao and Qu[112] have developed an analytical model to calculate the acoustic nonlinearity parameter induced by dislocation pileups in isotropic elastic solids. Since the elastic waves interact with the dislocations in the grains in the annealed and deformed conditions, the harmonic generation mechanism would be different.

2.5.1.1 Grain growth during annealing

During annealing, grain growth is driven by the reduction of total grain boundary energy such that the grain boundaries migrate towards their centre of curvature with a speed that is proportional to the curvature.[113] Therefore, different grains grow differently under the same heating conditions, and the kinetic model predicts exponential grain growth.[114,115] The grain growth phenomena may be categorized into two; normal and abnormal grain growth. The microstructure evolves uniformly during normal grain growth. On the other hand, during the abnormal grain growth, a subset of grains grows at a high rate at the expense of their neighbours and result in a microstructure dominated by a few very-large grains. A synthetic microstructure with normal and abnormal grain growth is represented in Fig. 2.4. There exist several methods to distinguish between normal and abnormal grain growth. Shirdel et al.[116,117] proposed the ratio of the maximum grain size (D_{max}) to the mean grain size (D_{mean}) higher than 5 to

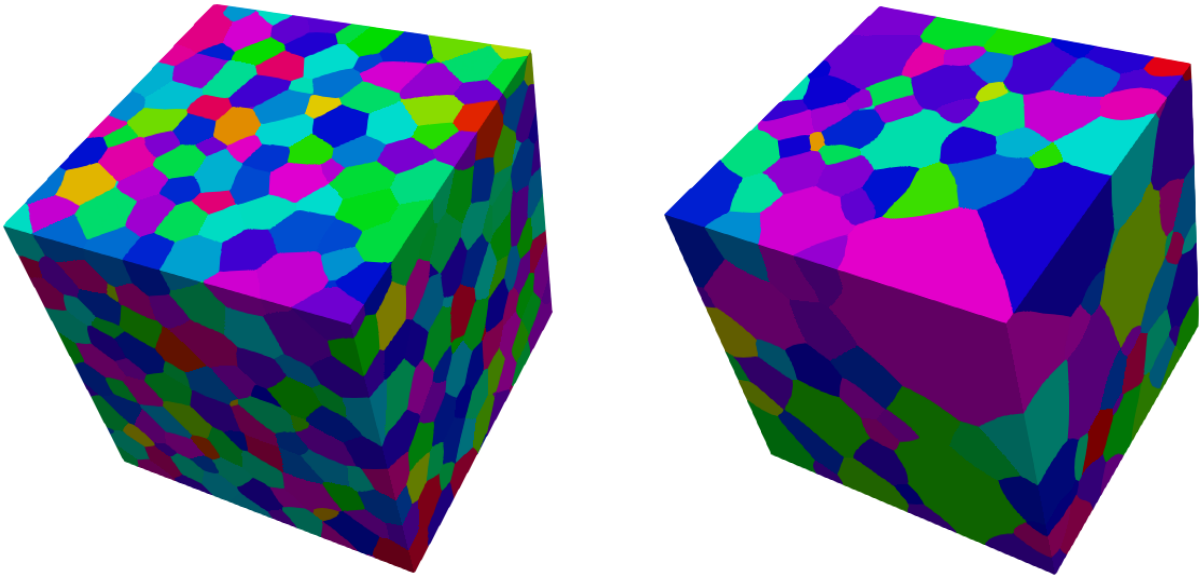

Fig. 2.4: Synthetic microstructures with (a) normal and (b) abnormal grain growth. The colour in each grain is only to differentiate them.

represent an abnormal grain growth. A transition from normal to abnormal grain growth generally occurs at $0.8\,T_H$ where, T_H the homologous temperature during solutionising heat treatments. Although β is extensively used for material characterization, Mini et al.[68] was the first to investigate nonlinear response of grain boundaries in polycrystalline materials. They have reported a quadratic like variation of β with increasing grain size. Similar behaviour was observed in a recent work by Choi et al.[118] on stainless steel grade 304L also.

2.5.1.2 Deformation of grains

During deformation, the constraints imposed by the continuity at the grain boundaries cause considerable differences in the deformation between nearby grains and within each grain. This is due to the difference in dislocations within the volume of the grains and at the grain boundaries.[79] Deformation of a polycrystalline material generates additional geometrically necessary dislocations. In addition, metastable materials can produce strain-induced martensite during plastic deformation.[81] The initial grain size, microstructural constituents, and the strain determines the density of the geometrically necessary dislocations. Viswanath et. al[12] have shown a considerable increase in the dislocation density and strain-induced martensite in cold-worked AISI 304 austenitic stainless steel. The nonlinearity parameter was increased to 168% with 47% cold rolling, which is due to the increased dislocation density and the strain-induced martensite. Zhang et. al[80] also reported a 77% increase in the nonlinearity parameter of the

austenitic stainless steel, which is subjected to a true strain of 40%. These studies indicate the sensitivity of the NLU on the characterization of deformation behaviour.

2.5.2 Nonlinear wave propagation in solids

In general, the constitutive stress-strain relationship in a homogeneous isotropic material can be written as

$$\sigma_{ij} = C_{ijkl}\varepsilon_{kl} \tag{2.38}$$

where, σ_{ij} is the Cauchy stress tensor, ε_{kl} is the finite-amplitude strain tensor and C_{ijkl} is the fourth-order elastic stiffness tensor with 81 components. In the case of an isotropic solid, the number of components of the stiffness tensor reduces to 2, i.e., λ and μ, the Lame parameters. Hence, the nonlinear wave equation in an isotropic material with quadratic nonlinearity can be written as

$$\rho\frac{\partial^2 u}{\partial t^2} = (\lambda + 2\mu)\frac{\partial^2 u}{\partial x^2}\left[1 - \frac{\partial u}{\partial x}\right] \tag{2.39}$$

However, a single-phase polycrystalline material consists of grains of random crystallographic orientation separated by the grain boundaries, as shown in Fig. 2.4. Individual grains within a polycrystalline material are single crystals, each with its own size, shape and crystallographic orientation. The crystallographic axes of the individual grains generally do not coincide with the reference axes of the global reference frame. The structure of packing of these grains is generally referred to as a microstructure, and an example microstructure is illustrated in Fig. 2.5 where the crystallographic axes and the global reference frames are represented. However, by angular rotations using the Euler angles $(\varphi_1, \phi, \varphi_2)$, the crystallographic system can be brought to the reference frame. Orientation changes from grain-to-grain lead to a continuously changing set of elastic properties, which makes the medium polycrystalline. In a polycrystalline material, the nonlinear wave equation can be written in terms of the stiffness matrix (C^*) as

$$\rho\frac{\partial^2 u}{\partial t^2} = C^*\frac{\partial^2 u}{\partial x^2}\left[1 - \frac{\partial u}{\partial x}\right] \tag{2.40}$$

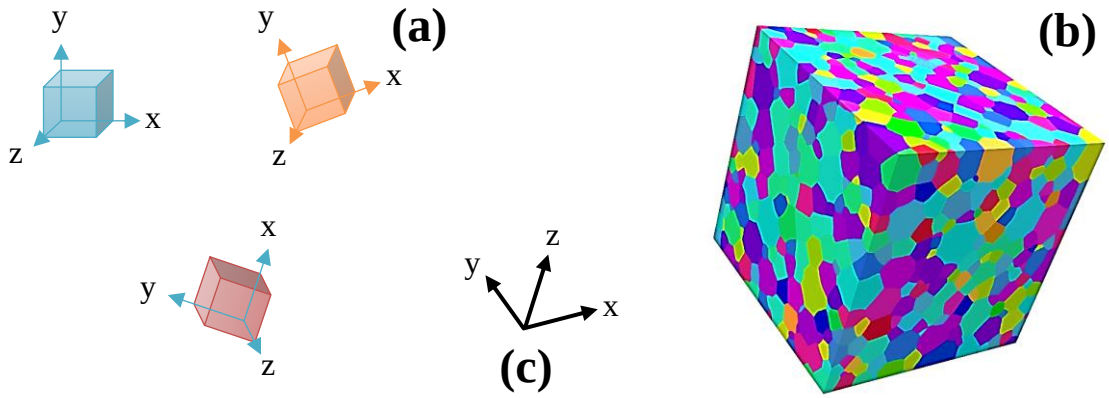

Fig. 2.5: Schematic representation of (a) the crystallographic axes and orientation, (b) polycrystalline microstructure and (c) a global reference frame.

For a polycrystalline material, the elastic stiffness matrix C^* is defined as $R_D C R_D^T$ where C is the stiffness tensor composed of C_{11}, C_{12} and C_{44}, for cubic system, and R_D is the bond-transformation matrix in terms of the Euler angles.[119]

Snapshots of a 2D finite element visualization of the propagation of a monochromatic elastic wave of frequency 2 MHz through an isotropic homogeneous medium (using Eq. (2.39)) and through a polycrystalline medium (using Eq. (2.40)) are shown in Fig. 2.6. In the polycrystalline medium, the elastic waves interact with the grain boundaries where the atomic periodicity is not maintained and hence causes a difference in the acoustic impedance between the grain volume and the boundary. As a result, the waves undergo scattering, diffraction, mode conversion, as well as harmonic generation. A three-cycle sinusoidal input of frequency 2 MHz was assigned for this visualization. The random polycrystalline microstructure was generated using Voronoi tessellations.[120] Individual grains were generated using the rotation of the stiffness matrix about a global reference frame. The grain boundaries were modelled as displacement continuous while the edge boundaries were assigned low reflection boundary conditions. The element size used was one-tenth of the wavelength used. The material properties used to represent the isotropic medium was the Lame constants $\lambda = 107.05$ GPa and $\mu = 77.52$ GPa and that used to represent the polycrystalline medium[121] was $C_{11} = 204.6$ GPa, $C_{12} = 137.7$ GPa and $C_{44} = 126.2$ GPa. In both cases, longitudinal and shear wave velocity was taken as 5800 m/s and 3200 m/s respectively and the density (ρ) as 7930 g/m^3.

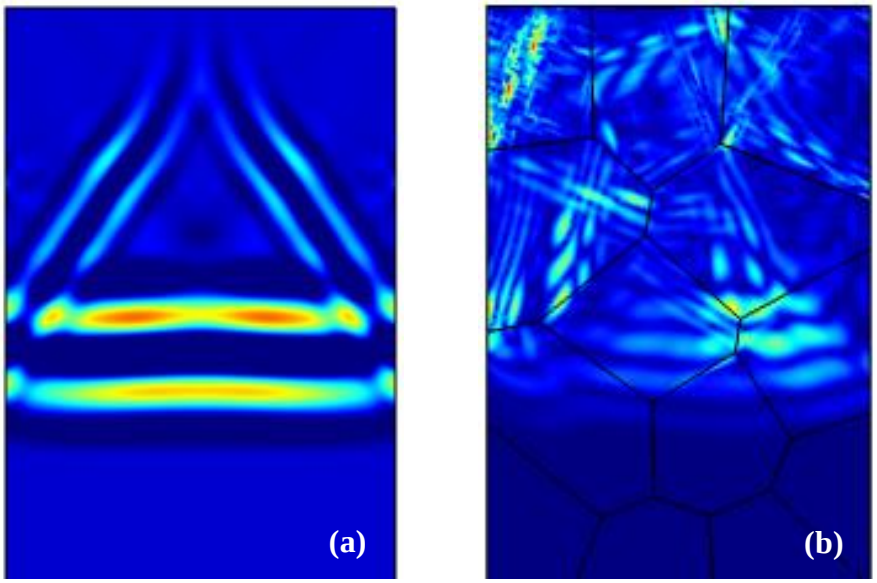

Fig. 2.6: Snap shots of the wave propagation in (a) an isotropic homogeneous medium and (b) in a polycrystalline medium.

2.5.2.1 Direction dependent nonlinearity

When a monochromatic waveform is propagating through a polycrystalline material, it encounters different crystallographic directions based on the relation between the crystallographic axes in each grain and the global reference frame described in Fig. 2.5. As the harmonic generation is a function of the crystallographic direction, corresponding nonlinear responses in C_{11}, C_{12} and C_{44} directions are obtained by solving the one-dimensional finite difference approximation to Eq. (2.40) given by

$$\rho\left[\frac{u_i^{j+1}-2u_i^j+u_i^{j-1}}{\Delta t^2}\right]=C_{ij}\left[\frac{u_{i+1}^j-2u_i^j+u_{i-1}^j}{\Delta x^2}\right]\left[1-\left(\frac{u_{i+1}^j-u_{i-1}^j}{2\Delta x}\right)\right] \quad (2.41)$$

with the boundary conditions

$$u(x,0) = I(x) \quad (2.42)$$

$$\frac{\partial}{\partial t}u(x,0)=0 \quad (2.43)$$

$$u(0,t)=0 \quad (2.44)$$

$$u(L,t)=0 \quad (2.45)$$

where, $I(x)$ is the waveform introduced into a material with the temporal domain and the spatial domains defined by $[0,T]$ and $[0,L]$, respectively. The Eq. (2.41) implies that the displacement characteristics in a polycrystalline medium depend on the stiffness parameter, C_{ij}. For a waveform of input frequency 5MHz, the nonlinear responses in C_{11}, C_{12} and C_{44} directions are plotted in Fig. 2.7. In this model, the grain boundaries were not incorporated, and hence the grain boundary harmonics were not present. The difference in the fundamental as well as harmonic amplitudes are evident for different C_{ij} directions. Also, there exists no consistent correlation between these amplitudes with C_{ij} values which indicates the directional dependence of the nonlinear interactions. This suggests that the geometry and shape of the local atomic arrangement are the dominant factors in determining the magnitude of the nonlinearity parameter, as indicated in Eq. (2.26) and Table 2.1. However, in a polycrystalline material with equiaxed grains, random orientations of single-phase crystallites imply statistical isotropy and homogeneity. For this reason, one may average out the orientation effects induced by the individual grains. The nonlinear measurements provide a spatial average of the individual

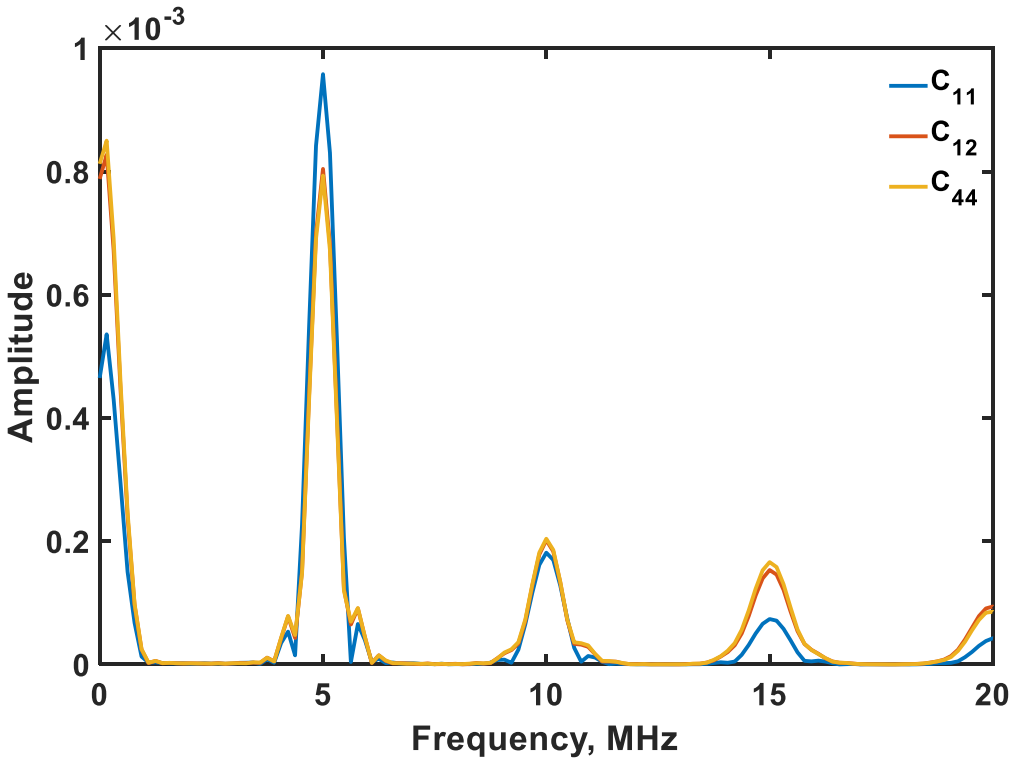

Fig. 2.7: Harmonic amplitudes for a 5.0 MHz input as the wave propagates along the C_{11}, C_{12} and C_{44} directions

contributions of C_{ij} over a large volume and, therefore, the resultant harmonics are the collective representation of the lattice discontinuities such as grain boundaries.

It is to be noted that the zero-frequency components displayed in Fig. 2.7 are called the static displacement components, which arises from the third-order elastic constants. The static displacement component, which is generally denoted as β_{dc} has been used by researchers for material characterization.[122,123] Meanwhile, the third-order nonlinearity parameter, which is defined as

$$\gamma = \frac{32}{k^4 x^2}\frac{A_3}{A_1^3} \tag{2.46}$$

for the third harmonic amplitude A_3 has also been used for material characterization.[124,125] However, the present thesis is limited to the use of the second-order (quadratic) nonlinearity parameter (β) to characterize the microstructural features and to interpret the associated physical phenomena.

2.6 Factors affecting the acoustic nonlinearity parameter

The nonlinearity parameter measured using the Eq. (2.25) can be influenced by several experimental factors such as coupling conditions, instrument nonlinearity, source diffraction and attenuation.[126] Under proper experimental conditions, nonlinear effects related to the coupling and instrumentation do not have any significant impact because these effects exist alike at all measurement intervals. But, the effects of diffraction due to the finite size of the source (transducer) and the attenuation due to material absorption need to be considered carefully.

2.6.1 Source diffraction

The diffraction coefficients to the fundamental and second harmonic components respectively are given by[127]

$$D(\omega) = 1 - exp(-ika^2/x)[J_0(ka^2/x) + iJ_1(ka^2/x)] \tag{2.47}$$

and,

$$D(2\omega) = \frac{\left|\int_0^x [D(\omega, x-\sigma/2, a]^2 d\sigma\right|}{x} \tag{2.48}$$

with the J_0 and J_1 being the Bessel functions. The Lommel's diffraction correction factor accounted for the beam divergence due to the finite size of the radiation source[128] is given by

$$D_\beta = \frac{|D(\omega)|^2}{|D(2\omega)|} \tag{2.49}$$

Generally, the diffraction coefficients are considered negligible for longitudinal waves used in nonlinear measurements over short propagation distances, as shown in Fig. 2.8.

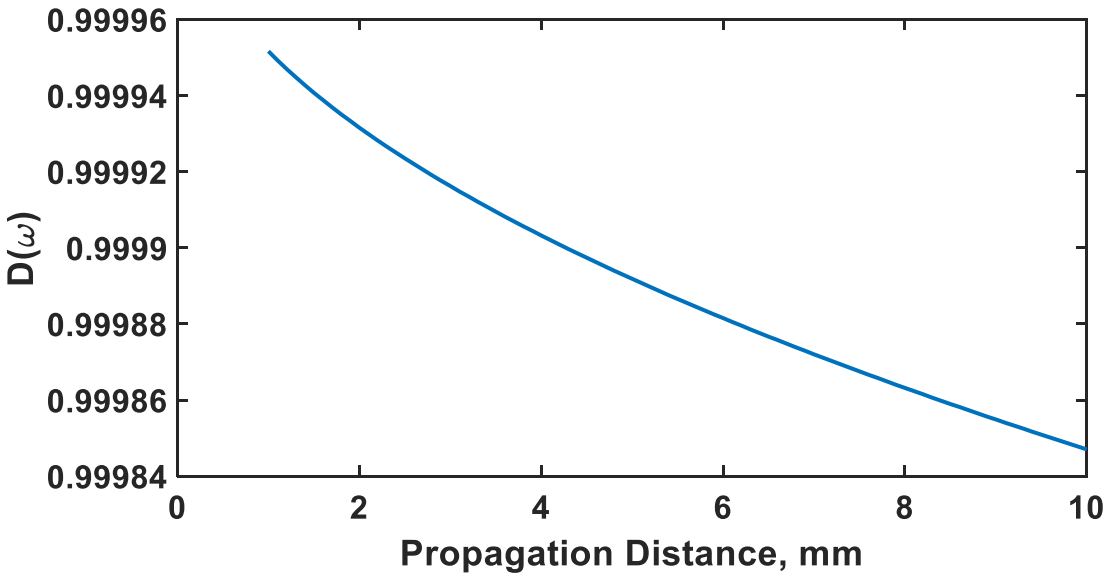

Fig. 2.8: Diffraction coefficient as a function of the wave propagation distance

2.6.2 Material attenuation

In a material, interaction mechanisms of the fundamental and harmonic components are different as they differ in their wavelength. The second harmonic wave grows with propagation distance due to the nonlinear interactions and also diminishes due to attenuation, which is independent of the cumulative growth effect.[129] On the other hand, the fundamental wave is subjected only to attenuation losses. For small propagation distances, the energy transfers from the fundamental to the second harmonic mode during harmonic generation is negligible compared to the energy of the propagating fundamental wave as the second harmonic

amplitude (A_2) is several orders smaller than that of the fundamental (A_1). Therefore, in non-linear ultrasonics, attenuation of fundamental and harmonic components is addressed separately.

Addition of dissipative terms to the linear wave equation (2.13) gives[69]

$$\frac{\partial^2 u}{\partial t^2} = v^2 \frac{\partial^2 u}{\partial x^2} + b \frac{\partial^3 u}{\partial t \partial x^2} \tag{2.50}$$

where *b* is the damping constant. The solution of this equation yields:

$$u = A_1 e^{i(k_1 x - \omega t)} \tag{2.51}$$

where

$$A_1 = (A_1)_0 e^{-\alpha_1 x} \tag{2.52}$$

$k_1 = \omega_1 / v$ and α_1 is the coefficient of attenuation for the fundamental wave; $(A_1)_0$ is the amplitude of the fundamental wave at $x = 0$.

Equation (2.52) implies

$$\frac{dA_1}{d\mathrm{x}} = -\alpha_1 A_1 \tag{2.53}$$

It is assumed that the second harmonic component's attenuation is independent of the attenuation of the fundamental wave. In analogy to Eq. (2.53) we can write,

$$\left(\frac{dA_2}{dx}\right)_{attn} = -\alpha_2 A_2 \tag{2.54}$$

According to Eq. (2.25), the amplitude of the second harmonic signal also increases with the propagation distance. Therefore,

$$\left(\frac{dA_2}{dx}\right)_{SHG} = \frac{1}{8}\beta k^2 {A_1}^2 \tag{2.55}$$

where, SHG denotes second harmonic generation. Hence the net spatial change in A_2 is

$$\frac{dA_2}{dx} = \left(\frac{dA_2}{dx}\right)_{SHG} + \left(\frac{dA_2}{dx}\right)_{attn} = \frac{1}{8}\beta k^2 {A_1}^2 - \alpha_2 A_2$$
$$= \frac{1}{8}\beta k^2 (A_1)_0{}^2 e^{-2\alpha_1 x} - \alpha_2 A_2 \tag{2.56}$$

The solution to this equation subjected to the boundary condition $A_2 = 0$ at $x = 0$ is

$$A_2 = \frac{1}{8}\beta k^2 (A_1)_0{}^2 \left[\frac{e^{-2\alpha_1 x} - e^{-\alpha_2 x}}{\alpha_2 - 2\alpha_1}\right] \tag{2.57}$$

Therefore, losses in the fundamental and second harmonic amplitudes due to the attenuation within the medium is governed by the Eqns. (2.52) and (2.57), respectively. These equations may be used to determine the proper nonlinearity parameter of the material from the experimentally measured nonlinearity parameter. The experimentally measured nonlinearity parameter β_{meas} is determined from Eq. (2.25) as

$$\beta_{meas} = \frac{8}{k^2 x}\frac{A_2}{{A_1}^2} \tag{2.58}$$

Substituting Eqns. (2.52) and (2.57) in Eq. (2.58) yields

$$\beta_{meas} = \beta\left[\frac{\{1 - \exp[-(\alpha_2 - 2\alpha_1)x]\}}{(\alpha_2 - 2\alpha_1)x}\right] \tag{2.59}$$

which implies that, in an attenuating medium, the material nonlinearity gets modified by the term given in the square bracket, which is a function of the attenuation coefficients (α_i) of the material. This term, hereafter denoted as β_{α_i}, shows how the material nonlinearity which has been arisen from the β^{lat} and β^{ex} of a medium gets modified due to the attenuation of the fundamental (α_1) and harmonic (α_2) components. In a polycrystalline material, the attenuation is predominantly due to the grain boundary scattering governed by the power-law relations to the grain size D and the frequency f (or wavelength λ) of the elastic wave which defines different scattering regimes summarized in Table 2.2 where, C_R, C_S and C_G corresponds with the constants of proportionality.[130]

Table 2.2: Scattering Regimes in a Polycrystalline Material				
Conditions		Type of Scattering	Scattering Dependency	
$\lambda > 2\pi D$	$kD < 1$	Rayleigh	$C_R D^3\, \lambda^{-4}$	$C_R D^3\, f^4$
$\lambda < 2\pi D$	$kD > 1$	Stochastic	$C_S D\, \lambda^{-2}$	$C_S D\, f^2$
$\lambda << D$	$kD >> 1$	Geometric	$C_G D^{-1}$	$C_G D^{-1}$

Attenuation coefficients for the longitudinal elastic waves in the Rayleigh and stochastic regimes can be written as[131]

$$\alpha_L^R = \frac{4}{1125}\frac{\pi^2\mu^2}{\rho^2 v_L^3}\left[\frac{2}{v_L^5} + \frac{3}{v_s^5}\right] D^3 f^4 \tag{2.60}$$

and,

$$\alpha_L^S = \frac{16}{525}\frac{\pi^2\mu^2}{v_L^6\rho^2} D f^2 \tag{2.61}$$

From the Taylor series expansion of Eq. (2.59), such modifications to the nonlinearity parameter are no longer valid for the cases where $(\alpha_2 - 2\alpha_1)x \ll 1$. During an NLU measurement, the calculated β from the amplitudes of the A_2 and A_1^2 is a cumulative contribution of all the terms mentioned in Eq. (2.59), and hence the interpretation of the results must be judicious. Meanwhile, several authors have attempted correction factors to compensate for the diffraction and attenuation losses.[24,25,132,133] But such compensations can be achieved either through simultaneous measurement of attenuation coefficients[25] or through finding out the transfer functions[24] of the ultrasonic transducers used. Such attempts are time-consuming, tedious and challenging to implement when the material is coarse-grained, anisotropic or thick and have limited application on the field components. Therefore, correction methods cannot be generalized, and the measured β needs to be interpreted judiciously.

2.7 Methodologies in nonlinear ultrasonics

In general, the acoustic nonlinearity parameter can be measured using any of the four methodologies, which are schematically represented in Fig. 2.9. Researchers generally employ longitudinal bulk wave through-transmission mode for material characterization due to its

simplicity in implementation. The characteristic behaviour of the bulk nonlinear response to microstructural changes has been widely used to establish a correlation between the structure and property, as well as to characterize different processing and degradation mechanisms of materials, which include, but not limited to fatigue,[6,134] creep,[8,9,97,135] aging,[10] cold work,[12] irradiation damage,[14] thermal damage,[136] precipitation,[16–18,99,137,138] dislocation,[19,20,139] residual stress[140] and cracks[21]. These studies show that the bulk nonlinear response in the through-transmission mode is highly sensitive to the microstructural features associated with the early stages of degradations. The Rayleigh wave mode has also been used in the nonlinear characterization of fatigue damage,[96] precipitates[100] and thermal degradation.[13] However, the Rayleigh mode is confined to a shallow region on the surface of the test material and hence reveals only the surface characteristics.

Recently, research in nonlinear ultrasonics has got its interest in wave mixing methods. In this method, the resultant sum and difference frequencies are received from the interaction of two monochromatic waves of slightly different frequencies. In the wave mixing method, elastic waves interact among themselves (phonon-phonon interaction) provided the law of conservation of energy and momentum of phonons are satisfied.[141–143] However, these conservation laws demand favourable angle of incidents, wave modes and the frequencies to happen the wave mixing. Both collinear and non-collinear wave mixing methods have been

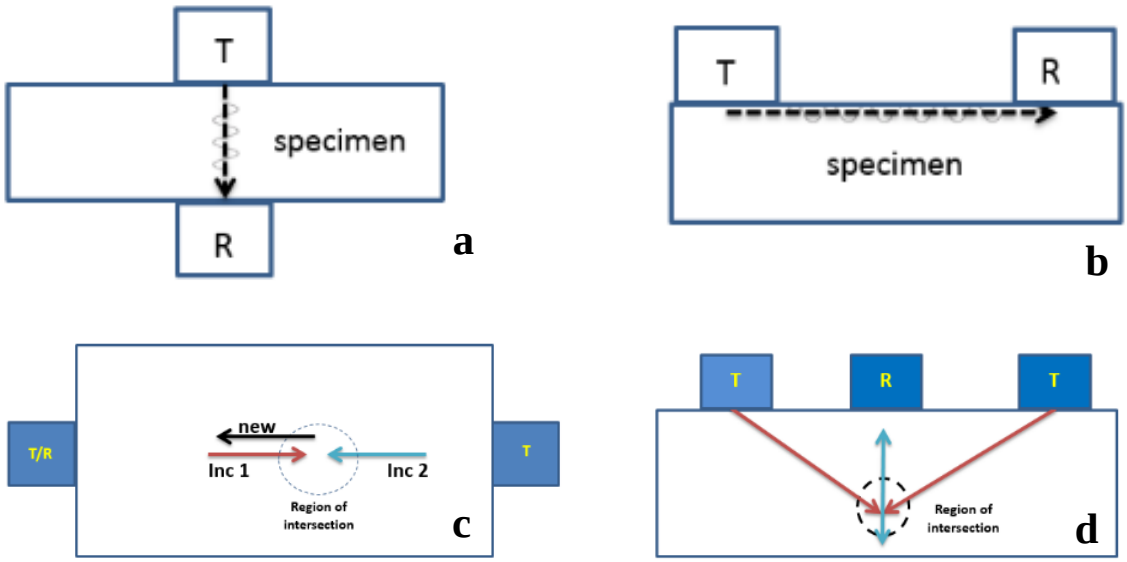

Fig. 2.9: Schematic representations of different methodologies for nonlinear measurements; (a) through-transmission, (b) Rayleigh, (c) collinear wave mixing and (d) non-collinear wave mixing.

used to characterize the intergranular corrosion,[144] micro-cracks,[22] ageing,[145,146] fatigue damage[147] and plasticity.[147,148]

The present thesis, however, is confined only to the longitudinal mode bulk through-transmission method (Fig. 2.9(a)) using different excitation frequencies and thereby studying the harmonic response under different microstructural conditions.

2.8 Summary and the way forward

This chapter reviewed the relevant literature on the non-destructive evaluation methods using linear and nonlinear ultrasonic techniques. The nonlinear ultrasonic technique is susceptible to the marginal changes in the microstructural features where linear ultrasonic methodologies are not sufficient. However, in a polycrystalline material, the mean grain size, its distribution and the associated scattering regimes can influence the acoustic nonlinearity parameter. In the previous studies correlating the nonlinearity parameter with the microstructure, a single length scale, the mean grain size, was often used to describe the size of all the grains within a polycrystalline material.[68,118] The natural materials are generally organized with a distribution of grain sizes, most often lognormal,[3] so that different scattering regimes coexist. The fundamental and harmonic components interact differently with these scattering regimes and, therefore, correlation of the measured acoustic nonlinearity parameter with the microstructural features would be tedious. It is emphasised that the correction methods are not always feasible to be implemented during the NLU measurements. Hence a detailed investigation on the effect of grain size distribution and the associated scattering regimes on the acoustic nonlinearity parameter is essential, which has found to be the potential problem identified for the present research.

2.9 The gap areas for research

Though a considerable amount of literature exists on the use of nonlinear ultrasonics for material characterization, there remain certain gap areas with respect to the objective of demonstrating the feasibility of nonlinear ultrasonics as a potential NDE technique for characterizing the grain size variations in bulk metallic materials. The gap areas identified for research are briefed below.

- The grain size distribution in materials is lognormal so that different scattering regimes can coexist. Therefore, the characterization of such materials using only a single frequency or assuming a single mean grain size is insufficient. Hence, it is essential to investigate the influence of grain size distribution and the associated scattering regimes on the nonlinear response of a polycrystalline material.
- Though grain size variation in different specimens with uniform average grain size has been demonstrated using NLU, it has not yet attempted to characterize the grain size variation present in large components across its thickness or diameter. This is particularly important to demonstrate the feasibility of nonlinear ultrasonics to study the grain size variation in actual industrial applications.
- Though nonlinear ultrasonics has been used to characterize the plastic deformation in structural materials, a combined effect of the grain size and the plastic deformation has yet to be explored. Such an investigation is essential to understand the nonlinear response of any structural component which is under loading.

These areas were turned out to be the basis of the present research. A novel multi-frequency nonlinear measurement approach is introduced for the first time in this thesis for the characterization of the heterogeneous microstructure in single-phase polycrystalline materials. The multi-frequency approach enables visualizing the influence of different scattering regimes on the acoustic nonlinearity parameter.

Chapter 3
Experimental Methods

3.1 Introduction

The present chapter describes the materials and the general experimental procedures used in this thesis. Section 3.2 provides a brief description of the material selection and the processing methods chosen for the investigation. Section 3.3 describes the linear ultrasonic measurement procedure, which includes the methodology followed for the C-scan imaging and calculation of the attenuation coefficients from the frequency spectrum of received signals. Section 3.4 describes the experimental set up used for nonlinear ultrasonic measurements which include the selection of the ultrasonic transducers, calibration of the equipment and normalization procedures. Beyond this, the signal processing methodology adapted to obtain the nonlinearity parameter is also explained. Subsequently, the procedure for microstructure analysis using optical microscopy and electron backscatter diffraction is explained in Section 3.5. It is to be noted that any specific deviation from these experimental procedures and the specimen preparation in the subsequent parts of the thesis will be addressed accordingly in their corresponding sections.

3.2 Material selection

Materials used in this thesis is of austenitic stainless steels, AISI 304 and 304L grades. Austenitic stainless-steel was chosen for the present investigation owing to its enormous industrial applications and single-phase microstructure. Annealed, forged and deformed microstructural conditions were used to investigate the ultrasonic nonlinear response. Details of the selection and processing of materials are described in the following sub-sections.

3.2.1 Austenitic stainless steel with different mean grain size

In order to study the effect of grain size variations and the associated scattering regimes on the nonlinearity parameter, large variations in grain size are generated in AISI Type 304 austenitic stainless-steel material through systematic annealing heat treatments. The chemical composition (wt.%) of the selected material is given in Table 3.1.

Table 3.1: Chemical composition of the AISI 304 material											
C	Cr	Ni	Mn	Si	P	S	Cu	Co	Mo	W	Fe
0.074	19.07	10.22	0.816	0.438	0.044	0.022	0.047	0.095	0.308	0.286	Balance

Specimens of dimension 50mm × 50mm × 12mm were solutionized in a muffle furnace under different annealing conditions, as given in Table 3.2. The furnace temperature was calibrated using a reference thermocouple with an accuracy of ±2 ℃. The annealed specimens were further machined to a thickness of 10 ± 0.01 mm, maintaining plane parallelism between the major surfaces. Specimens of dimension 10 mm^3 were cut from each annealed specimen for optical microscopy and EBSD analysis.

Table 3.2: Annealing heat treatment to the AISI 304 specimens									
Specimen ID	A	B	C	D	E	F	G	H	I
Temperature (˚C)	As Received	1050	1100	1100	1150	1150	1200	1200	1200
Soaking Time (min)		60	60	120	60	120	60	90	120

3.2.2 Forged components with heterogeneous microstructure across the diameter

Two AISI 304L austenitic stainless-steel forgings (F_1 & F_2) of diameter 200 mm were chosen to study the heterogeneous microstructure using nonlinear ultrasonics. The chemical composition (in wt.%) of the F_1 & F_2 is given in Table 3.3. Strips each of 20 mm wide in the cross-sectional plane (transverse axis) were cut along the diameter as shown schematically in Fig. 3.1. These strips were machined to a uniform thickness of 10 ± 0.02 mm, and a surface finish of 1 µm was ensured. Both the strips were subjected to radiographic examination and found to be free from any volumetric defects. These strips were then subjected to immersion C-scan imaging as well as nonlinear ultrasonic measurements. Specimens of dimension 10 mm^3 for microstructure analysis were cut from the locations where nonlinear ultrasonic measurements were performed. Subsequent to the microstructure analysis, energy dispersive

spectroscopy (EDS), electron backscatter diffraction (EBSD) and the hardness measurements were also performed on these specimens.

Table 3.3: Chemical composition of the Forgings

	C	Cr	Ni	Mn	Si	P	S	Cu	W	Fe
F1	0.031	17.79	8.85	1.614	0.413	0.029	0.025	0.179	0.128	Balance
F2	0.032	17.82	9.08	1.625	0.405	0.028	0.017	0.579	0.128	Balance

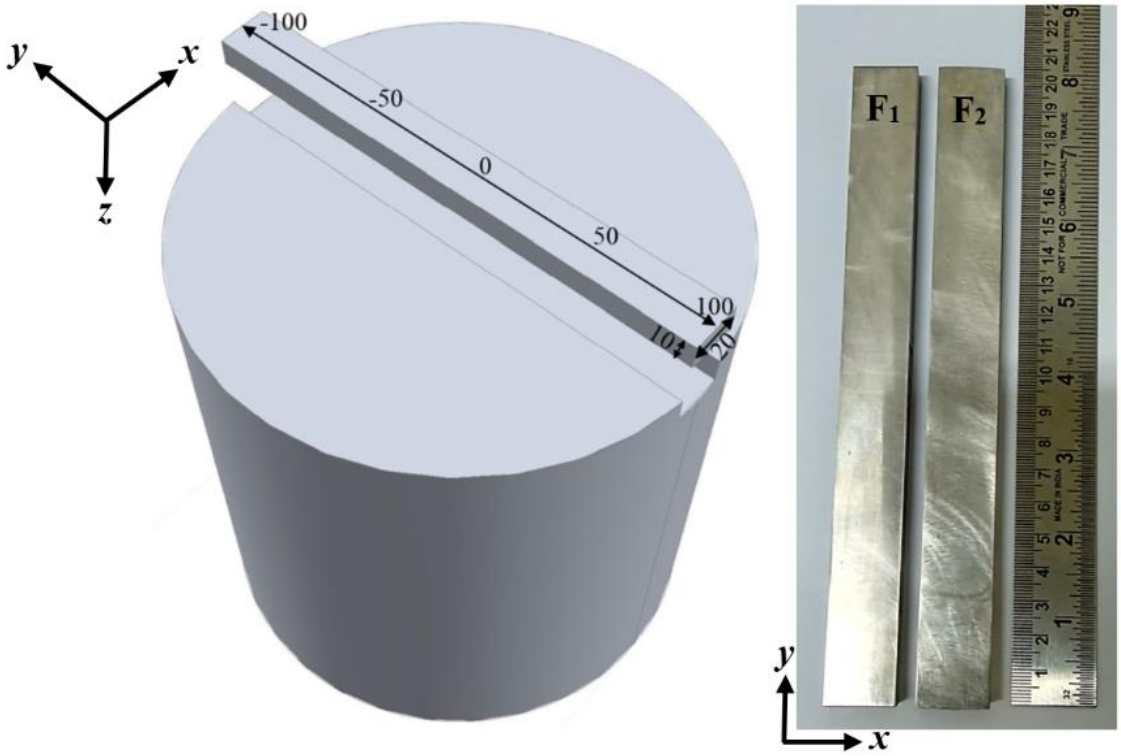

Fig. 3.1: Schematic representation and the photographs of the strips extracted from the forging of diameter 200 mm

3.2.3 Materials with similar mean grain size but different grain size distribution

Two AISI 304 austenitic stainless-steel plates (designated as P_1 and P_2) from different production lots were used to investigate the effect of grain size distribution on the measured acoustic nonlinearity parameter. It has a chemical composition given in Table 3.1. The plates were subjected to similar hot rolling conditions and heat treatment cycles. Specimens of dimension 100mm × 100mm × 12mm were cut from these plates and machined to a thickness

10 ± 0.01 mm with uniform surface finish and plane parallelism for the linear and nonlinear ultrasonic measurements. Specimens for metallography were also prepared, and the mean grain size (D_{mean}) and the standard deviation (σ) were measured as described in Section 3.5.1. Twins were also considered when measuring the grain boundaries as it is a common practice in the ultrasonic characterization of microstructure.[149]

3.2.4 Materials subjected to pre-defined plastic deformation

AISI type 304 austenitic stainless steel material of chemical composition given in Table 3.1 was used for generating deformed microstructure. Specimens of dimension 220mm × 25mm × 12mm were solutionized in a muffle furnace for different annealing conditions as given in Table 3.4 in order to produce four different grain sizes. The annealed specimens were further machined to flat tensile specimens of dimensions shown in Fig. 3.2.

Table 3.4: Heat Treatment Matrix and the Grain Size Measurement

Specimen ID	K	L	R	S
Temperature (˚C)	1050	1050	1100	1150
Soaking Time (min)	30	60	60	60

The experimental set up for the tensile deformation consists of a computer servo control material testing machine of capacity 250 kN (HT-2402). Specimens from each unique grain size were subjected to 6.6 × 10^{-4}/s strain rate under uniaxial tension and tested to fracture to obtain the stress-strain curve. The elastic and plastic deformation limits for each specimen were estimated from these curves. The fracture behaviour of the specimens was studied under a scanning electron microscope. In addition, confocal microscopy and surface profilometry were used to estimate the surface roughness near the fracture.

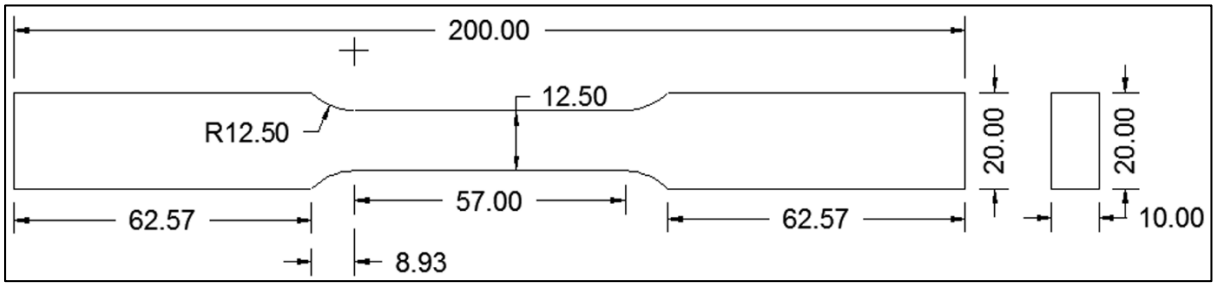

Fig. 3.2: Schematic of the flat tensile test specimen

Subsequently, a set of tensile specimens of specific grain size were deformed separately into the true strains of 0.33, 0.51 and 0.67 which are well below the UTS. The deformed specimens were further machined to a surface finish of better than 1 micron to achieve a smooth surface for ultrasonic contact measurements. For microscopic studies, small specimens were cut from the middle of the gauge length of the deformed specimens. The ferrite number and the strain-induced martensite within the gauge length of the deformed specimens were evaluated using a ferritscope magnetic Barkhausen emission (MBE) as described in sections 3.7 and 3.8, respectively.

3.3 Linear ultrasonics

3.3.1 C-scan imaging

It is clear from the literature that a quantitative measurement of the ultrasonic attenuation is not always feasible or, in certain situations, inferior to the acoustic nonlinearity measurements. However, in order to have a qualitative comparison, the attenuation behaviour of the specimens was evaluated at the frequencies used for the NLU. One of the well-known methods for ultrasonic non-contact attenuation mapping is immersion C-scan imaging. The specimens were immersed in water and held in the far-field of the unfocused immersion transducers of centre frequency, f_c. Such a non-contact method eliminates the effect of contact pressure and coupling conditions on the ultrasonic signals and to accomplish an automated scanning for the C-scan imaging. The water column height between the transducer face and the specimen surface was more than r^2/λ_w, where r is the radius of the transducer and λ_w is the wavelength in water. Care has been taken to keep the surface of the specimen normal to the ultrasound beam. A schematic representation of the experimental set up used for the C-scan imaging is shown in Fig. 3.3. The system is equipped by an automated 6-axis manipulator (DHVANI make) to perform an X-Y raster scan. The ultrasonic pulses were generated and received in pulse-echo mode by means of a JSR DPR-300 pulser-receiver and digitized using an NI data acquisition card of 100 MHz sampling rate.

The received signals were stored in a digital storage oscilloscope (DSO), and the frequency-dependent attenuation was calculated from their spectral amplitudes using Eq. (2.7). Fig. 3.4 shows a typical time domain signal in which the front wall echo (u_0), the first (u_1) and second (u_2) back-wall echoes are indicated. The receiver gain of the pulser-receiver was adjusted to

keep the first back-wall echo above 80% of the full-screen height. However, in order to construct the frequency-dependent C-scan images, the received time domain signals were further processed through a Bessel bandpass filter with a bandwidth f_c ± 0.5 MHz.

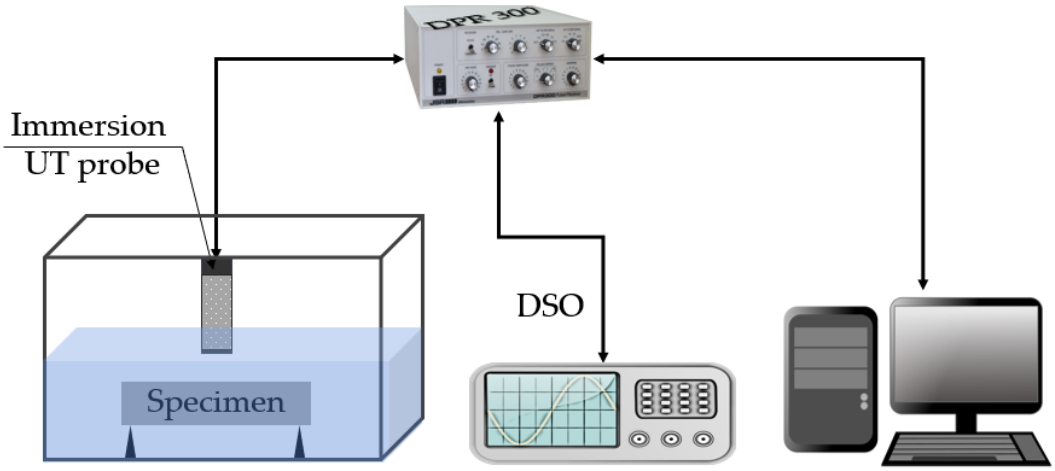

Fig. 3.3: Schematic of the experimental set up used for the immersion-based (C-scan imaging) attenuation measurement

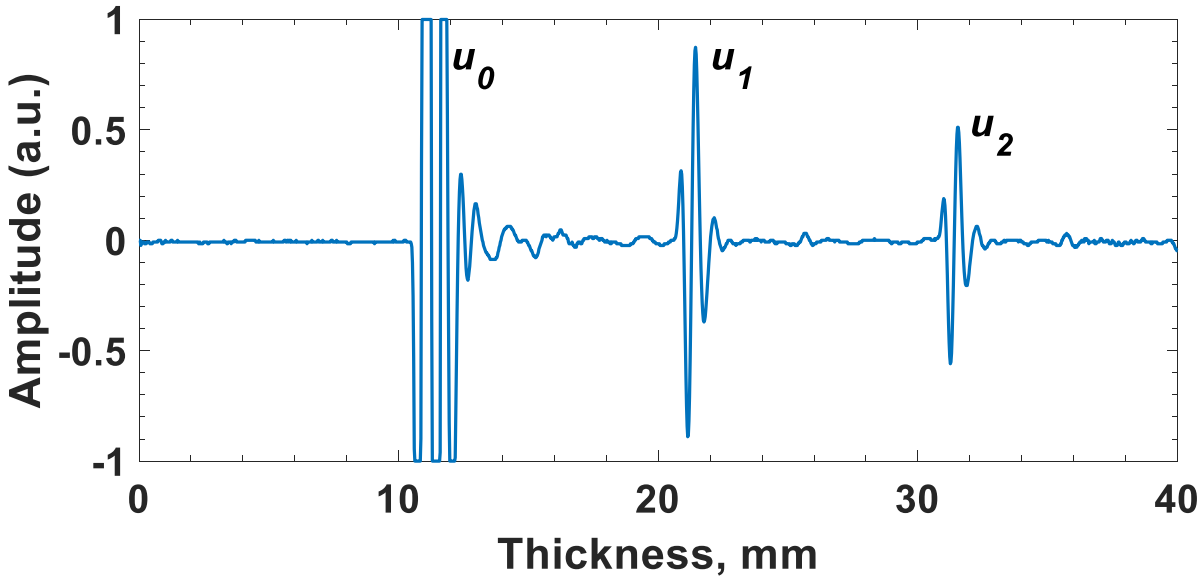

Fig. 3.4: Time domain signals in immersion mode showing the front wall echo (u_0), the first (u_1) and second (u_2) back-reflected signals

3.3.2 Frequency-dependent attenuation

Attenuation of ultrasonic waves in a medium causes frequency shift, and, as a result, the spectral peak (f_p) need not be at the centre frequency (f_c). Such a shift is dominant at higher frequencies and with the order of back-wall reflection. Therefore, for a given input pulse, the frequency shift will be large for the second back-wall echo compared to the first. Fig. 3.5(a) highlights the first (u_1) and second (u_2) back wall echoes received from an AISI type 304 austenitic stainless-steel plate of thickness 10 mm in the immersion pulse-echo mode using a transducer of centre frequency 10 MHz (f_c). It is evident from Fig. 3.5(b) that the peak frequency of the first back-wall echo ($f_p^{u_1}$) was shifted to 9.5 MHz and that of the second back-wall echo ($f_p^{u_2}$) was shifted to 8.8 MHz as a result of the dispersion and scattering effects. Therefore, amplitude-based attenuation measurements in the time-domain would be erroneous. Hence, the frequency spectrum of the first and second back-wall echoes need to be obtained, and the frequency-dependent attenuation can be calculated using Eq. (2.7) from the amplitudes

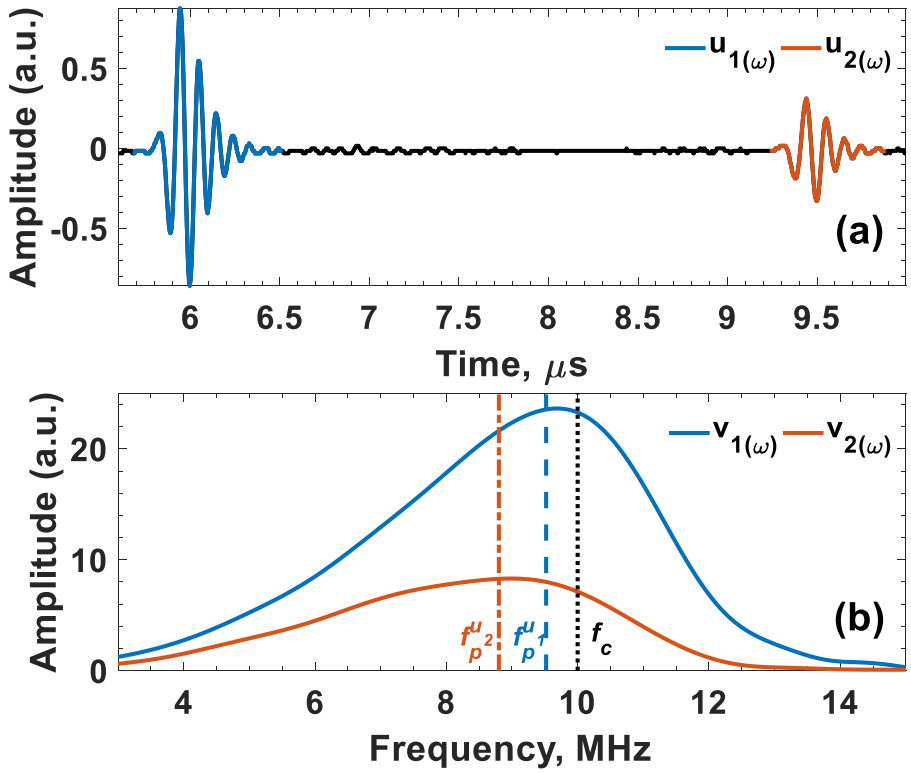

Fig. 3.5: (a) A time domain signal with the first ($u_{1(\omega)}$) and second ($u_{2(\omega)}$) back wall echoes and (b) the corresponding FFTs ($v_{1(\omega)}$) and second ($v_{2(\omega)}$). The frequency spectrum shows a shift in the peak frequencies ($f_p^{u_1}$ = 9.52 MHz and $f_p^{u_2}$ = 8.8 MHz) from the excitation frequency (f_c = 10 MHz).

of the $v_{1(\omega)}$ and $v_{2(\omega)}$. However, for thick materials with abnormal grain growth and larger mean grain sizes, high-frequency attenuation measurements would be difficult due to the severe scattering losses.

3.4 Nonlinear ultrasonics

3.4.1 Experimental set-up for nonlinear ultrasonics

The experimental set up used for measuring the nonlinearity parameter includes a RITEC make RAM-5000 SNAP system, a 50 Ω load, transducers, digital storage oscilloscope (DSO), probe fixture, cables and a personal computer as schematically illustrated in Fig. 3.6. The SNAP is a computer-controlled transmitter-receiver unit with an operational frequency ranging from 250 kHz to 80 MHz. It can provide high power RF tone burst signals modulated with a rectangular or a Hann window to drive the transducers without any induced harmonic distortions. It consists of two gated amplifiers of different frequency ranges, a superheterodyne receiver that can filter, reverse the phase and sweep the frequency of the fundamental and harmonics. The number of cycles can be adjusted, and the signal phase can be inverted using the software interface. A special probe holder assembly has ensured the coaxial alignment of the transducers. This

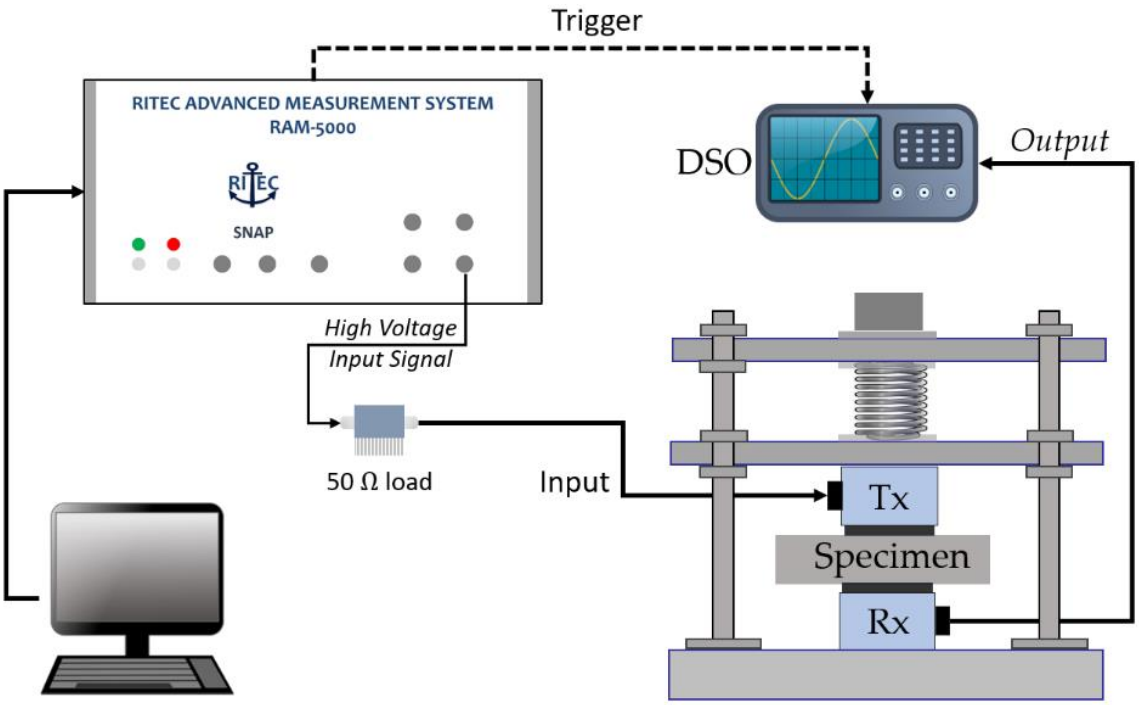

Fig. 3.6: Schematic of the experimental setup for the NLU measurements

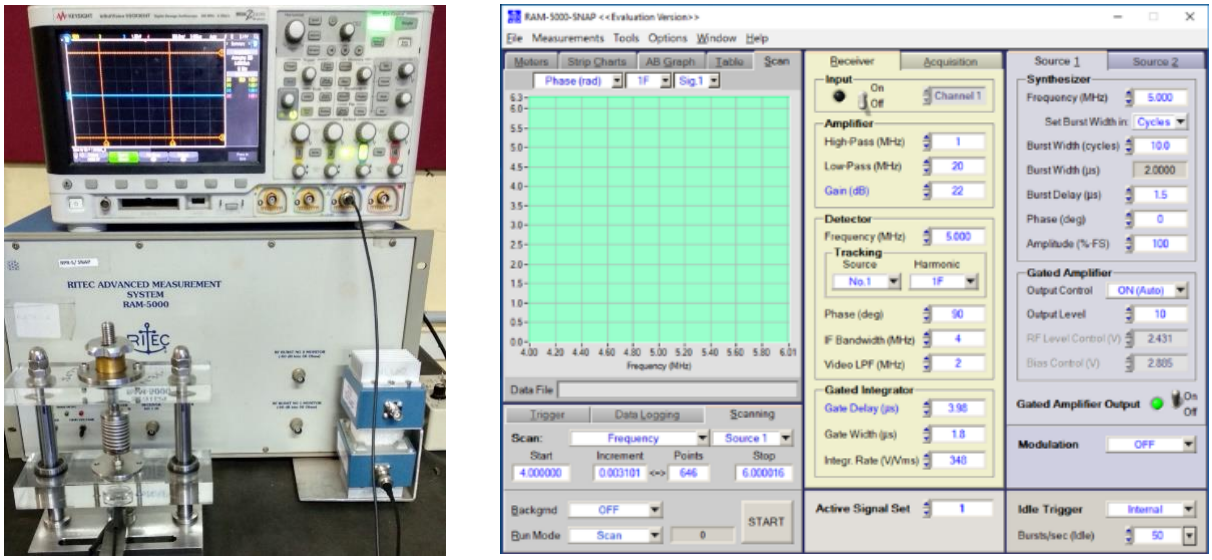

Fig. 3.7: (a) Photograph of the NLU experimental set up and (b) the computer interface to control the RAM-5000 NLU system.

spring-loaded assembly could maintain constant coupling pressure on the transducers during the measurements. A photograph of the experimental setup and the computer interface to control the RAM-5000 SNAP are shown in Fig. 3.7.

3.4.1.1 Transducers

Longitudinal piezoelectric transducers were used in the through-transmission mode for the NLU measurements. The transducers were of Panametrics (Olympus) make, and the details are given in Table 3.5. They are untuned transducers that provide heavily damped broadband performance. The transmitter and receiver transducers are designated as T_x and R_x, respectively, as indicated in Fig. 3.6. Three sets of T_x - R_x pairs: 2.25 MHz - 5.0 MHz, 5.0 MHz - 10.0 MHz and 7.5 MHz - 15.0 MHz were used for nonlinearity measurement. Due to the non-availability of the 4.5 MHz transducer, a 5.0 MHz transducer was used to receive the second harmonic component when the input frequency was 2.25 MHz. The range of frequency combinations (2.25 MHz to 15.0 MHz) was chosen in such a way that, the ultrasonic waves in this range interact through the Rayleigh and/or stochastic mechanisms with the grain sizes of the materials used in the present thesis (mean grain size varies from 33 μm to 391 μm). However, the experiments were conducted independently for each pair of transducers.

Table 3.5: Details of the ultrasonic transducers used for NLU measurements			
	Frequency	Part No	Nominal Element Size
1	2.25 MHz	V133-RM	6.25 mm
2	5.0 MHz	V110-RM	
3	7.5 MHz	V121-RM	
4	10.0 MHz	V112-RM	
5	15.0 MHz	V113-RM	

3.4.1.2 Linearity check

Prior to the commencement of actual experiments, the SNAP system and the transducers were ensured to have a linear response against the system power levels and the transducer output. The transducers (Tx) were excited at their rated frequencies using sinusoidal tone bursts. The excitation power level was varied from 10% to 100% of the maximum output power of the SNAP system. The ultrasonic wave thus generated was transmitted to a fused silica disc of thickness 9.3 mm, and the propagated wave was received from the opposite side using the

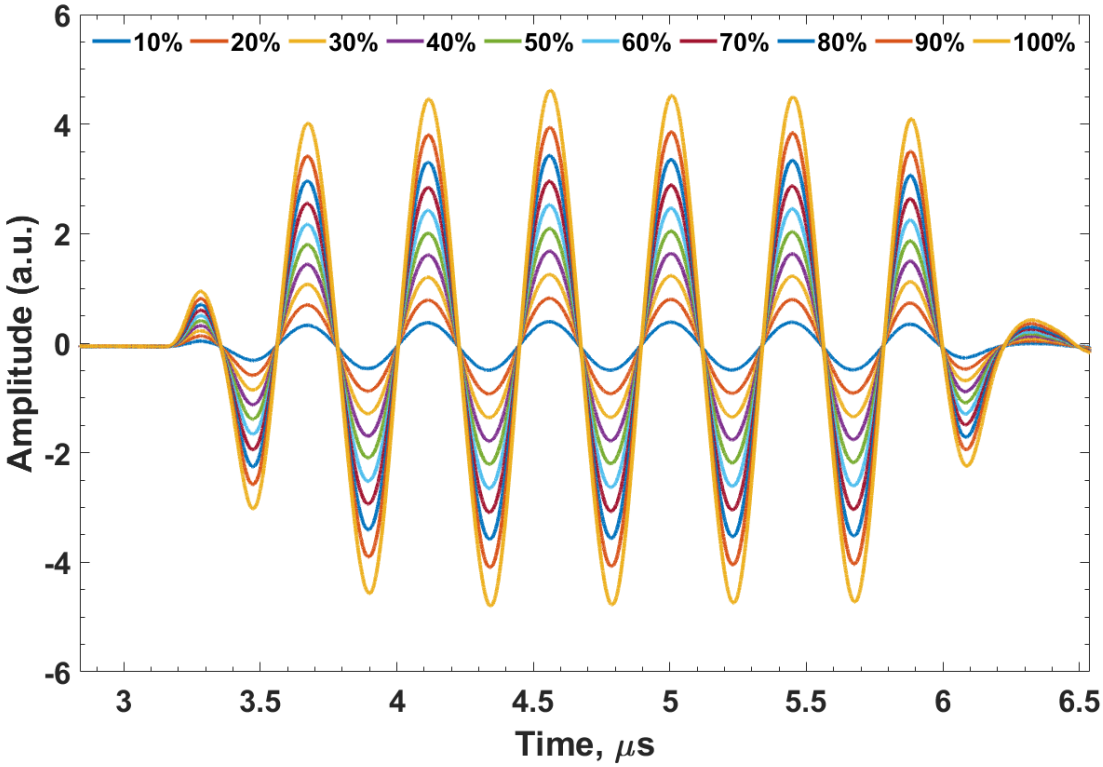

Fig. 3.8: Amplitude of 6-cycle 2.25MHz waveform with power level varying from 10% to 100% of the SNAP system. Signal amplitude increases proportionally with the power level.

respective pair transducers. The received signal was then subjected to Fast Fourier Transform (FFT), and the amplitude of the fundamental frequency was plotted against the corresponding SNAP power levels. A typical waveform of a 6-cycle 2.25 MHz input and the corresponding frequency spectra for different power levels are shown in Fig. 3.8 and Fig. 3.9, respectively. A similar analysis was conducted for other frequencies also. In each case, the tone burst length of the input waveform was kept identical.

The spectral amplitudes for all three input frequencies were measured at different SNAP power levels (%) and plotted in Fig. 3.10. In all three cases, a linear regression fit with the R^2 values of 0.99 was observed. This has ensured the linear behaviour of the SNAP system towards the frequencies used in the NLU measurements. It is worth noting that the difference in their slope among the frequencies is due to the difference in the transducer response, which is expected. However, such differences will be normalized by the procedure described in section 3.4.7. Therefore, it would not affect the interpretation of the results in a relative measurement of the nonlinearity parameter being pursued throughout the present thesis.

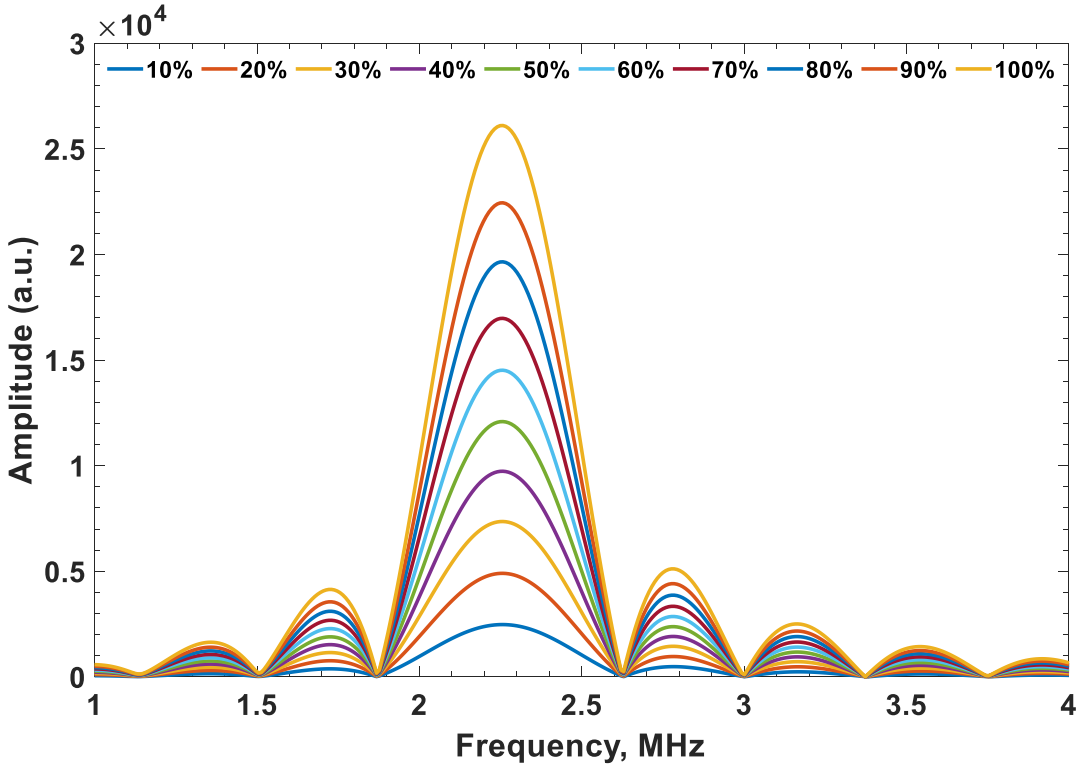

Fig. 3.9: Spectral amplitude of 6-cycle 2.25MHz waveform with power level varying from 10% to 100% of the SNAP system. The amplitude increases with the power level.

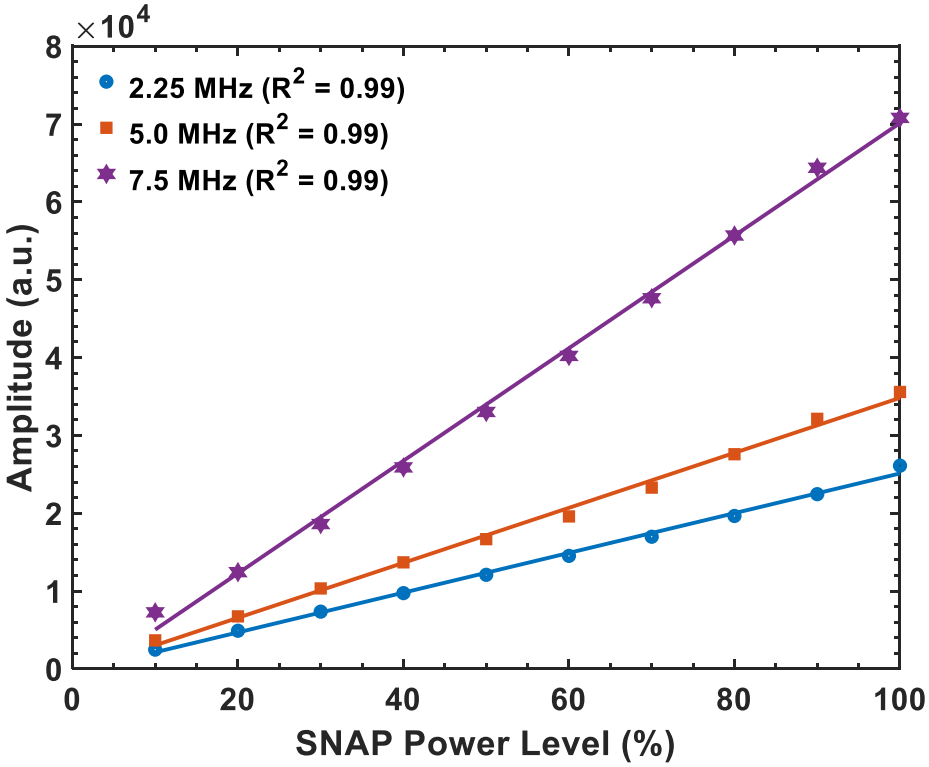

Fig. 3.10: Linear relationship between the input power levels and the output amplitudes for different transducers. Power levels are in % of the maximum output power of the SNAP system.

3.4.2 Nonlinear ultrasonic measurements

A uniform layer of couplant was applied between the specimen and the transducers in order to displace any air gap in between. It was ensured that the same transducers, excitation range and surface conditions were maintained for repeatability and to reduce the experimental and instrumental nonlinearities. The NLU measurements were carried out at multiple locations in each specimen, and, at each location, the material response for six different power levels of the RITEC system (40% to 90% with an increment of 10%) was obtained. Reducing the range of the applied power levels during the experiment minimized the number of measurements and at the same time ensured a realistic estimate of the acoustic nonlinearity from the slope of the A_2 vs. A_1^2 plot. The output from the receiver was stored in a digital storage oscilloscope (KEYSIGHT InfiniiVision DSOX3024T), which digitized the received signal into 16000 data points at a sampling rate of 200 MHz. These data were further used to extract the harmonic content of the signal.

3.4.2.1 Signal analysis

Fast Fourier transform (FFT) is an efficient algorithm generally employed to analyse the frequency components embedded in a signal. For a signal $f(x)$, the FFT is performed as

$$f(t) = \int_{-\infty}^{\infty} f(x)\, e^{-2\pi i t}\, dx \tag{3.1}$$

However, the leading (transient) and trailing (ringing) edges of a purely sinusoidal waveform get distorted due to the damping effect of the piezoelectric crystal, surface characteristics of the transducer face and the specimen roughness. A typical sinusoidal waveform of fundamental frequency 5 MHz received from a 10 mm thick austenitic stainless-steel material used in this study is shown in Fig. 3.11. Distortions to the sinusoidal nature can be observed in the transient and ringing regions due to the damping effects mentioned above. A distortion-free region can be identified at the middle of the time domain waveform if a sufficient number of cycles (signal length) are provided. This region can be segmented and utilized to extract the harmonic response of the material. However, this methodology cannot be implemented on thin specimens or while applying low-frequency inputs since the number of waveform cycles is limited in both cases. In this context, windowing of the received signals followed by the FFT is of the right choice.

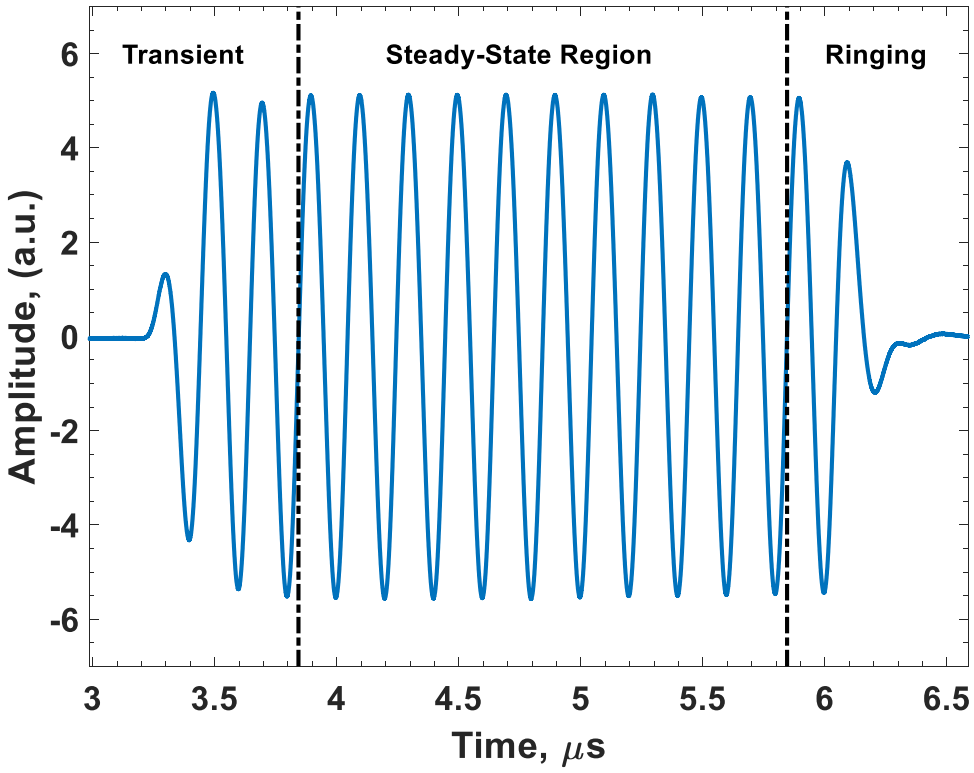

Fig. 3.11: Distortions in the received time domain signal due to the transient and ringing effects

3.4.2.2 Windowing functions

The spectral leakage associated with the Fourier transform is one of the major drawbacks of any windowing function. Fourier transform algorithm is based on the assumption that the time record is exactly repeated throughout all time and that the signals contained in a time record are thus periodic at intervals that corresponds to the length of the time record. Spectral leakage is a result of this assumption. If the signal has a non-integer number of cycles, this assumption is violated, and spectral leakage occurs where energy from a given frequency component is spread over adjacent frequencies. A proper window is to be selected in order to minimize this effect over a non-integer number of cycles. For an integral number of cycles, all windows yield the same spectral amplitude and have excellent amplitude accuracy. The frequency resolution of the windowed signal is limited by the width of the main lobe, and the amplitude resolution is limited by the spectral leakage. The rectangular window has the narrowest main lobe, and other windows introduce a significant spread. As the primary lobe narrows and spectral resolution improves, the window energy spreads into its side lobes, and spectral leakage strengthens. In general, there is a trade-off between the suppression of spectral leakage and the frequency resolution.

Windowing of the input data is equivalent to convolving the spectrum of the original signal with that of the window. The sinusoidal signal shown in Fig. 3.8 may be considered as modulated with a rectangular window which is defined by

$$w(n) = \begin{cases} 1, & 0 \le n \le N \\ 0, & otherwise \end{cases} \tag{3.2}$$

However, the selection of a proper window function is based on the frequency components of interest, spectral resolution, amplitude accuracy and flatness of the spectrum. A proper window function may be selected based on the peak sidelobe level (PSL) and the side lobe roll-off rate. The sidelobe level is the maximum value of the side lobes relative to the main lobe, and the side lobe roll-off rate is the asymptotic decay rate of the side lobes. If the signal contains frequency components distant from the frequency of interest, choose a window with a high sidelobe roll-off rate and if there are components near the frequency of interest, choose a window with a lower PSL. Therefore, processing of the time domain signal to extract the harmonics and thereby the β using the fast Fourier transform heavily depends on the windowing functions used. Some of the most commonly used windowing functions[150] are introduced in Eqns. (3.3) to (3.6).

Hanning window function

$$w(n) = \begin{cases} 0.5\left(1 - cos\left(\frac{2\pi n}{N}\right)\right), & 0 \le n \le N \\ 0, & otherwise \end{cases} \quad (3.3)$$

Hamming window function

$$w(n) = \begin{cases} 0.54 - 0.46\left(\frac{2\pi n}{N}\right), & 0 \le n \le N \\ 0, & otherwise \end{cases} \quad (3.4)$$

Blackman window function

$$w(n) = \begin{cases} 0.42 - 0.50cos\left(\frac{2\pi}{N}n\right) - 0.08cos\left(\frac{4\pi}{N}n\right), & 0 \le n \le M-1 \\ 0, & otherwise \end{cases} \quad (3.5)$$

where, $M = N/2$ for N even and $M = (N+1)/2$ for N odd.

Bartlett window function

$$w(n) = \begin{cases} \frac{2n}{N}, & 0 \le n \le \frac{N}{2} \\ 2 - \frac{2n}{N}, & \frac{N}{2} \le n \le N \end{cases} \quad (3.6)$$

Table 3.6: Windowing Functions and Parameters

Window Function	PSL (dB)	Side Lobe Roll-Off Rate (dB/octave)	Main Lobe Width
Hanning	-31	-18	$8\pi/N$
Hamming	-42	-6	$8\pi/N$
Blackman	-58.1	-18	$12\pi/N$
Bartlett	-26.5	-12	$8\pi/N$
Rectangular	-13	-6	$4\pi/N$

The window function, which gives high resolution to the harmonics in a signal, should be chosen. The resolution of a window function is characterized by its peak sidelobe level, side lobe roll-off rate and main lobe width, which are tabulated in Table 3.6. Also, the filter visualization for these window functions is shown in Fig. 3.12.

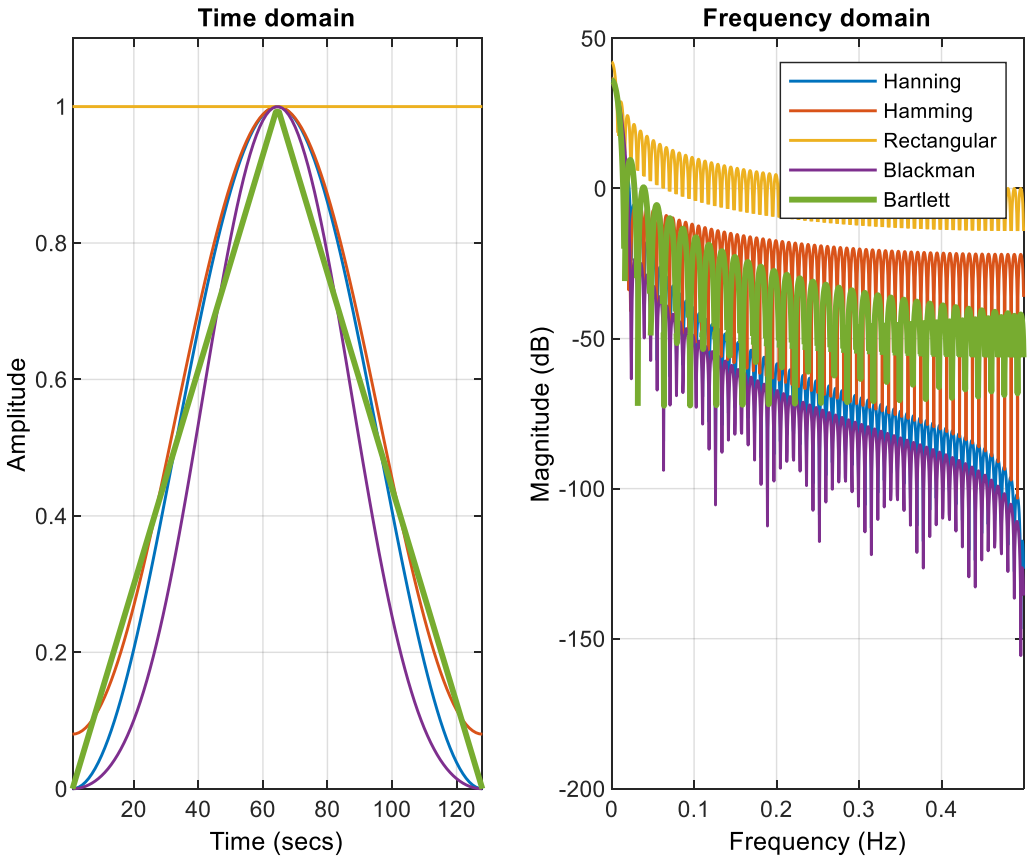

Fig. 3.12: Filter visualization in time domain and frequency domain for different window functions

3.4.2.3 Optimization of the window function

Effect of various windowing functions on a sinusoidal time domain (TD) signal of fundamental frequency 5 MHz and the corresponding FFT are compared in Fig. 3.13. The fundamental (A_1) and the second harmonic (A_2) components are clearly visible in the spectrum, and their amplitudes can be measured accurately. As it is seen, the amplitude of the side lobes of the windowed (modulated) signals is significantly reduced compared to that of the unmodulated (raw) signal.

The A_2 vs A_1^2 plot for a typical received signal modulated with the five windowing functions is compared in Fig. 3.14. The output power level of the SNAP system was varied from 40% to 90% of the maximum power level in steps of 10%, and a linear regression fit was found to be the best fit connecting A_2 and A_1^2 for all six power levels. This linearity holds good even with the modulation. However, the change in the slope of the A_2 vs. A_1^2 plot with modulation is the characteristic property of each window function which is related to the spectral leakage while

performing the FFT. Spectral leakage of the A_1 component into the side lobes is drastically reduced with modulation, which causes an increase in the slope. Therefore, the nonlinearity parameter derived from the slope of the A_2 vs. A_1^2 depends on the modulation. However, the modulation will not affect the interpretation of the results as long as the nonlinearity parameter is measured as a relative variable for a fixed windowing function. The Hanning window function is one of the simple and most popular windowing functions which has the highest side lobe roll-off rate (-18 dB/octave) and lower main lobe width. Hence, in this thesis, the received waveforms are Hann modulated in order to eliminate the fluctuations at the leading and trailing edges and then performed the FFT to compute the harmonic components. As it is seen from Fig. 3.14, the A_1^2 which is in the denominator of Eq. (2.25) is several orders of magnitude higher than the A_2. Therefore, any change in the amplitude of A_1 due to, for example, attenuation of the fundamental wave in the material, can affect the measured β significantly due to the way Eq. (2.25) is defined.

Fig. 3.15 shows the typical time-domain signals modulated with the Hanning window function and the corresponding frequency spectra for three different input frequencies used in this thesis. The amplitude of the fundamental (A_1) and the second harmonic (A_2) components was measured from the frequency spectrum, and the slope of the A_2 vs A_1^2 curve was used to calculate the β.

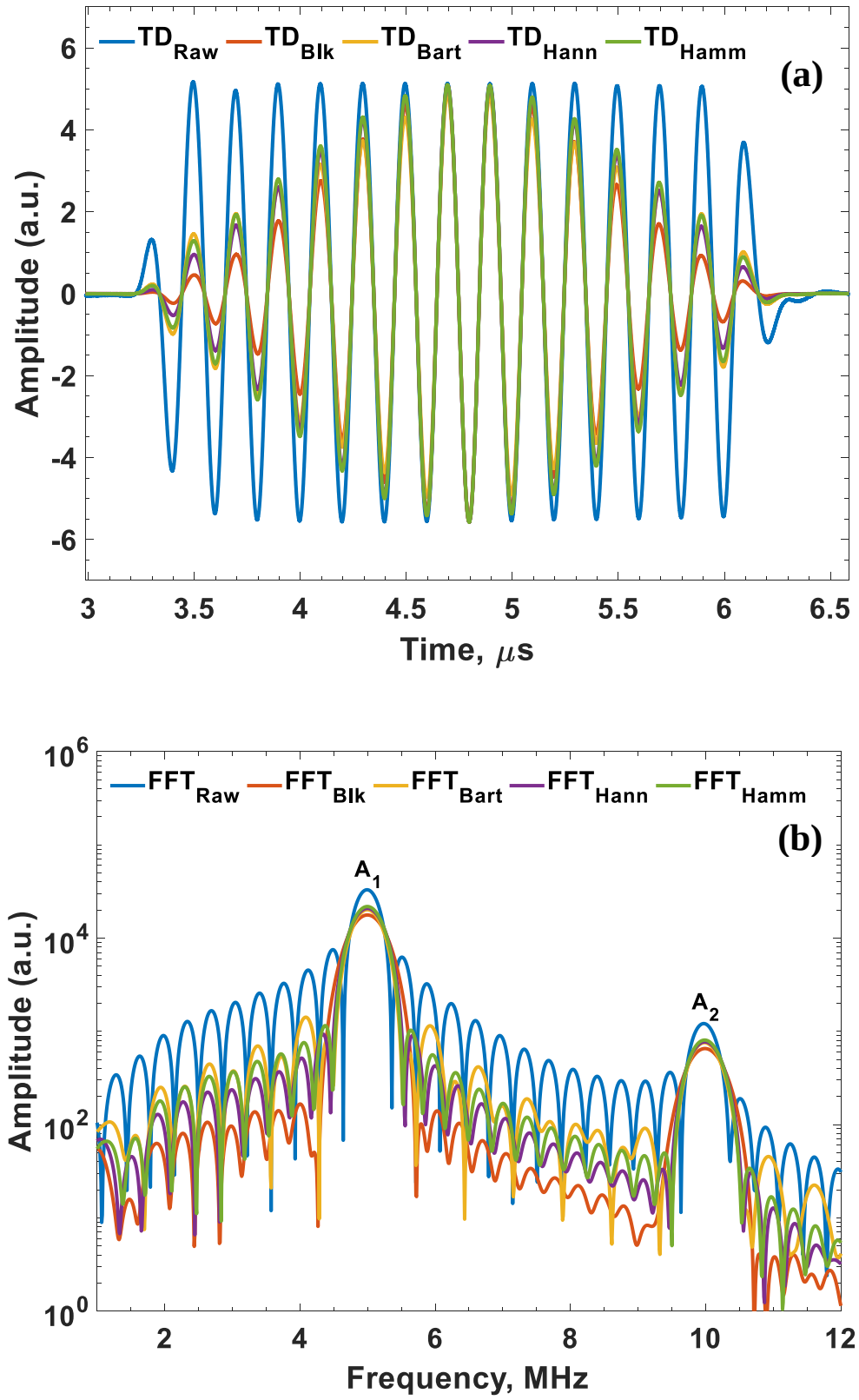

Fig. 3.13: (a) Received time domain signal (TD_{Raw}) modulated using the Blackman (TD_{Blk}), Bartlett (TD_{Bartt}), Hanning (TD_{Hann}) and Hamming (TD_{Hamm}) windowing functions and (b) the corresponding FFTs

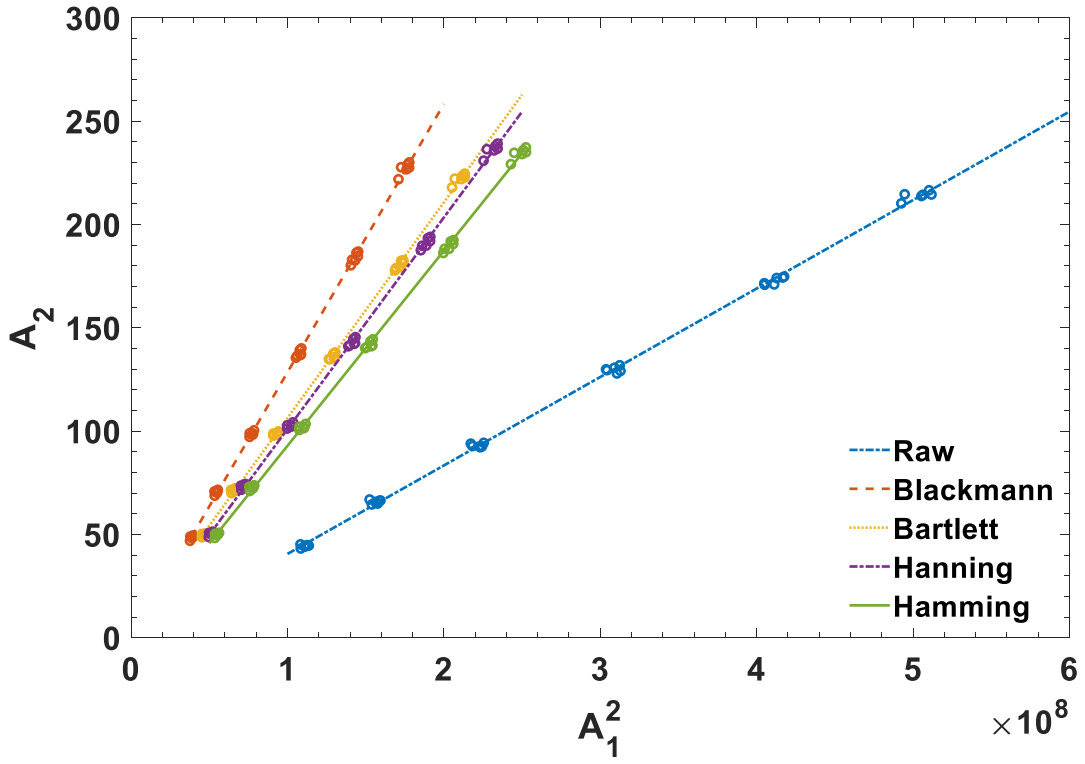

Fig. 3.14: The A_2 vs A_1^2 for the signals modulated with different windowing functions

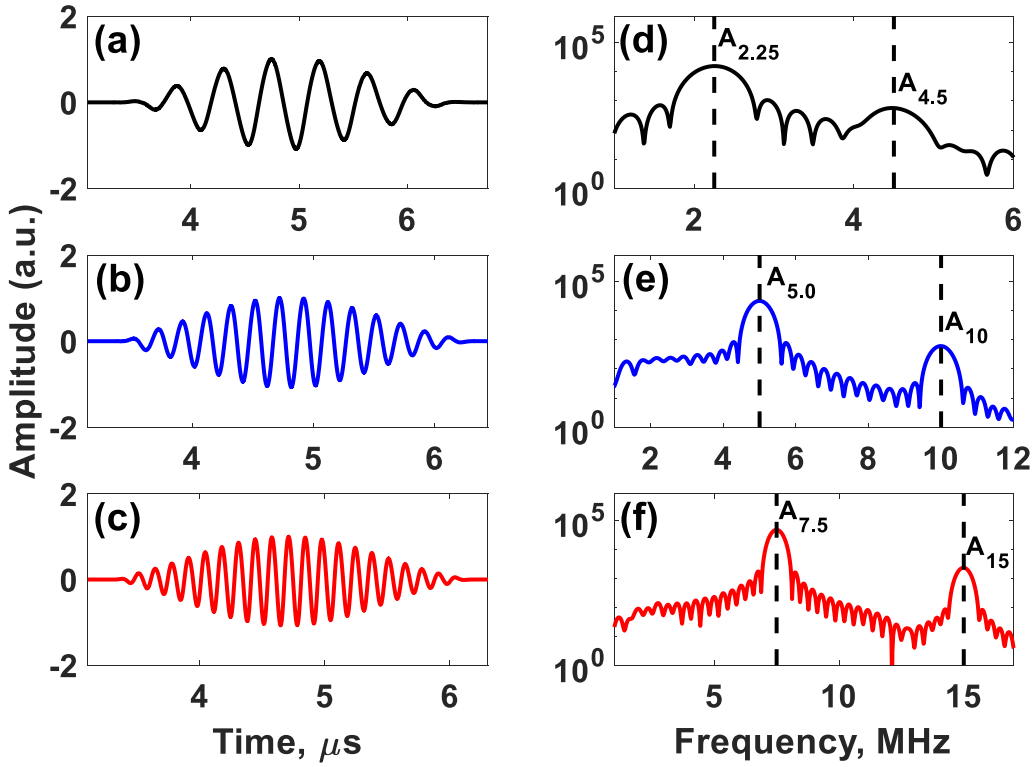

Fig. 3.15: Typical time-domain signals of frequency (a) 2.25 MHz, (b) 5.0 MHz and (c) 7.5 MHz and (d-f) the corresponding frequency spectra

3.4.2.4 Signal duration

It is worth noting that, when the waveform duration (signal length) is longer, the probability of the anharmonic interactions with the crystalline lattice increases, which raises the harmonic amplitude. The effect of pulse duration on the spectral amplitude is illustrated in Fig. 3.16 for a 5 MHz tone burst transmitted to an AISI type 304 austenitic stainless-steel material of thickness 10 mm. The signal length was varied from 1 cycle to 13 cycles and, in each case, the corresponding FFT of the received signal was plotted. The spectral response indicates that,

- as the signal length increases, amplitudes of both the fundamental and second harmonic components increases, and,
- the spectrum becomes smoother and narrower as the number of cycles increases.

It is evident from Fig. 3.16 that, larger the number of cycles, the sharper the spectrum and hence higher will be the accuracy in measurement of harmonic amplitude. However, the number of cycles is limited by the thickness of the material in order to avoid the interactions between the propagating and reflected waves. In addition, the tone burst length of the input waveform was kept identical (2.6 μs) for all three input frequencies, and the details are given in Table 3.7. The finite element visualization of each waveform inside the AISI type 304 austenitic stainless-steel specimen of thickness 10 mm (Fig. 3.17) confirms that the applied tone burst length does not cause the reflected echoes reaching the receiver transducer.

Table 3.7: Details of tone burst length and waveform duration

Frequency	Tone burst length	Number of Cycles
2.25 MHz	2.6 μs	6
5.0 MHz		13
7.5 MHz		21

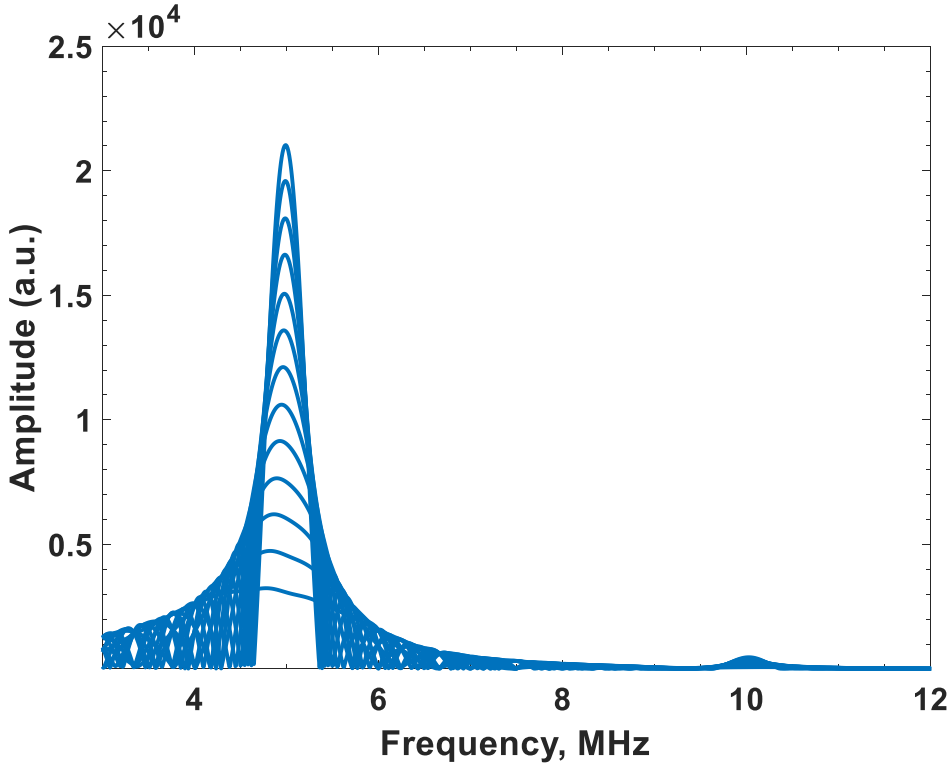

Fig. 3.16: Spectral amplitudes as a function of number of cycles. The spectral amplitude increases with the number of cycles (from 1 to 13 cycles for the given case).

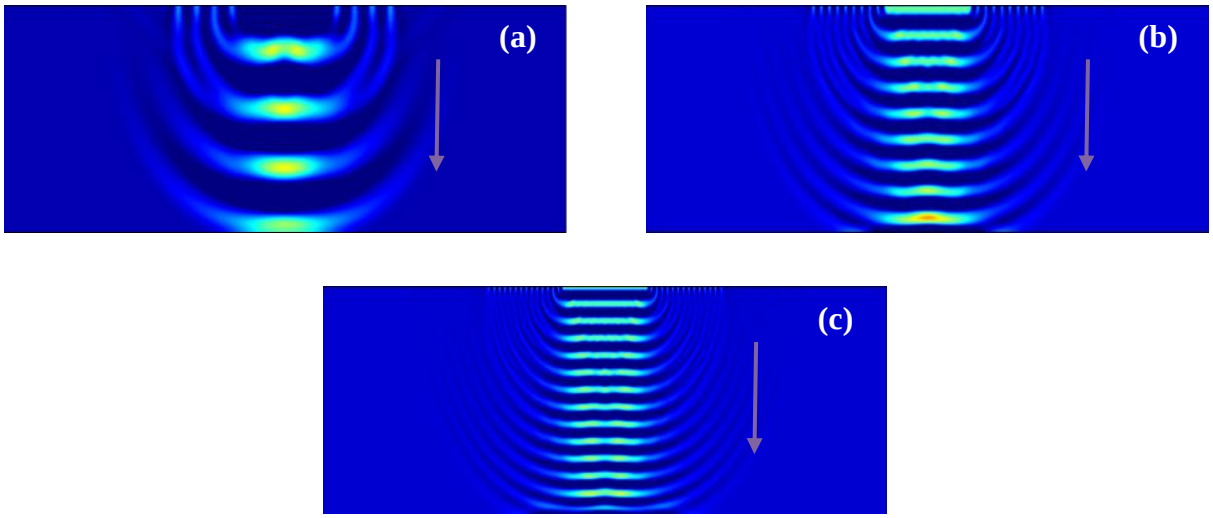

Fig. 3.17: Waveform visualization of input sinusoidal signals of frequency (a) 2.25 MHz, (b) 5.0 MHz and (c) 7.5 MHz propagated through a material of thickness 10 mm. Propagation direction in indicated by an arrow.

3.4.2.5 Normalization procedure

Normalization of the measured β with that of a reference specimen is a standard procedure to remove nonlinearities from other sources, such as instrumental or experimental. In general, the normalization can be performed by $\beta_{norm} = \beta_{m,\omega_i}/\beta_{r,\omega_i}$ where m stands for the test specimen, r stands for the reference for a given frequency, ω_i. The normalization also enables us to compare the relative variation of the nonlinearity parameter in materials while performing the NLU with different input frequencies. However, the reference specimen chosen for normalization would vary depending on the scope of the analysis and hence will be described promptly in the respective sections.

3.5 Evaluation of the microstructure and mechanical properties

3.5.1 Optical microscopy

Small specimens cut for grain size measurements were polished to diamond finish and subjected to electrolytic etching in 60 wt.% HNO_3 solution to reveal the grain boundaries. The photomicrographs were obtained using an inverted optical microscope (Olympus GX51).

3.5.1.1 Grain size measurement

In a polycrystalline material, different grains grow independently under the same heating conditions, and hence the size of a single grain cannot be used for explaining the microstructure. The mean grain size (D_{mean}) and the standard deviation (σ_D) in the materials used for the present investigation were estimated from the photomicrographs as per the ASTM standard E112. In metallography, the grain size is usually expressed by the mean grain diameter, D_{mean}, which is defined as the average orthogonal distance between the infinite pairs of parallel planes tangent to the surface of the grain. Therefore, from now on, the grain size refers to the D_{mean}. In polycrystalline materials, grains follow the lognormal distribution, which can be written as

$$P(D) = \frac{1}{D\sigma\sqrt{2\pi}} exp\left[-\frac{ln^2(D/\widetilde{D})}{2\sigma^2}\right] \tag{3.7}$$

where the median of the grain size distribution $\widetilde{D} = e^{\mu}$ which is related to the volumetric mean of the distribution $\overline{D} = \widetilde{D}\, e^{(\sigma^2/2)}$ where σ is the logarithmic distribution width, and μ is the mean of the normal distribution.

3.5.1.2 Aspect ratio measurement

The aspect ratio (length-to-breadth ratio represented as a/b) of each grain of the specimens subjected to the plastic deformation was estimated from the photomicrographs. The aspect ratio measurements were elaborately discussed in Chapter 7.

3.5.2 Electron backscatter diffraction

Specimens used for the optical microscopy were further polished by 0.25 μm diamond suspension followed by colloidal silica treatment. The specimens were then etched electrolytically in 1:9 Perchloric acid and Methanol solution, and the EBSD data was collected at a step size of 2 μm. The EBSD data were further processed using the OIM^{TM} software for the inverse pole figure (IPF) maps and the grain orientation spread (GOS).

3.5.3 Hardness measurement

Hardness was taken at multiple locations on the specimens using a micro Vickers hardness tester (MMT-X7, Matsuzawa make). A diamond indenter ground in the form of a square pyramid with an angle of 136° between the faces was used for indentation. Micro indentation corresponding to a load of 200gf was imparted to each specimen. From the length of the diagonals of indentation, the hardness was determined. Measurements were taken at multiple locations to obtain a statistical distribution of the hardness.

3.5.4 Measurement of strain-induced martensite

The presence of martensite in austenite would influence the acoustic nonlinearity as its crystal structure (bct) is different from that of the austenite (fcc) matrix. Metallography or X-ray diffraction (XRD) techniques are widely used to measure the strain-induced martensite in metallic materials. Though such measurement provides good qualitative results of the martensite phase, their results appear to be overestimated since they are restricted to the surface,[151] and hence the absolute errors in the estimated martensite content can be higher. Therefore, measuring the magnetization of the material is a more effective and representative technique to determine the volume fraction of the martensite phase.[152] Hence, the magnetic Barkhausen emission (MBE) measurement on the gauge length of the plastically deformed specimens was carried out. The MBE measurements provide the spatial average of the martensite content over a large volume, which eliminates the inaccuracies associated with the surface preparation. The MBE was measured using a Rollscan 300 system (M/s Stresstech,

Finland) with MicroScan-600 magneto elastic analyser equipped with a standard sensor S1-138-15-01 consists of an excitation coil with a magnetizing core and a detecting coil placed between the magnetizing core legs. The excitation was given at a magnetizing voltage of 7V and magnetizing frequency of 125 Hz. The measurements were made within the gauge length in each specimen with properly maintaining the similar coupling conditions. The received signals were sampled at a frequency of 1 MHz without any digital frequency filter and were exported as .txt files for post-processing.

In addition to the MBE analysis, the ferrite number of each specimen was measured using a feritscope (Fishcher FMP30). It may be noted that the ferrite number is commonly used to estimate the delta ferrite content in austenitic stainless steels and can also be used to detect deformation-induced martensite. It is therefore used only for the qualitative assessment of the microstructure.

3.6 Summary

This chapter detailed the experimental methodology adopted in the present thesis. Experimental investigations organized in the subsequent chapters are

- studies on a set of annealed microstructures in AISI Type 304 austenitic stainless steel to understand the frequency dependence of the nonlinearity parameter at different scattering regimes,
- characterization of the microstructural heterogeneity in large diameter forgings where all possible variations in grain size coexist within a single material,
- investigation on the effect of grain size distribution on the acoustic nonlinearity parameter, and
- investigations on the characterization of the combined effect of grain size variations and plastic deformation on the acoustic nonlinearity parameter.

Chapter 4
Influence of Scattering Regimes on the Acoustic Nonlinearity Parameter

4.1 Introduction

From the detailed literature review presented in the previous chapter and the scope of objectives identified for the present work, it is clear that there is potential for developing nonlinear ultrasonics as a non-destructive evaluation technique to study the grain size variations in polycrystalline materials. There are little works already reported in this area but were confined to the elastic waves of a single frequency.[68,118] However, a single frequency analysis is not adequate in polycrystalline materials because various acoustic scattering regimes can coexist within the material, allowing the fundamental and harmonic frequency components to have different interaction mechanisms. As stated earlier, correction mechanisms are not always feasible to be implemented. Therefore, the nonlinear response at different acoustic scattering regimes in a polycrystalline material needs to be investigated systematically, considering the difference in the interaction mechanisms of the fundamental and harmonic components. A multi-frequency nonlinear ultrasonic methodology is introduced in this chapter to study the nonlinear response at different scattering regimes in a polycrystalline material.

4.2 Materials and methods

Austenitic stainless-steel type AISI304 has been selected for this study due to its single-phase polycrystalline nature. The thickness of the material was fixed to 10 mm as it falls within the thickness range most often employed for the fabrication of storage tanks and vessels in chemical and nuclear industries using this material. Grain size variation in the material was achieved by subjecting the material to solid solution annealing at different peak temperature and duration as described in Section 3.2.1. Subsequently, the specimens were subjected to ultrasonic C-scan imaging for attenuation mapping followed by nonlinearity measurements as per the procedures described in Section 3.3 and 3.4, respectively.

4.3 Results and discussions

4.3.1 Microstructure

The photomicrographs of the annealed specimens are shown in Fig. 4.1, and the corresponding histogram representation of the grain size distribution is presented in Fig. 4.2. The grain size in each annealed specimen was measured from the optical micrographs as per the ASTM standard E112. The average grain size and the standard deviation are given in Table 4.1. The histograms were superposed with the lognormal distribution curve since the grain size distribution in polycrystalline engineering materials is mostly lognormal.[3] Coexistence of fine as well as coarse grains in the annealed specimens is evident from the histograms. The mean grain size (D_{mean}), and the boundary at which the Rayleigh to stochastic scattering transition occurs ($D_{2.25}$, $D_{5.0}$ and $D_{7.5}$) for three different input frequencies (2.25 MHz, 5.0 MHz and 7.5

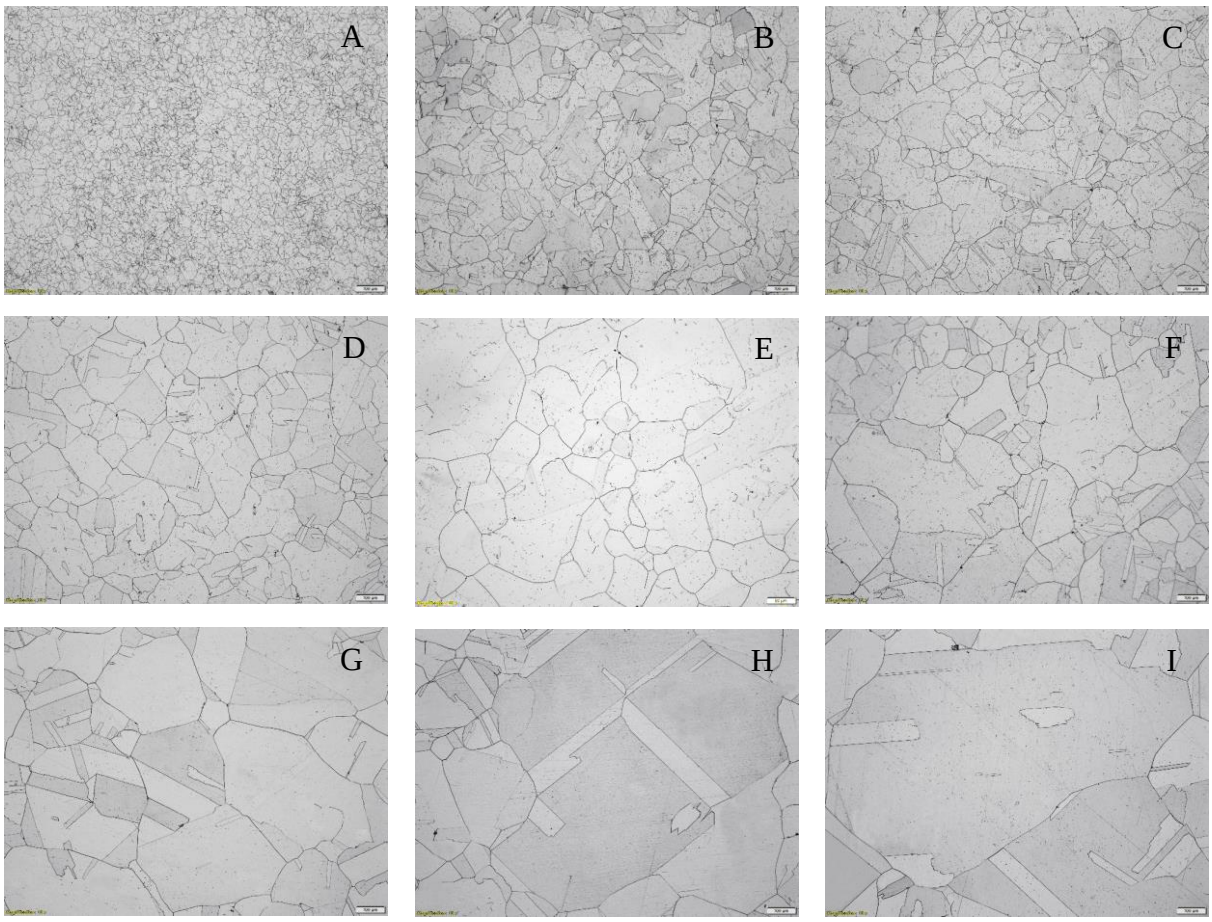

Fig. 4.1: Optical micrographs of the AISI 304 austenitic stainless-steel specimens subjected to different annealing conditions: (A) as-received, (B) 1050 ℃ / 60 min, (C) 1100 ℃ / 60 min, (D) 1100 ℃ / 120 min, (E) 1150 ℃ / 60 min, (F) 1150 ℃ / 120 min, (G) 1200 ℃ / 60 min, (H) 1200 ℃ / 90 min, and (I) 1200 ℃ / 120 min.

MHz) used in this investigation are also indicated. These transition boundaries and their positions to the D_{mean} have a significant effect on the measured β, which will be discussed in the subsequent sections. The scales of the histograms are not maintained consistently for clear visualization of the grain size distribution.

Table 4.1: The mean grain size and the standard deviation of the annealed specimens

Specimen ID	A	B	C	D	E	F	G	H	I
D_{mean} (µm)	44	101	121	153	176	210	228	274	391
σ_D (µm)	16	41	51	66	93	124	150	189	327

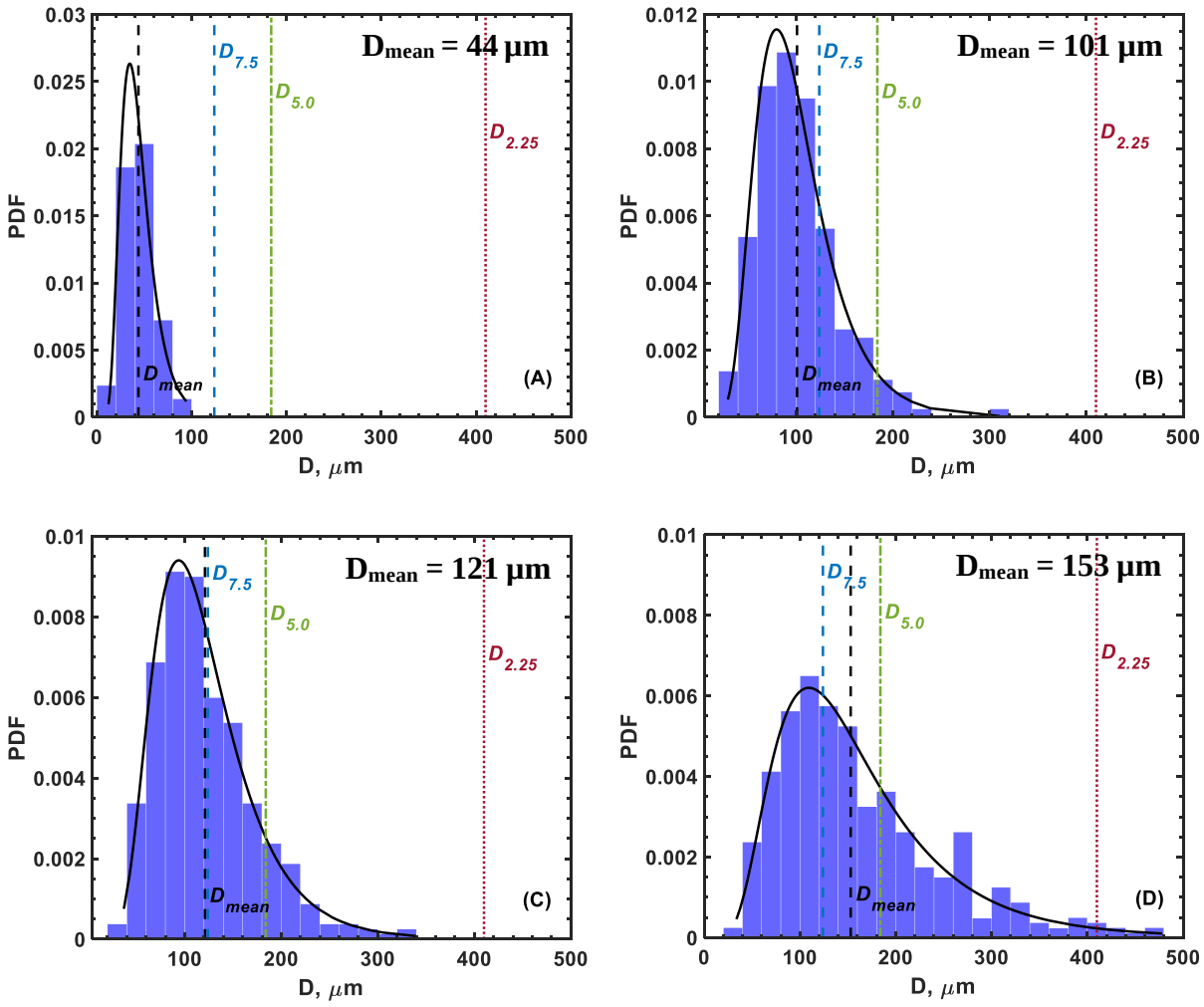

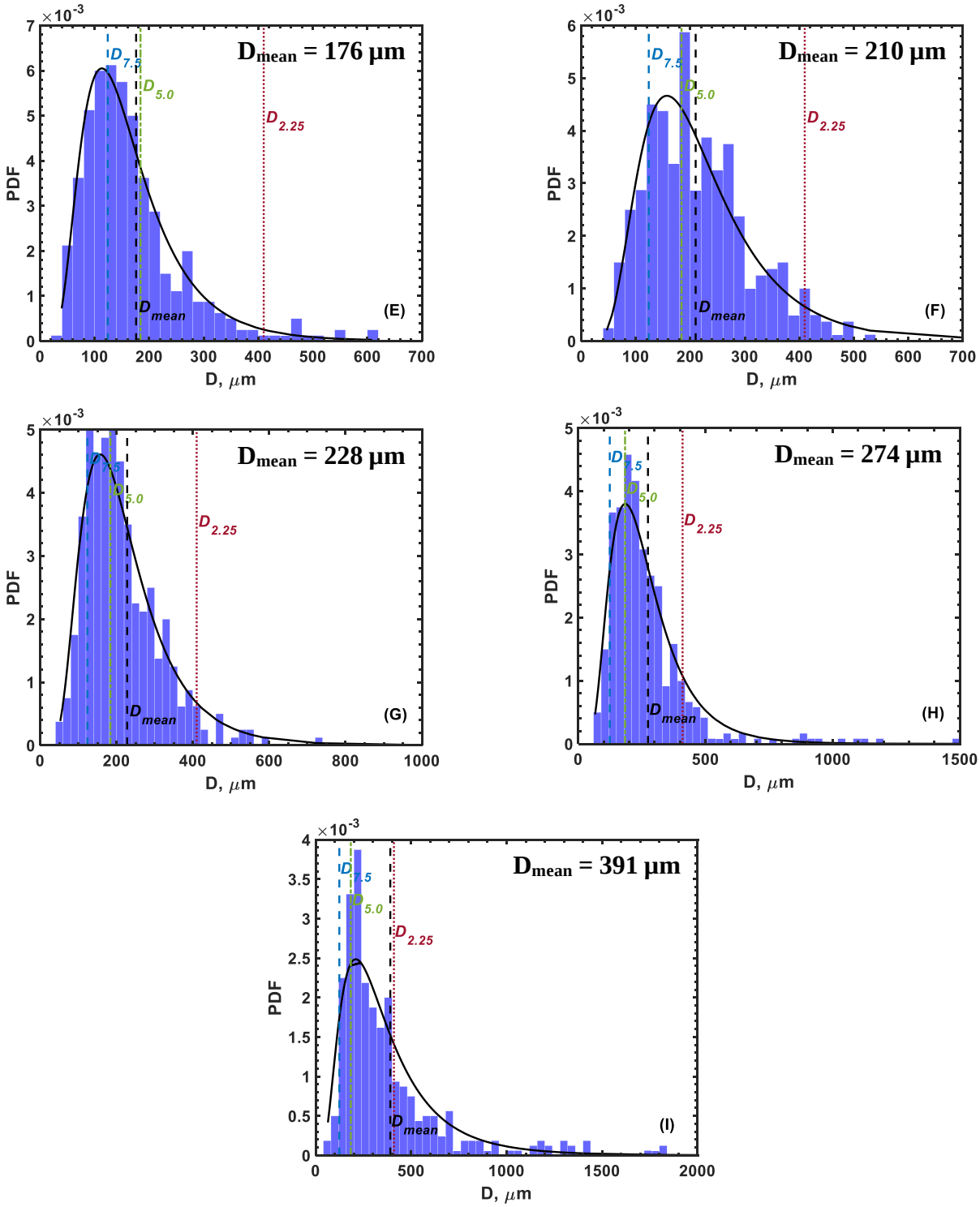

Fig. 4.2: Grain size distribution histogram of the annealed specimens. The D_{mean} and the boundary (D_{ω_i}) between the Rayleigh and stochastic scattering regimes for three excitation frequencies are also indicated by dotted lines.

The inverse pole figure (IPF) maps obtained from the electron backscatter diffraction (EBSD) analysis are shown in Fig. 4.3, which indicates the absence of any texture. The annealing process also dissolved all precipitates like chromium carbide ($Cr_{23}C_6$), which was confirmed through electrochemical methods. However, an increase in D_{mean} and σ_D with temperature and soaking time illustrates that the substantial grain growth happens at elevated temperatures, which are evident in the corresponding histograms. As proposed by Shirdel et al.[116,117] the ratio of D_{max} to D_{mean} is plotted in Fig. 4.4 for the given set of annealed specimens. The specimens with this ratio more than 5 is said to have abnormal grain growth. Abnormal grain growth happens in a material due to the phenomenon that certain energetically favourable grains grow rapidly, resulting in a bimodal distribution. The main factors which lead to abnormal grain growth are texture, second phases and grain boundary faceting, which governs the kinetics of grain growth. Therefore, Table 4.1 and Fig. 4.4 infer that the abnormal grain growth occurs at 0.8 T_H or higher, where T_H (1450 °C) is the homologous temperature of AISI 304 stainless steel.

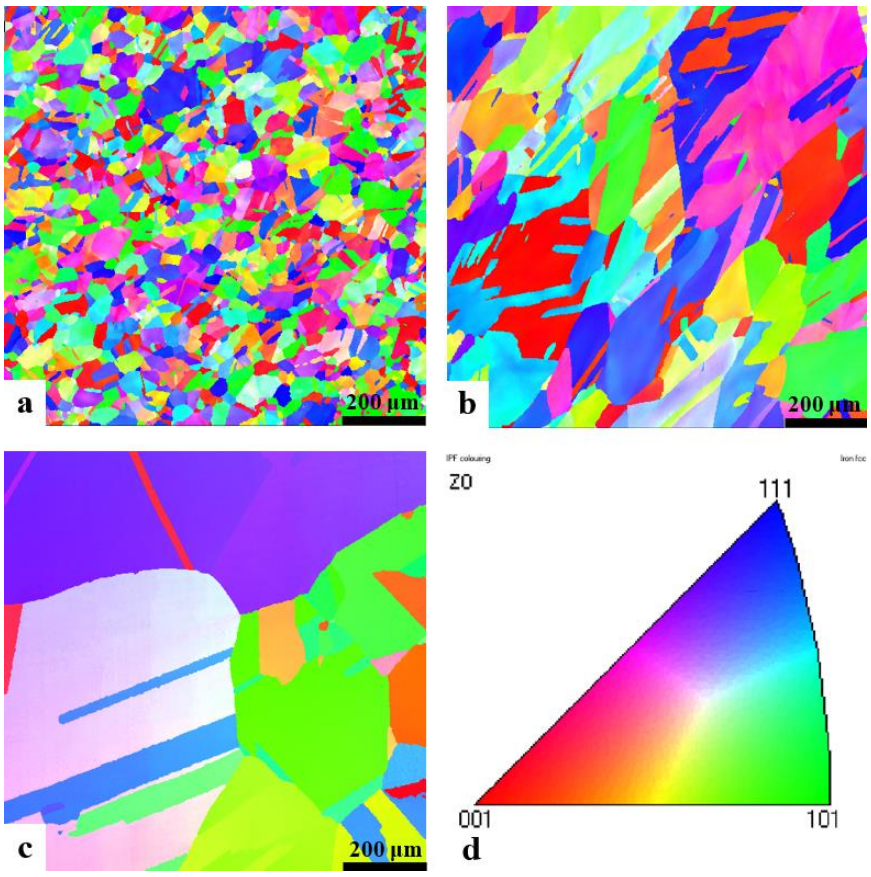

Fig. 4.3: The IPF maps of annealed specimens with average grain size (a) 44 μm, (b) 153 μm and (c) 274 μm shows no texture; (d) IPF legend

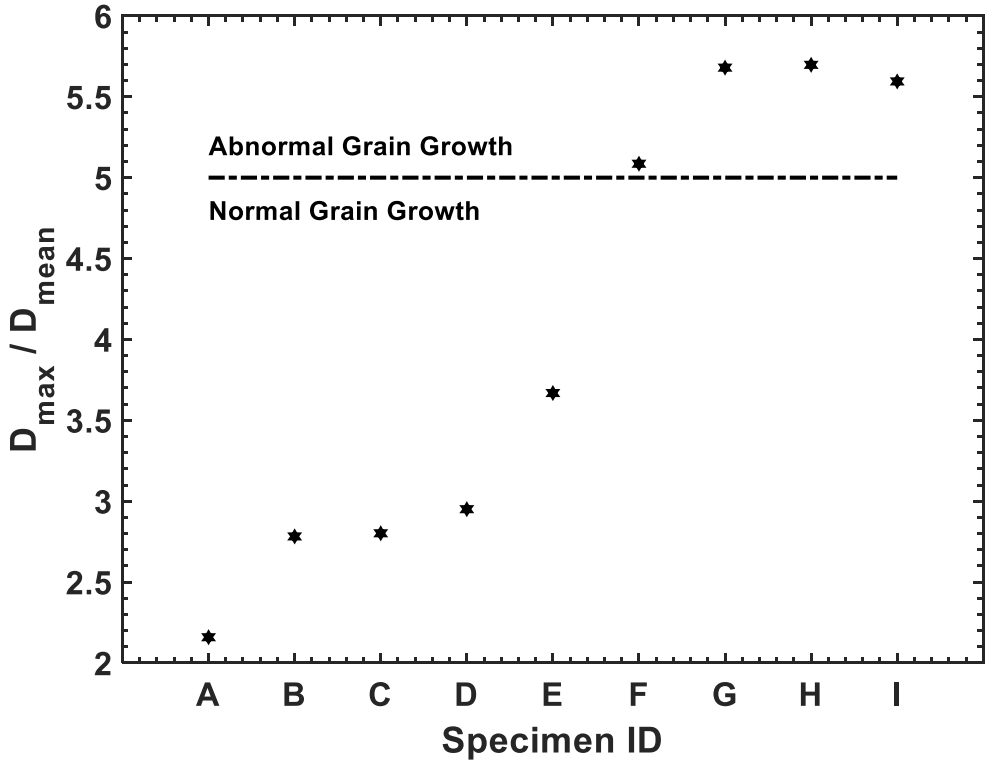

Fig. 4.4: Normal and abnormal grain growth is categorized based on the D_{max} to D_{mean} ratio

4.3.2 Ultrasonic attenuation

The C-scan representation of the first (u_1) and second (u_2) back-wall echoes for ω = 5 MHz is shown in Fig. 4.5 and Fig. 4.6 respectively. The colour code represents the signal amplitude at each point in the specimen mapped to its position. In order to obtain the frequency-dependent C-scan images corresponding to the input frequency of 5 MHz, the received time domain signals were passed through a Bessel bandpass filter with bandwidth 5.0 ± 0.5 MHz. Index and scan length in the C-scan images indicate the raster scan lengths in two perpendicular directions while scanning in the immersion system. The time domain signals received from the specimens G (D_{mean}= 228 μm), H (D_{mean}= 274 μm) & I (D_{mean}= 391 μm) in comparison with that of the specimen A (D_{mean}= 44 μm) in Fig. 4.7 reveals that severe attenuation of the back-wall echoes happened in the specimens with abnormal grain growth. The amplitudes (u_1 and u_2) of the back-reflected echoes from the specimens with abnormal grain growth were decreased drastically closer to the noise levels (originated from the grain boundary backscattering). In these specimens, severe attenuation would be expected at higher frequencies. Therefore, in such cases, Eq. (2.7) cannot be so useful, and the attenuation measurements would be inaccurate on the specimens with abnormal grain growth. Fig. 4.8 shows the C-scan

representation of the attenuation. The specimens with abnormal grain growth display a noisy pattern in their attenuation C-scan images due to the prominent backscatter echoes which overcome the second back-reflected echo amplitudes. Therefore, high-frequency attenuation measurements are not feasible on specimens with coarse (abnormal) grains.

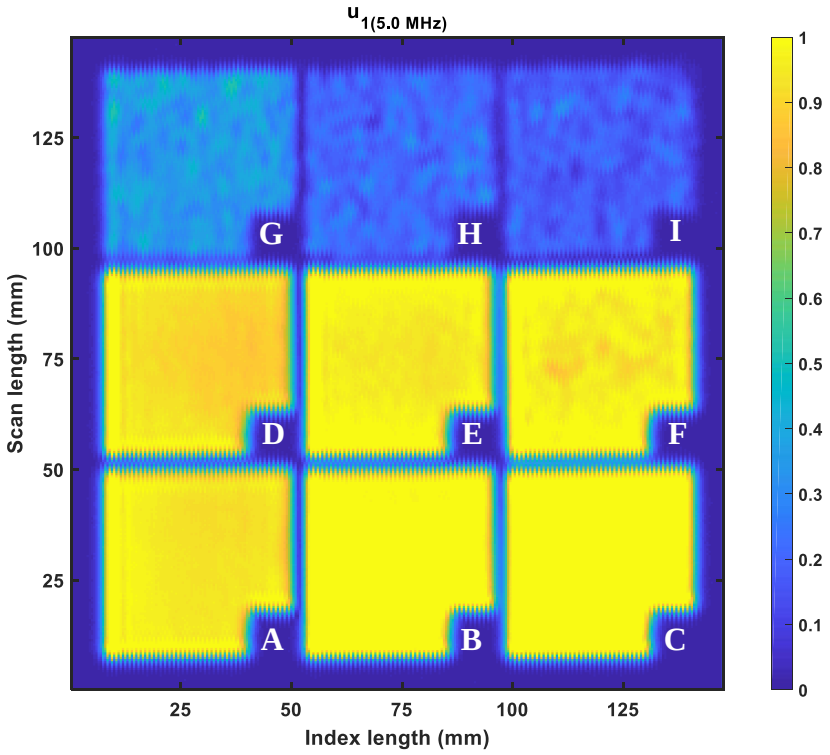

Fig. 4.5: C-scan images obtained from the 1st back-wall echo of the annealed specimens for ω = 5 MHz. Index and scan length indicate the raster scan length in two perpendicular directions. Color code indicates the reflected amplitude from the back wall.

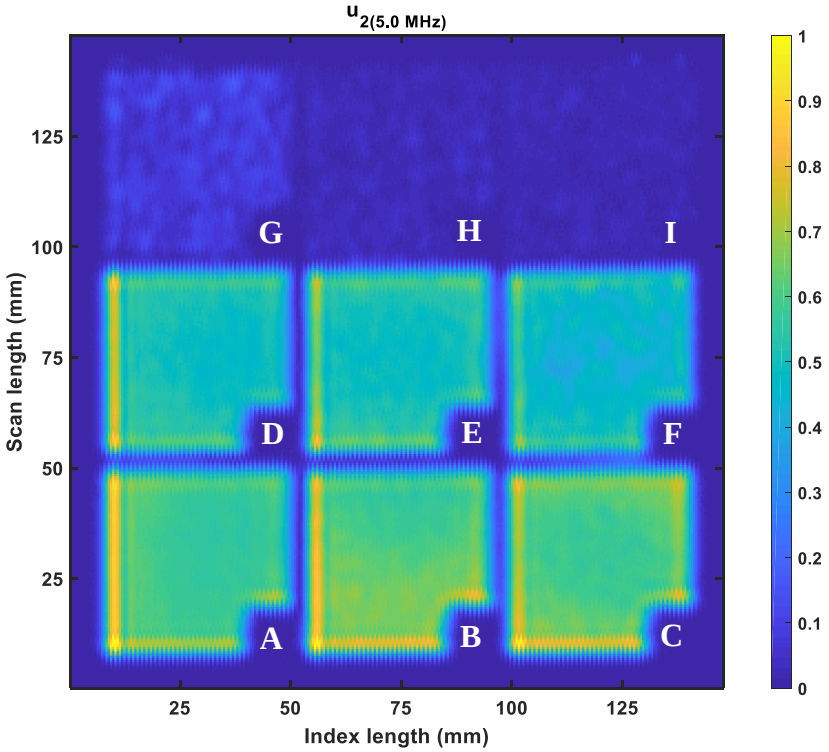

Fig. 4.6: C-scan images obtained from the 2nd back-wall echo of the annealed specimens for ω = 5 MHz.

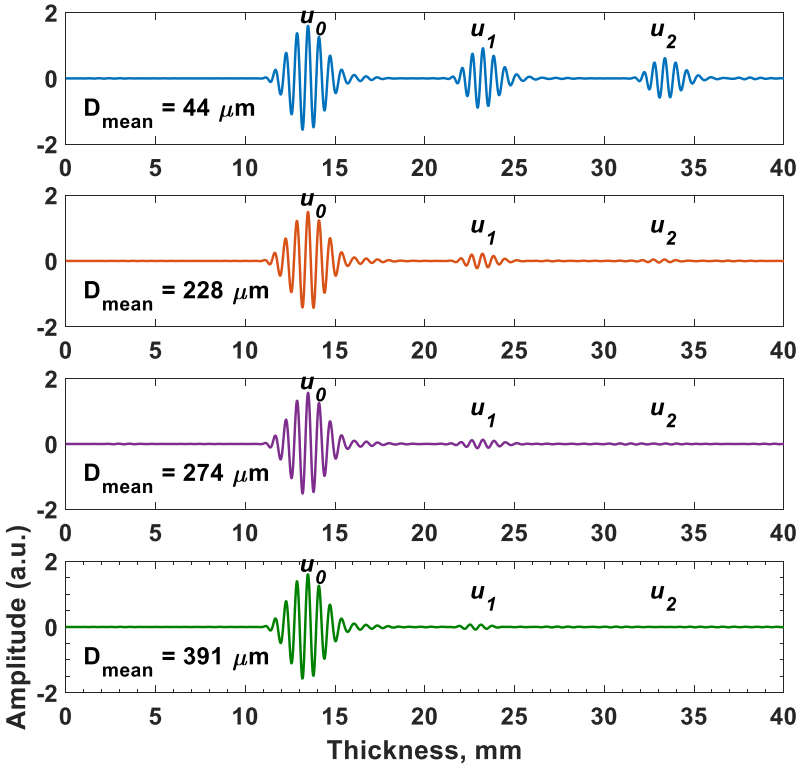

Fig. 4.7: Amplitude losses of the first and second back reflected echoes for ω = 5 MHz of the specimens A (D_{mean}= 44 μm), G (D_{mean}= 228 μm), H (D_{mean}= 274 μm) and I (D_{mean}= 391 μm)

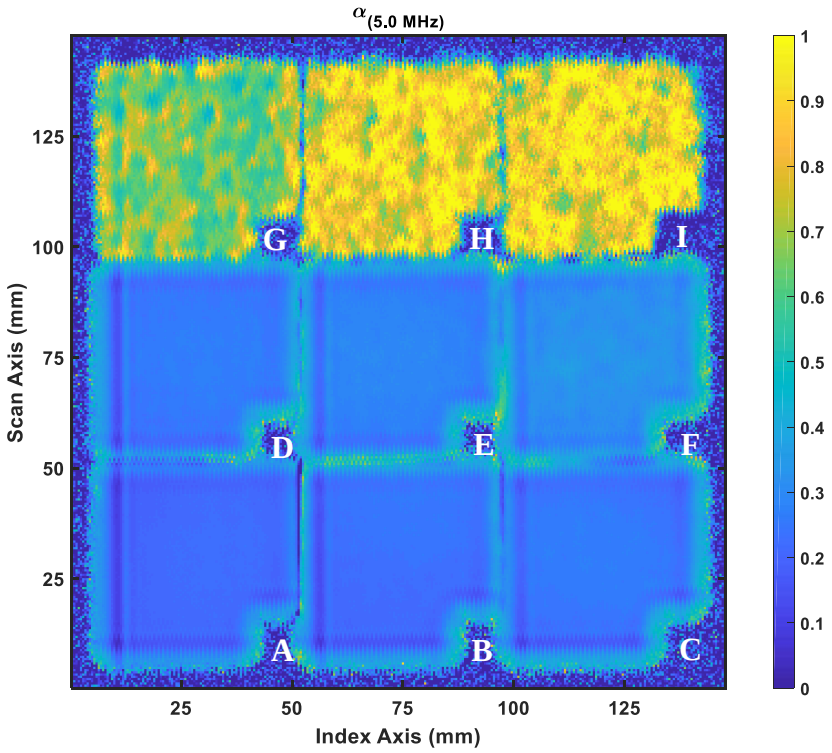

Fig. 4.8: Attenuation C-scan images of the annealed specimens obtained for ω = 5 MHz.

4.3.3 Nonlinear ultrasonics

The ultrasonic nonlinearity parameters of the annealed specimens for three input frequencies were measured as described in section 3.4. The measured nonlinearity parameter (β_{meas}) was normalized (β_{norm}) to that of the as-received material according to the procedure described in section 3.4.7.

4.3.3.1 Change in β_{norm} with D_{mean}

Standard error prediction fit plot of the β_{norm} against the D_{mean} is plotted in Fig. 4.9. The β_{norm} for the input frequency of 2.25 MHz ($\beta_{2.25}$) decreases linearly with an increase in grain size. This linear dependency is deviated for $\beta_{5.0}$ and $\beta_{7.5}$ towards the higher grain sizes. For the easiness of discussion, a quantity $\Delta\beta_{\omega_{i,j}}$ is defined as $\Delta\beta_{\omega_{i,j}} = \beta_{\omega_i} - \beta_{\omega_j}$ where ω_i and ω_j corresponds with the lower and higher input frequencies under consideration. Few combinations of the $\Delta\beta_{\omega_{i,j}}$ are illustrated in Fig. 4.9. It is seen that the $\Delta\beta_{\omega_{i,j}}$ is changed its magnitude with grain growth. Also, the β_{norm}'S intersect at few locations and beyond this

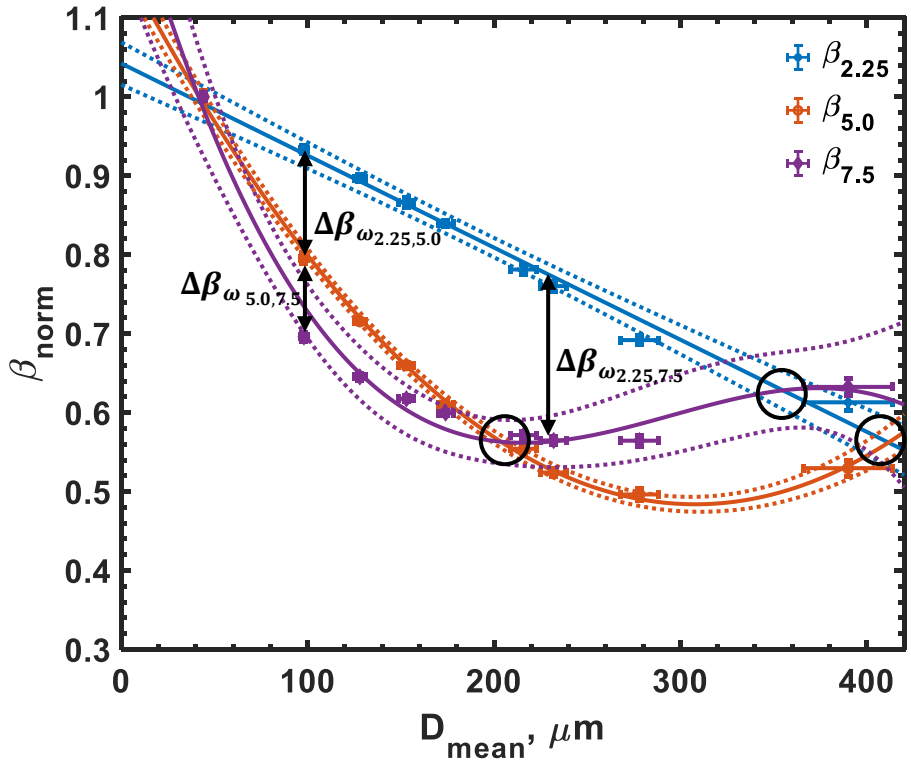

Fig. 4.9: The normalized β vs. the average grain size. Examples of the $\Delta\beta_{\omega_{i,j}}$ and the point of intersection of different β_{ω}'s are indicated.

point the $\Delta\beta_{\omega_{i,j}}$ has reversed its polarity. Besides, an order $\beta_{2.25} > \beta_{5.0} > \beta_{7.5}$ is maintained up to a particular D_{mean} and thereafter, this order is found lost.

4.3.3.2 Change in β with the reduced wavenumber

In the Fig. 4.10, the β_{norm} is plotted against the reduced wavenumber, kD, which is defined for the input wavelength. It is quite interesting to note that, the linear dependency of β holds only up to $kD \approx 1$ and then found to deviate, irrespective of the frequency. Polynomial regression analysis on β vs kD showed a linear, quadratic and cubic dependency for $\beta_{2.25}$, $\beta_{5.0}$ and $\beta_{7.5}$ respectively to be the best fits with maximum R^2 value (R^2= 0.99, 0.99 and 0.98 respectively) and the minimum norm of residuals. The polynomial regression fit has exhibited the following relations.

$$\beta_{2.25} = -0.49k_{2.25}D + 1 \tag{4.1}$$

$$\beta_{5.0} = 0.25(k_{5.0}D)^2 - 0.82k_{5.0}D + 1.2 \tag{4.2}$$

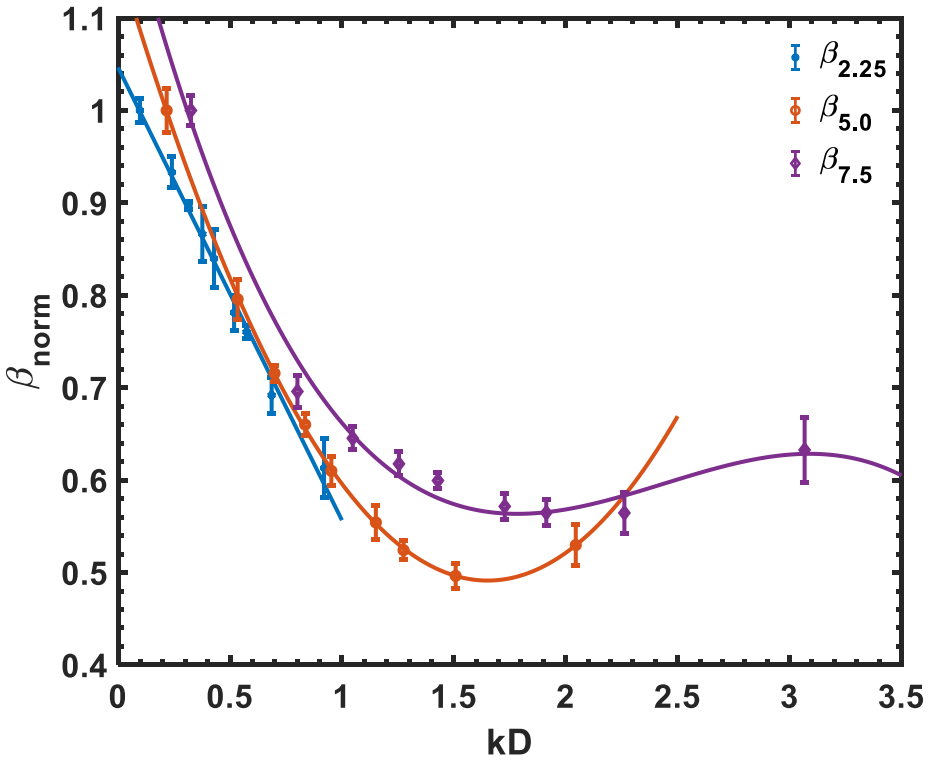

Fig. 4.10: Normalized β vs. the reduced wavenumber, kD. The linear dependency of β holds only up to $kD \approx 1$ and then found to deviate, irrespective of the frequency.

$$\beta_{7.5} = -0.058(k_{7.5}D)^3 + 0.43(k_{7.5}D)^2 - 0.97k_{7.5}D + 1.3 \qquad (4.3)$$

Deviation in β with grain size (Fig. 4.9) and applied frequency (Fig. 4.10) can be explained based on the classical scattering theory. According to Eq. (2.59), the measured β is a modified version of the material nonlinearity by the attenuation coefficients, α_1 and α_2. As briefed in section 2.6.2., the α_1 and α_2 fall into different scattering regimes based on the frequency and grain size values, and hence the β gets modified accordingly. Therefore, the behaviour of β with grain growth is associated with the difference in the scattering related attenuation of the fundamental and harmonic components.

4.3.3.3 The behaviour of β based on classical attenuation theory

The term β_{α_i} defined in Eq. (2.59) which represents the influence of the attenuation coefficients α_1 and α_2 on β is plotted in Fig. 4.11 for a set of grain sizes inclusive of that used in this study and for three input frequencies (denoted as superscripts to β_{α_i}). According to classical scattering theory, the transition from Rayleigh to stochastic regime occurs at kD = 1. For the fundamental and second harmonic frequency components used in this investigation, the grain

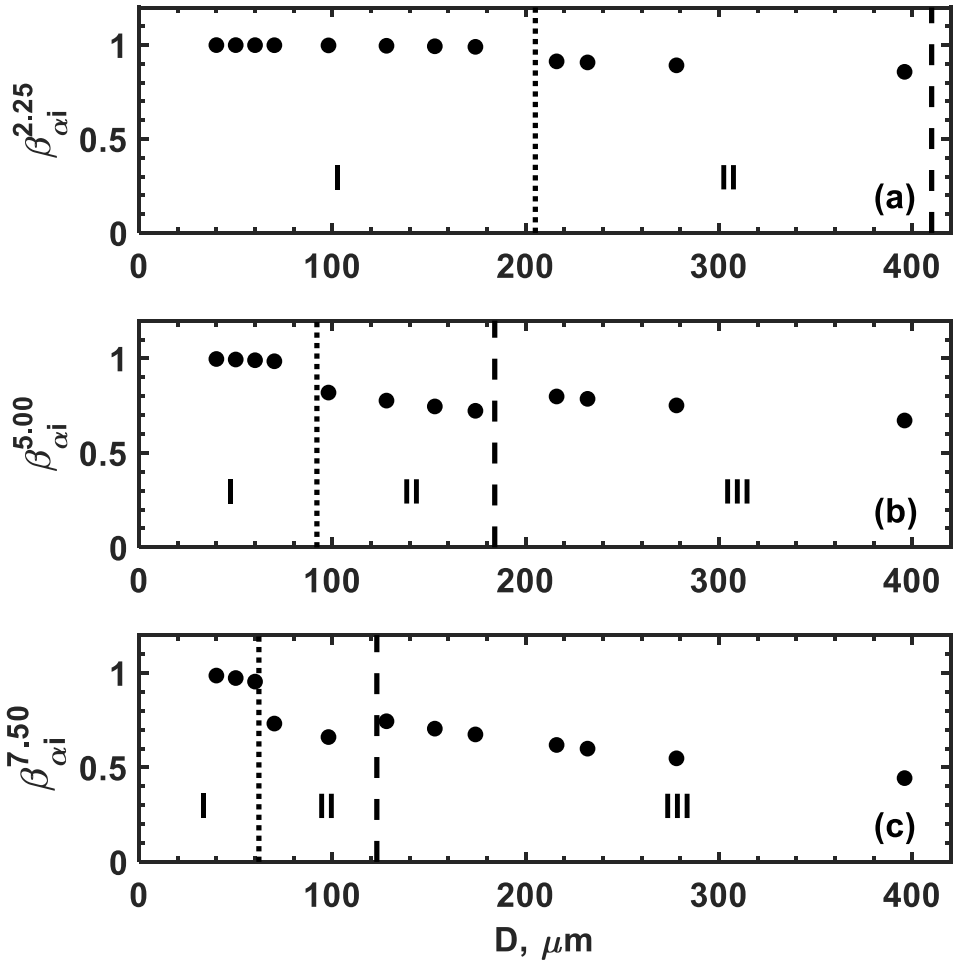

Fig. 4.11: The β_{α_i} against the mean grain size for the different excitation frequencies (a) 2.25 MHz, (b) 5.0 MHz and (c) 7.5 MHz. Dashed line indicates the D_ω satisfies kD_ω = 1 condition for the fundamental frequency and the dotted line is that for the second harmonic.

size (D_ω) where the suffix corresponds with the frequency at which the transition condition kD_ω = 1 encounters are tabulated in Table 4.2.

Table 4.2: The grain size (D_ω) at which the transition condition kD_ω = 1 for the fundamental and harmonic components

Fundamental		Second Harmonic	
2.25 MHz	410 μm	4.5 MHz	205 μm
5.0 MHz	184 μm	10.0 MHz	92 μm
7.5 MHz	123 μm	15.0 MHz	62 μm

In Fig. 4.11, the dashed line indicates the D_{ω_i} which satisfies the condition $kD = 1$ for the fundamental frequency and the dotted line is that for the second harmonic. Fig. 4.11 is divided into three regions based on the type of interactions. **Region I:** both the fundamental and second harmonic components are in the Rayleigh scattering regime; **Region II:** fundamental component in the Rayleigh regime while the second harmonic is in the stochastic regime; and **Region III:** both fundamental and second harmonic components are in the stochastic scattering regime. From this figure, it is evident that there exists an abrupt transition in β_{α_i} at each region boundaries. It should be noted that the influence of attenuation is negligible in the region I, especially at lower frequencies, as a result of $(\alpha_2 - 2\alpha_1)x \ll 1$ in Eq. (2.59). In region II, the second harmonic component (A_2) encounters stochastic scattering (whereas the fundamental component is still in the Rayleigh regime), and, due to an increase in α_2, the β_{α_i} lowers. The β_{α_i} decreases continuously from region I to II with grain growth because of the same reason. Meanwhile, in region III, the β_{α_i} lifts considerably from the previous decreasing trend once the fundamental component starts stochastic interactions. This is a consequence of the increased α_1 term in the β_{α_i} in Eq. (2.59). Minimal variation to the β_{α_i} for the 2.25 MHz input is also evident from Fig. 4.11 which indicates that the $\beta_{2.25}$ is not being influenced by the scattering dependent attenuation for the given set of grain sizes.

Therefore, the linear variation of $\beta_{2.25}$ and the deviation for $\beta_{5.0}$ and $\beta_{7.5}$ around $kD = 1$ (defined for the fundamental frequency) observed in Fig. 4.10 is justified. In this linear region, by knowing the values of k and β, the grain size D can be determined quantitatively. The linear, quadratic and cubic fit to the curves in Fig. 4.10 indicates that the measured acoustic nonlinearity parameter is frequency-dependent, which in turn depends on the scattering regime. However, a one-to-one correlation between Fig. 4.10 and Fig. 4.11 cannot be expected because the analysis in Fig. 4.11 was based on the D_{mean} and has not accounted for the distribution in grain sizes and its associated scattering losses which will be discussed in the subsequent chapters.

4.3.3.4 Order of the β_ω with the scattering regime

In Fig. 4.10, for all input frequencies in the Rayleigh scattering regime ($kD < 1$), an order $\beta_{2.25} > \beta_{5.0} > \beta_{7.5}$ is maintained which is a consequence of the increased attenuation of A_2 with frequency as the A_2 is in the numerator of Eq. (2.25). It is also evident that such an order does not hold for $kD > 1$. This is because of the quadratic term of A_1 in the denominator of

Eq. (2.25) which would either change the magnitude of $\Delta\beta_{\omega_{i,j}}$, or alter the above-mentioned order itself. Such occurrences are indicated by arrows in Fig. 4.9. For example, the $\beta_{5.0}$ intersects with $\beta_{7.5}$ at a particular grain size and thereafter the above order in β_ω deviates. At this point of intersection, the condition

$$\beta_{5.0} = \beta_{7.5} \tag{4.4}$$

is satisfied. Considering the longitudinal velocity 5800 m/s in stainless steel, the wavenumber $k = 2\pi/\lambda$ for different frequencies are $k_5 = 5.41 \times 10^3 m^{-1}$, $k_{7.5} = 8.12 \times 10^3 m^{-1}$, $k_{10} = 10.82 \times 10^3 m^{-1}$ and $k_{15} = 16.24 \times 10^3 m^{-1}$, where the subscript denotes the frequency in MHz. Substituting these values into Eq. (4.4) using Eq. (2.25) it reduces to

$$\frac{A_{10}}{A_5^2} = 0.444 \times \frac{A_{15}}{A_{7.5}^2} \tag{4.5}$$

Substituting Eqns. (2.52) and (2.57) into Eq. (4.5) yields,

$$\frac{e^{-2\alpha_5 x} - e^{-\alpha_{10} x}}{\alpha_{10} - 2\alpha_5} \times \frac{\alpha_{15} - 2\alpha_{7.5}}{e^{-2\alpha_{7.5} x} - e^{-\alpha_{15} x}} = \frac{e^{-\alpha_5 x}}{e^{-\alpha_{7.5} x}} \tag{4.6}$$

Rearranging Eq. (4.6) results in,

$$\left(\frac{e^{-2\alpha_5 x} - e^{-\alpha_{10} x}}{e^{-2\alpha_{7.5} x} - e^{-\alpha_{15} x}}\right) \times \left(\frac{\alpha_{15} - 2\alpha_{7.5}}{\alpha_{10} - 2\alpha_5}\right) = e^{-2(\alpha_5 - \alpha_{7.5})x} \tag{4.7}$$

where the coefficients of attenuation (α_i), in turn, influenced by the scattering regime. Similar solutions can be arrived for other points of intersection shown in Fig. 4.9. In such cases, the coefficients of attenuation in Eq. (4.7) will be of the corresponding frequency components. Therefore, change in the order of β_ω depends on the grain sizes and the applied frequencies, which defines the respective scattering regimes. The points of intersection in Fig. 4.9 can, therefore, be varied by changing the input frequency combinations. The results further suggest that a single frequency measurement would not be adequate for estimating the grain size variations in heterogeneous materials as the nonlinearity parameter is greatly affected by the scattering regime.

4.3.3.5 Statistical analysis of the scattering contribution to β

The number density of grains in the respective stochastic scattering regimes (N_{ω}^{s}) of specimens, for example, **B** (D_{mean} = 101 μm), **D** (D_{mean} = 153 μm) & **I** (D_{mean} = 391 μm) for three input frequencies is illustrated in Fig. 4.12. In the specimen B, an insignificant number of grains were present to produce stochastic interactions with the 2.25 MHz waves. A clear difference in the grain size distribution among the regimes as well as the specimens is evident in Fig. 4.12. All the annealed specimens, except specimen **A** in which all the individual grain sizes are well within the Rayleigh scattering regime for the three input frequencies, show a similar difference. The grain size in specimen **A** varies from 10 μm to 124 μm which is evident in the histogram representation given in Fig. 4.13. The number densities of grains in the respective stochastic scattering regimes of specimens **B**, **D** & **I** for the three input frequencies are compared with that of specimen **A** in Table 4.3. More the number of grains, more significant will be the scattering.

Table 4.3: Number density (%) of grains contributing to the stochastic scattering of fundamental and harmonic components in specimens A, B, D & I

Specimen ID	Fundamental		Second Harmonic	
A (D_{mean} = 44 μm)	$N_{2.25}$	---	$N_{4.5}$	---
	$N_{5.0}$	---	$N_{10.0}$	0.75
	$N_{7.5}$	---	$N_{15.0}$	14.0
B (D_{mean} = 101 μm)	$N_{2.25}$	---	$N_{4.5}$	1.25
	$N_{5.0}$	3.75	$N_{10.0}$	53.5
	$N_{7.5}$	23.25	$N_{15.0}$	83.5
D (D_{mean} = 153 μm)	$N_{2.25}$	1.49	$N_{4.5}$	24.5
	$N_{5.0}$	30.0	$N_{10.0}$	78.75
	$N_{7.5}$	59.25	$N_{15.0}$	93.0
I (D_{mean} = 391 μm)	$N_{2.25}$	27.5	$N_{4.5}$	73.75
	$N_{5.0}$	80.0	$N_{10.0}$	98.75
	$N_{7.5}$	96.25	$N_{15.0}$	100

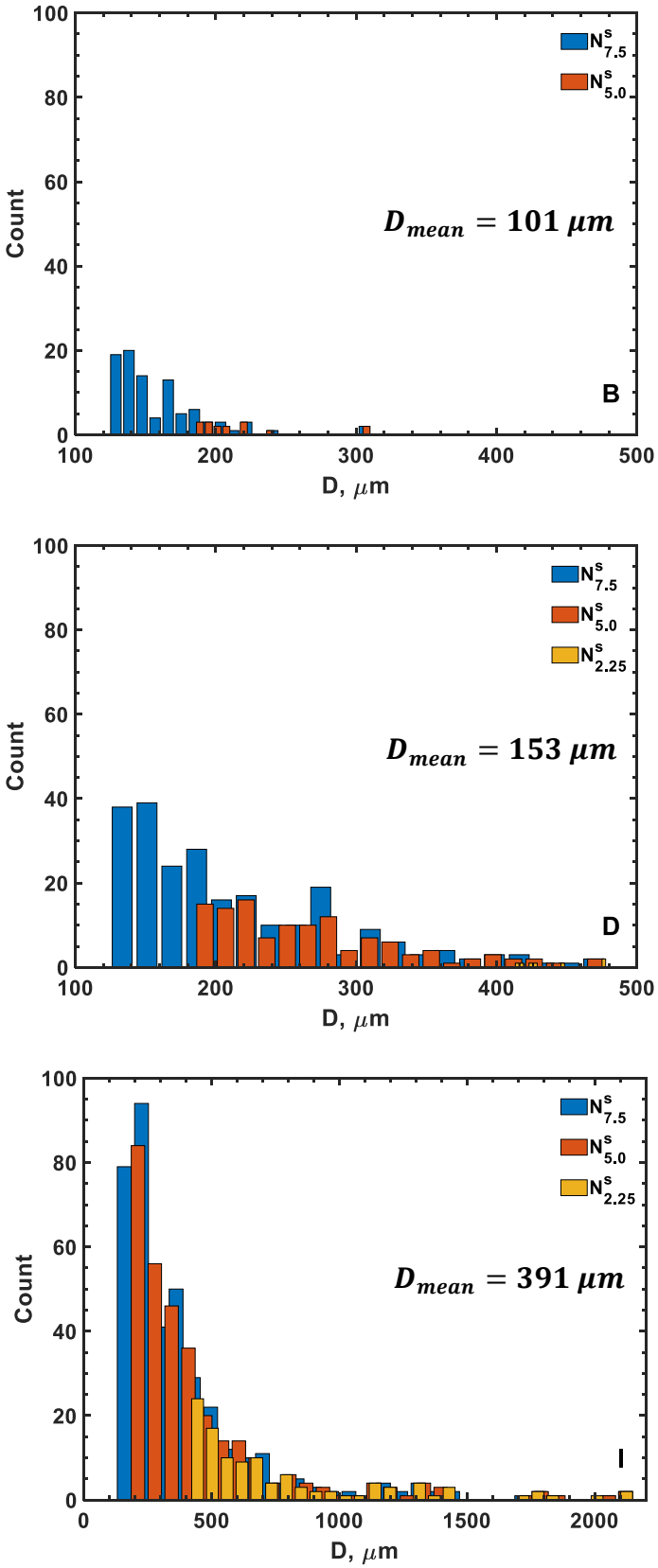

Fig. 4.12: Distribution of grain sizes in the respective stochastic scattering regimes of specimens B, D & I for the three input frequencies. For clear visualization, the x-scale is not maintained uniform.

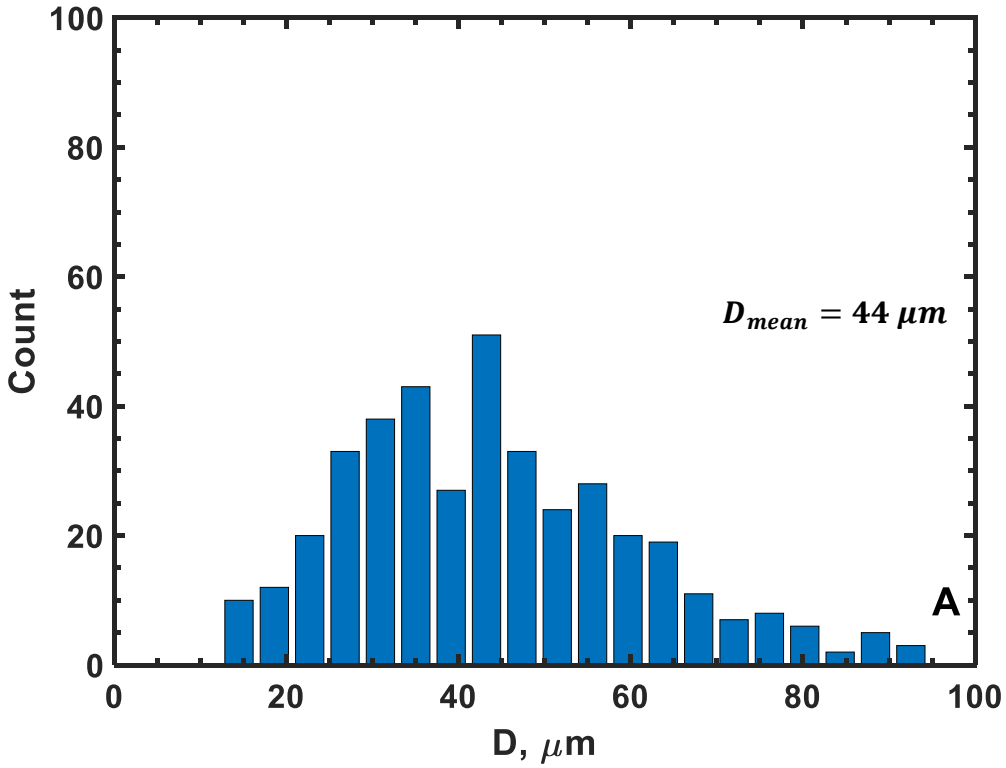

Fig. 4.13: Grain size distribution in the specimen A in which the $D_{mean} = 44\mu m$. All grains are within the Rayleigh scattering regime for all three input frequencies.

Therefore, in addition to the D_{mean}, the distribution of grains in a microstructure can have a considerable influence on the value of β. Hence, the degree and the coefficients of the polynomial equations (Eq. (4.2) – (4.4)) are related to the D_{mean} as well as the grain size distribution in a given microstructure.

In a previous study by Mini et.al.[68] the effect of scattering regimes on the acoustic nonlinearity parameter was not addressed even though they dealt with the D_{mean} in the scattering transition regime in polycrystalline copper. They have reported a quadratic like variation of β (for an input frequency of 5 MHz) with increasing grain size. Similar behaviour was also observed in a recent work by Choi et al.[118] on stainless steel grade 304L. Nevertheless, the results in the present chapter expose the dependence of the acoustic scattering regimes on the measured acoustic nonlinearity parameter. Therefore, characterization of microstructure in polycrystalline materials needs to be addressed cautiously.

4.4 Summary

Traditional attenuation measurements have limited application on the materials where abnormal grain growth (coarse grain) occurs, whereas, the nonlinearity parameter is very sensitive to the microstructural conditions. The frequency dependence of the nonlinearity parameter on the scattering regimes can be used to draw a reliable characterization of the microstructural conditions. To this end, a novel multi-frequency NLU methodology is introduced in this chapter. The observations are summarized below.

- The acoustic nonlinearity parameter β varies linearly in the Rayleigh scattering regime and deviates from linearity at the scattering transition zone. This behaviour was explained based on the classical scattering theories. A reliable evaluation of grain size in polycrystalline materials using a single frequency measurement, therefore, demands the Rayleigh scattering condition be satisfied so that the β would be independent of the scattering losses.
- The multi-frequency approach reveals a deviation in the $\Delta\beta_{\omega_{i,j}}$ and a change in the order of β_{ω_i} with grain growth. These changes can be used as a precursor for evaluating the undesired grain growth and can also be employed as an efficient tool for rapid screening of materials with unknown process history where wide variations and distribution of grain sizes are expected. In such cases, deviation from the linear variation in β_{ω_i} or a change in the order in β_{ω_i} may be set as the boundary where the desired properties (grain size dependent) are extinct. For a set of input frequencies (ω_i), a change in the order of β_{ω_i} is an indication that the mean grain size has deviated from the Rayleigh scattering regime corresponding to those frequencies. Therefore, the multi-frequency methodology can be used as a reliable stand-alone technique to characterize the microstructure evolution in polycrystalline materials.
- It is also observed that the grain size distribution, in addition to the mean grain size, can have an influence on the measured acoustic nonlinearity parameter.

This chapter has confined the measurements on different specimens of different average grain size. In the next chapter, the application of the proposed multi-frequency methodology is extended into components in which all sort of grain size variations coexist.

Chapter 5
Characterization of Heterogeneous Microstructure in Heavy Forgings

5.1 Introduction

In the previous chapter, it is clearly demonstrated that the nonlinearity parameter varies with grain size in the material, and this variation, in turn, depends on the scattering regime, i.e., the mean grain size and the frequency of the elastic wave. The nonlinearity parameter was found to be decreasing linearly with grain growth in the Rayleigh scattering regime, whereas it deviated from this linear trend at the Rayleigh-to-stochastic scattering transition zone. An explanation of this behaviour was made on the basis of the difference in the attenuation characteristics of the fundamental and harmonic components in polycrystalline materials.

It may be noted that the work reported in the previous chapter is based on the NLU measurements carried out on different samples of different average grain sizes, specifically produced by varying heat treatments independently on each sample. However, in practice, it is possible to have a wide variation in grain size in the same material, and this is especially true for thick plates, pipes with large wall thickness, heavy forgings and castings. Therefore, it is important to demonstrate that nonlinear ultrasonics can reveal such variations in a single component and hence this technique can be proposed for characterizing the industrial components and structures. Hence, in the present chapter, the multi-frequency methodology is applied on austenitic stainless steel forgings, which are apparently produced using different process routes. The multi-frequency NLU is drawn-out to investigate the grain size variations present in such components.

5.2 Materials and methods

Two AISI 304L austenitic stainless-steel forgings (F_1 & F_2) of diameter 200 mm whose details are given in Section 3.2.2 were chosen to study the heterogeneous variation of microstructure using nonlinear ultrasonics. Experiments were conducted on the strips extracted from the heavy forgings, as shown in Fig. 3.1. The strips were submerged in water, and the C-scan imaging

was made using two un-focused immersion transducers of central frequency (ω_c) 5.0 MHz and 10.0 MHz as described in section 3.3. The first (u_1) and second (u_2) back-wall echoes were obtained over an area of 200 × 20 mm^2 with a scanning resolution of 0.3 mm × 0.3 mm and the attenuation C-scan images were constructed.

Subsequent to the immersion scanning, the same strips were loaded into the experimental set up for nonlinear measurements described in Section 3.4. The NLU measurements were carried out independently for three pairs of transducers (T_x - R_x) kept at the location of the core and at a distance, 10 mm, 30 mm, 50 mm, 70 mm and 90 mm away from the core to either direction. These locations were identified from the C-scan images and later confirmed through microscopy that, the nonlinearity parameter (β) at these locations would represent the microstructural features across the diameter meaningfully.

5.3 Results and discussions

5.3.1 Microstructure

Photomicrographs and the corresponding histogram representation of the grain size distribution obtained at different cross-sectional locations in F_1 and F_2 are shown in Fig. 5.1 and Fig. 5.2, respectively. Grain size variations in these two forgings are significantly different. The mean grain size (D_{mean}) and the standard deviation (σ_D) in grain size distribution are given in Table 5.1. The standard deviations in Table 5.1 suggest that that the grain size variations are minimal in F_1 compared to F_2, which is evident in the histogram representations. It is to be noted that, for the forging F_2, maximum grain size (D_{max}) was found near the surface whereas, in the case of F_1, there is a decrease in grain size from the core to the surface. Also, in both forgings, the D_{mean} satisfy the Rayleigh scattering conditions for the three frequencies used in the present investigation.

The D_{max}, D_{mean} and the ratio D_{max}/D_{mean} are plotted against the distance from the core in Fig. 5.3, Fig. 5.4 and Fig. 5.5, respectively. As described in Section 4.3.1, the ratio of D_{max}/D_{mean} determines the abnormality in grain growth. Near the surface of F_2, the ratio of D_{max}/D_{mean} is found to be 5.8, which confirms the abnormal grain growth. Reason for the broader distribution of grains and the abnormal growth near the surface in F_2 is unknown. Probably, the forging ratio employed during the forging process of F_2 would have been high

resulting in high strain deformation on the surface and this would have resulted in an abnormal grain growth under intermittent annealing operation.

Table 5.1: Grain Size Measurements in the forgings F_1 and F_2					
Distance (mm) from the Core:	0	30	50	70	90
Forging, F_1					
$D_{mean}^{F_1}$, µm	103	71	79	53	38
σ_{F_1}, µm	43	31	24	21	15
Forging, F_2					
$D_{mean}^{F_2}$, µm	118	106	96	63	130
σ_{F_2}, µm	58	45	44	29	112

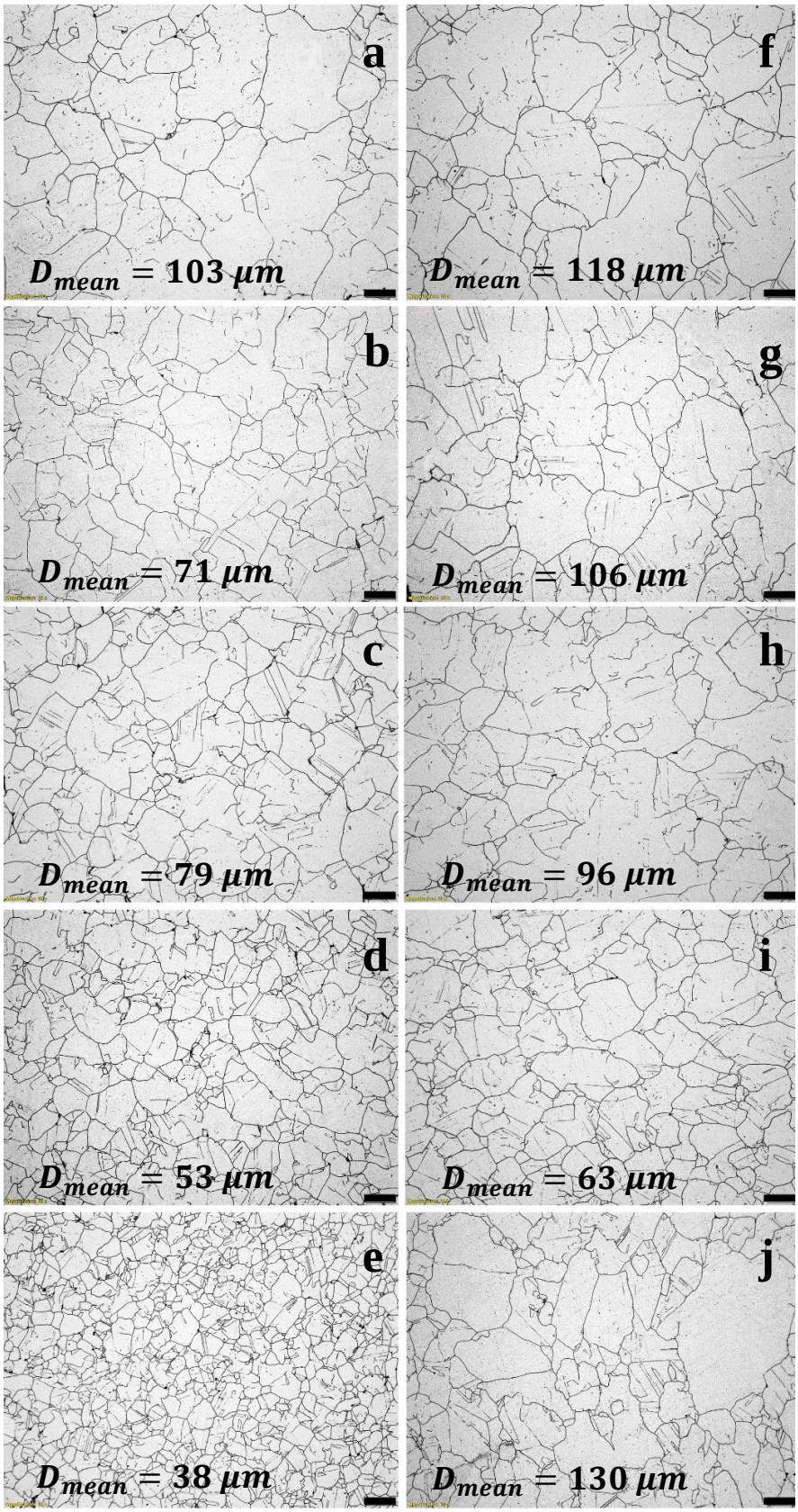

Fig. 5.1: Optical micrographs of the F_1 obtained at (a) the core and at distances (b) 30 mm (c) 50 mm (d) 70 mm and (e) 90 mm from the core and (f – j) indicate the corresponding micrographs of the F_2. Scale is set at 50 µm.

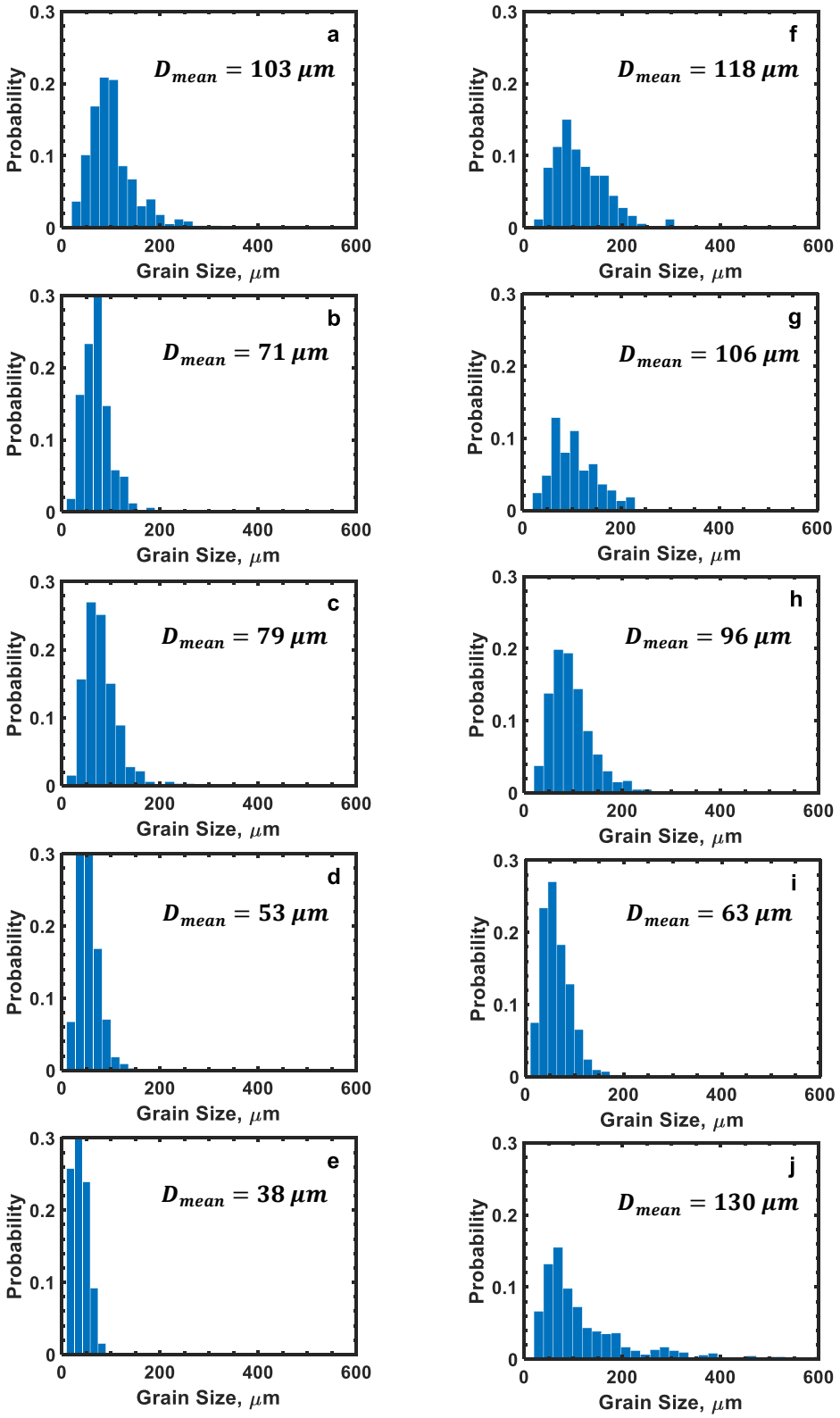

Fig. 5.2: Histogram representation of grain size distribution in F_1 obtained at (a) the core and at distances (b) 30 mm (c) 50 mm (d) 70 mm and (e) 90 mm from the core and (f – j) indicates the corresponding grain size distribution in F_2.

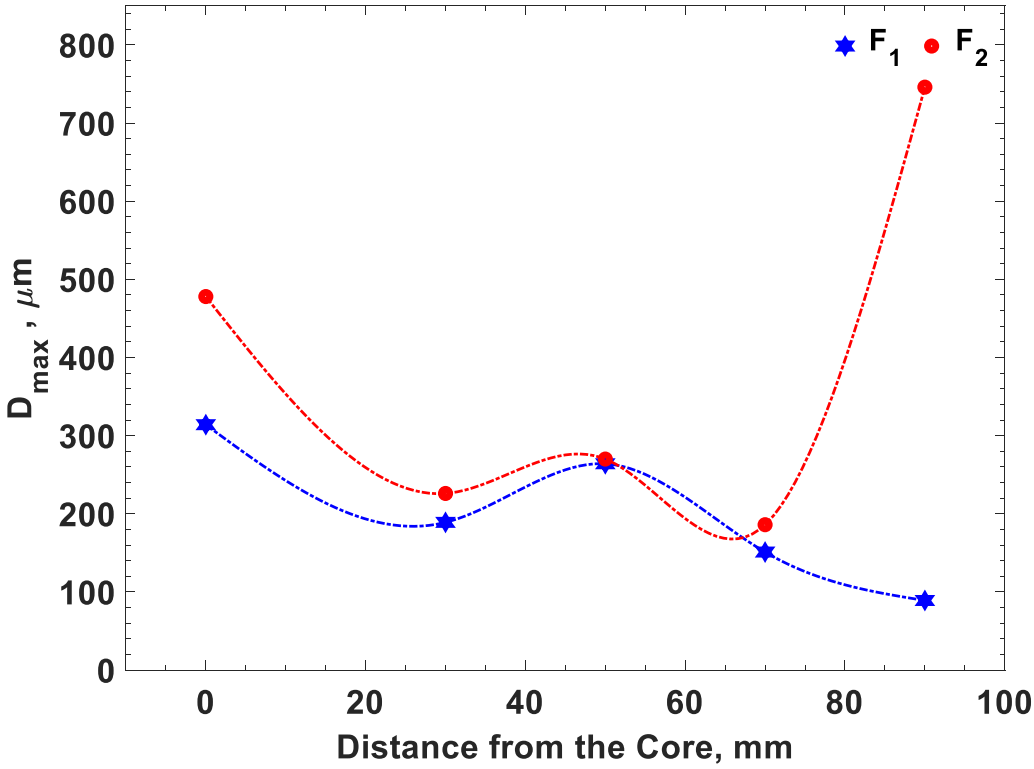

Fig. 5.3: Variations in the maximum grain size (D_{max}) as a function of distance from the core

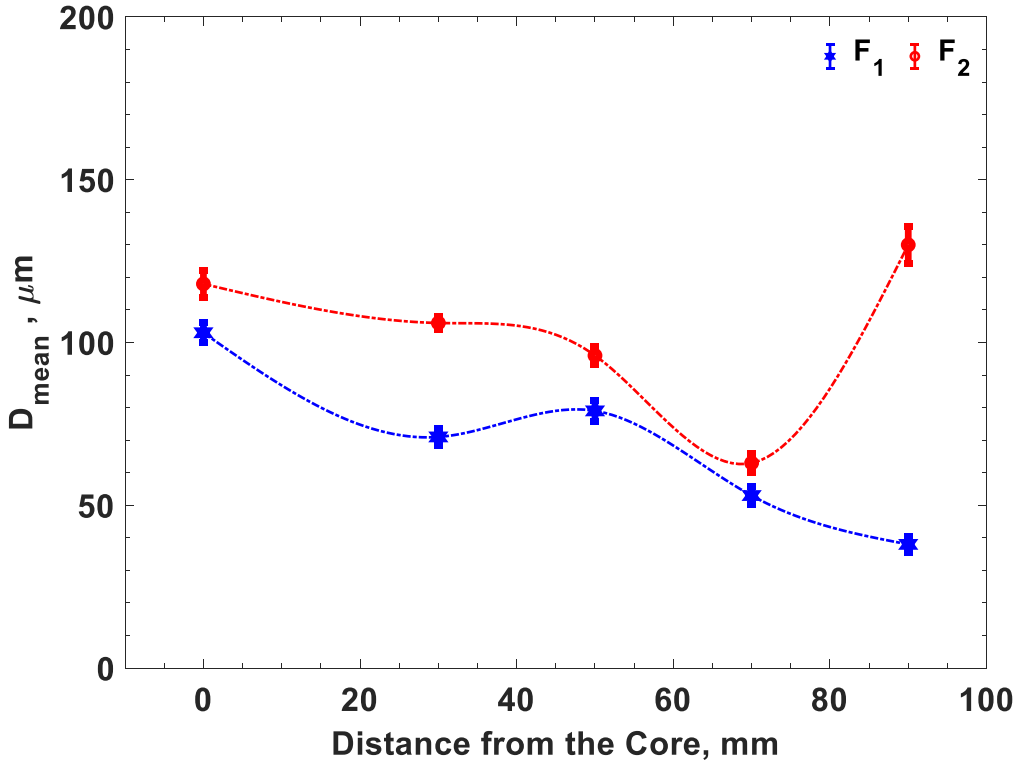

Fig. 5.4: Variation of the mean grain size (D_{mean}) as a function of distance from the core

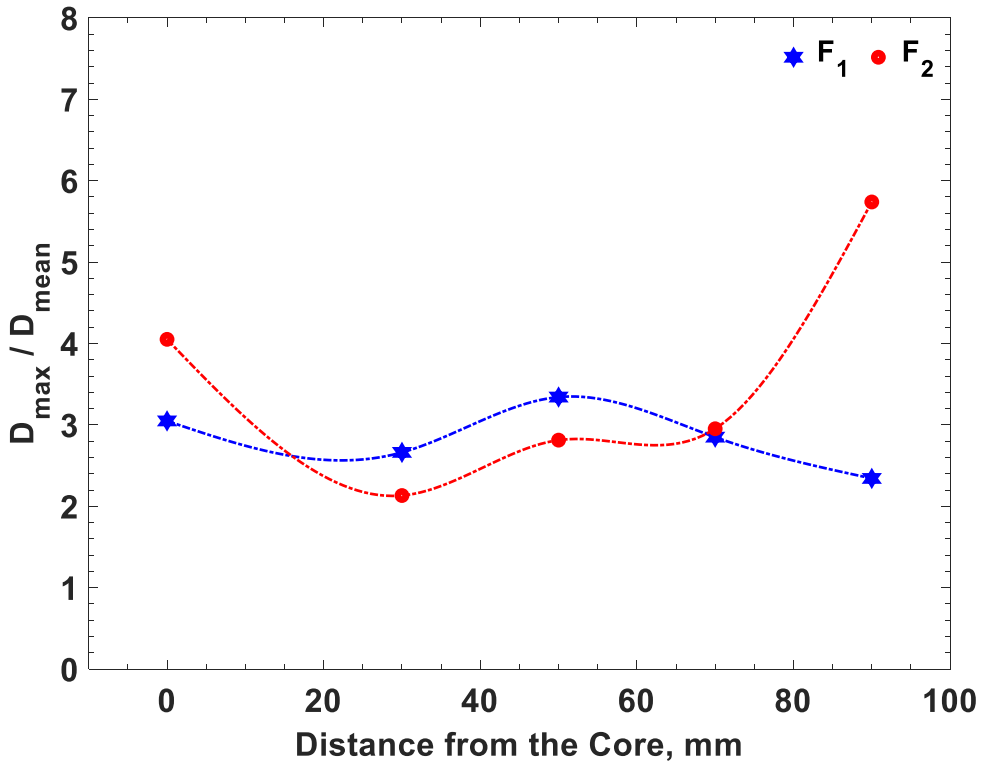

Fig. 5.5: Variation in the ratio D_{max}/D_{mean} as a function of distance from the core

5.3.2 Chemical heterogeneity

Energy-dispersive X-ray spectroscopy (EDS) analysis was conducted at different radial locations of the forgings to understand the chemical heterogeneity along the diameter. A typical EDS spectrum is shown in Fig. 5.6. The element wt.% was measured at various locations from the core and found that the chemical heterogeneity is absent in both the forgings. The element distribution as a function of the distance from the core is shown in Fig. 5.7.

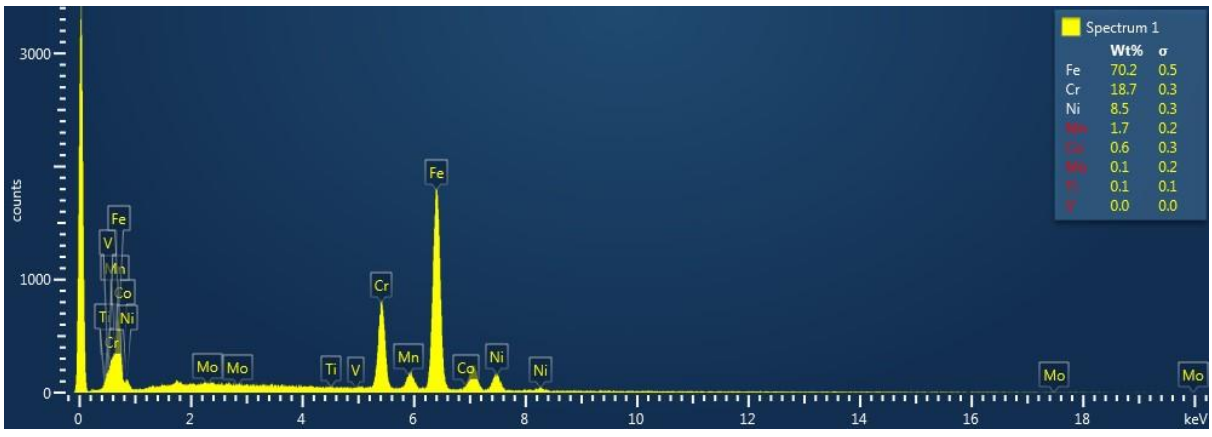

Fig. 5.6: Energy dispersive spectrum at a particular location of F1

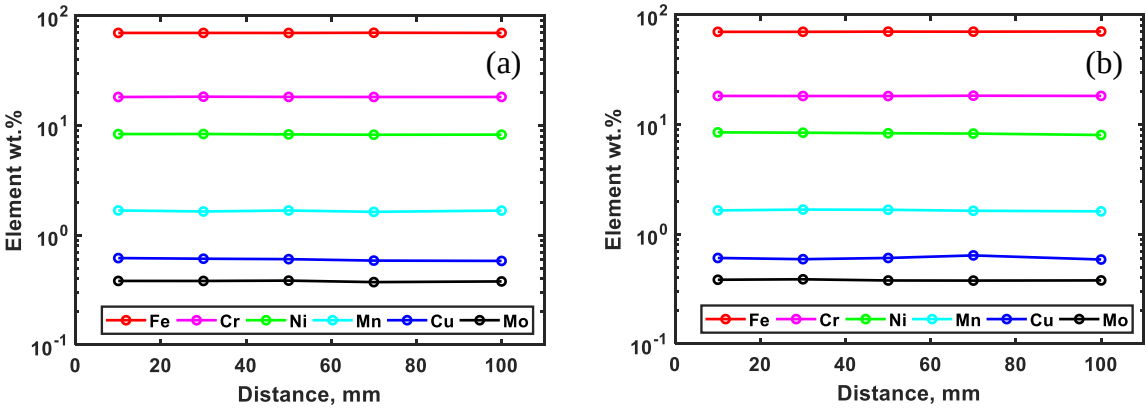

Fig. 5.7: Element (wt.%) distribution as a function of distance from the core in (a) F_1 and (b) F_2

5.3.3 Hardness

Vickers hardness measurements scrutinized the effectiveness of the recrystallization in the forgings. The hardness variation in the radial direction of the forgings is shown in Fig. 5.8. The hardness in both the forgings are much higher (262 to 275 $HV_{0.2}$ in F_1, whereas it varied from 305 to 326 $HV_{0.2}$ in F_2) compared to that commonly reported on solution annealed 304L grade steels (150 - 160 $HV_{0.2}$). An expected variation of hardness with grain size as per Hall-Petch relation is also found missing. Higher hardness in the forgings suggests that they would have supplied in cold-forged condition or forged at lower temperature and supplied not in the solution annealed condition. Contribution to hardness from the work hardening overrides the effect of grain size variations.

Relatively higher hardness of F_2 than that in F_1 is probably due to higher copper content in F_2 (0.579 wt.%) compared to 0.179 wt.% in F_1 (Table 3.3). The copper solubility in iron is limited, resulting in copper-rich precipitates during cooling in the forging operations or at an intermediate temperature where copper precipitation occurs.[153] As the forging was heavy, it would have undergone air cooling. Therefore, it can be assumed that the forgings would have seen a temperature range of 700 ℃ to 800 ℃ for a substantial period during which copper can precipitate easily. Ren et al.[153] studied the precipitation behaviour of Cu in type 304 austenitic stainless steel at different ageing stages and showed that the hardness changes with ageing time attributed to the nucleation and growth of Cu-rich phases. Similar studies by Xi et al.[154] in 316L austenitic stainless steel also showed that the hardness increased to a peak value at the early stage of aging and remained nearly unchanged with prolonged aging time. The mismatch in

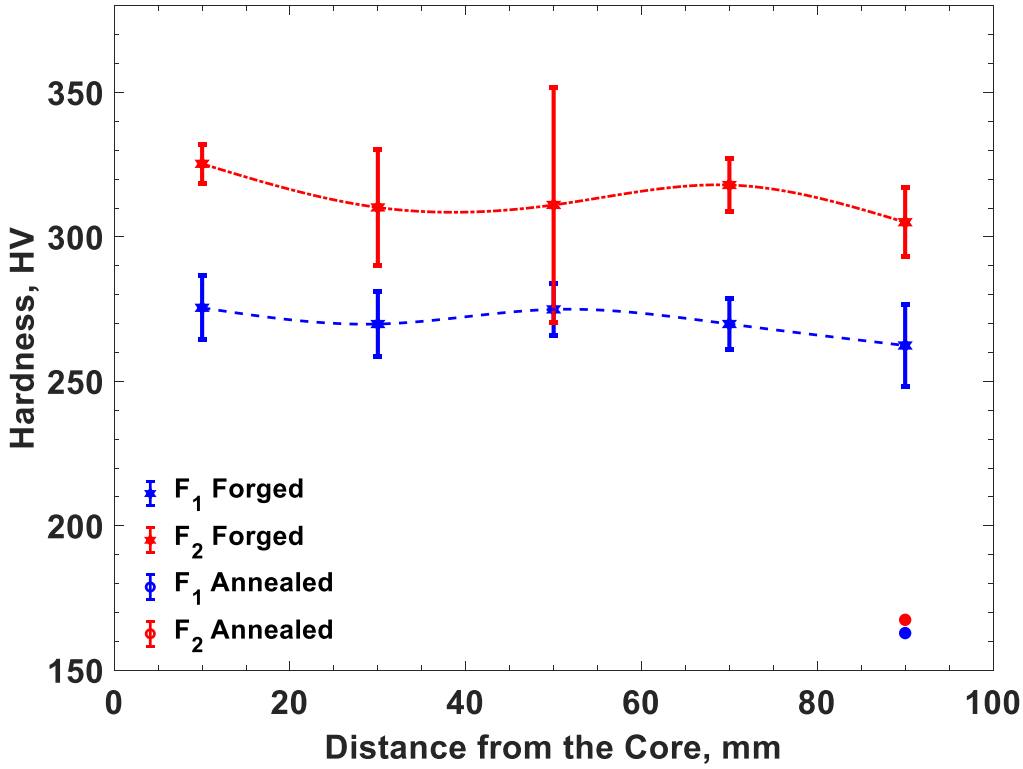

Fig. 5.8: Variation of hardness in F_1 and F_2 as a function of the distance from the core

the stress field caused by such insoluble precipitates rich in Cu would result in an increment in the hardness. However, the chemical homogeneity was maintained along the diameter.

One specimen near the surface from each forging were subjected to annealing at 1050 ℃ for a soaking period of 30 min. The hardness was lowered to 163 $HV_{0.5}$ in F_1 and 167 $HV_{0.5}$ in F_2, after annealing, which confirms the possibility of anomalies happened during the forging process.

5.3.4 Grain orientation spread

The grain orientation spread (GOS) is a quantitative tool extensively used for the assessment of microstructure evolution.[155,156] In a study reported on pure aluminium,[155] the GOS less than 6° was defined for fully recovered microstructure. Later, Alvi et al.[157] defined this cut off value to be 3° to distinguish the recrystallized and non-recrystallized grains. Cheong and Weiland[156] have used the GOS as a quantitative tool to study the microstructural evolution occurring during annealing. They could discern the alloying effect on the recrystallization in hot deformed Al-Cu-Mg alloys.

The EBSD data was collected on the specimens in the forged and annealed conditions at a step size of 0.5 μm for a scan area of 200 μm^2. The local orientation at each point was collected using TSLOIM^{TM} software version 7.01 attached to the Carl Zeiss, Supra 40 FESEM. The EBSD data were further processed using the OIM^{TM} software. Inverse pole figure (IPF) maps which show the surface orientation at each point with respect to the normal to the specimen surface and the grain orientation spread (GOS) were also generated using the OIM^{TM} software. The inverse pole figure (IPF) maps obtained from the specimens near the surface of F_1 and F_2 (both in forged and annealed conditions) are shown in Fig. 5.9. The GOS obtained from the EBSD analysis are shown in Fig. 5.10 and found to be lower than the above-mentioned cut-off values suggesting that the forgings were recrystallized completely. However, the higher hardness observed may be due to the residual work hardening effects remains as a result of the improper heat treatments after the forging process. Nevertheless, from the hardness data, it can be inferred that the work hardening effect is uniform across the diameter.

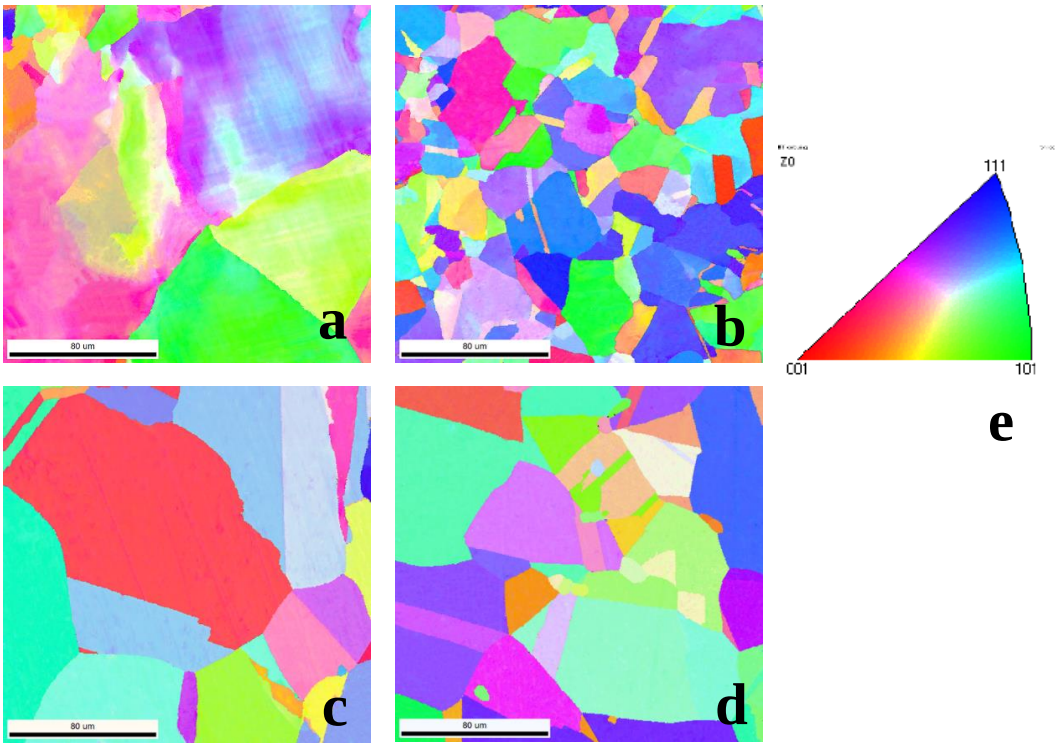

Fig. 5.9: IPF maps obtained from (a) F_1 and (b) F_2 in forged conditions and, (c) and (d) are in the corresponding annealed conditions; (e) represents the IPF legend.

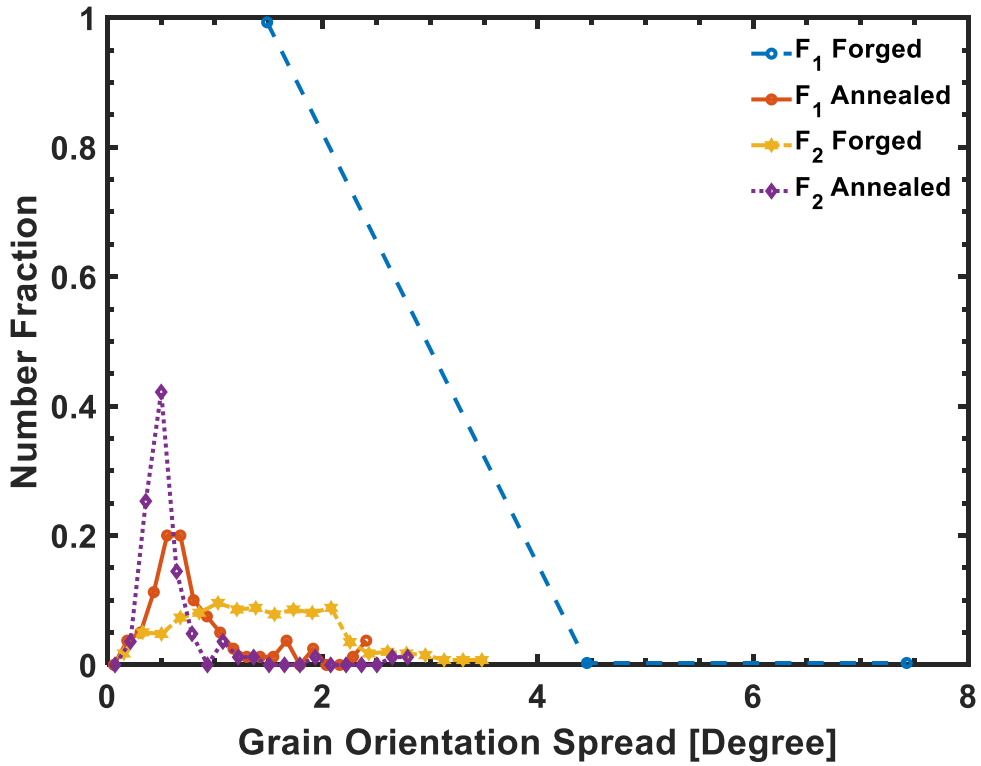

Fig. 5.10: Grain orientation spread in obtained in the forged and annealed conditions

5.3.5 Ultrasonic attenuation

The ultrasonic C-scan images of the first back-wall echo (u_1), the second back-wall echo (u_2) and the attenuation (α) obtained for ω = 5 MHz and ω = 10 MHz are shown in Fig. 5.11(a) and Fig. 5.11(b), respectively. The line-profiles of the attenuation obtained from the attenuation C-scan images is plotted in Fig. 5.12. The coefficient of attenuation for ω = 5 MHz ($\alpha_{5\ MHz}$) is observed to be similar in both F_1 and F_2 to a distance of ~80 mm from the core. However, there is a marginal variation in the $\alpha_{10\ MHz}$ among the forgings within this range (Fig. 5.12(b)). A considerable increase in $\alpha_{10\ MHz}$ compared to $\alpha_{5\ MHz}$ closer to the surface in F_2 is attributed to the frequency-dependent attenuation of elastic waves in a coarse grain microstructure. The higher the frequency and larger the grains, the greater will be the attenuation which explains why the $\alpha_{10\ MHz} > \alpha_{5\ MHz}$ near the surface of F_2. The fluctuations in the $\alpha_{10\ MHz}$ near the surface of F_2 is because of the coarse grain microstructure which scatters the 10 MHz waves considerably. The $u_{2(10\ MHz)}$ is feeble near the surface of F_2 and the backscatter noise would dominate in amplitude. In such conditions, accurate measurement of the $u_{2(10\ MHz)}$ alone would be difficult and hence results in a noisy appearance, as shown in the attenuation plot.

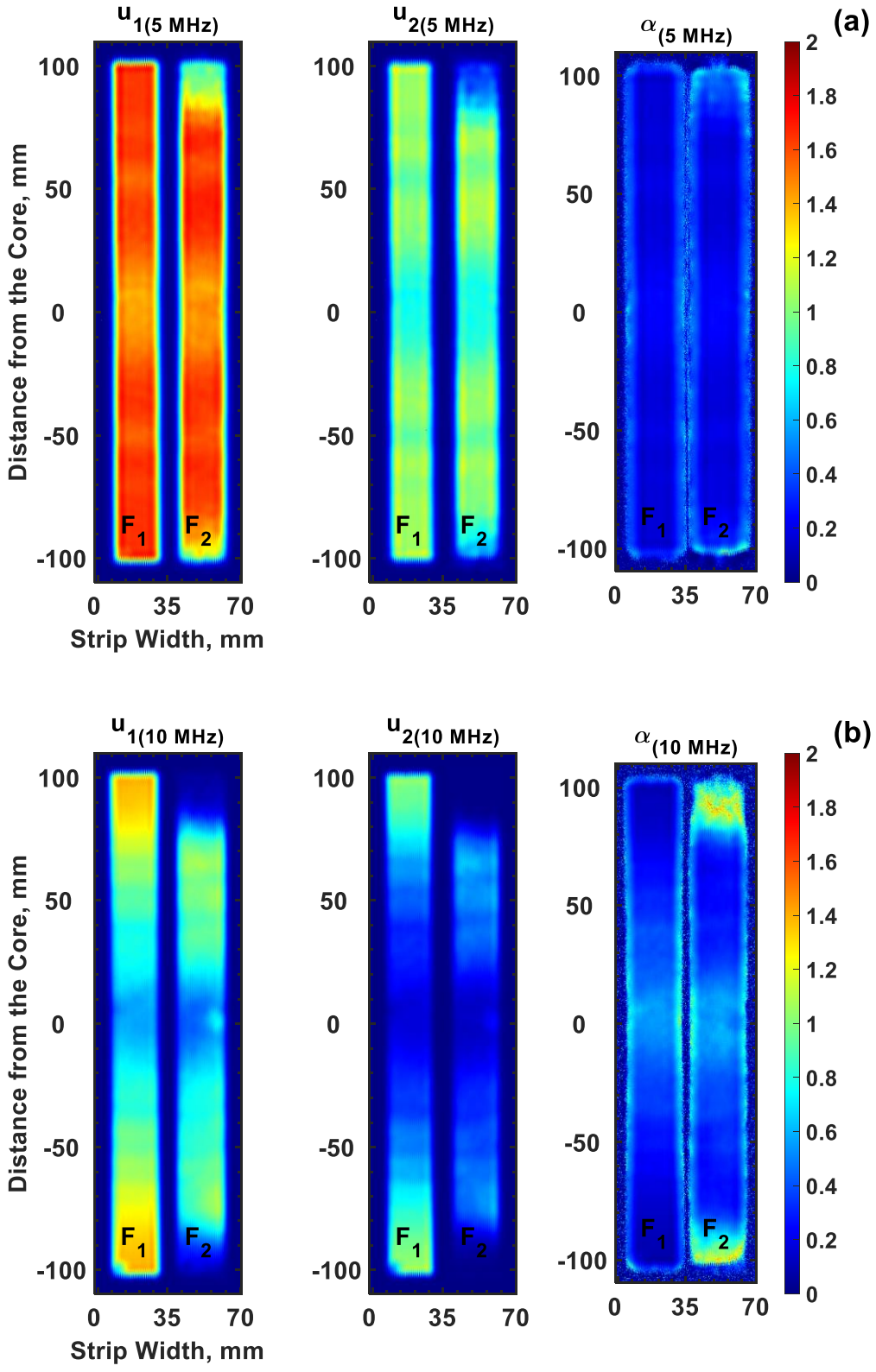

Fig. 5.11: C-scan images corresponding to first back-wall echo ($u_{1(\omega)}$), second back-wall echo ($u_{2(\omega)}$) and the attenuation ($\alpha_{(\omega)}$) in F_1 & F_2 for (a) ω = 5 MHz and (b) ω = 10 MHz

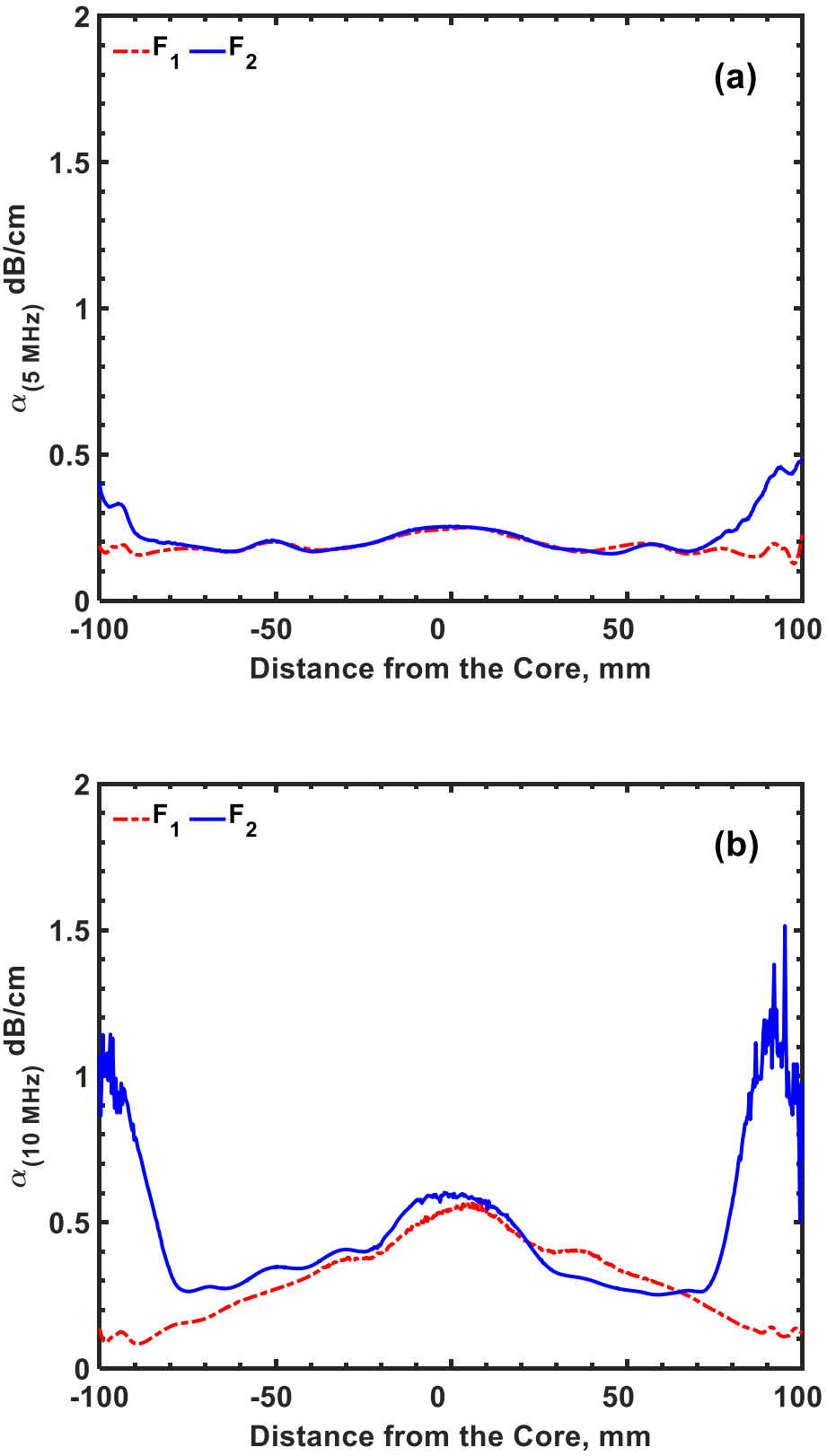

Fig. 5.12: Attenuation profile as a function of distance from the core in F_1 & F_2 for (a) ω = 5 MHz and (b) ω = 10 MHz

Similar noisy pattern was seen in the attenuation C-scan images which have been obtained for the annealed specimens with abnormal grain growth (Fig. 4.8). In the case of the forgings, it is also worth noting that the attenuation varies symmetrically in the radial direction about the core, which is apparent in the corresponding C-scan images. Though the high-frequency attenuation is very sensitive to the grain size variations (Fig. 5.12(b)), its application is limited to the materials with more refined grains or thin specimens owing to the scattering losses.

5.3.6 Nonlinear ultrasonics

The nonlinear response of the forgings for three different input frequencies was calculated and then normalized separately with that of the maximum β obtained for each frequency. This normalization provides a quantitative and relative comparison of the grain size variation across the diameter of each forging. The β will be maximum at the location where the grains are small. From Table 5.1 and Fig. 5.2, it is clear that the smaller grains appear near the surface of F_1 whereas it appears around 30 mm below the surface of F_2.

5.3.6.1 Nonlinear response in F_1

Fig. 5.13 plots the β_{norm} for each input frequencies. Since β was symmetric to the core, only a radial portion is illustrated to enhance the clarity in the discussions. The β is maximum near the surface which is in line with the $D_{mean}^{F_1}$ given in Table 5.1. It is important to note that an order $\beta_{7.5} < \beta_{5.0} < \beta_{2.25}$ is consistently maintained from core to the surface. However, a closer look reveals that, the $\beta_{2.25}$ and $\beta_{5.0}$ varies linearly from the core to the surface whereas $\beta_{7.5}$ showed a deviation in its linearity near the core even though the $D_{mean}^{F_1}$ lie in the Rayleigh scattering regime for 7.5MHz.

The deviation in $\beta_{7.5}$ can be understood on account of the grain size distribution. The classical attenuation theory was formulated based on the assumption that all grains have the same volume, and the grain size distribution is small. The power-law dependency in the Rayleigh and stochastic regimes are valid at the theoretical Rayleigh point defined as kD = 0.1 and at the stochastic point defined as kD = 10, respectively. In the Rayleigh-to-stochastic transition zone (KD varies from 0.1 to 10), the attenuation exhibits neither fourth-order nor quadratic dependency on frequency. The variations in the dependency are due to the simultaneous occurrence of the Rayleigh and stochastic scattering due to the coexistence of fine and coarse grains in the microstructure.[47,48,149] However, KD = 1 has been widely accepted as the Rayleigh

to the stochastic scattering transition point. Attenuation due to the stochastic interactions with larger grains is predominant even though there exists Rayleigh scattering.[158,159] Arguelles and Turner[160] analytically demonstrated the influence of grain size distribution on attenuation and subsequently verified it on Titanium alloys.[49,161] These studies illustrate that the coexistence of the fine and coarse grains in a microstructure can have significant effects on the attenuation coefficients.

As given in Table 4.2, the Rayleigh to stochastic scattering transition condition for the three input frequencies used in the present study occurs at the grain sizes $D_{2.25}$ = 410 μm, $D_{5.0}$ = 184 μm and $D_{7.5}$ = 123 μm. Though the D_{mean} along the diameter of the F_1 lie in the Rayleigh scattering regime for all three input frequencies, the actual microstructure consists of a wide distribution of grain sizes (Table 5.1). The grains with dimensions larger than the D_{ω} defined above cause stochastic attenuation to the corresponding input frequency (ω_i) even though the $k_{\omega_i}D_{mean}$ lies in the classical Rayleigh regime. Table 5.2 shows the measured $k_{\omega_i}D_{mean}$ values for three input frequencies (ω_i) as a function of the distance from the core.

Table 5.2: The kD values for the three input frequencies

Distance (mm) from the Core:	0	30	50	70	90
Mean Grain Size (D_{mean}), μm	103	71	79	53	38
$k_{2.25}D_{mean}$	0.251	0.173	0.192	0.129	0.092
$k_{5.0}D_{mean}$	0.557	0.384	0.427	0.286	0.205
$k_{7.5}D_{mean}$	0.836	0.576	0.641	0.430	0.308

Fig. 5.14 represents the histogram of grains 10 mm away from the core and at the core, which contributes to the stochastic scattering of the input wave of 7.5 MHz. It is evident that the number of grains that interacts stochastically to the 7.5 MHz input wave is increasing towards the core. A higher probability of larger grains that could not be confined within a lognormal distribution curve was also noticed. It is also evident from Table 5.2 that, the KD value for 7.5 MHz input frequency near the core approaches the classical scattering transition condition ($KD \approx 1$). As a result, an increased attenuation of the 7.5 MHz occurs which, in turn, lifts the $\beta_{7.5}$ as a consequence of the quadratic dependency of A_1 in the denominator of Eq. (2.25). This suggests that the condition for D_{mean} to be in the stochastic scattering regime need not be

necessary to observe a deviation in the linear behaviour of β with grain growth. The importance of considering the grain size distribution in a microstructure emerges at this juncture.

The grains whose dimensions larger than the scattering transition condition can cause a deviation in the behaviour of β. Such deviation in β can be seen on close observation of Fig. 4.9 plotted for the solution annealed microstructures in SS 304 also. Therefore, it is worth noting that the difference in β value with frequency ($\Delta\beta_{\omega_{i,j}} = \beta_{\omega_i} - \beta_{\omega_j}$ where $\omega_j > \omega_i$) is a qualitative representation of the number density of grains in the respective scattering regime. The $\Delta\beta_{\omega_{i,j}}$ is illustrated schematically in Fig. 5.13. It is also to be noted that, such analysis of $\Delta\beta_{\omega_{i,j}}$ is valid only for the β_{norm} since the β_{meas} does have an influence on the transducer response, which varies among different transducers (Fig. 3.10). However, the above-said order will be lost if a sufficient number of grains interact stochastically with the input frequencies, and such an occurrence is evident in the case of F_2.

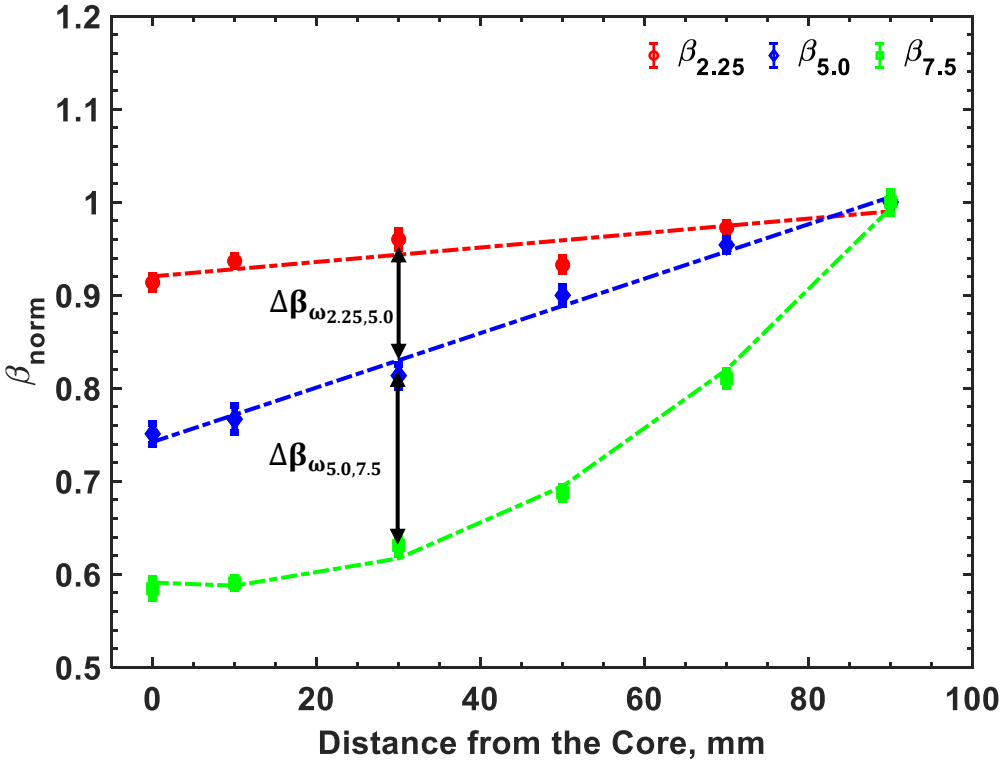

Fig. 5.13: Normalized β as a function of distance from the core in F_1. The $\Delta\beta_{\omega_{i,j}}$ at a particular location is illustrated.

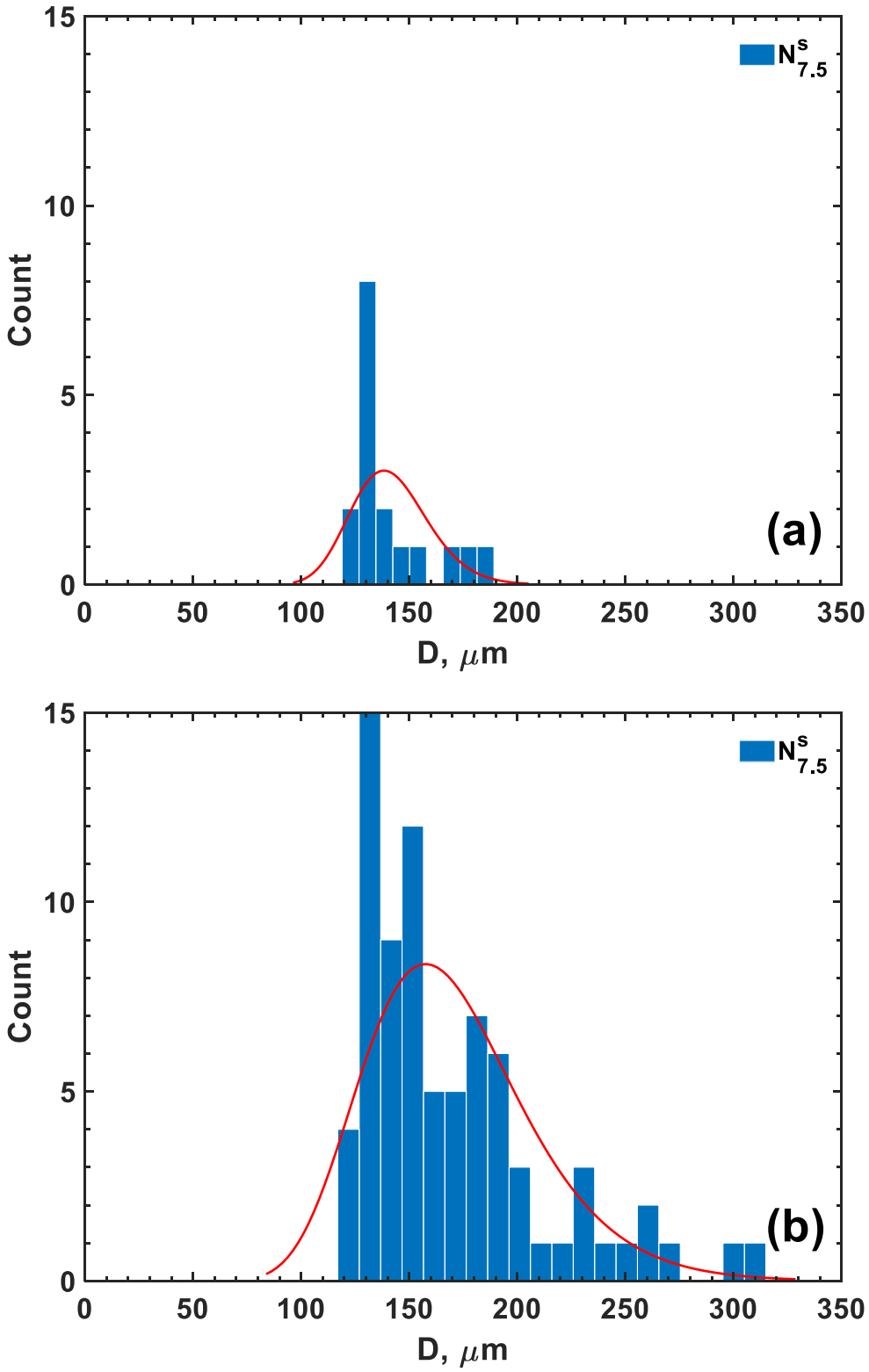

Fig. 5.14: The distribution of grains contributing to stochastic scattering for an input excitation of 7.5 MHz in F_1 (a) at 10 mm away from the core, and (b) at the core.

5.3.6.2 Nonlinear response in F_2

The β_{norm} as a function of distance from the core in F_2 is plotted in Fig. 5.15. The nonlinear response in F_2 is found to be different from the F_1. Irrespective of the frequency, maximum β was observed around 30 mm beneath the surface corresponding to the location of minimum grain size of $D_{mean}^{F_2}$. From this location, the β decreases gradually towards the core but maintaining the relation $\beta_{7.5} < \beta_{5.0} < \beta_{2.25}$. However, only a marginal difference between $\beta_{7.5}$ and $\beta_{5.0}$ is seen within the inner volume of F_2 on contrary to that observed in F_1. This can be understood from the relatively higher D_{mean} as well as σ compared to that in F_1 (Table 5.1). Higher σ value indicates the presence of larger grains and hence the coexistence of different scattering regimes, which influence the β as discussed in the previous sections.

In addition, the order $\beta_{7.5} < \beta_{5.0} < \beta_{2.25}$ is lost near the surface of F_2, with swapping of $\beta_{7.5}$ and $\beta_{5.0}$. Such swapping in the order of β_{ω} and variation in the $\Delta\beta_{\omega_{i,j}}$ happens if there exists a sufficient number of grains that interact stochastically with the input frequencies. This has a resemblance to the Fig. 4.9 in which such swapping were observed at certain D_{mean}'s. The relative position of β_{ω_i} depends on the number density of grains contributing to the stochastic scattering of the fundamental and harmonic frequencies. To illustrate this fact, a comparison

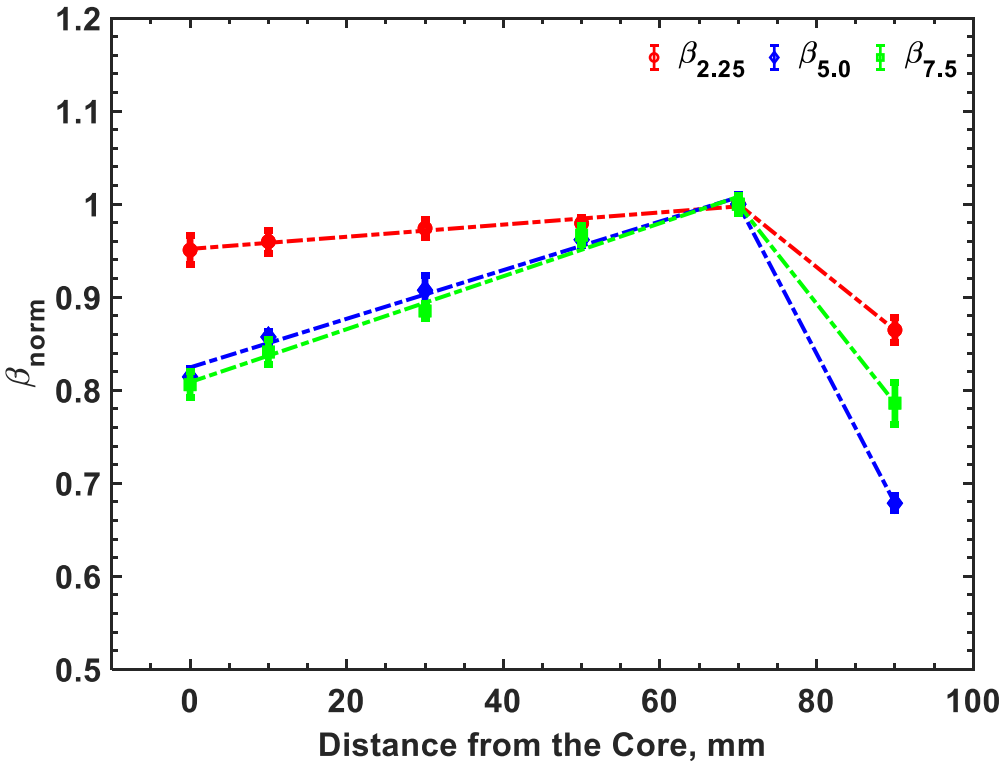

Fig. 5.15: Normalized β as a function of distance from the core in F_2

of the number density of grains in the stochastic scattering regime for fundamental and harmonic frequencies near the surface ($N^s_{\omega_i}$) and at the core ($N^c_{\omega_i}$) is tabulated in Table 5.3. Similar tabulation for the F_1 is presented in Table 5.4 and a clear difference among the $N^s_{\omega_i}$ and $N^c_{\omega_i}$ is evident. Relatively closer $N^s_{\omega_i}$ and $N^c_{\omega_i}$ is evident in the case of F_2 (Table 5.3) whereas, there exist a distinct difference among the $N^s_{\omega_i}$ and $N^c_{\omega_i}$ in F_1 (Table 5.4). More the number of grains and higher the frequency, larger will be the scattering losses. Therefore, abnormal behaviour of β in F_2 is attributed to the heterogeneity in the grain size distribution. On the other hand, in both forgings, $\beta_{2.25}$ showed a linear variation towards the grain coarsening as a consequence of the scattering independent nonlinear interactions since the size of all the grains falls within the Rayleigh scattering regime for this frequency.

Table 5.3: Number density (%) of grains contributing to the stochastic scattering of fundamental and harmonic components near the surface and at the core in F_2

	Fundamental		Second Harmonic	
Surface	$N^s_{2.25}$	3.43	$N^s_{4.5}$	15.79
	$N^s_{5.0}$	19.37	$N^s_{10.0}$	48.43
	$N^s_{7.5}$	34.43	$N^s_{15.0}$	71.83
Core	$N^c_{2.25}$	0.59	$N^c_{4.5}$	6.23
	$N^c_{5.0}$	12.05	$N^c_{10.0}$	61.27
	$N^c_{7.5}$	38.45	$N^c_{15.0}$	85.46

Table 5.4: Number density (%) of grains contributing to the stochastic scattering of fundamental and harmonic components near the surface and at the core in F_1

	Fundamental		Second Harmonic	
Surface	$N^s_{2.25}$	---	$N^s_{4.5}$	---
	$N^s_{5.0}$	---	$N^s_{10.0}$	---
	$N^s_{7.5}$	---	$N^s_{15.0}$	7.69
Core	$N^c_{2.25}$	---	$N^c_{4.5}$	3.38
	$N^c_{5.0}$	7.69	$N^c_{10.0}$	52.9
	$N^c_{7.5}$	23.4	$N^c_{15.0}$	82.7

It is therefore worth emphasizing that the NLU measurement using a single frequency would also be able to monitor the grain size variations along the diameter of the forgings as the nonlinearity parameter is related to the grain size variation which is evident in Fig. 5.13 & Fig. 5.15 in comparison with the D_{mean} in Table 5.1. However, the results presented here and in the previous chapter infer that the influence of the grain size distribution will not be revealed in the conventional single frequency measurement as a multi-frequency approach is required to observe the changes in the linear trend of β_{ω_i} and changes in the order of β_{ω_i} and thereby the deviation in the $\Delta\beta_{\omega_{i,j}}$ with grain coarsening. The multi-frequency NLU methodology has a reasonable correlation with the microstructure and has reliability in assessing the heterogeneous distribution of the grain size in large forgings. The existence of heterogeneous microstructure that was not disclosed in the hardness values could be revealed in the order of β_{ω_i} as well as the $\Delta\beta_{\omega_{i,j}}$. Therefore, this methodology can be used as a reliable NDE tool to be applied in process industries for quality assurance of the materials. In the following section, this methodology is further validated on a third forging (F_3) of similar material and dimension for which the process history was also unknown.

5.4 Validation of the multi-frequency nonlinear approach

The nonlinear measurements were carried out on the third forging, F_3, of the same diameter as per the procedure adopted for other two forgings. The normalized β as a function of the distance from the core is plotted in Fig. 5.16. Within the inner volume of the forging, there exists only a marginal difference between the $\beta_{2.25}$ and $\beta_{5.0}$. Also, the $\Delta\beta_{\omega_{i,j}}$ is much reduced compared to that was seen in the F_1 and F_2. However, the order $\beta_{7.5} < \beta_{5.0} < \beta_{2.25}$ is maintained within the inner volume as well as near the surface on the contrary to that observed in the case of F_2. From the variations of β as a function of the distance from the core, the following assumptions have arrived.

1. The maximum value of the β around 30 mm beneath the surface indicates that the grains are smaller at that location resembling F_2.
2. Relatively smaller variation in β_{norm} (in the inner volume) indicates that the variation in D_{mean} as a function of distance from the core is minimal. Also, smaller variations in

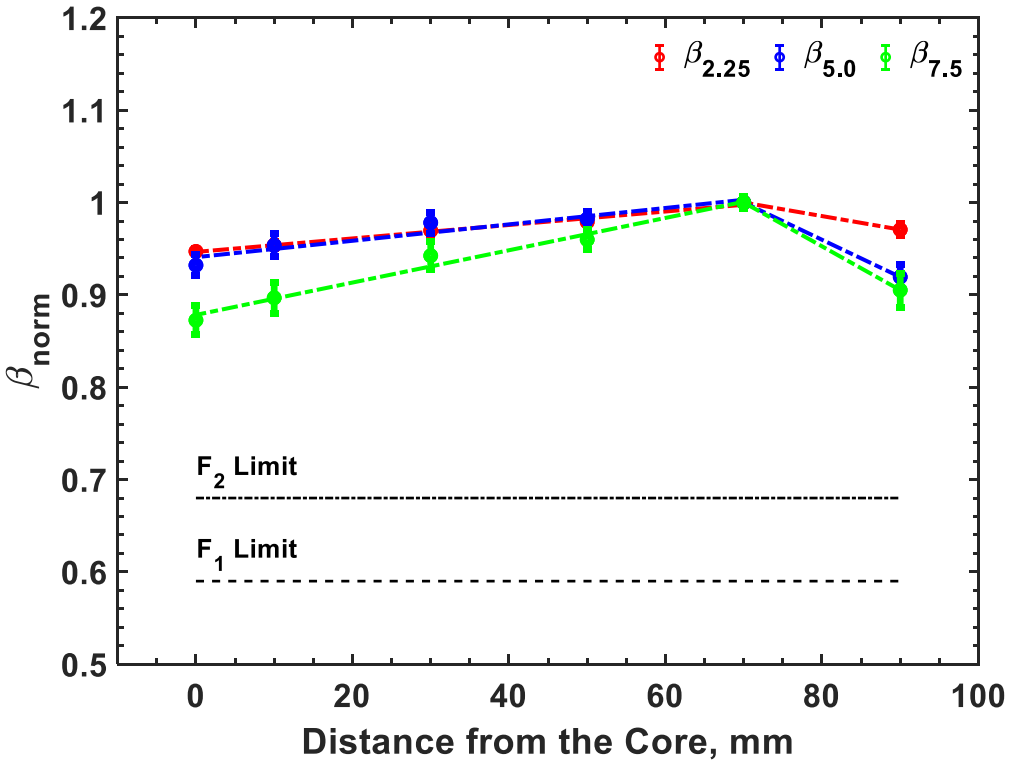

Fig. 5.16: Normalized β for F_3 as a function of distance from the core. The F_1 limit indicates the extent to which the β_{norm} in F_1 varies as a function of the distance from the core.

the $\Delta\beta_{\omega_{i,j}}$ indicates that the standard deviation in grain size is smaller in F_3 compared to that in F_1 and F_2.

3. Linear variation of β_{norm} (in the inner volume) indicates that the mean grain size is within the Rayleigh scattering regime as far as three input frequencies are concerned. The relatively lower $\beta_{7.5}$ in the inner volume may be due to the presence of grains whose sizes are big enough to cause considerable attenuation to the corresponding second harmonic component (15 MHz).
4. The difference in the behaviour of $\Delta\beta_{\omega_{i,j}}$ near the surface indicates that the standard deviation in the grain size distribution is relatively higher at this location compared to the rest of the material.

Fig. 5.17 depicts the microstructure and the grain size distribution as a function of distance from the core in F_3. The mean grain size and the standard deviation were measured from the micrographs and tabulated in Table 5.5. The above assumptions drawn from the nonlinearity measurements are hereby validated through the obtained photomicrographs. The conclusions are:

1. The minimum mean grain size (53 µm) around 30 mm beneath the surface confirms the maximum value of the β obtained at that location.
2. The variation in D_{mean} along the diameter of F_3 is small (53 µm to 73 µm) compared to that in F_1 (38 µm to 103 µm) and F_2 (63 µm to 130 µm). Also, the standard deviation is minimal compared to other forgings. For comparison, the F_1 and F_2 limits in Fig. 5.17 indicate the extent to which the β_{norm} in those forgings were varied as a function of the distance from the core. A one-to-one correlation and thereby a prediction of the grain size in F_3 is not possible at this stage since the normalization of the β was made to the β obtained at the minimum D_{mean} which is different in each forging. In addition, the standard deviation of grain size in F_3 is small (27 µm to 39 µm) so that the number density of grains which can stochastically interact with the input frequencies are insignificant.
3. The mean grain sizes observed in the rage 53 µm to 73 µm and minimal standard deviation in F_3 ensures the Rayleigh scattering regime for all three input frequencies. However, the grain size distribution would have provided a sufficient fraction of grains to have stochastic interactions to the 15.0 MHz harmonic component which caused a relatively lower $\beta_{7.5}$ in the inner volume.
4. Table 5.6 indicates that the number density of grains which are responsible for the stochastic scattering of the fundamental and harmonic components near the surface and at the core are almost similar whereas distinct variations are in the case of F_1 (Table 5.3) and F_2 (Table 5.4). There exists a considerable fraction of grains near the surface which can interact stochastically with the 10 MHz and the 15 MHz components (Table 5.6) that would have caused a lower value to $\beta_{5.0}$ and $\beta_{7.5}$ near the surface. Near the surface, the D_{mean} = 69 µm and the σ = 39 µm would have caused a difference in the behaviour of $\Delta\beta_{\omega_{i,j}}$ in comparison with the inner volume.

Table 5.5: Grain size measurement in the forging F_3

Distance (mm) from the Core:	0	30	50	70	90
Forging, F_3					
$D_{mean}^{F_3}$, µm	73	64	62	53	69
σ_{F_3}, µm	31	33	32	27	39

The assumptions derived from the nonlinearity parameter, therefore, matches with the microstructural variations. Hence, the multi-frequency nonlinear ultrasonics is a reliable method to characterize the heterogeneous microstructure.

Table 5.6: Number density (%) of grains contributing to the stochastic scattering of fundamental and harmonic components near the surface and at the core in F_3

	Fundamental		Second Harmonic	
Surface	$N^s_{2.25}$	---	$N^s_{4.5}$	---
	$N^s_{5.0}$	0.4	$N^s_{10.0}$	20.0
	$N^s_{7.5}$	5.6	$N^s_{15.0}$	52.0
Core	$N^c_{2.25}$	---	$N^c_{4.5}$	---
	$N^c_{5.0}$	1.0	$N^c_{10.0}$	25.4
	$N^c_{7.5}$	8.8	$N^c_{15.0}$	54.4

5.5 Industrial relevance of multi-frequency approach

Large structural components like forgings used in the power plants are obtained by continuous forging/casting routes and ingot metallurgy. The cast structure is modified to wrought structures by the process of hot or cold forging operations which involve intermediate annealing. Hot forging is the most commonly used method for the manufacturing of large components, considering the minimum power requirements. Strain, strain rate, and forging temperature are three essential parameters in the hot forging process, and the final microstructure in the finished product is a function of these interlinked parameters. However, variation in the grain size and its distribution cannot be ruled out in a large component.[162–164] As steels are hot forged typically in the austenite phase, variation in the prior austenite grain size (PAGS) across the thickness can be expected,[165] suggesting variations in mechanical properties. Variation in grain size across the thickness of large components is inevitable, and such variations lead to variations in mechanical properties, especially ductility and fracture toughness. Therefore, a non-destructive evaluation technique that can predict the grain size and its variation across the thickness or cross-section would be useful as quality control or inspection tool for qualifying such components. The results in this chapter suggest that the multi-frequency NLU is a reliable NDE tool to be applied in process industries for quality assurance. However, a detailed investigation of the contribution of the grain size distribution, which makes a microstructure heterogeneous, is necessary.

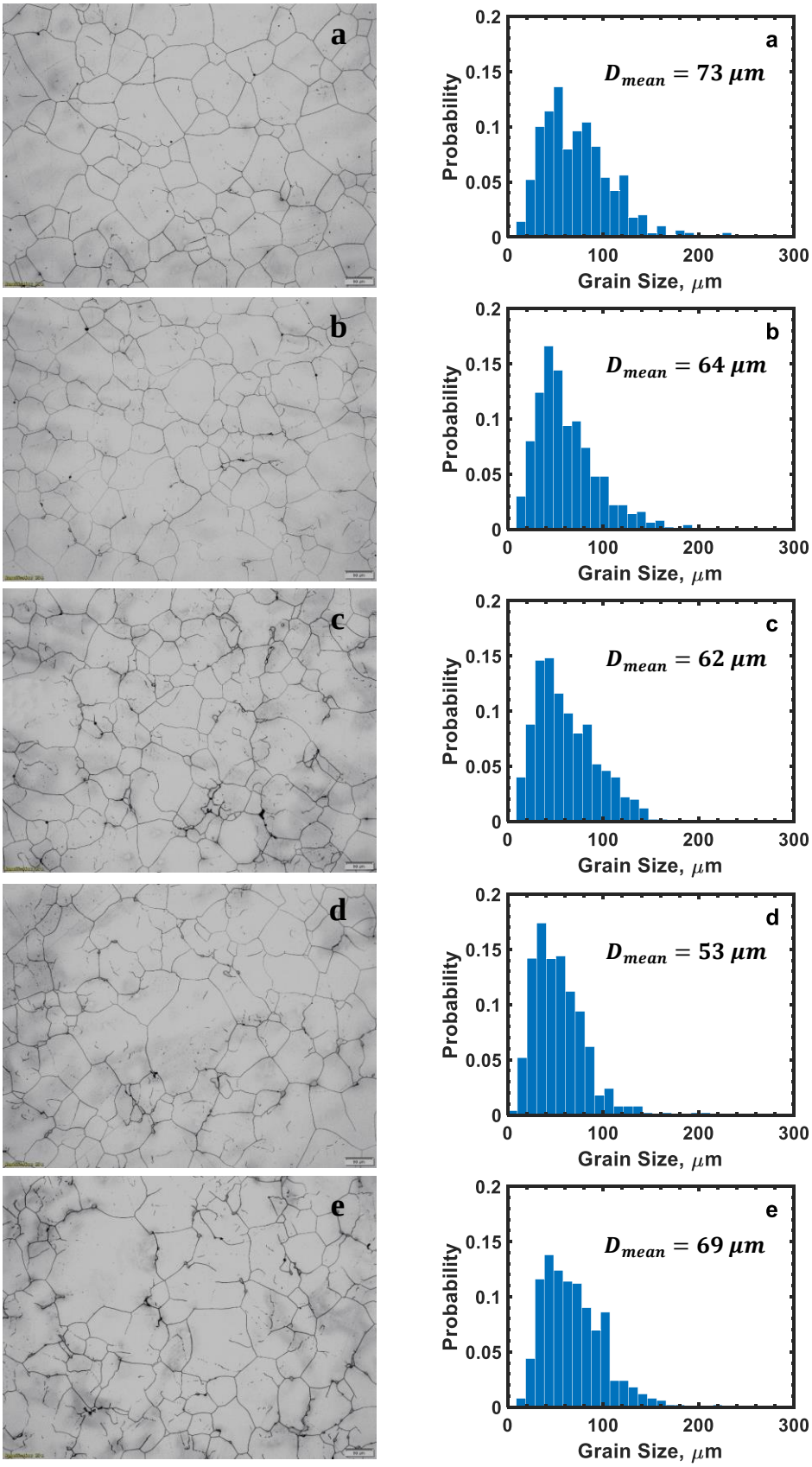

Fig. 5.17: Optical micrographs and the corresponding grain size histogram of the F_3 obtained at (a) the core and at distances (b) 30 mm (c) 50 mm (d) 70 mm and (e) 90 mm away from the core. Mean grain size is also indicated.

5.6 Summary

The observations in this chapter are summarized below.

- Though the high-frequency attenuation is very sensitive to the microstructure, its applicability is restricted on coarse grain parts and therefore not practical on large forgings in which significant variation in grain size is expected.
- The existence of heterogeneous microstructure in large diameter forgings that was not disclosed in the hardness values could be revealed by evaluating the order of β_{ω_i} as well as the $\Delta\beta_{\omega_{i,j}}$ which has got a one-to-one correlation with the microscopy results.

However, it is also observed that even if the D_{mean} lies in the Rayleigh scattering regime, there is a deviation in the linear behaviour of the β with grain growth. This is because of the influence of grain size distribution on the acoustic nonlinearity parameter, which is investigated in detail in the next chapter.

Chapter 6
Effect of Grain Size Distribution on the Acoustic Nonlinearity Parameter

6.1 Introduction

The mean grain size and its distribution in polycrystalline materials have a vital influence on the measured acoustic nonlinearity parameter. As seen in Chapter 4, the nonlinearity parameter varies linearly in the Rayleigh scattering regime, and it deviates from its linearity in the Rayleigh-to-stochastic scattering transition regime which is a function of the mean grain size and the applied frequency. However, it was found in the analysis on the heterogeneous microstructure of forgings in Chapter 5 that, even if the D_{mean} lies in the Rayleigh scattering regime, there is a deviation in the linear behaviour of the β with grain growth (Fig. 5.13). An attempt was made to explain such deviation on the basis of the grain size distribution.

The grain size in any polycrystalline material is distributed lognormally.[3] The effect of such distribution on the nonlinearity parameter has to be considered for a reliable characterization of the microstructure. Extensive studies have been reported in the literature on the influence of grain size distribution on the attenuation of elastic waves[159–161], but such an attempt has yet to be extended to the acoustic nonlinearity parameter. Therefore, this chapter investigates the effect of grain size distribution on the measured acoustic nonlinearity parameter. Results are provided for the austenitic stainless-steel materials having comparable mean grain size and distinct distribution assuming equiaxed grains and random crystallographic orientation.

6.2 Materials and methods

Two AISI grade 304 austenitic stainless-steel plates (designated as P_1 and P_2) from different production lots as mentioned in section 3.2.3 were used in this study.

6.3 Results and discussions

6.3.1 Microstructure

The photomicrographs of the specimen P_1 and P_2 are shown in Fig. 6.1. The grain size in the specimen P_1 was measured to be within 12 to 110 μm and that in P_2 ranges from 8 to 124 μm with an identical mean grain size of 42 μm. The dimension of all the grains was confined within the Rayleigh scattering regime for the three input excitation frequencies used in the present investigation. The standard deviation (σ) in grain size in these specimens was, however, distinct and the logarithmic distribution was measured to be $\sigma^{P_1} = 0.45$ and, $\sigma^{P_2} = 0.52$, where the superscript denotes the specimen. Therefore, the nonlinearity parameter derived from P_1 and P_2 would be influenced by the grain size distribution only.

The probability distribution function (PDF) of the grain size is represented as histograms fitted with lognormal distribution curves in Fig. 6.2. Presence of larger grains in specimen P_2 is seen in the histogram. Careful observation of Fig. 6.2 shows that the fitted lognormal distribution function did not envelope the real distribution of grain sizes completely. The statistical parameters associated with the distribution of the random variables can be calculated using the method of moments such as the mean, standard deviation, skewness, kurtosis, mode and the median. For the given specimens, these parameters in logarithmic distribution are listed in Table 6.1. It is evident from the table that, higher the standard deviation, more is the skewness which has led to the probability of occurrence of larger grains in the microstructure. Presence of such larger grains in a microstructure, in turn, affects the β considerably due to the scattering assisted attenuation.

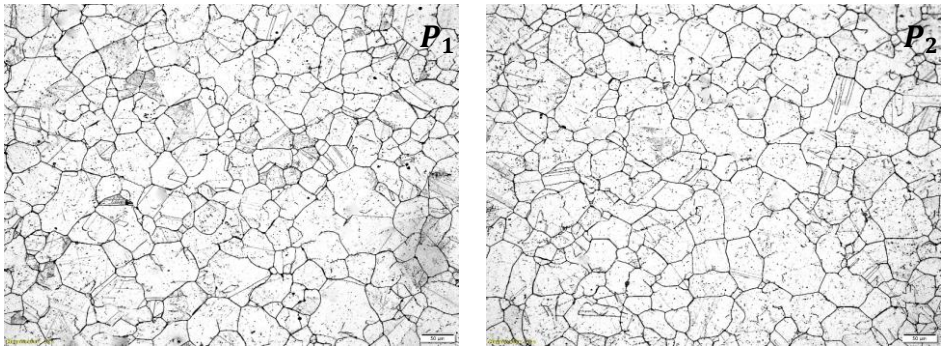

Fig. 6.1: Optical micrographs of the specimens P_1 and P_2

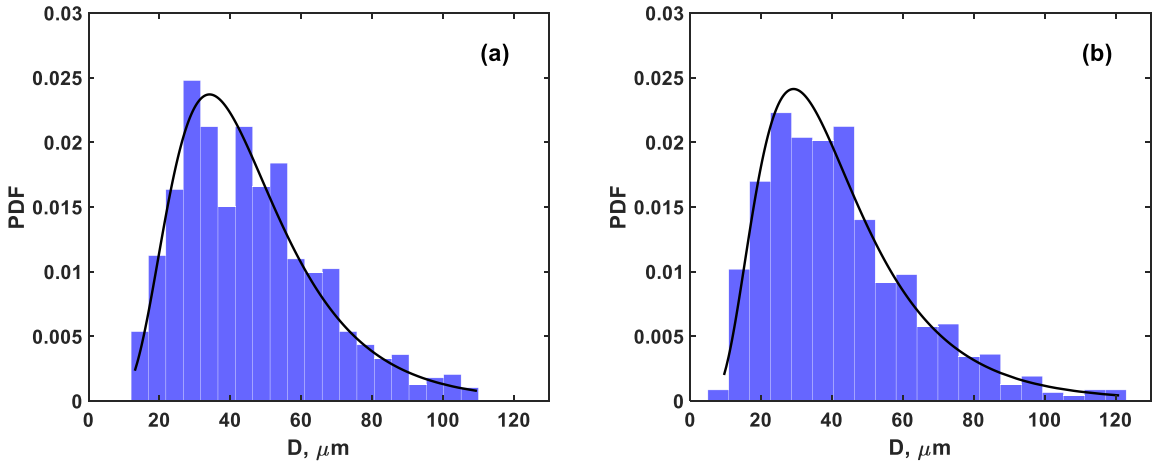

Fig. 6.2: Grain size distribution in the specimens with (a) $\sigma^{P_1} = 0.45$ and (b) $\sigma^{P_2} = 0.52$ presented as histograms with fitted curves for lognormal distribution.

Table 6.1: Grain Size Distribution Statistics			
Parameters	Specimen P_1	Specimen P_2	Remarks
Mean (μ)	3.7375	3.7380	
Std Dev. (σ)	0.446	0.520	
Skewness	0.781	1.061	+1 to +0.3: strongly positive skewed
Kurtosis	3.298	4.178	> 3.0: extremely leptokurtic
Mode	3.378	3.333	
Median	3.761	3.652	

6.3.2 Nonlinearity parameter

The measured β was normalized with that of the fused silica of the same thickness according to the procedure given in section 3.4.7. Fused silica was selected as the reference material for normalization because of its isotropic nature to the acoustic wavelengths used and consistency in the β value.[128] The β_{norm} for the given specimens measured for three input frequencies is plotted in Fig. 6.3. It is seen that, an order $\beta_{2.25} > \beta_{5.0} > \beta_{7.5}$ (suffix corresponds to the applied frequency) is maintained, and in each case, the specimen with wider σ shows a relatively lower β consistently. Variation in β_{norm} with distribution in grain size can be explained as follows.

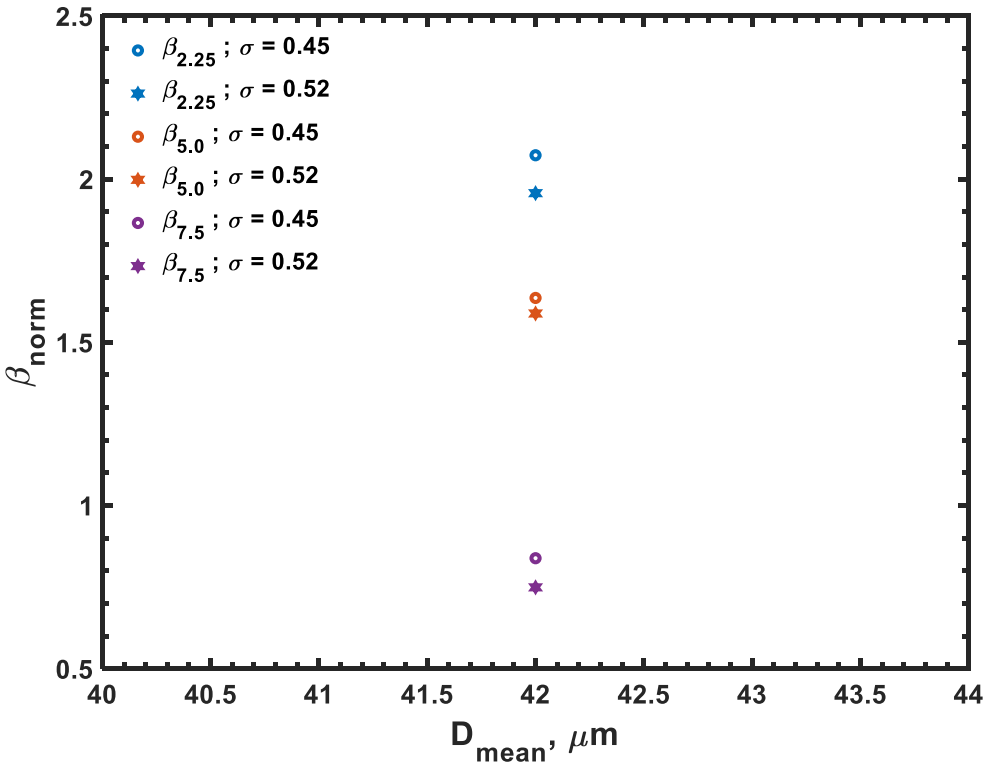

Fig. 6.3: Normalized β in P_1 and P_2 for three input frequencies 2.25MHz, 5.0 MHz and 7.5 MHz. The specimens are represented in terms of their σ values in the legend.

In a polycrystalline material, the probability distribution function $P(D)$ of the grain sizes (D) is defined as

$$P(D) = \frac{1}{D\sigma\sqrt{2\pi}} exp\left[-\frac{ln^2(D/\widetilde{D})}{2\sigma^2}\right] \tag{6.1}$$

where the median of the distribution $\widetilde{D} = e^{\mu}$ which relates to the volumetric mean of the distribution $\overline{D} = \widetilde{D}\, e^{\sigma^2/2}$ where σ is the logarithmic distribution width, and μ is the mean of the normal distribution. For a continuous lognormal distribution of grain sizes D, the spatial correlation function, describing the probability that two points at correlation distance (r) fall in the same grain, maybe written as[160]

$$\eta(r) = \int_0^{\infty} P(D) \exp\left(-\frac{r}{D}\right) dD \tag{6.2}$$

The $P(D)$ is plotted in Fig. 6.4(a) for a constant $\overline{D}$ and varying σ, and the corresponding $\eta(r)$ is plotted in Fig. 6.4(b). The $\eta(r)$ has a higher amplitude at larger r for broader distributions which indicates the presence of bigger grains. Fig. 6.5 shows the synthetic microstructures

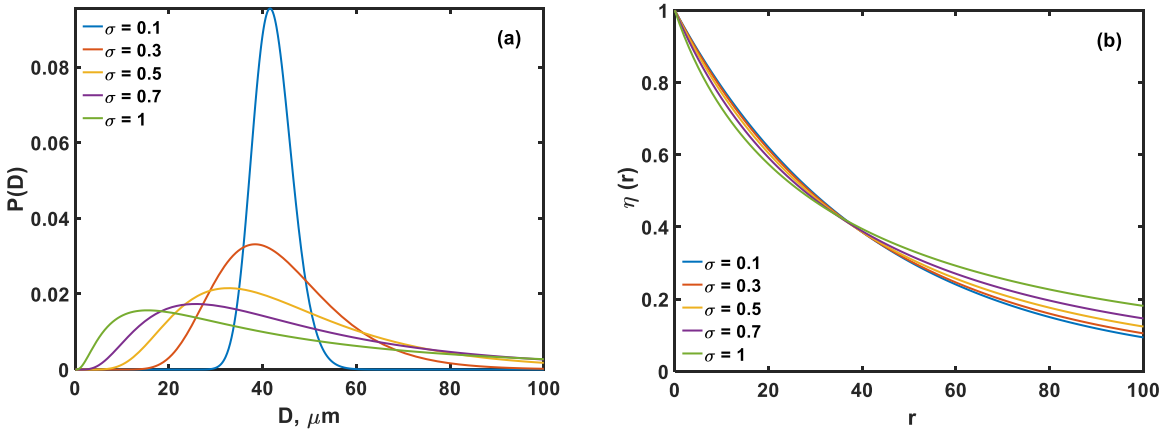

Fig. 6.4: (a) Probability distribution for a constant mean, $D_{mean} = 42\ \mu m$, and varying distribution widths (σ = 0.1, 0.3, 0.5, 0.7, 1.0) and (b) the corresponding spatial correlation function

developed for the mean grain size and the distribution given above. These microstructures were obtained using a digital representation environment for the analysis of microstructure in 3D (DREAM.3D®). With an increase in grain size distribution, the presence of larger grains is apparent in the microstructure.

Attenuation of longitudinal waves in a polycrystalline material with a grain size distribution can analytically be written as[160]

$$\alpha_L = \frac{k_L^2 \pi}{4\rho^2 c_L^2} \int_0^{\pi} \tilde{\eta}(\theta_{ps}) M_1(\theta_{ps}) sin\theta_{ps} d\theta_{ps} \tag{6.3}$$

with

$$\tilde{\eta}(\theta_{ps}) = \int_0^{\infty} P(D) \frac{D^3}{\pi^2 \left[1 + D^2(k^2 + k_s^2 + 2kk_s cos\theta_{ps})\right]^2} dD \tag{6.4}$$

where $\tilde{\eta}(\theta_{ps})$ is the Fourier transform of the spatial correlation function, θ_{ps} is the scattering angle, M_1 is the autocorrelation function of the elastic constants for the corresponding incident and scattered wave modes of wave vectors k and k_s respectively and k_L and c_L are the wavenumber and velocity of incident longitudinal waves. In the Rayleigh scattering regime where $kD \ll 1$ Eq. (6.4) becomes

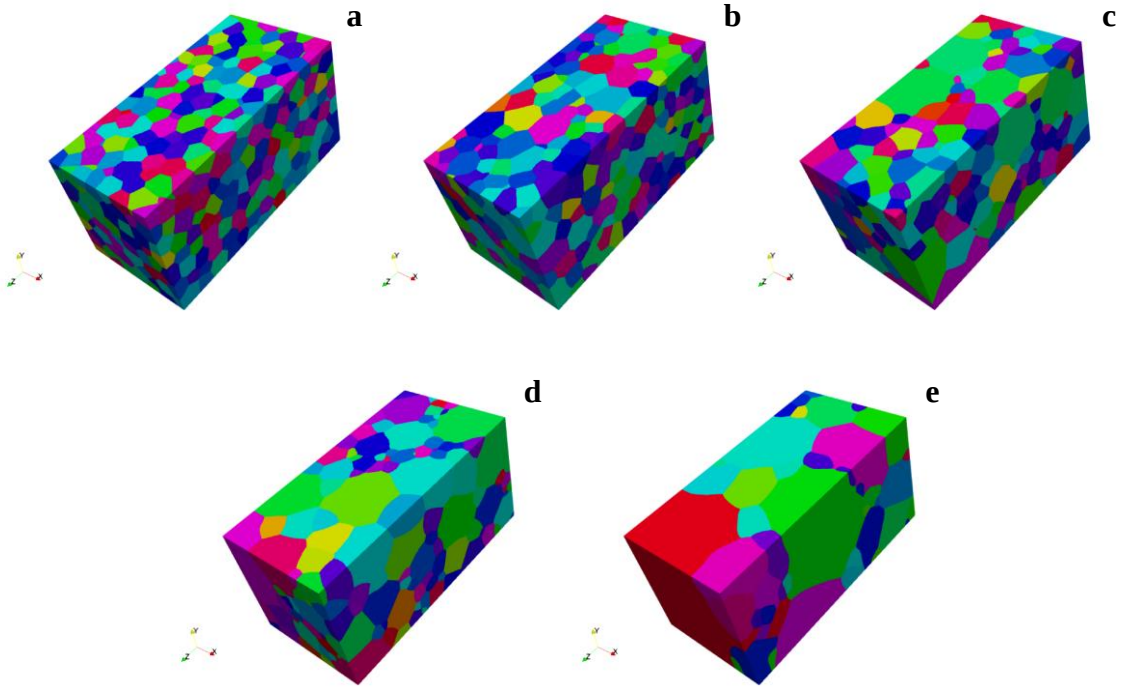

Fig. 6.5: Synthetic microstructures for the $D_{mean} = 42\ \mu m$ and the grain size distributions (a) $\sigma = 0.1$ (b) $\sigma = 0.3$, (c) $\sigma = 0.5$, (d) $\sigma = 0.5$ and (e) $\sigma = 1.0$ respectively.

$$\tilde{\eta}(\theta_{ps}) = \int_0^\infty P(D)\frac{D^3}{\pi^2}dD \tag{6.5}$$

In a single-phase polycrystalline material, it may be assumed that the anisotropy in the bulk modulus vanishes considering the bulk modulus of a single crystallite of cubic symmetry is equal to that of a polycrystal containing the cubic crystallites.[166] Also, random orientations of single-phase crystallites imply statistical isotropy and homogeneity to the polycrystal. In this condition, the Eq. (6.3) reduces to[160]

$$\alpha_L^R = \frac{1}{15}\frac{\tilde{D}^3 k_L^4}{\rho^2 c_L^4}\exp\left(\frac{9\sigma^2}{2}\right) \times \left[\frac{672}{36}\mu + \frac{1344}{48}\frac{\mu\, c_L^5}{c_T^5}\right] \tag{6.6}$$

where $\mu = 3(C_{11} - C_{12} - 2C_{44})^2/175$ is the second order anisotropy[166] in the shear modulus. The attenuation coefficients for a monochromatic plane wave of frequency $5\ MHz$ and a set of distributions illustrated in Fig. 6.4(a) is plotted in Fig. 6.6. Assuming cubic symmetry of the material, the elastic constants were taken as $C_{11} = 200.4\ GPa$, $C_{12} = 129.3\ GPa$ and $C_{44} = 125.8\ GPa$.[167] Fig. 6.6 illustrates that the distribution of grain size influences the ultrasonic attenuation measurably. The deviations from the theoretical prediction by Stanke and Kino[48]

which was observed while measuring the attenuation in low carbon steels,[158] copper alloy,[149] Nickel,[159] and titanium alloys[49,161] were also accounted for the distribution in grain size. Therefore, the σ can substantially influence the measured β as it is decided by the attenuation coefficients, α_i, according to Eq. (2.59). This influence, termed as β_{α_i} in Eq. (2.59), is graphically exemplified in Fig. 6.7 for a propagating monochromatic elastic wave of frequency 5 MHz. It is evident from this figure that the β_{α_i} reduces considerably with an increase in σ and the D_{mean}.

Therefore, the drop in measured β (Fig. 6.3) with an increase in applied frequency is a consequence of the difference in the attenuation of the A_1 and A_2 components as discussed in the previous chapters. The scattering transition condition for the respective second harmonic components occur at $D_{4.5} = 205\ \mu m$, $D_{10.0} = 92\ \mu m$ and $D_{15.0} = 62\ \mu m$. This implies that, the higher harmonic components of 10 MHz and 15 MHz are likely to undergo stochastic interactions with few grains in the microstructure. In such cases, the attenuation coefficient

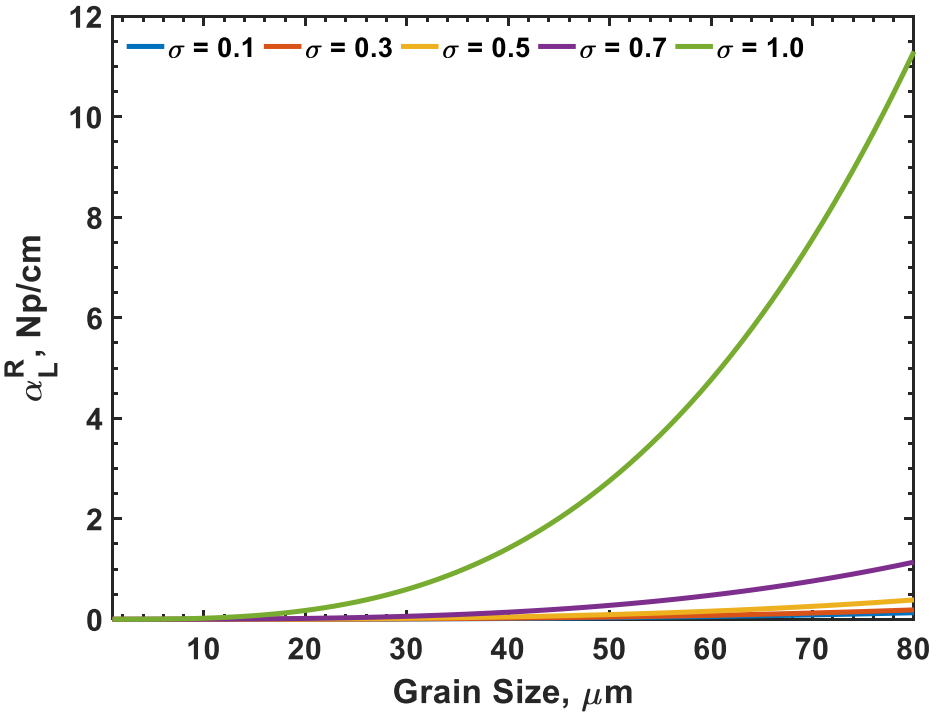

Fig. 6.6: Attenuation coefficients for different grain size distributions for an input monochromatic plane waves of frequency 5 MHz

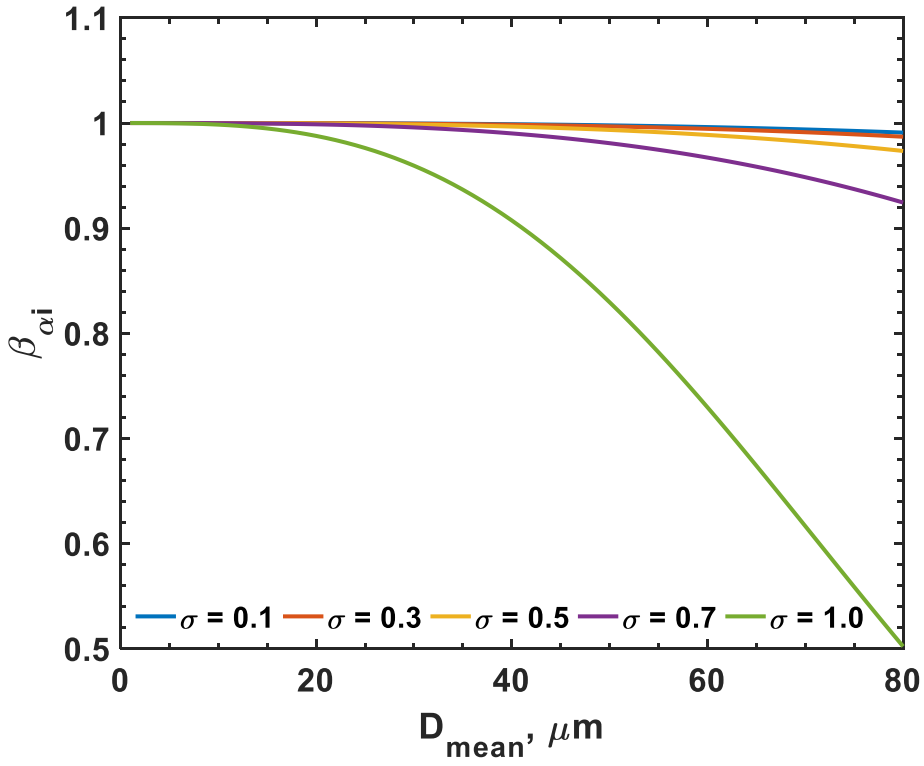

Fig. 6.7: β_{α_i} vs. D_{mean} for different grain size distributions for an input frequency of 5 MHz

varies as $D\omega^2$ which impose higher attenuation even if Rayleigh type of interactions occur. The histogram representation of grains contributing to the stochastic scattering of 10 MHz (D_{10}^{s}) and 15 MHz (D_{15}^{s}) components is superimposed on the total distribution (TD) and illustrated in Fig. 6.8. The volume fraction (V_{ω}^{s}) and the corresponding logarithmic mean (μ_{ω}^{s}) and distribution width (σ_{ω}^{s}) in each stochastic scattering regime is determined and tabulated in Table 6.2. These parameters decide the attenuation coefficients of the corresponding harmonic

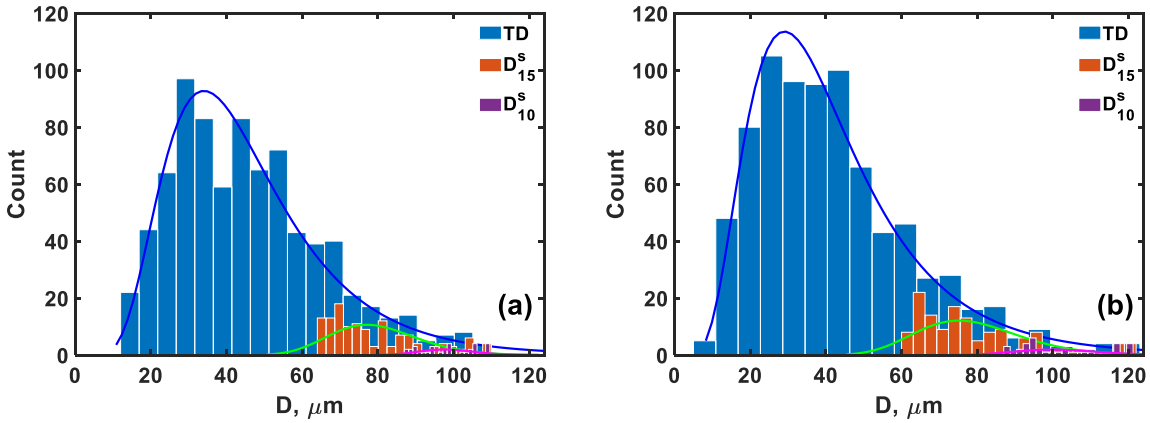

Fig. 6.8 Total grain size distribution (TD) superimposed with the distribution at the scattering regimes for 10 MHz (D_{10}^{s}) and 15 MHz (D_{15}^{s}) in specimens with (a) $\sigma = 0.45$ and (b) $\sigma = 0.52$

components. Higher the volume fraction (V_ω^s) and the applied frequency, higher will be the attenuation which results in $\alpha_{15\,MHz} > \alpha_{10\,MHz}$ leading to $A_{2\,(15\,MHz)} < A_{2\,(10\,MHz)}$. Consequently the β drops with an increase in the applied frequency.

Table 6.2: The grain distribution parameters contributing to the stochastic scattering of harmonic components

P_1	$\mu_{10.0}^s$	4.37	P_2	$\mu_{10.0}^s$	4.31
	$\sigma_{10.0}^s$	0.15		$\sigma_{10.0}^s$	0.19
	$V_{10.0}^s$	3.73		$V_{10.0}^s$	3.75
	$\mu_{15.0}^s$	4.59		$\mu_{15.0}^s$	4.62
	$\sigma_{15.0}^s$	0.07		$\sigma_{15.0}^s$	0.11
	$V_{15.0}^s$	16.50		$V_{15.0}^s$	19.65

The observed order in β ($\beta_{2.25} > \beta_{5.0} > \beta_{7.5}$) in Fig. 6.3 has a similarity with that shown in Fig. 6.9 where the β_{α_i} defined in Eq. (2.59) is plotted for the similar distribution widths and

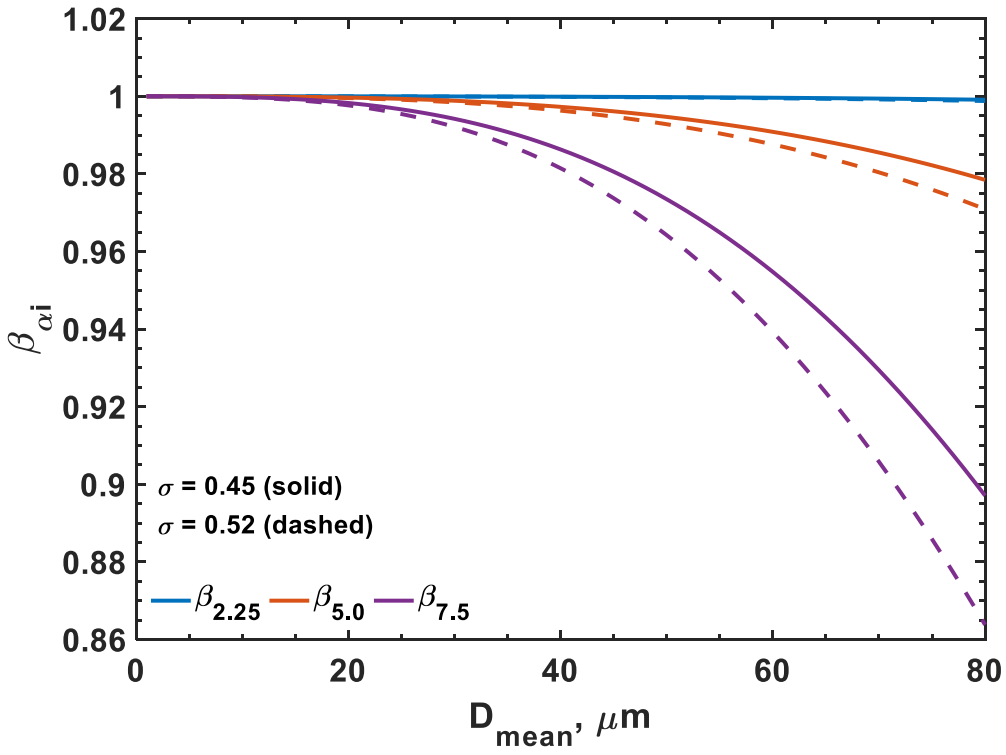

Fig. 6.9: Variation of β_{α_i} for three different frequencies and two grain size distributions

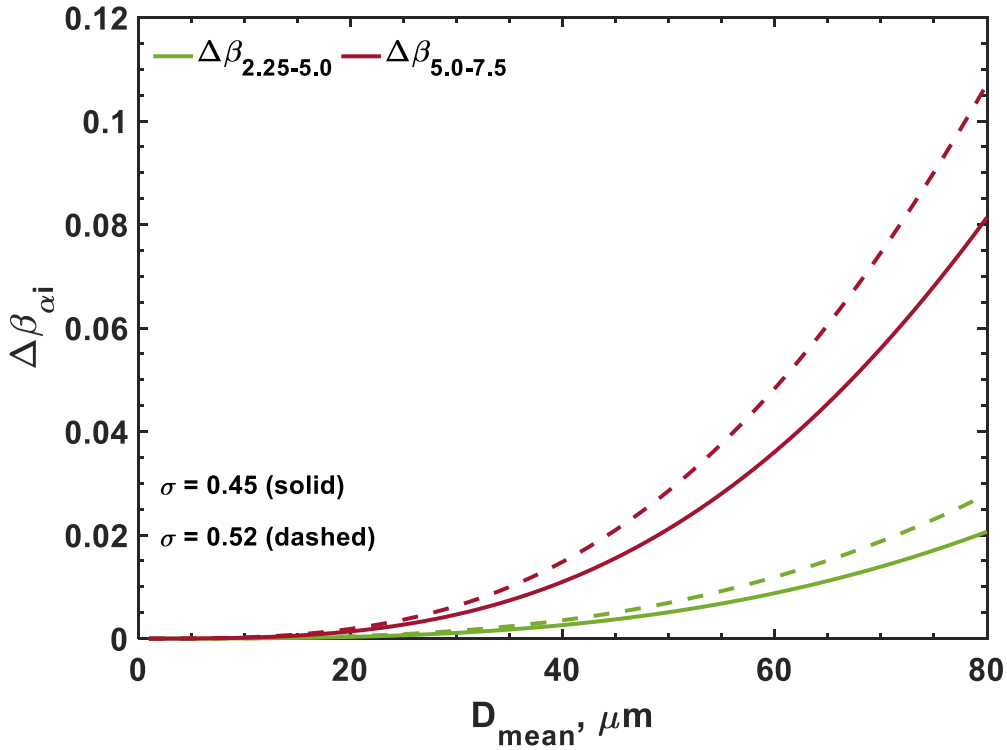

Fig. 6.10: $\Delta\beta_{\omega_{i,j}}$ against the mean grain size. A relation $\beta_{2.25} - \beta_{5.0} < \beta_{5.0} - \beta_{7.5}$ is exhibited which is a function of the grain size distribution, σ.

input frequencies. The difference in β with the applied frequency exhibits the relation $\beta_{2.25-5.00} < \beta_{5.0-7.5}$ similar to that observed from the numerical results plotted in Fig. 6.10. However, the difference between the experimental and the numerical results are expected which is attributed to the deviation in the distribution of grain size in P_1 and P_2 from an ideal lognormal distribution which is evident by comparing Fig. 6.2 with the Fig. 6.11.

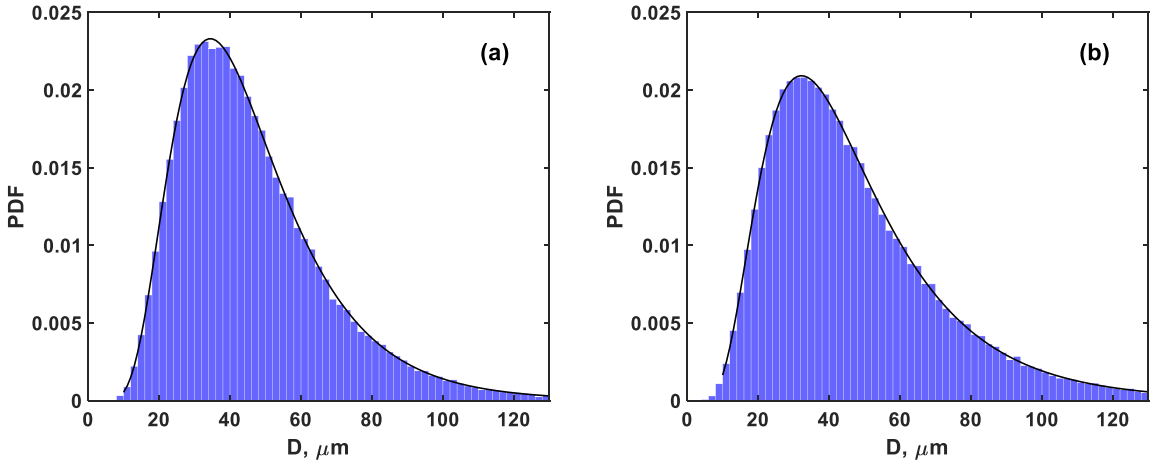

Fig. 6.11: Ideal lognormal distribution for (a) $D_{mean}^{P_1} = 3.7401\ \mu m$, $\sigma^{P_1} = 0.45$ and (b) $D_{mean}^{P_2} = 3.7375\ \mu m$, $\sigma^{P_2} = 0.52$

In summary, the results demonstrate that the grain size distribution has a considerable impact on the measured acoustic nonlinearity parameter. Although the results discussed here are in the context of the Rayleigh scattering regime, a similar influence of the distribution on β is expected for other scattering regimes also. Hence, deviation from the linear trend in β with grain growth observed in the annealed (Fig. 4.9) and forged microstructures (Fig. 5.13), can be accounted for the effect of grain size distribution on the measured acoustic nonlinearity parameter. Therefore, the distribution of grain size should be considered in order to interpret the findings correctly. This fact was not adequately addressed in literature while correlating the nonlinearity parameter and the grain size in copper[68] and stainless steel.[118]

The results in this chapter have industrial relevance. As the size of the component increases, grain size variation occurs across the thickness.[168] The manufacturing practices may also lead to the development of prior austenite grain size variations across the dimensions resulting in changes in mechanical properties.[165] The ultrasonic attenuation or velocity measurements are not effective in characterizing such changes. Though property variation can be evaluated with several destructive tests, such practices are costly and time-consuming and cannot be implemented on a finished product. In such cases, nonlinear ultrasonic testing would be an ideal choice due to its superior response towards the microstructural changes in contrast to the linear ultrasonic methods.[169] However, most research in nonlinear ultrasonics accounts for only the mean grain size when characterizing material degradation. These models need to be modified more comprehensively to include the role of grain size distribution which is crucial for reliable characterization of microstructural features that meet the design requirements.

6.4 Summary

The effect of grain size distribution on the acoustic nonlinearity parameter is investigated in this chapter. The numerical results were validated for two austenitic stainless-steel materials with similar mean grain sizes having distinct distribution widths. It was found that the material with a wider distribution exhibits reduced nonlinearity. Results demonstrated the significance of the distribution width in characterizing the microstructural features from the nonlinear response of the material. This observation is vital for accurate characterization of microstructure as the reliability of the nonlinear measurements depends heavily on the knowledge of the mean grain size as well as its distribution.

Chapter 7
Combined Effect of Grain Size and Plastic Deformation on Nonlinear Response

7.1 Introduction

It is quite possible in industries that the metallic components are supplied not always in solution annealed condition. Also, the fabrication processes like bending and forming may introduce deformation induced residual cold-work in the components. Further, in the case of austenitic stainless steel, cold working is widely employed to improve its strength. In prototype fast breeder reactor (PFBR), cold worked austenitic stainless steel components are used for reactor core applications because of the beneficial effects of cold working in improving the resistance to radiation-induced void swelling of the clad.[170] Hence it is appropriate to characterize such deformations effectively. The objective of the present chapter is, therefore, to explore how the nonlinearity parameter would be affected in the presence of not fully annealed or deformed microstructure that could be presented in a component. This understanding will help to consider the nonlinear ultrasonics as a potential nondestructive evaluation tool for inspection of the components primarily for the evaluation of the variations in grain size. Therefore, the combined effect of grain size and the plastic deformation is studied in this chapter using the nonlinear ultrasonics.

7.2 Materials and methods

Specimens with four different grain sizes were generated by annealing heat treatments as described in Section 3.2.4. Subsequently, a set of tensile specimens in each grain size were tested up to fracture to obtain the stress-strain properties. In each grain size, another set of specimens were deformed to the true strains of 0.33, 0.51 and 0.67. The acoustic nonlinearity parameter was measured in the gauge length of these deformed specimens using an input frequency of 5.0 MHz. This frequency was chosen in order to keep the mean grain size in all the specimens within the Rayleigh scattering regime for the fundamental frequency component.

Since the final thickness of the specimens is reduced to 7 mm after machining, duration of the sinusoidal input of 5.0 MHz was limited to eight-cycles.

7.3 Results and discussion

7.3.1 Microstructure

Fig. 7.1 shows the photomicrographs of the specimens in the annealed condition, which reveals that the grains are equiaxed. The grain size histograms given adjacent to the photomicrographs reveals the variation in grain size distribution with an increase in mean grain size. The mean grain size (D_{mean}) and the standard deviation (σ) are tabulated in Table 7.1.

Table 7.1: Heat treatment matrix and the grain size measurement

Specimen ID	K	L	R	S
Temperature (˚C)	1050	1050	1100	1150
Soaking Time (min)	30	60	60	60
$D_{mean}, \mu m$	81	97	131	183
$\sigma, \mu m$	37	45	63	96

7.3.2 The stress-strain curves

The engineering stress-strain curves and the true stress-strain curves of these annealed specimens are shown in Fig. 7.2 and Fig. 7.3, respectively. The strain exponential coefficients of the specimens K, L, R and S were measured to be 0.397, 0.381, 0.336 and 0.359 respectively.

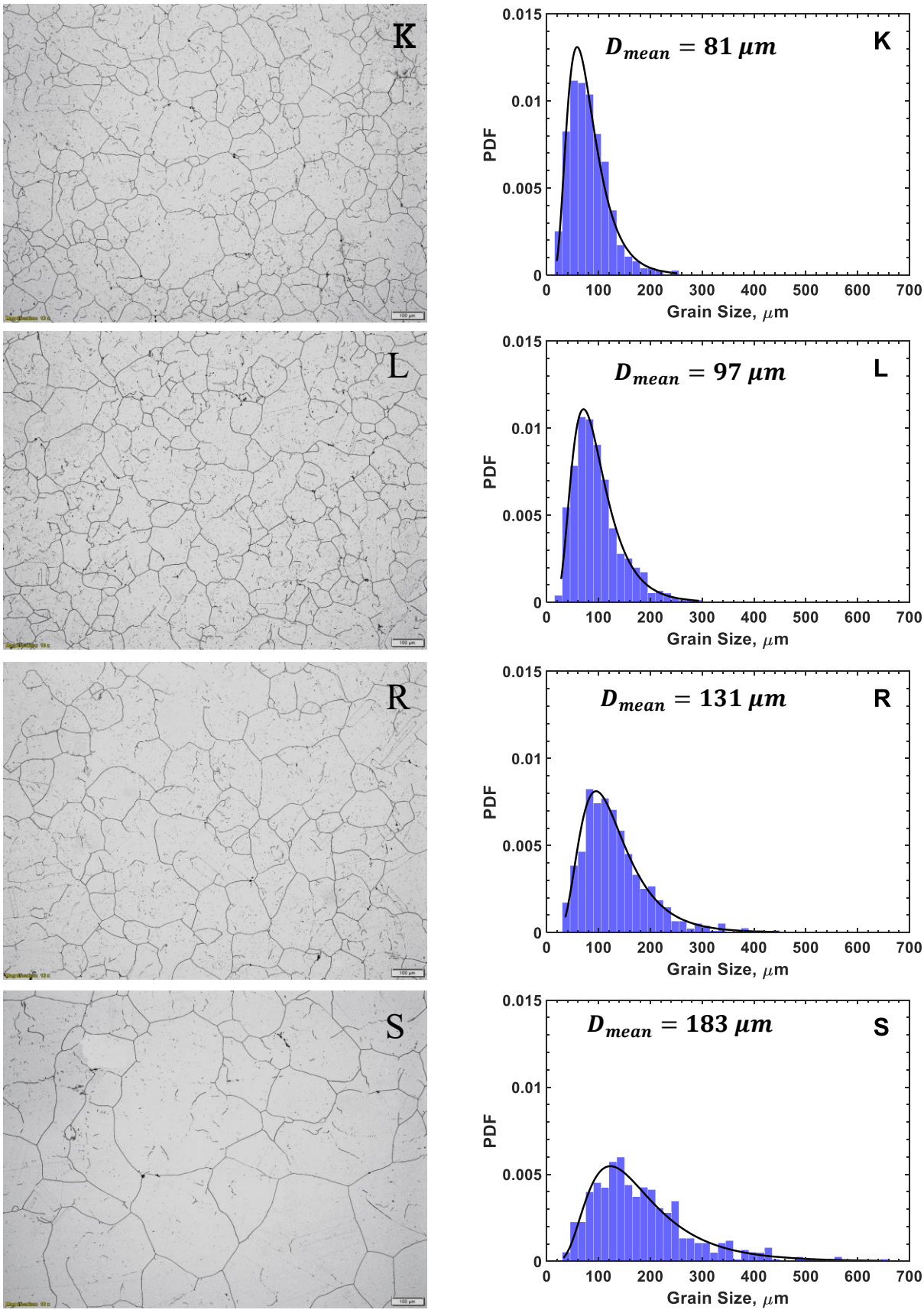

Fig. 7.1: Optical micrographs of the annealed specimens and the histogram representation of the grain size distribution. Scale in the micrographs is set to 100 μm.

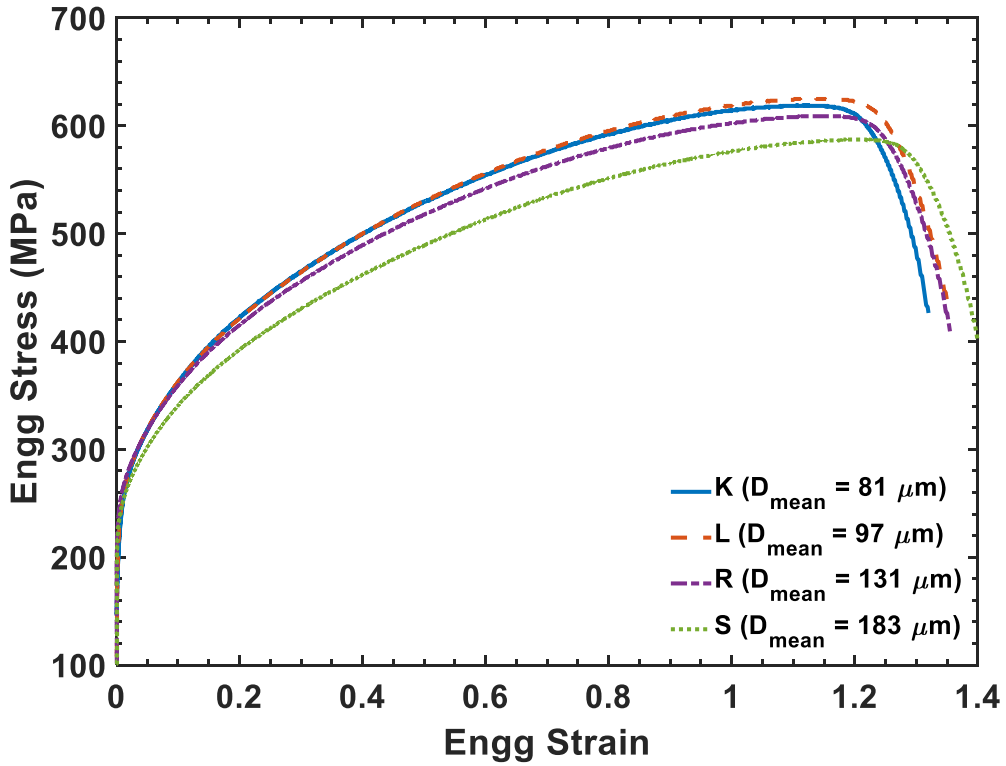

Fig. 7.2: Engineering stress-strain plots for the given annealed specimens

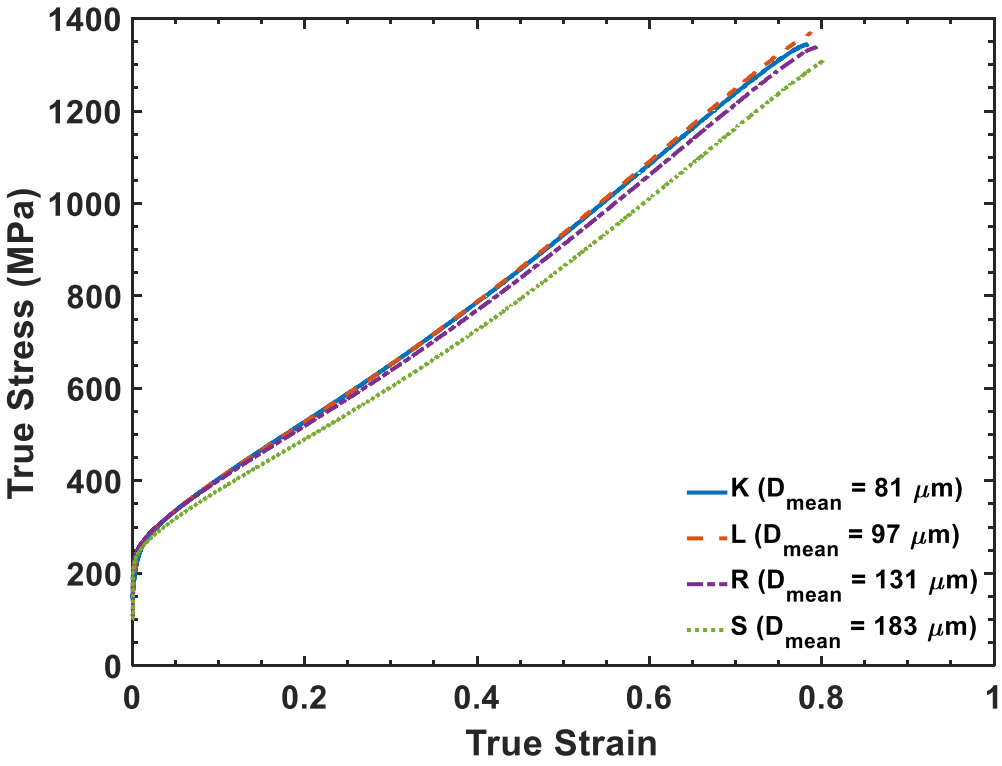

Fig. 7.3: True stress-strain plot for the given annealed specimens

7.3.3 Effect of strain on the polycrystalline grains

Photomicrographs obtained at the centre of the gauge length of the specimens deformed up to the strain levels of 0.33, 0.51 and 0.67 are shown in Fig. 7.4 to Fig. 7.7, in which the subscript denotes the true strain. In comparison to the microstructure of the annealed condition (Fig. 7.1), it is evident that the grains are elongated in the loading direction of the specimen. The deformation of the grains is represented in terms of their aspect ratio in Table 7.2. The histogram representation of the aspect ratio is shown adjacent to the photomicrographs. It is worth noting that the distribution of the aspect ratio is found to be lognormal. The standard deviation in the aspect ratio of the specimens in the annealed condition was minimal irrespective of the grain size, whereas it is substantial and inconsistent with deformation. Depending on the orientation of the grains with respect to the preferred crystallographic direction for deformation and the loading axis, there could be grain rotation as well as elongation during uniaxial tensile loading. The difference in the preferred crystallographic direction among the grains increased the standard deviation in the aspect ratio of the deformed grains. Further, this ratio depends on the initial dimension of the annealed grains and the applied strain.

Table 7.2: Mean aspect ratio (a/b) of the elongated grains and the standard deviation (σ)

True Strain	Specimen ID							
	K		L		R		S	
	a/b	σ	a/b	σ	a/b	σ	a/b	σ
Annealed	1.23	0.31	1.24	0.31	1.24	0.30	1.22	0.27
0.33	1.77	0.49	1.83	0.48	1.82	0.58	1.65	0.38
0.51	1.99	0.58	2.08	0.62	2.13	0.64	1.98	0.55
0.67	2.49	0.85	2.62	0.76	2.44	0.69	2.29	0.58

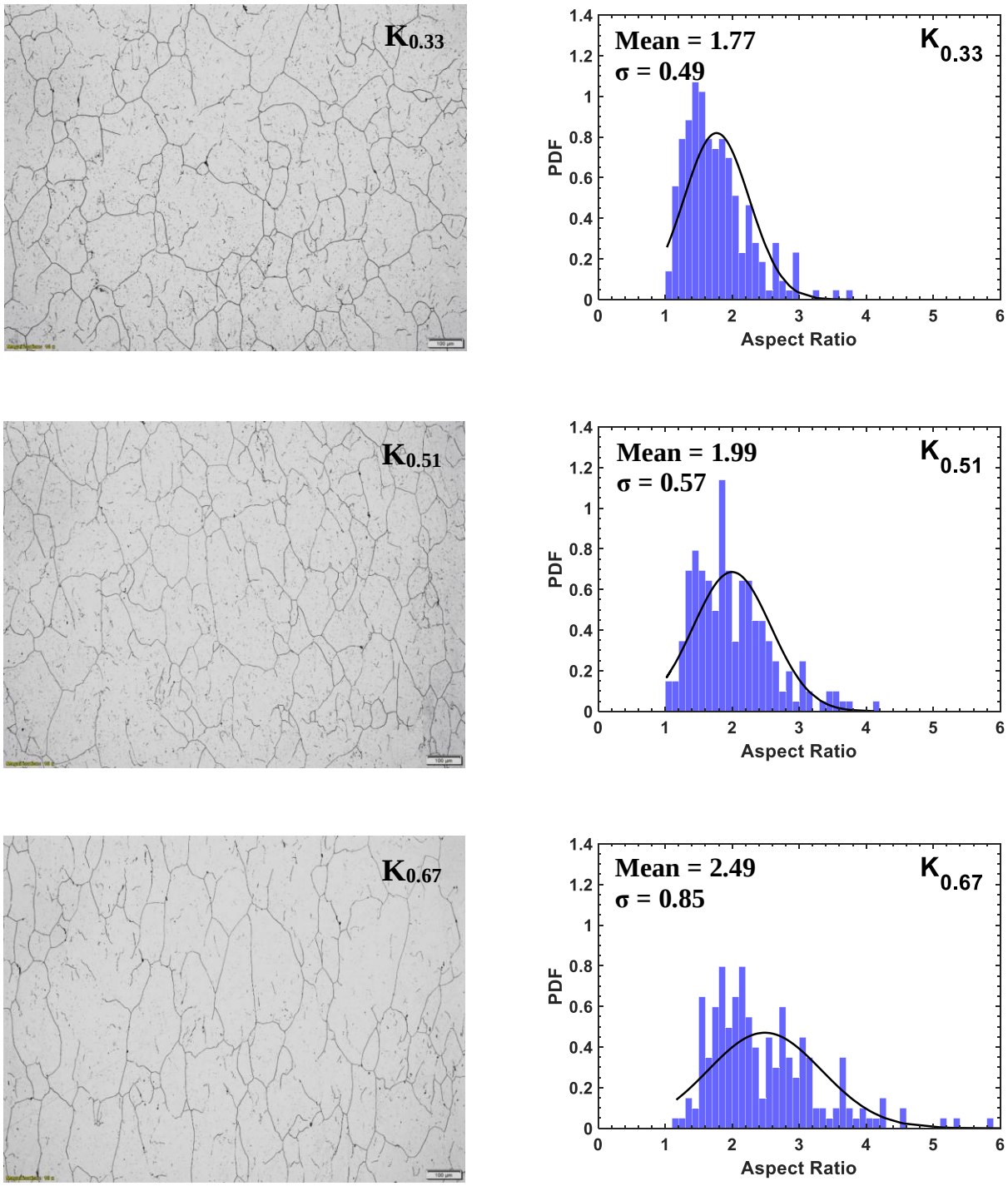

Fig. 7.4: Optical micrographs of the specimen K (D_{mean} = 81 μm) subjected to the true strain (a) 0.33, (b) 0.51 and (c) 0.67 and the corresponding distribution of the aspect ratio. Suffix represents the true strain.

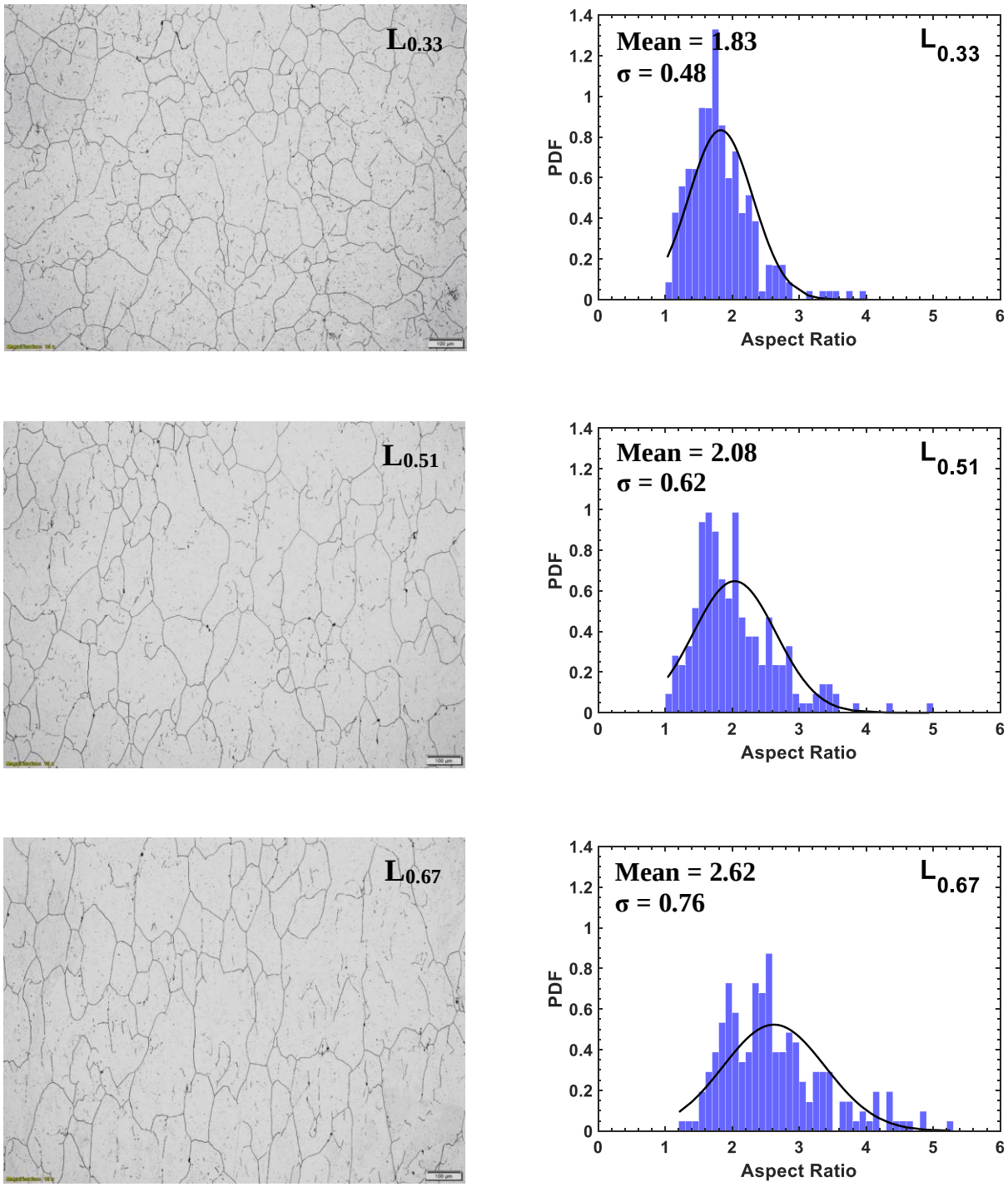

Fig. 7.5: Optical micrographs of the specimen L (D_{mean} = 97 μm) subjected to the true strain (a) 0.33, (b) 0.51 and (c) 0.67 and the corresponding distribution of the aspect ratio. Suffix represents the true strain.

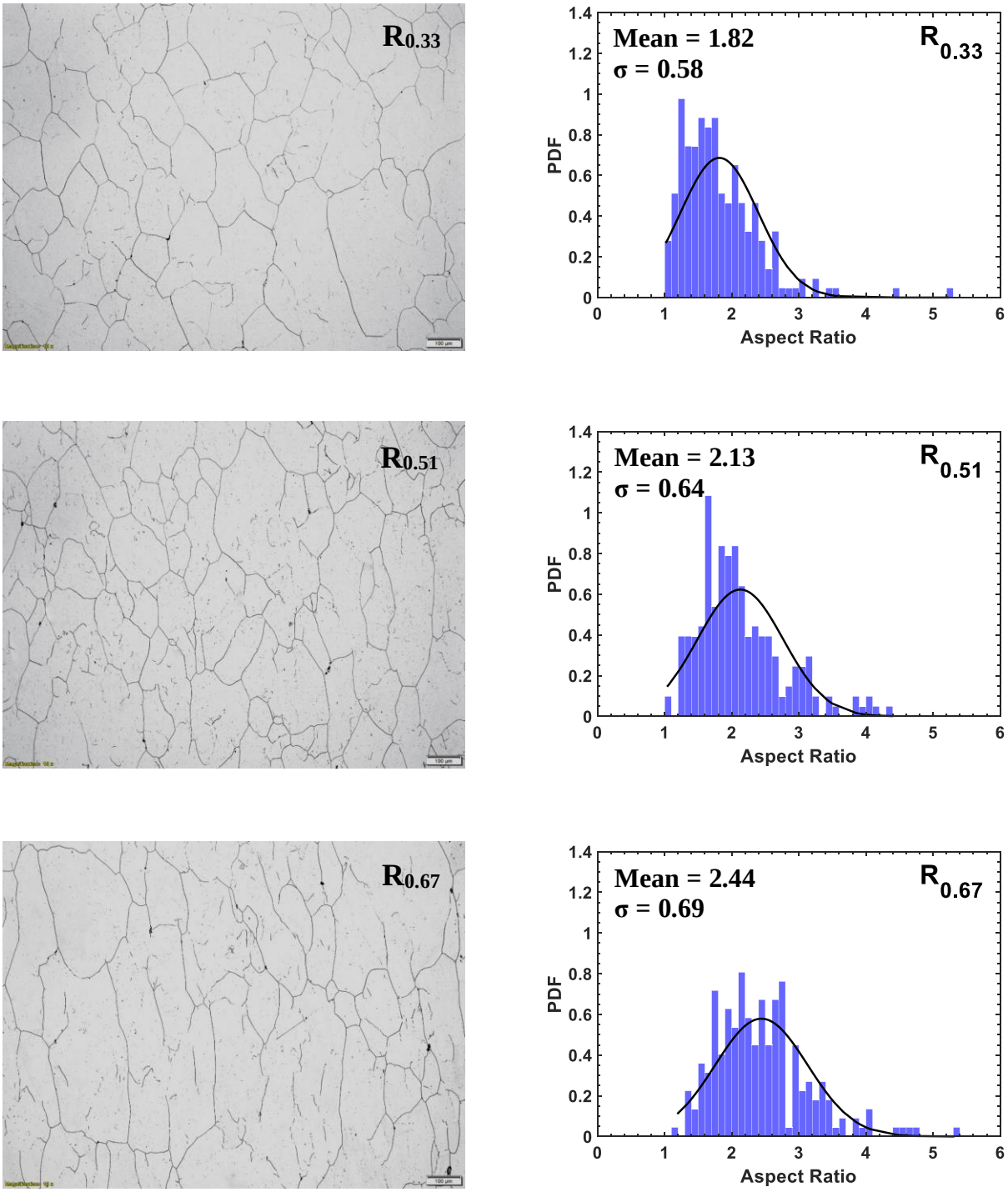

Fig. 7.6: Optical micrographs of the specimen R (D_{mean} = 131 μm) subjected to the true strain (a) 0.33, (b) 0.51 and (c) 0.67 and the corresponding distribution of the aspect ratio. Suffix represents the true strain.

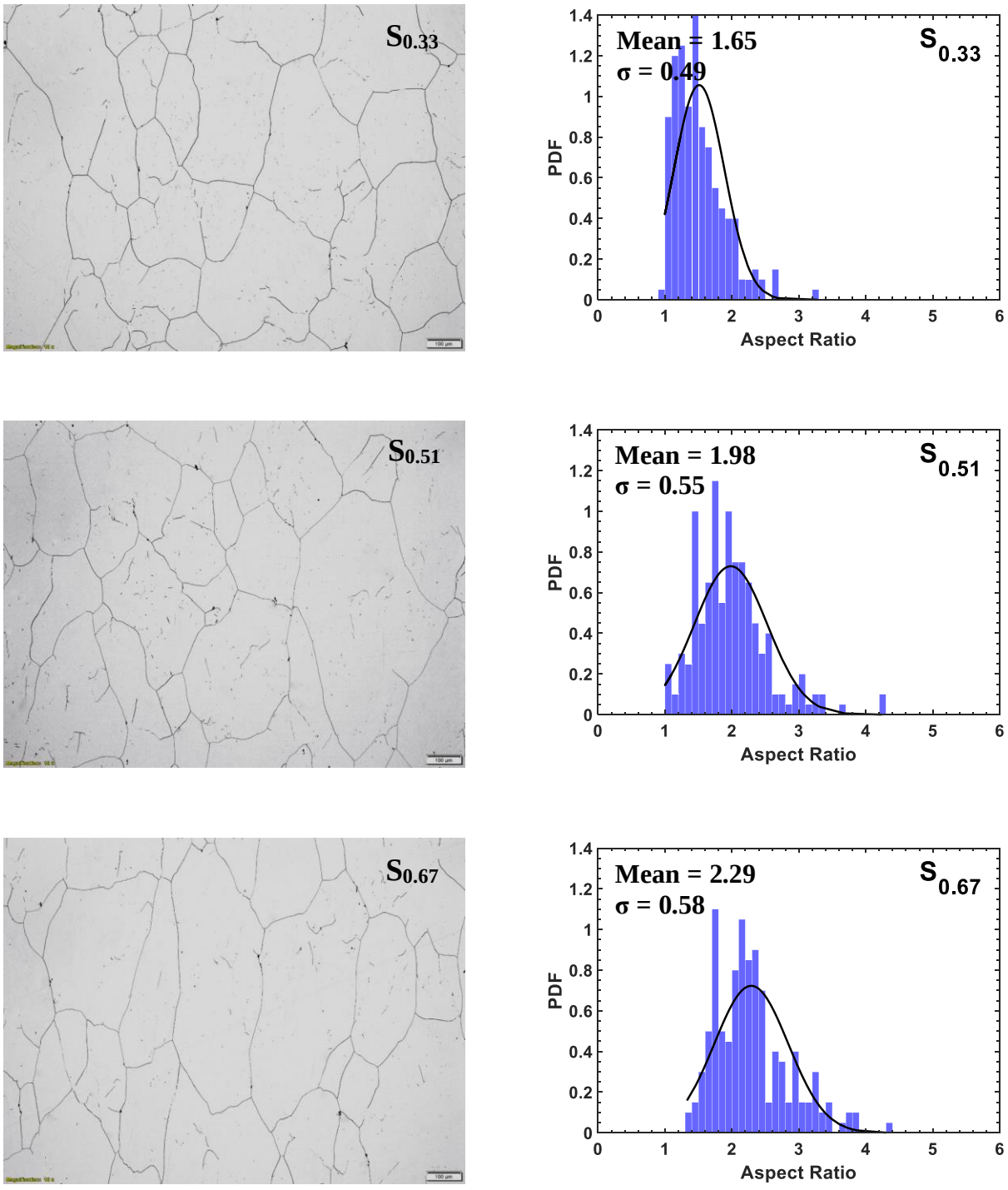

Fig. 7.7: Optical micrographs of the specimen S (D_{mean} = 183 μm) subjected to the true strain (a) 0.33, (b) 0.51 and (c) 0.67 and the corresponding distribution of the aspect ratio. Suffix represents the true strain.

7.3.4 The acoustic nonlinearity

The nonlinear response of the materials in the annealed and deformed conditions is calculated from the amplitude ratio of the fundamental to the harmonic components. The normalization was carried out separately for the annealed and deformed conditions with the β of the smallest grain size specimen (K, D_{mean} of 81 µm) obtained at the same condition. The results are plotted against the mean grain size in Fig. 7.8. This normalization process enables to visualize the relative change in β as a function of grain size and the applied strain. The percentage variation of β due to deformation, with respect to the annealed conditions, is plotted in Fig. 7.9. From Fig. 7.8 and Fig. 7.9 it can be inferred that

1. There is a significant increase in β from the solution annealed condition with the application of the plastic deformation. For example, the β has increased by 89%, 116%, 183% and 226% on the specimens with the D_{mean} of 81 µm, 97 µm, 131 µm and 183 µm respectively for a true strain of 0.67, whereas, the variation was found to be79%, 101%, 165% and 196% for the true strain 0.51 and 76%, 96% 145% and 161% for the true strain 0.33. The change in β is the maximum at the initial stages of the deformation.
2. The quadratic type variation of β with grain size observed for the annealed conditions is changed to linear with the deformation (Fig. 7.8),
3. The linear variation of β (for the specimens in the deformed condition) with grain size retains irrespective of the strain but with a change in their slope (Fig. 7.8), and
4. The percentage variation of β due to deformation is related to the strain and the grain size of the material (Fig. 7.9), which shows a quadratic behaviour with grain size.

The observed behaviour of the nonlinearity parameter can be explained based on the microstructural changes happened within the material during deformation. The acoustic nonlinearity in a deformed polycrystalline material originates from the grain boundaries, strain-induced phase changes and dislocations.[12] In general, the size of the grains do not vary during deformation except its aspect ratio, and hence, the grain boundary area after deformation would be the same as that of the annealed condition. Strain-induced martensite is common in stainless steels subjected to deformation.[171] However, in the present specimens, the martensite formation was negligible which has been ensured by magnetic Barkhausen emission (MBE) and ferrite number (FN) measurements. Absence of the martensite formation during deformation is due to the high stacking fault energy of the material used in this study (29.15 mJ/m^2) and

unfavourable strain rate and temperature. Therefore, change in the nonlinearity parameter observed in the deformed specimens is due to the strain-induced dislocations. Though the dislocation density on the deformed specimens was not measured, the results are validated from the data available in the literature. Viswanath et. al[12] have shown a considerable increase in the dislocation density with cold-work in AISI 304 austenitic stainless steel. Zhang et. al[80] have also shown a significant increase in dislocation density with plastic deformation in austenitic stainless steel. Though both authors have reported the formation of induced martensite during deformation, they have not mentioned about the SFE of their materials.

The hardness of a material is an indirect way of representing the dislocation density. Grace et al.[172] has shown that the dislocation density estimated from the hardness in Ni using the Nix-Gao model consistent with those obtained by transmission electron microscopy. Fig. 7.10 shows the variation of the acoustic nonlinearity parameter with hardness. The β showed a linear relationship to the hardness, and the consistency of the hardness with grain size was also maintained regardless of the strain applied. Therefore, it is reasonable to assume that the change in the acoustic nonlinearity parameter with deformation is directly related to the generation and

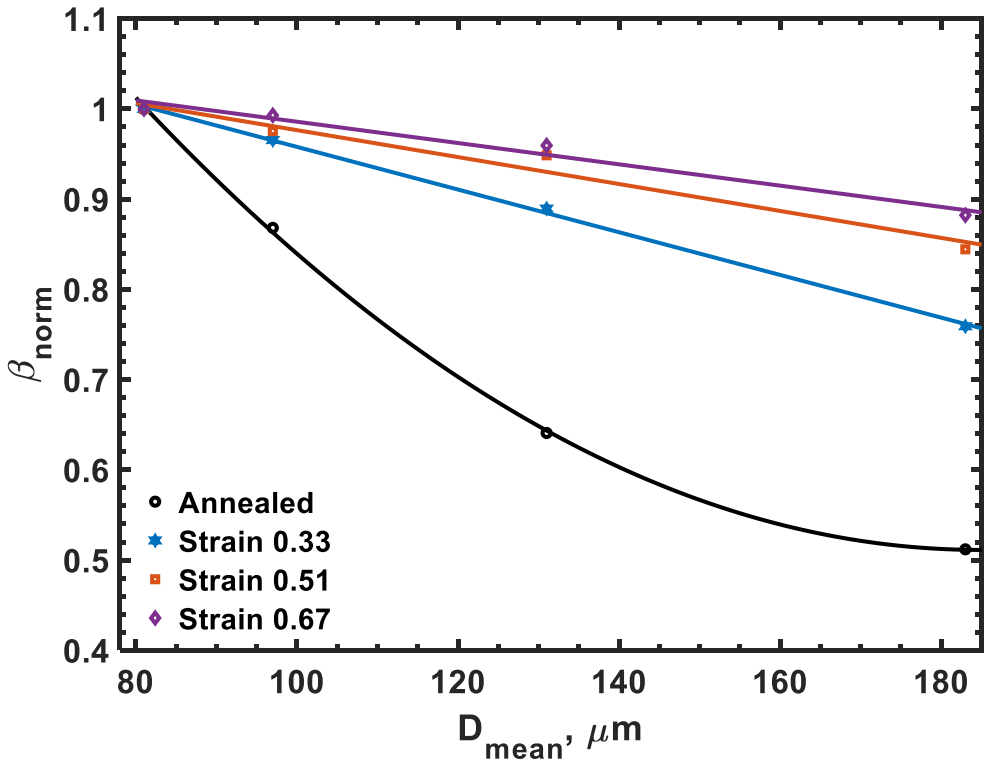

Fig. 7.8: Nonlinear response in the annealed and deformed conditions as a function of mean grain size.

accumulation of the dislocations in the matrix which in turn related to the grain size and the applied strain.

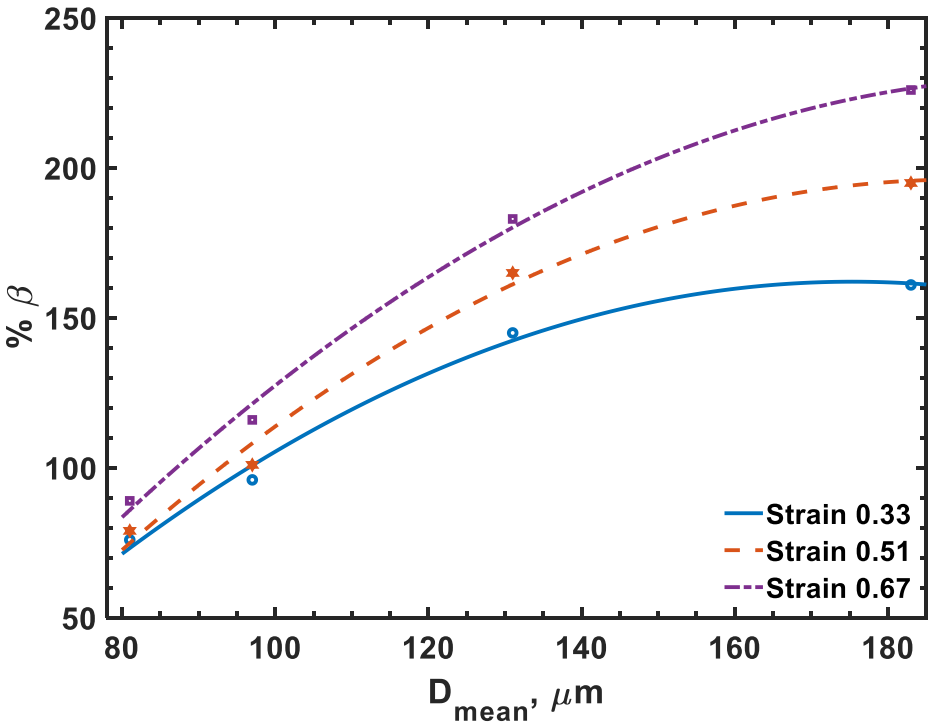

Fig. 7.9: Percentage variation of the nonlinearity parameter with respect to the annealed condition as a function of the applied strain

A significant increase in the nonlinearity parameter initially in Fig. 7.8 is due to the sudden generation of dislocations once the material in the unstrained condition is subjected to strain. The dislocations stored in the matrix contributes to the work hardening behaviour of the material. With increasing deformation, the dislocations lead to the formation of cell structures made of dislocation dipoles. During plastic deformation, the individual grains sub-divide into volume elements called cell blocks and separated by dense dislocation walls.[80,173] Zhang et. al[80] showed that the dislocation density was increased significantly with plastic strain. These authors have also reported the formation of dislocation cells and heavily tangled dislocations as well as shear bands with increasing strain. With an increase in plastic deformation, these cell blocks further sub-divided into cells to accommodate additional plastic deformation and the cell size shrinks and the number of cells increases. The cell boundaries are of high-density dislocations, whereas the cell interior is relatively free from dislocations. Schematic illustration of the dislocation cell structure is shown in Fig. 7.11. The mean free path for dislocation slip

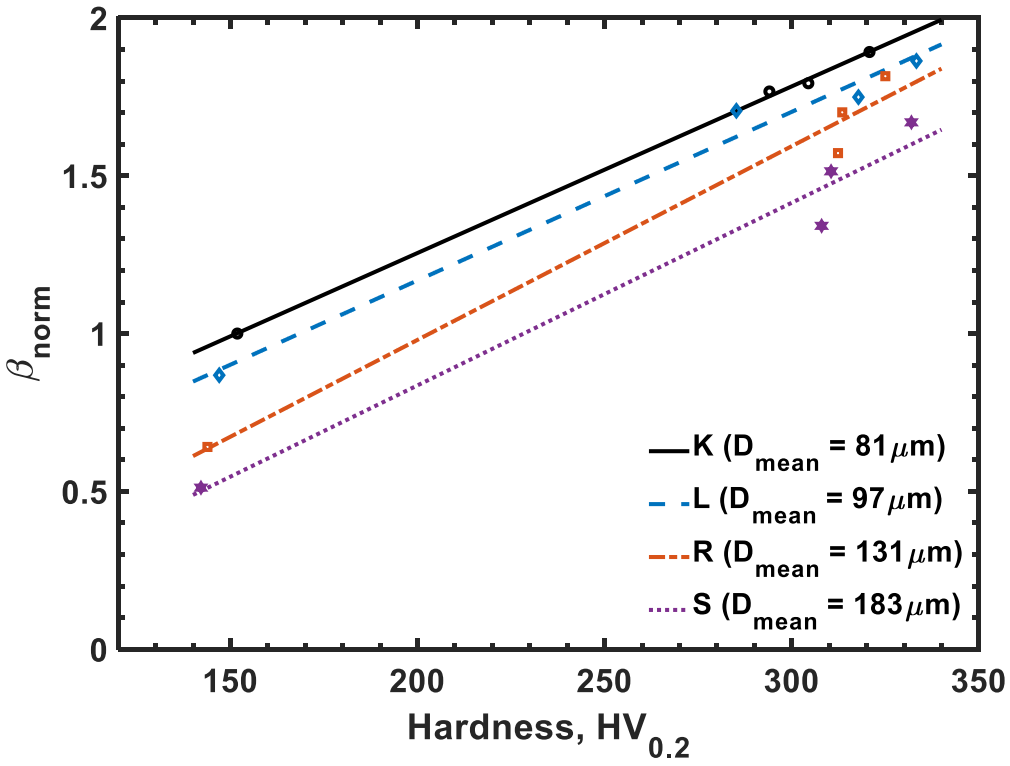

Fig. 7.10: The acoustic nonlinearity parameter vs. the hardness. Consistency in the hardness with grain size also maintained irrespective of the applied strain.

during deformation is proportional to the grain size at low dislocation density and to the sub-grain size at high densities. The increase in dislocation density during deformation is due to the mutual trapping of dislocations into low-energy cell walls. In the absence of deformation-induced martensite, the cell blocks and the dislocation walls determine the nonlinear response of the material.

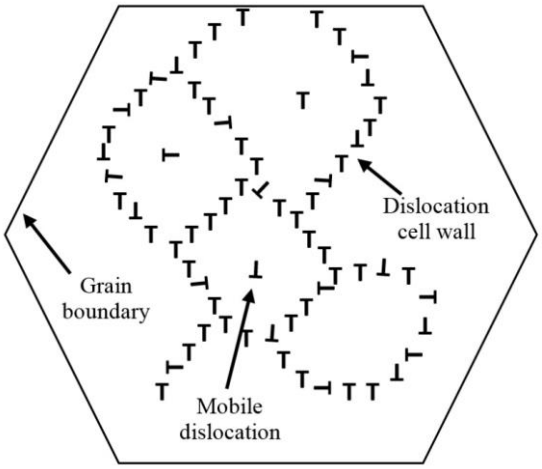

Fig. 7.11: Schematic illustration of dislocation cell structure within a prior austenite grain

The quadratic type behaviour of β observed in Fig. 7.8 at larger mean grain size (for the specimens in the annealed condition) is due to the presence of larger grains, as discussed in Chapter 4 and 5. Interestingly, this quadratic behaviour was lost after deformation and showed a linearly decreasing trend with grain size. A possible explanation to this behaviour is the formation of cell blocks as discussed above, which act as grain boundaries. Therefore, effective size of the scatterer is decreased and the probability of occurring stochastic interactions to the fundamental frequency component is reduced.

The difference in the change in β with strain presented in Fig. 7.9 is in contrast with the reported values of 168% increase[12] in β for a true strain of 0.38 and 77% increase[80] in β for a true strain of 0.4. The possible reasons for this difference could be (1) the initial grain size and its distribution, (2) initial state of the material, (3) deformation process, (4) cell size variations (5) attenuation of elastic waves at fundamental and harmonics frequencies and (6) thickness of the material. For example, cold rolling[12] of AISI 304 from 12 mm thickness to 6.5 mm thickness introduced different textures and more dislocations compared to the tensile deformation. Besides, Viswanath et. al[12] has reported a 13% volume fraction of induced martensite in the specimen with 38.5% true strain. Meanwhile, in the present study, the deformation-induced martensite was negligible. Also, the studies by Viswanath et. al[12] and Zhang et. al[80] were conducted on a single material and have not mentioned about the mean grain size and its distribution. The mean grain sizes of 81 μm, 97 μm, 131 μm and 183 μm used in the present study can be assumed to be larger than the grain sizes of the specimens used by these researchers. Therefore, a one-to-one comparative analysis with the present results is not possible at this stage. However, the changes in the acoustic nonlinearity parameter with the strain (Fig. 7.9) is qualitatively in line with the results reported in the literature. It is also worth noting from Fig. 7.8 that the nonlinearity parameter is sufficiently sensitive to the variations in grain size even though there exist deformation induced changes in the microstructure. Though we did not measure the cell structure in the present study, it reasonably assumes that for a given strain, deformation is more homogeneous in fine grain material compared to coarse grain material. This suggests that the cell structure would be finer in the material with smaller D_{mean} compared to the material with larger D_{mean}. Probably this could be the reason for change in β is the maximum at the initial stages of the deformation as seen in Fig. 7.8 and the divergence in β variation against the grain size observed in Fig. 7.9.

From the results and discussions presented above, it is clear that even in materials that have undergone plastic deformation or in materials that are not subjected to solution annealing treatment to remove the effect of prior deformation (like the materials supplied in as-rolled or as-forged condition), NLU can be used to study the grain size variations. However, variation in the nonlinearity parameter with grain size decreases in the presence of a deformed structure (Fig. 7.8). In this context, it may be noted that in the case of forgings F_1 and F_2, for which the variation in grain size across the diameter is studied and reported in Chapter 5, hardness value reported is higher than that is expected for solution annealed material indicating these forgings are supplied not in completely solution annealed condition. Yet, the nonlinear response was able to clearly reveal the grain size variation in these forgings. It is to be noted that in a finished product like forgings, pipe or plates, the deformation experienced would be more or less uniform and change in the nonlinear response would be mostly due to change in grain size. However, if there is localized deformation, as often occur in the fabrication of components, the nonlinearity parameter would vary at the location of this deformation. In fact, variations in the nonlinearity parameter can be used to have an estimate of the extent of such deformations undergone locally.

7.4 Summary

This chapter explored the combined effect of the grain size variation and plastic deformation on the acoustic nonlinearity parameter. The nonlinearity parameter is sufficiently sensitive to the variations in grain size even though there exist deformation-induced changes in the microstructure. This parameter was found changing linearly with the hardness which is closely linked to the increase in dislocation density with deformation. However, more investigations using other microscopic tools like transmission electron microscopy and X-ray diffraction is needed to understand such changes in the deformed materials. Also, a detailed investigation is required to extract the effect of texture, deformation-induced phase transformation and precipitates, if any, on the nonlinearity parameter which has not been encountered in the present study.

Chapter 8
Conclusions

8.1 Conclusions

This research work experimentally investigated the influence of the grain size distribution and the associated scattering regimes on the acoustic nonlinearity parameter. The combined effect of grain size variation and the plastic deformation on the polycrystalline materials also studied using nonlinear ultrasonics. To this end, the thesis explored the microstructural characterization on the annealed, forged and deformed microstructures of austenitic stainless steel material using the ultrasonic nonlinearity parameter. A novel multi-frequency nonlinear ultrasonic methodology is introduced in this thesis for a reliable characterization of the heterogeneous microstructures in polycrystalline materials.

The key findings this thesis has made are concluded below.

1. The acoustic nonlinearity parameter β was found reducing linearly with grain growth in the Rayleigh scattering regime and deviating from this linearity in the Rayleigh to stochastic transition zone. A reliable evaluation of grain size in polycrystalline materials using a single frequency measurement, therefore, requires the Rayleigh scattering condition to be satisfied so that the β would be independent of the scattering losses.
2. The multi-frequency approach reveals that the change in the order of β_{ω_i} or the deviation in $\Delta\beta_{\omega_{i,j}}$ with grain coarsening can be used as a precursor for undesired grain growth in polycrystalline materials. For a set of input frequencies (ω_i), these changes indicate that the mean grain size has deviated from the Rayleigh scattering regime corresponding to those frequencies. This approach can be employed as an efficient tool for rapid screening of materials with unknown process history where wide variations and distributions of grain sizes are expected. The frequencies can be chosen such that the event at which the nonlinearity parameter deviates from its linear trend may be set as the boundary where the grain size-dependent properties are extinct. Hence, this methodology can be brought out as a stand-alone technique to be deployed to characterize the microstructural variations.

3. The results further infer that the conventional single-frequency NLU measurement would not be reliable against the grain size variation or distribution as the multi-frequency approach is required to observe the changes in the linear trend of β_{ω_i} and changes in the order of β_{ω_i} and thereby the deviation in the $\Delta\beta_{\omega_{i,j}}$ with grain coarsening. The multi-frequency NLU methodology has a reasonable correlation with the microstructure, and its reliability was evaluated against the heterogeneous microstructure in large diameter forgings.
4. A study on the effect of grain size distribution on the acoustic nonlinearity parameter has revealed that the material with wide distribution exhibited reduced nonlinearity. The result infers the significance of considering the distribution width in characterizing the microstructural features from the nonlinear response of the material. Though the results discussed here are in the context of the Rayleigh scattering regime, a similar influence of the distribution on β is expected for other scattering regimes also.
5. The nonlinearity parameter is very sensitive to the variations in grain size, even in the presence of deformed microstructure. Hence, nonlinear ultrasonics is an efficient tool for characterizing the combined effect of grain size variations and plastic deformation in metallic materials.

From the present research, it is understood that the role of grain size distributions and thereby the scattering regimes need to be considered while interpreting the results based on the measured acoustic nonlinearity parameters in single-phase polycrystalline materials. This understanding is vital for reliable characterization of microstructural features and to enhance the consistency in structure-property correlations using nonlinear ultrasonics. The results obtained in this thesis infer that, the multi-frequency approach can be used as a reliable tool to

1. Measure the grain size in a polycrystalline material
2. Evaluate the grain size distribution and heterogeneity in the microstructure
3. Assess the effect of deformation in polycrystalline structural materials.

These understandings are very important in solving the inverse problems in nonlinear ultrasonics, leading to a non-destructive evaluation method of polycrystalline materials with a minimum of a priori information.

Chapter 9
Future Works

9.1 Scope for future work

Several directions may be explored to extend the findings in this thesis. Some of them are briefed below.

9.1.1 Need for modelling studies

It was experimentally observed that, there exist a relationship between the β_{ω_i}, $\Delta\beta_{\omega_{i,j}}$, D_{mean} and σ_D which can be used to characterize the microstructure evolution. Though the findings in this thesis were based solely on the experimental measurements, a generalized approach cannot be drawn out of these results as, for example, similar heat treatment may cause difference in the D_{mean} and σ_D. This is because of the differences in the kinetics of grain growth which in fact depends on chemical composition as well as the annealing conditions.[174]

There exists considerable deviation in the experimentally measured grain size distribution from an ideal lognormal distribution curve. For example, measured grain size distributions in specimen **A** (D_{mean} = 3.71, σ = 0.40) and specimen **I** (D_{mean} = 5.74, σ = 0.63) mentioned in Chapter 4 which are being superposed with the lognormal distribution curves are compared with that of the ideal distribution in Fig. 9.1. Careful observation of Fig. 9.1 shows that the fitted lognormal distribution function did not envelope the real distribution of grain sizes completely. Such differences in the distribution of grain size will vary with the kinetics of grain growth and hence influence the nonlinearity parameter considerably. Consequently, the β_{ω_i} and $\Delta\beta_{\omega_{i,j}}$ observed in the experimental curves of Fig. 4.9 may not always be accurate to predict the microstructural evolution during annealing process in polycrystalline single-phase materials though the trend is to remain the same. A similar argument is valid for the experimental curves obtained in Fig. 5.13, Fig. 5.15 and Fig. 5.16 for the forged microstructures. Such facts should be addressed more systematically through rigorous modelling studies generating ideal curves connecting different combinations of D_{mean} and σ_D to the β_{ω_i}. However, the difference between the experimental and the numerical results reported in Chapter 6 are expected and is attributed to the deviation in the distribution of grain

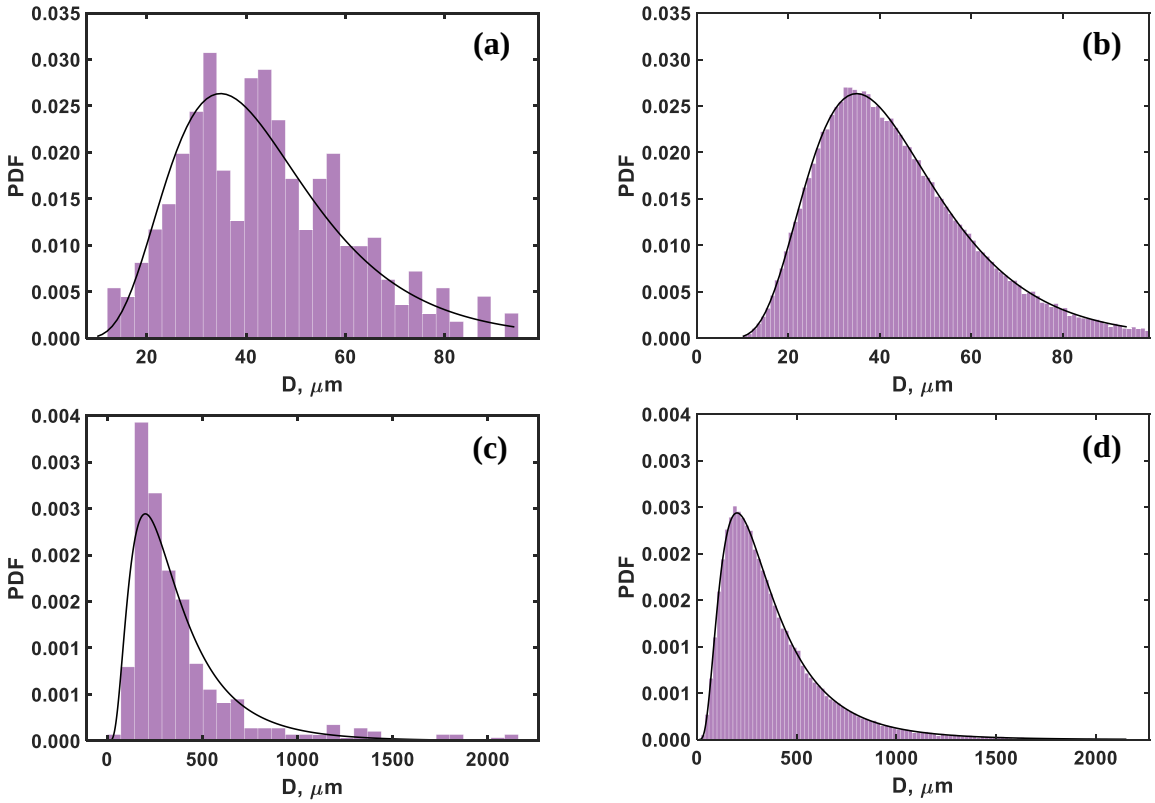

Fig. 9.1: (a) Experimental and (b) theoretical grain size distribution for specimens with D_{mean} = 3.71, σ = 0.40 and (c & d) for specimens with D_{mean} = 5.74, σ = 0.63

size from the perfect lognormal distribution which is evident by comparing Fig. 6.2 with Fig. 6.11.

9.1.2 Effect of scattering from defects on the measured β

The investigations on the effect of scattering regimes on the acoustic nonlinearity parameter revealed a novel methodology in the characterization of microstructure. However, the investigations were limited to the grain boundary scattering and the associated changes in the nonlinearity parameter. Since the scattering related attenuation to the fundamental and harmonic components depends on the size of the scatterer and the wavelength, a similar analysis may be extended to the characterization of micro cracks, inclusions and porosity in structural materials. These defects are strong scatterers to the elastic waves used in the ultrasonic testing and hence their effect on the acoustic nonlinearity parameter should be studied in detail for establishing reliable structure-property correlations.

9.1.3 Effect of the sub-grains on the measured β

In this thesis, the grain size was measured from the optical micrographs in which the grain boundaries with high misorientation angle (> 10°) are visible during electrochemical etching. Though the analysis has given a good correlation with the microstructure, the grains are also divided into recrystallized and deformed grains with a mean disorientation angle < 3° and < 1°, respectively. A study that considers such low-angle grain boundaries would enhance the understanding of microstructural properties based on the nonlinear response. The combination of EBSD studies of the evolved sub-grains provides good opportunities to expand the knowledge of this relation.

9.1.4 Solving inverse problems of nonlinear ultrasonics

Inverse problems are the ultimate resolution to imply any nondestructive evaluation method with a minimum of a priori information. Though the multi-frequency nonlinear ultrasonics has found to be a reliable tool in characterizing grain size variation and their distribution in polycrystalline materials, inverse problems are of prime interest in the industry to characterize the grains. Nonlinear inverse problems constitute an inherently more difficult family of inverse problems, and, to this end, the development of a forward model is needed as a first step. Such an attempt is indeed necessary for creating models to predict the abnormal grain growth in polycrystalline materials reliably. However, this direction remains underdeveloped.

9.1.5 Collinear wave mixing for inspection of large diameter forgings

It is apparent that the multi-frequency nonlinear ultrasonic measurements are more precise and comprehensive in monitoring heterogeneous grain size variations in large diameter forgings. However, detaching a strip of material with the required surface finish and plane parallelism for ultrasonic measurements would be difficult, non-economic and time-consuming during production stages in industries. In such cases, a nonlinear wave-mixing methodology can be well adapted. The nonlinear wave-mixing method is based on the principle of three-phonon interactions.[175] During such interactions, the law of conservation of energy

$$\omega_1 \pm \omega_2 \leftrightarrow \omega_3 \tag{9.1}$$

and, momentum

$$k_1 \pm k_2 \leftrightarrow k_3 \tag{9.2}$$

of phonons are satisfied. These conservation laws demand favourable angle of incidents, wave modes and the frequencies to perform the wave mixing.[146,147,176] A schematic representation of the proposed non-collinear wave-mixing method, which can be implemented on large diameter forgings during production and processing stages is depicted in Fig. 9.2. Transducers (T_1 & T_2) for sending the ultrasonic waves into the component and a transducer (R) to receive the resultant interactions are aligned in such a way that the resonant wave generated at the sum and difference frequencies of the interacting waves in the region of interest reaches the receiver. Nevertheless, the region of intersection can be altered by moving the transducers as indicated by the arrows, thereby a quantitative scanning of the component is possible. This methodology has implication in the inspection of bigger forgings which are being used for the fabrication of critical components in power and automobile industries.

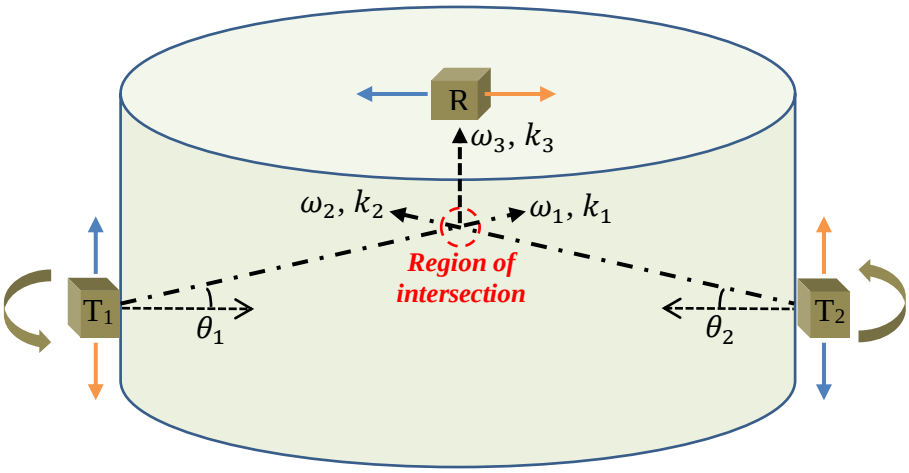

Fig. 9.2: Schematic of the proposed non-collinear wave mixing method for inspection of cylindrical forgings during different stages of manufacturing

Never give up on a dream just because of the time it will take to accomplish it. The time will pass anyway.

- *Earl Nightingale*

References

1. Hall, E. O. The Deformation and Ageing of Mild Steel: II Characteristics of the Luders Deformation. in *Proceedings of the Physical Society. Section B* **64**, 742–747 (1951).

2. Petch, N. J. The cleavage strength of polycrystals. *J. Iron Steel Inst.* **174**, 25–28 (1953).

3. Núñez, C. & Domingo, S. Statistical considerations on uniform grain size. *Metall. Trans. A* **19**, 2937–2944 (1988).

4. Day, A. P. & Quested, T. E. A comparison of grain imaging and measurement using horizontal orientation and colour orientation contrast imaging, electron backscatter pattern and optical methods. *J. Microsc.* **195**, 186–196 (1999).

5. Nagy, P. B. Fatigue damage assessment by nonlinear ultrasonic materials characterization. *Ultrasonics* **36**, 375–381 (1998).

6. Cantrell, J. H. Dependence of microelastic-plastic nonlinearity of martensitic stainless steel on fatigue damage accumulation. *J. Appl. Phys.* **100**, 063508 (2006).

7. Kumar, A., Adharapurapu, R. R., Jones, J. W. & Pollock, T. M. In situ damage assessment in a cast magnesium alloy during very high cycle fatigue. *Scr. Mater.* **64**, 65–68 (2011).

8. Baby, S. *et al.* Creep damage assessment in titanium alloy using a nonlinear ultrasonic technique. *Scr. Mater.* **59**, 818–821 (2008).

9. Valluri, J. S., Balasubramaniam, K. & Prakash, R. V. Creep damage characterization using non-linear ultrasonic techniques. *Acta Mater.* **58**, 2079–2090 (2010).

10. Metya, A., Ghosh, M., Parida, N. & Palit Sagar, S. Higher harmonic analysis of ultrasonic signal for ageing behaviour study of C-250 grade maraging steel. *NDT E Int.* **41**, 484–489 (2008).

11. Viswanath, A., Rao, B. P. C., Mahadevan, S., Jayakumar, T. & Baldev Raj. Microstructural characterization of M250 grade maraging steel using nonlinear ultrasonic technique. *J. Mater. Sci.* **45**, 6719–6726 (2010).

12. Viswanath, A. *et al.* Nondestructive assessment of tensile properties of cold worked AISI type 304 stainless steel using nonlinear ultrasonic technique. *J. Mater. Process. Technol.* **211**, 538–544 (2011).

13. Ruiz, A., Ortiz, N., Medina, A., Kim, J. Y. & Jacobs, L. J. Application of ultrasonic methods for early detection of thermal damage in 2205 duplex stainless steel. *NDT E Int.* **54**, 19–26 (2013).

14. Matlack, K. H. *et al.* Evaluation of radiation damage using nonlinear ultrasound. *J. Appl. Phys.* **111**, 203–206 (2012).

15. Xiang, Y., Deng, M., Xuan, F.-Z. Z. & Liu, C.-J. J. Experimental study of thermal degradation in ferritic Cr–Ni alloy steel plates using nonlinear Lamb waves. *NDT E Int.* **44**, 768–774 (2011).

16. Abraham, S. T. *et al.* Assessment of sensitization in AISI 304 stainless steel by nonlinear ultrasonic method. *Acta Metall. Sin. (English Lett.* **26**, 545–552 (2013).

17. Cantrell, J. H. & Yost, W. T. Determination of precipitate nucleation and growth rates from ultrasonic harmonic generation. *Appl. Phys. Lett.* **77**, 1952–1954 (2000).

18. Mondal, C., Mukhopadhyay, A. & Sarkar, R. A study on precipitation characteristics induced strength variation by nonlinear ultrasonic parameter. *J. Appl. Phys.* **108**, (2010).

19. Hikata, A., Chick, B. B. & Elbaum, C. Dislocation contribution to the second harmonic generation of ultrasonic waves. *J. Appl. Phys.* **36**, 229–236 (1965).

20. Cash, W. D. & Cai, W. Dislocation contribution to acoustic nonlinearity: The effect of orientation-dependent line energy. *J. Appl. Phys.* **109**, 014915 (2011).

21. Lee, T. H. & Jhang, K. Y. Experimental investigation of nonlinear acoustic effect at crack. *NDT E Int.* **42**, 757–764 (2009).

22. Jiao, J. *et al.* Micro-crack detection using a collinear wave mixing technique. *NDT E Int.* **62**, 122–129 (2014).

23. Papadakis, E. P. Ultrasonic Attenuation Caused by Scattering in Polycrystalline Metals. *J. Acoust. Soc. Am.* **37**, 711–717 (1965).

24. Jeong, H., Barnard, D., Cho, S., Zhang, S. & Li, X. Receiver calibration and the nonlinearity parameter measurement of thick solid samples with diffraction and attenuation corrections. *Ultrasonics* **81**, 147–157 (2017).

25. Li, W. *et al.* Characterization of microstructural evolution by ultrasonic nonlinear parameters adjusted by attenuation factor. *Metals (Basel).* **9**, 271 (2019).

26. Zhang, S., Jeong, H., Cho, S. & Li, X. Simultaneous evaluation of acoustic nonlinearity parameter and attenuation coefficients using the finite amplitude method. *AIP Adv.* **5**, (2015).

27. Allan Kupcis, O. Detection, Sizing and Monitoring of Defects by Nondestructive Evaluation: An Overview. *Can. Metall. Q.* **19**, 23–34 (1980).

28. Felice, M. V & Fan, Z. Sizing of flaws using ultrasonic bulk wave testing: A review. *Ultrasonics* **88**, 26–42 (2018).

29. Doyle, P. A. & Scala, C. M. Crack depth measurement by ultrasonics: a review. *Ultrasonics* **16**, 164–170 (1978).

30. Zimmer, A. *et al.* Evolution of the ultrasonic inspection of heavy rotor forgings over the last decades. *AIP Conf. Proc.* **1211**, 1631–1638 (2010).

31. Ricci, M. *et al.* Pulse-compression ultrasonic technique for the inspection of forged steel with high attenuation. *Insight Non-Destructive Test. Cond. Monit.* **54**, 91–95 (2012).

32. Senni, L., Battaglini, L., Burrascano, P., Laureti, S. & Ricci, M. Industrial Applications: Ultrasonic Inspection of Large Forgings. in *Ultrasonic Nondestructive Evaluation Systems* 245–258 (Springer International Publishing, 2015). doi:10.1007/978-3-319-10566-6_9

33. Fendt, K. T., Mooshofer, H., Rupitsch, S. J. & Ermert, H. Ultrasonic Defect Characterization in Heavy Rotor Forgings by Means of the Synthetic Aperture Focusing Technique and Optimization Methods. *IEEE Trans. Ultrason. Ferroelectr. Freq. Control* **63**, 874–885 (2016).

34. Drinkwater, B. W. & Wilcox, P. D. Ultrasonic arrays for non-destructive evaluation: A review. *NDT E Int.* **39**, 525–541 (2006).

35. Dupont-Marillia, F., Jahazi, M., Lafreniere, S. & Belanger, P. Design and optimisation of a phased array transducer for ultrasonic inspection of large forged steel ingots. *NDT E Int.* **103**, 119–129 (2019).

36. Alavudeen, S. *et al.* Improved Imaging of Fatigue Crack Profile in Thick Cruciform Samples Using Ultrasonic Phased Array Models. *J. Press. Vessel Technol.* **132**, (2010).

37. Baskaran, G., Balasubramaniam, K. & Krishnamurthy, C. V. Inspection Using Shear

Wave Time of Flight Diffraction (S-TOFD) Technique. in *AIP Conference Proceedings* **820**, 97–102 (AIP, 2006).

38. Nath, S. K., Balasubramaniam, K., Krishnamurthy, C. V. & Narayana, B. H. Detection and Sizing of Defects in Complex Geometry Weld by Manual Ultrasonic Time of Flight Diffraction Inspection. *J. Press. Vessel Technol.* **131**, (2009).

39. Abraham, S. T., Venkatraman, B., Raj, B. & Chetal, S. C. Application of TOFD Technique for Imaging Crack in Rod Specimens. *Mater. Eval.* **71**, 411–419 (2013).

40. Subbaratnam, R., Abraham, S. T., Menaka, M., Venkatraman, B. & Raj, B. Time of flight diffraction testing of austenitic stailess steel weldments at elevated temperatures. *Mater. Eval.* 332–337 (2007).

41. Palanichamy, P., Joseph, A., Jayakumar, T. & Raj, B. Ultrasonic velocity measurements for estimation of grain size in austenitic stainless steel. *NDT E Int.* **28**, 179–185 (1995).

42. Vasudevan, M. & Palanichamy, P. Characterization of microstructural changes during annealing of cold worked austenitic stainless steel using ultrasonic velocity measurements and correlation with mechanical properties. *J. Mater. Eng. Perform.* **11**, 169–179 (2002).

43. Dupont-Marillia, F., Jahazi, M. M., Lafreniere, S. & Belanger, P. Influence of Local Mechanical Parameters on Ultrasonic Wave Propagation in Large Forged Steel Ingots. *J. Nondestruct. Eval.* **38**, 73 (2019).

44. Wiskel, J. B., Kennedy, J., Ivey, D. G. & Henein, H. Ultrasonic Velocity and Attenuation Measurements in L80 Steel and their Correlation with Tensile Properties. in *19th World Conference on Non-Destructive Testing* 1–9 (2016).

45. Dupont-Marillia, F., Jahazi, M., Lafreniere, S. & Belanger, P. Influence of local mechanical properties of high strength steel from large size forged ingot on ultrasonic wave velocities. in *AIP Conference Proceedings* **1806**, (AIP Publishing LLC, 2017).

46. Kumar, A., Laha, K., Jayakumar, T., Rao, K. B. S. & Raj, B. Comprehensive microstructural characterization in modified 9Cr-1Mo ferritic steel by ultrasonic measurements. *Metall. Mater. Trans. A Phys. Metall. Mater. Sci.* **33**, 1617–1626 (2002).

47. Zeng, F., Agnew, S. R., Raeisinia, B. & Myneni, G. R. Ultrasonic attenuation due to

grain boundary scattering in pure niobium. *J. Nondestruct. Eval.* **29**, 93–103 (2010).

48. Stanke, F. E. & Kino, G. S. S. A unified theory for elastic wave propagation in polycrystalline materials. *J. Acoust. Soc. Am.* **75**, 665–681 (1984).

49. Dong, F. *et al.* In-situ measurement of Ti-6Al-4V grain size distribution using laser-ultrasonic technique. *Scr. Mater.* **154**, 40–44 (2018).

50. Weaver, R. L. L. Diffusivity of ultrasound in polycrystals. *J. Mech. Phys. Solids* **38**, 55–86 (1990).

51. Adler, L., Rose, J. H. & Mobley, C. Ultrasonic method to determine gas porosity in aluminum alloy castings: Theory and experiment. *J. Appl. Phys.* **59**, 336–347 (1986).

52. Pan, J. H., Shong, S. B. & Li, J. W. Influence of different forging processes on the ultrasonic response in titanium alloys TC6 and TC11. *NDT Int.* **23**, 103–106 (1990).

53. Du, H. & Turner, J. A. Ultrasonic attenuation in pearlitic steel. *Ultrasonics* **54**, 882–887 (2014).

54. Li, X. *et al.* Grain size evaluation of structural materials in nuclear power plant using a thickness independent ultrasonic method. *Nucl. Instruments Methods Phys. Res. Sect. B Beam Interact. with Mater. Atoms* **351**, 16–22 (2015).

55. Maio, L., Ricci, F., Memmolo, V., Monaco, E. & Boffa, N. D. Application of laser Doppler vibrometry for ultrasonic velocity assessment in a composite panel with defect. *Compos. Struct.* **184**, 1030–1039 (2018).

56. Ghoshal, G. & Turner, J. A. Diffuse ultrasonic backscatter in a two-dimensional domain. *Acta Mech.* **205**, 35–49 (2009).

57. Rose, J. H. Ultrasonic Backscattering from Polycrystalline Aggregates using Time-Domain Linear Response Theory. in *Review of Progress in Quantitative Nondestructive Evaluation* 1715–1720 (Springer US, 1991). doi:10.1007/978-1-4615-3742-7_75

58. Lobkis, O. I., Yang, L., Li, J. & Rokhlin, S. I. Ultrasonic backscattering in polycrystals with elongated single phase and duplex microstructures. *Ultrasonics* **52**, 694–705 (2012).

59. Dupond, O. *et al.* Relation between ultrasonic scattering and microstructure of polycrystalline materials. *J. Phys. Conf. Ser.* **269**, 012010 (2011).

60. Li, J., Yang, L. & Rokhlin, S. I. Effect of texture and grain shape on ultrasonic backscattering in polycrystals. *Ultrasonics* **54**, 1789–1803 (2014).

61. Zhang, J., Song, Y., Li, X. & Zhong, C. Comparison of Experimental Measurements of Material Grain Size Using Ultrasound. *J. Nondestruct. Eval.* **39**, 30 (2020).

62. Margetan, F. J., Gray, T. A. & Thompson, R. B. A Technique for Quantitatively Measuring Microstructurally Induced Ultrasonic Noise. in *Review of Progress in Quantitative Nondestructive Evaluation* 1721–1728 (Springer US, 1991). doi:10.1007/978-1-4615-3742-7_76

63. Ghoshal, G., Turner, J. A. & Weaver, R. L. Wigner distribution of a transducer beam pattern within a multiple scattering formalism for heterogeneous solids. *J. Acoust. Soc. Am.* **122**, 2009–2021 (2007).

64. Hu, P. & Turner, J. A. Contribution of double scattering in diffuse ultrasonic backscatter measurements. *J. Acoust. Soc. Am.* **137**, 321–334 (2015).

65. Matlack, K. H., Kim, J.-Y., Jacobs, L. J. & Qu, J. Review of Second Harmonic Generation Measurement Techniques for Material State Determination in Metals. *J. Nondestruct. Eval.* **34**, 273 (2015).

66. Bjørnø, L. Forty years of nonlinear ultrasound. *Ultrasonics* **40**, 11–17 (2002).

67. Muir, T. G. & Carstensen, E. L. Prediction of nonlinear acoustic effects at biomedical frequencies and intensities. *Ultrasound Med. Biol.* **6**, 345–357 (1980).

68. Mini, R. S., Balasubramaniam, K. & Ravindran, P. An Experimental Investigation on the Influence of Annealed Microstructure on Wave Propagation. *Exp. Mech.* **55**, 1023–1030 (2015).

69. Kundu, T. *Ultrasonic nondestructive evaluation : engineering and biological material characterization*. (CRC Press, 2004).

70. Breazeale, M. A. Whither Nonlinear Acoustics? in *Review of Progress in Quantitative Nondestructive Evaluation* **9**, 1653–1660 (Springer US, 1990).

71. Cantrell, J. H. Crystalline structure and symmetry dependence of acoustic nonlinearity parameters. *J. Appl. Phys.* **76**, 3372–3380 (1994).

72. Mini, R. S., Ravindran, P., Krishnamurthy, C. V. & Balasubramaniam, K. Experimental

and Numerical Investigation of Second Harmonic Generation by Creep Induced Micro-voids. *Exp. Mech.* **60**, 1017–1032 (2020).

73. Rauter, N. & Lammering, R. Numerical simulation of elastic wave propagation in isotropic media considering material and geometrical nonlinearities. *Smart Mater. Struct.* **24**, 045027 (2015).

74. Cantrell, J. H. Nonlinear dislocation dynamics at ultrasonic frequencies. *J. Appl. Phys.* **105**, 043520 (2009).

75. Cash, W. D. & Cai, W. Contribution of dislocation dipole structures to the acoustic nonlinearity. *J. Appl. Phys.* **111**, 074906 (2012).

76. Gao, X. & Qu, J. Acoustic nonlinearity parameter induced by extended dislocations. *J. Appl. Phys.* **124**, 125102 (2018).

77. Hurley, D. C., Balzar, D. & Purtscher, P. T. Nonlinear ultrasonic parameter in quenched martensitic steels. *J. Appl. Phys.* **83**, 4584–4588 (1998).

78. Meikandamurthy, C. *et al.* Effect of cold-work on self-welding susceptibility of austenitic stainless steel (alloy D9) in high temperature flowing sodium. *J. Nucl. Mater.* **407**, 165–170 (2010).

79. Ashby, M. F. The deformation of plastically non-homogeneous materials. *Philos. Mag. A J. Theor. Exp. Appl. Phys.* **21**, 399–424 (1970).

80. Zhang, J., Li, S., Xuan, F.-Z. & Yang, F. Effect of plastic deformation on nonlinear ultrasonic response of austenitic stainless steel. *Mater. Sci. Eng. A* **622**, 146–152 (2015).

81. Shin, H. C., Ha, T. K. & Chang, Y. W. Kinetics of deformation induced martensitic transformation in a 304 stainless steel. *Scr. Mater.* **45**, 823–829 (2001).

82. Lee, T.-H., Shin, E., Oh, C.-S., Ha, H.-Y. & Kim, S.-J. Correlation between stacking fault energy and deformation microstructure in high-interstitial-alloyed austenitic steels. *Acta Mater.* **58**, 3173–3186 (2010).

83. Schramm, R. E. & Reed, R. P. Stacking fault energies of seven commercial austenitic stainless steels. *Metall. Trans. A* **6**, 1345–1351 (1975).

84. Rao, V. V. S. J., Kannan, E., Prakash, R. V. & Balasubramaniam, K. Observation of two stage dislocation dynamics from nonlinear ultrasonic response during the plastic

deformation of AA7175-T7351 aluminum alloy. *Mater. Sci. Eng. A* **512**, 92–99 (2009).

85. Zhang, J., Xuan, F. & Xiang, Y. Dislocation characterization in cold rolled stainless steel using nonlinear ultrasonic techniques: A comprehensive model. *EPL (Europhysics Lett.* **103**, 68003 (2013).

86. Zhang, J. & Xuan, F. A general model for dislocation contribution to acoustic nonlinearity. *EPL (Europhysics Lett.* **105**, 54005 (2014).

87. Cantrell, J. H. Quantitative assessment of fatigue damage accumulation in wavy slip metals from acoustic harmonic generation. *Philos. Mag.* **86**, 1539–1554 (2006).

88. Kim, J.-Y., Jacobs, L. J., Qu, J. & Littles, J. W. Experimental characterization of fatigue damage in a nickel-base superalloy using nonlinear ultrasonic waves. *J. Acoust. Soc. Am.* **120**, 1266–1273 (2006).

89. Cantrell, J. H. & Yost, W. T. Nonlinear ultrasonic characterization of fatigue microstructures. *Int. J. Fatigue* **23**, 487–490 (2001).

90. Amura, M. & Meo, M. Prediction of residual fatigue life using nonlinear ultrasound. *Smart Mater. Struct.* **21**, (2012).

91. Cantrell, J. H. Ultrasonic harmonic generation from fatigue-induced dislocation substructures in planar slip metals and assessment of remaining fatigue life. *J. Appl. Phys.* **106**, 093516 (2009).

92. Palit Sagar, S., Das, S., Parida, N. & Bhattacharya, D. K. Non-linear ultrasonic technique to assess fatigue damage in structural steel. *Scr. Mater.* **55**, 199–202 (2006).

93. Kumar, A., Torbet, C. J., Pollock, T. M. & Wayne Jones, J. In situ characterization of fatigue damage evolution in a cast Al alloy via nonlinear ultrasonic measurements. *Acta Mater.* **58**, 2143–2154 (2010).

94. Ogi, H., Hirao, M. & Aoki, S. Noncontact monitoring of surface-wave nonlinearity for predicting the remaining life of fatigued steels. *J. Appl. Phys.* **90**, 438–442 (2001).

95. Ellwood, R., Stratoudaki, T., Sharples, S. D., Clark, M. & Somekh, M. G. Investigation of the fatigue process using nonlinear ultrasound. *J. Phys. Conf. Ser.* **278**, 012013 (2011).

96. Walker, S. V., Kim, J. Y., Qu, J. & Jacobs, L. J. Fatigue damage evaluation in A36 steel

using nonlinear Rayleigh surface waves. *NDT E Int.* **48**, 10–15 (2012).

97. Balasubramaniam, K., Valluri, J. S. & Prakash, R. V. Creep damage characterization using a low amplitude nonlinear ultrasonic technique. *Mater. Charact.* **62**, 275–286 (2011).

98. Wang, X. X., Wang, X. X., Niu, X. guang, Xiao, D. ming & Hu, X. long. Application of nonlinear ultrasonic technique to characterize the creep damage in ASME T92 steel welded joints. *NDT E Int.* **98**, 8–16 (2018).

99. Cantrell, J. H. & Yost, W. T. Effect of precipitate coherency strains on acoustic harmonic generation. *J. Appl. Phys.* **81**, 2957–2962 (1997).

100. Matlack, K. H. *et al.* Nonlinear ultrasonic characterization of precipitation in 17-4PH stainless steel. *NDT E Int.* **71**, 8–15 (2015).

101. ROKHLIN, S. & KIM, J. In situ ultrasonic monitoring of surface fatigue crack initiation and growth from surface cavity. *Int. J. Fatigue* **25**, 41–49 (2003).

102. Buck, O., Morris, W. L. & Richardson, J. M. Acoustic harmonic generation at unbonded interfaces and fatigue cracks. *Appl. Phys. Lett.* **33**, 371–373 (1978).

103. Nazarov, V. E. & Sutin, A. M. Nonlinear elastic constants of solids with cracks. *J. Acoust. Soc. Am.* **102**, 3349–3354 (1997).

104. Solodov, I. Y. Ultrasonics of non-linear contacts: propagation, reflection and NDE-applications. *Ultrasonics* **36**, 383–390 (1998).

105. Wegner, A. *et al.* Assessment of the adhesion quality of fusion-welded silicon wafers with nonlinear ultrasound. *Ultrasonics* **38**, 316–321 (2000).

106. Hirsekorn, S. Nonlinear transfer of ultrasound by adhesive joints – a theoretical description. *Ultrasonics* **39**, 57–68 (2001).

107. Chen, X. J. *et al.* Characterization of progressive microcracking in Portland cement mortar using nonlinear ultrasonics. *NDT E Int.* **41**, 112–118 (2008).

108. Burgers, J. M. Geometrical considerations concerning the structural irregularities to be assumed in a crystal. in *Proceedings of the Physical Society* **23**, (1940).

109. Bragg, W. L. Discussion. Part I. *Proc. Phys. Soc.* **52**, 54–57 (1940).

110. T., R. W., W., S., Read, W. T. T. & Shockley, W. Dislocation Models of Crystal Grain Boundaries. *Phys. Rev.* **78**, 275 (1950).

111. Berdichevsky, V. L. On dislocation models of grain boundaries. *Contin. Mech. Thermodyn.* **23**, 185–209 (2011).

112. Gao, X. & Qu, J. Contribution of dislocation pileups to acoustic nonlinearity parameter. *J. Appl. Phys.* **125**, 215104 (2019).

113. Mullins, W. W. Two-Dimensional Motion of Idealized Grain Boundaries. *J. Appl. Phys.* **27**, 900–904 (1956).

114. Yue, C., Zhang, L., Liao, S. & Gao, H. Kinetic Analysis of the Austenite Grain Growth in GCr15 Steel. *J. Mater. Eng. Perform.* **19**, 112–115 (2010).

115. Rodrigo Pinto de Siqueira, José Flávio Silveira Feiteira, Dionísio José Rodrigues da Costa & Jefferson Fabrício Cardoso Lins. Investigation of the Grain Growth Evolution in the AISI 304H Austenitic Stainless Steel. *J. Mech. Eng. Autom.* **6**, (2016).

116. Shirdel, M., Mirzadeh, H. & Parsa, M. H. Materials Characterization Abnormal grain growth in AISI 304L stainless steel. *Mater. Charact.* **97**, 11–17 (2014).

117. Shirdel, M., Mirzadeh, H. & Habibi Parsa, M. Microstructural Evolution During Normal/Abnormal Grain Growth in Austenitic Stainless Steel. *Metall. Mater. Trans. A* **45**, 5185–5193 (2014).

118. Choi, S., Ryu, J., Kim, J.-S. & Jhang, K.-Y. Comparison of Linear and Nonlinear Ultrasonic Parameters in Characterizing Grain Size and Mechanical Properties of 304L Stainless Steel. *Metals (Basel).* **9**, 1279 (2019).

119. Krishnamurthy, S. S. C. V *et al.* Numerical Modelling Methods for Ultrasonic Wave Propagation Through Polycrystalline Materials. *Trans. Indian Inst. Met.* **72**, 31–33 (2019).

120. Shivaprasad, S., Pandala, A., Krishnamurthy, C. V & Balasubramaniam, K. Wave localized finite-difference-time-domain modelling of scattering of elastic waves within a polycrystalline material. *J. Acoust. Soc. Am.* **144**, 3313–3326 (2018).

121. Ledbetter, H. M. Monocrystal-Polycrystal Elastic Constants of a Stainless Steel. *Phys. Status Solidi* **85**, 89–96 (1984).

122. Narasimha, K. T., Kannan, E., Balasubramaniam, K., Thompson, D. O. & Chimenti, D. E. STATIC DISPLACEMENT COMPONENT AND ITS SIGNIFICANCE IN NONLINEAR ULTRASONIC MEASUREMENTS. in *AIP Conference Proceedings* **975**, 1282–1289 (AIP, 2008).

123. Cantrell, J. H. Acoustic-radiation stress in solids. I. Theory. *Phys. Rev. B* **30**, 3214–3220 (1984).

124. Ren, G., Kim, J. & Jhang, K. Y. Relationship between second- and third-order acoustic nonlinear parameters in relative measurement. *Ultrasonics* **56**, 539–544 (2015).

125. Liu, X., Li, J., Gong, X., Zhu, Z. & Zhang, D. Theoretical and experimental study of the third-order nonlinearity parameter C/A for biological media. *Phys. D Nonlinear Phenom.* **228**, 172–178 (2007).

126. Siming Liu, Croxford, A. J., Neild, S. A. & Zhenggan Zhou. Effects of experimental variables on the nonlinear harmonic generation technique. *IEEE Trans. Ultrason. Ferroelectr. Freq. Control* **58**, 1442–1451 (2011).

127. Rogers, P. H. & Van Buren, A. L. An exact expression for the Lommel-diffraction correction integral. *J. Acoust. Soc. Am.* **55**, 724–728 (1974).

128. Hurley, D. C. & Fortunko, C. M. Determination of the nonlinear ultrasonic parameter β using a Michelson interferometer. *Meas. Sci. Technol.* **8**, 634–642 (1997).

129. Kundu, T. *Ultrasonic nondestructive evaluation: Engineering and biological material characterization*. *Ultrasonic Nondestructive Evaluation: Engineering and Biological Material Characterization* (CRC Press, 2003).

130. Papadakis, E. P. Revised Grain-Scattering Formulas and Tables. *The Journal of the Acoustical Society of America* **36**, 1019–1019 (1964).

131. Papadakis, E. P. Rayleigh and Stochastic Scattering of Ultrasonic Waves in Steel. *J. Appl. Phys.* **34**, 265–269 (1963).

132. Jeong, H., Zhang, S., Barnard, D. & Li, X. Significance of accurate diffraction corrections for the second harmonic wave in determining the acoustic nonlinearity parameter. *AIP Adv.* **5**, (2015).

133. Torello, D. *et al.* Diffraction, attenuation, and source corrections for nonlinear Rayleigh

wave ultrasonic measurements. *Ultrasonics* **56**, 417–426 (2015).

134. Cantrell, J. H., Thompson, D. O. & Chimenti, D. E. Nondestructive Evaluation of Metal Fatigue Using Nonlinear Acoustics. *AIP Conf. Proc.* **28**, 19–32 (2009).

135. Xiang, Y.-X. X., Deng, M.-X. X., Xuan, F.-Z. Z., Chen, H. & Chen, D.-Y. Y. Creep damage evaluation of titanium alloy using nonlinear ultrasonic lamb waves. *Chinese Phys. Lett.* **29**, 106202 (2012).

136. Deng, M.-X., Xiang, Y.-X. & Liu, L.-B. Time-Domain Second-Harmonic Generation of Primary Lamb-Wave Propagation in an Elastic Plate. *Chinese Phys. Lett.* **28**, 074301 (2011).

137. Xiang, Y., Deng, M., Xuan, F.-Z. Z. & Liu, C.-J. J. Effect of precipitate-dislocation interactions on generation of nonlinear Lamb waves in creep-damaged metallic alloys. *J. Appl. Phys.* **111**, 104905 (2012).

138. Kim, C. S. & Lissenden, C. J. Precipitate contribution to the acoustic nonlinearity in nickel-based superalloy. *Chinese Phys. Lett.* **26**, (2009).

139. Hikata, A., Sewell, F. A. & Elbaum, C. Generation of ultrasonic second and third harmonics due to dislocations. II. *Phys. Rev.* **151**, 442–449 (1966).

140. Liu, M. *et al.* MEASURING RESIDUAL STRESS USING NONLINEAR ULTRASOUND. in *AIP Conference Proceedings* **1211**, 1365–1372 (2010).

141. Taylor, L. H. & Rollins, F. R. Ultrasonic study of three-phonon interactions. I. Theory. *Phys. Rev.* **136**, A591–A596 (1964).

142. Childress, J. D. & Hambrick, C. G. Interactions Between Elastic Waves in an Isotropic Solid. *Phys. Rev.* **136**, A411–A418 (1964).

143. Korneev, V. A. & Demčenko, A. Possible second-order nonlinear interactions of plane waves in an elastic solid. *J. Acoust. Soc. Am.* **135**, 591–598 (2014).

144. Jingpin, J., Junjun, S., Guanghai, L., Bin, W. & Cunfu, H. Evaluation of the intergranular corrosion in austenitic stainless steel using collinear wave mixing method. *NDT E Int.* **69**, 1–8 (2015).

145. Demčenko, A., Koissin, V. & Korneev, V. A. A. Noncollinear wave mixing for measurement of dynamic processes in polymers: Physical ageing in thermoplastics and

epoxy cure. *Ultrasonics* **54**, 684–693 (2014).

146. Demčenko, A., Akkerman, R., Nagy, P. B. & Loendersloot, R. Non-collinear wave mixing for non-linear ultrasonic detection of physical ageing in PVC. *NDT E Int.* **49**, 34–39 (2012).

147. Croxford, A. J., Wilcox, P. D., Drinkwater, B. W. & Nagy, P. B. The use of non-collinear mixing for nonlinear ultrasonic detection of plasticity and fatigue. *J. Acoust. Soc. Am.* **126**, EL117–EL122 (2009).

148. Sun, M., Xiang, Y., Deng, M., Xu, J. & Xuan, F. Z. Scanning non-collinear wave mixing for nonlinear ultrasonic detection and localization of plasticity. *NDT E Int.* **93**, 1–6 (2018).

149. Zhang, X.-G. *et al.* Ultrasonic attenuation due to grain boundary scattering in copper and copper-aluminum. *J. Acoust. Soc. Am.* **116**, 109–116 (2004).

150. Harris, F. J. On the use of windows for harmonic analysis with the discrete Fourier transform. *Proc. IEEE* **66**, 51–83 (1978).

151. Celada-Casero, C., Kooiker, H., Groen, M., Post, J. & San-Martin, D. In-Situ Investigation of Strain-Induced Martensitic Transformation Kinetics in an Austenitic Stainless Steel by Inductive Measurements. *Metals (Basel).* **7**, 271 (2017).

152. Vincent, A., Pasco, L., Morin, M., Kleber, X. & Delnondedieu, M. Magnetic Barkhausen noise from strain-induced martensite during low cycle fatigue of 304L austenitic stainless steel. *Acta Mater.* **53**, 4579–4591 (2005).

153. Ren, L., Nan, L. & Yang, K. Study of copper precipitation behavior in a Cu-bearing austenitic antibacterial stainless steel. *Mater. Des.* **32**, 2374–2379 (2011).

154. Xi, T. *et al.* Copper precipitation behavior and mechanical properties of Cu-bearing 316L austenitic stainless steel: A comprehensive cross-correlation study. *Mater. Sci. Eng. A* **675**, 243–252 (2016).

155. Humphreys, A. O. & Humphreys, F. J. The microstructure and microtexture of pure aluminium during recovery. in *Proceedings of ICAA-4* 211–218 (1994).

156. Cheong, S. W. & Weiland, H. Understanding a Microstructure Using GOS (Grain Orientation Spread) and Its Application to Recrystallization Study of Hot Deformed Al-

Cu-Mg Alloys. *Mater. Sci. Forum* **558**–**559**, 153–158 (2007).

157. Alvi, M. H., Cheong, S. W., Weiland, H. & Rollett, A. D. Recrystallization and Texture Development in Hot Rolled 1050 Aluminum. *Mater. Sci. Forum* **467**–**470**, 357–362 (2004).

158. Smith, R. L. The effect of grain size distribution on the frequency dependence of the ultrasonic attenuation in polycrystalline materials. *Ultrasonics* **20**, 211–214 (1982).

159. Norouzian, M., Islam, S. & Turner, J. A. Influence of microstructural grain-size distribution on ultrasonic scattering. *Ultrasonics* **102**, 106032 (2020).

160. Arguelles, A. P. & Turner, J. A. Ultrasonic attenuation of polycrystalline materials with a distribution of grain sizes. *J. Acoust. Soc. Am.* **141**, 4347–4353 (2017).

161. Bai, X., Zhao, Y., Ma, J., Liu, Y. & Wang, Q. Grain-Size Distribution Effects on the Attenuation of Laser-Generated Ultrasound in α-Titanium Alloy. *Materials (Basel).* **12**, 102 (2018).

162. Cândido, N. *et al.* Microstructural variations at different distance from the surface in forged 18 Ni C300 maraging steel. *Integr. Med. Res.* **8**, 284–291 (2018).

163. Castro Güiza, G. M. & Oliveira, C. A. S. Microstructural changes produced by hot forging in a C300 Maraging Steel. *Mater. Sci. Eng. A* **655**, 142–151 (2016).

164. Shen, X., Yan, J., Zhang, L., Gao, L. & Zhang, J. Austenite Grain Size Evolution in Railway Wheel During Multi-Stage Forging Processes. *J. Iron Steel Res. Int.* **20**, 57–65 (2013).

165. Prawoto, Y., Jasmawati, N. & Sumeru, K. Effect of Prior Austenite Grain Size on the Morphology and Mechanical Properties of Martensite in Medium Carbon Steel. *J. Mater. Sci. Technol.* **28**, 461–466 (2012).

166. Kube, C. M. & Norris, A. N. Bounds on the longitudinal and shear wave attenuation ratio of polycrystalline materials. *J. Acoust. Soc. Am.* **141**, 2633–2636 (2017).

167. Benyelloul, K. & Aourag, H. Elastic constants of austenitic stainless steel: Investigation by the first-principles calculations and the artificial neural network approach. *Comput. Mater. Sci.* **67**, 353–358 (2013).

168. Sinczak, J., Majta, J., Glowacki, M. & Pietrzyk, M. Prediction of mechanical properties

of heavy forgings. *J. Mater. Process. Technol.* **80**–**81**, 166–173 (1998).

169. Nagy, P. B. Fatigue damage assessment by nonlinear materials characterization. *Ultrasonics* **36**, 375–381 (1998).

170. Raj, B. Materials and Manufacturing Technologies for Sodium Cooled Fast Reactors and Associated Fuel Cycle: Innovations and Maturity. *Energy Procedia* **7**, 186–198 (2011).

171. Nagy, E., Mertinger, V., Tranta, F. & Sólyom, J. Deformation induced martensitic transformation in stainless steels. *Mater. Sci. Eng. A* **378**, 308–313 (2004).

172. Graça, S., Colaço, R., Carvalho, P. A. & Vilar, R. Determination of dislocation density from hardness measurements in metals. *Mater. Lett.* **62**, 3812–3814 (2008).

173. Bay, B., Hansen, N., Hughes, D. A. & Kuhlmann-Wilsdorf, D. Overview no. 96 evolution of f.c.c. deformation structures in polyslip. *Acta Metall. Mater.* **40**, 205–219 (1992).

174. Chen, R. C., Hong, C., Li, J. J., Zheng, Z. Z. & Li, P. C. Austenite grain growth and grain size distribution in isothermal heat-treatment of 300M steel. *Procedia Eng.* **207**, 663–668 (2017).

175. Long, D., Viovy, J., Ajdari, A., Zarembo, L. K. & Krasil Nikov, V. A. Nonlinear phenomena in the propagation of elastic waves in solids. *J. physics. Condens. matter* **8**, 9471 (1996).

176. Escobar-Ruiz, E. *et al.* Non-linear ultrasonic NDE of titanium diffusion bonds. *J. Nondestruct. Eval.* **33**, 187–195 (2014).

Thesis Highlights

Name of the Student: SAJU T ABRAHAM
Name of the CI/OCC: IGCAR **Enrolment No.:** ENGG02201304007
Thesis Title: Characterization of polycrystalline microstructure using ultrasonic nonlinearity parameter
Discipline: Engineering Sciences **Sub-Area of Discipline:** Materials Science
Date of viva voce: 16-02-2021

This thesis deals with the nonlinear ultrasonic studies on the polycrystalline austenitic stainless steel material. The lognormal distribution of grain size results in different acoustic scattering regimes to coexist and have different effects on the acoustic nonlinearity parameter. Therefore, characterization of a polycrystalline material using a single-frequency nonlinear response, assuming a mean grain size, is insufficient.

To this end, detailed experimental investigations were carried out on the annealed, forged and deformed microstructures. The novel multi-frequency (ω_i) methodology introduced in this thesis significantly improves the reliability of structure-property correlations in polycrystalline materials. The acoustic nonlinearity parameter β was found reducing linearly with grain growth in the Rayleigh scattering regime and deviating from this linearity in the Rayleigh to stochastic transition zone. The multi-frequency approach reveals that the change in the order of β_{ω_i} or the deviation in $\Delta\beta_{\omega_{i,j}}$ with grain coarsening can be used as a precursor for undesired grain growth in polycrystalline materials. This approach can be employed for rapid screening of materials with unknown process history where wide variations and distributions of grain sizes are expected. Experimental and numerical studies on the effect of grain size distribution have revealed that the material with wide grain size distribution exhibits reduced nonlinearity. The results infer the significance of considering the distribution width in characterizing the microstructural features from the nonlinear response of the material. It is also demonstrated that the nonlinearity parameter can be used to study the plastic deformation even in the presence of grain size variations. The results are important in developing nonlinear ultrasonics as a robust nondestructive evaluation technique for microstructural characterization of polycrystalline materials.

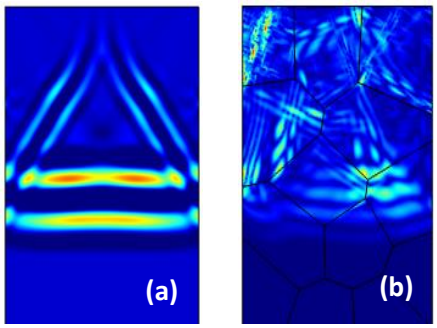

Wave propagation in (a) isotropic and (b) polycrystalline medium.

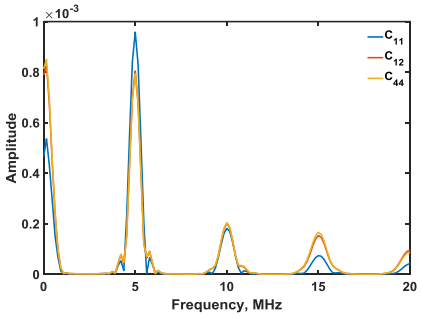

Harmonic generation in different crystallographic directions

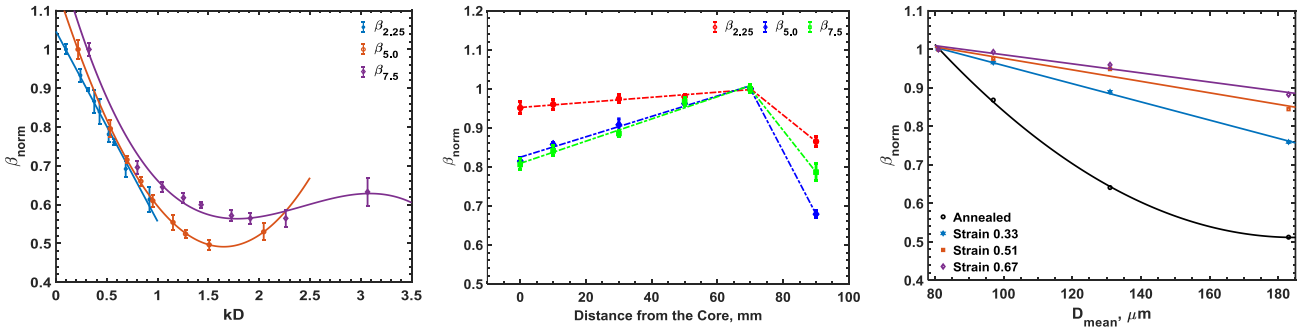

Acoustic nonlinearity parameter as a function of (a) the reduced wavenumber, kD, (b) heterogeneous microstructure and abnormal grain growth and (c) grain size and plastic deformation